Development of graphene-based composite materials for electrochemical storage applications

Harish Banda

▶ To cite this version:

HAL Id: tel-02003297
https://theses.hal.science/tel-02003297

Submitted on 1 Feb 2019

THÈSE

Pour obtenir le grade de

DOCTEUR DE LA COMMUNAUTE UNIVERSITE GRENOBLE ALPES

Spécialité : **Chimie Physique Moléculaire et Structurale**

Arrêté ministériel : 25 mai 2016

Présentée par

Harish BANDA

Thèse dirigée par **Lionel DUBOIS, Chercheur, CEA Grenoble**, et codirigée par **Florence DUCLAIROIR, Chercheure, CEA Grenoble**

préparée au sein du **Laboratoire de Systèmes Moléculaires et Nanomatériaux pour l'Energie et la Santé**
dans **l'École Doctoral Chimie et Sciences du Vivant**

Développement de matériaux composites à base de graphène pour des applications en stockage électrochimique

Development of graphene-based composite materials for electrochemical storage applications

Thèse soutenue publiquement le **19 octobre 2018**
devant le jury composé de :

Madame Encarnacion, RAYMUNDO
Directrice de Recherche CNRS, CEMHTI Orléans, Rapporteur
Monsieur Daniel, BELANGER
Professeur, Université du Québec à Montréal, Rapporteur
Madame Fannie, ALLOIN
Directrice de Recherche CNRS, Université de Grenoble Alpes-LEPMI, Président
Monsieur Patrice, SIMON
Professeur, Université de Toulouse-CIRIMAT, Examinateur
Monsieur Lionel, DUBOIS
Chercheur CEA, SyMMES, CEA Grenoble, Directeur de thèse
Madame Florence, DUCLAIROIR
Chercheure CEA, SyMMES, CEA Grenoble, Membre invitée

A quiet and modest life brings more happiness than the pursuit of success and the constant restlessness that comes with it.

<div align="right">

-Albert Einstein's note to a courier-boy

</div>

Acknowledgements

Thanks to Yves for helping me settle in the lab and being there whenever necessary. I have certainly learnt a lot from you including swimming, fishing, hunting crystals & mushrooms, cementing walls, making pasta and so on. I enjoyed learning these life skills and will certainly carry on these in to my life hereafter. Johan, it was so much fun to have you around. It was you that has brought in the office coffee-culture into the lab and I feel that I get undeserved credit for that. Regardless, it was amazing to have had so many discussions and have shared many more beers at the Bristrot d'Emile. Sandy, I cannot thank you enough for a super work-attitude and efficiency that you have brought to me in the last one year. I appreciate your amazing patience in putting up with my poor management style. All in all, I must mention, we were a good team and I will miss that.

I would like to thank Chady, Fanny, Romain and Seydou for advising me with their experience and guidance about the hard PhD life. I thank Jeremy, Julia, Coralie, Laura, Marc, Aditya, Guillaume, Elena, Celine, Jordan and Friaume for all the fun at the lunches, bars, dinners, barbeques and all over Grenoble! Tugce, I thank you for the humour and positive attitude. It's a pity that we didn't know each other for almost a year but then, god bless the Global Young Scientists Summit in Singapore for making things right. I thank my friends Vinil, Ramesh, Ashok and Ajay for all the encouragement, support and understanding all through the tough times (ధన్యవాదాలు మిత్రులారా).

I thank the Trippers; Sarang, Prasanna, Ram, Sumanth, Rathod, Gali, Siva and Daniel for the amazing five years at IISER and the continued friendship and support ever after (धन्यवाद दोस्तों). It gives me great comfort in knowing that you are always there. I thank Gourab, Cinzia, Push, Shashank, Keerthi, Aditya, Ritesh, Nishit and Arindham for making my Grenoble life an enjoyable one.

I express my heartfelt gratitude towards all my family members and all well-wishers. Finally, I thank my parents and brother & sister-in law for their constant support, confidence and understanding all through my career and especially during the PhD.

నేను నా కుటుంబ సభ్యులకు (బండ మరియు కర్క) మరియు శ్రేయోభిలాషులకు వారి మద్దతు కోసం కృతజ్ఞతలు తెలియజేస్తున్నాను. ముఖ్యంగా, నా తల్లిదండ్రులు మద్దతు మరియు విశ్వాసం నా ప్రయత్నాలలో గొప్పగా సహాయపడింది. నేను ఈ నిరంతర మద్దతు కోసం వారికి నా కృతజ్ఞతలు తెలియజేస్తున్నాను. చిన్ననాటి నుండి సహాయం కోసం నా తాత, అమ్మమ్మ మరియు మధు అన్నలకు నేను ప్రత్యేకంగా కృతజ్ఞతలు తెలుపుతున్నాను.

Abbreviations

SCs: Supercapacitors

EDLC: Electrical Double Layer Capacitor

2D: Two-Dimensional

3D: Three-Dimensional

AC: Activated Carbon

CDC: Carbide-Derived Carbon

CNT: Carbon Nanotubes

GO: Graphene Oxide

RGO: Reduced Graphene Oxide

GHs: Graphene Hydrogels

RPs: Reduced Pillar Graphene Materials

CVD: Chemical Vapor Deposition

FT-IR: Fourier Transform – Infrared

TGA: Thermal Gravimetric Analysis

XRD: X-Ray Diffraction

XPS: X-Ray Photoelectron Spectroscopy

SEM: Scanning Electron Microscopy

BET: Brunauer-Emmett-Teller method

DFT: Density Functional Theory

SSA: Specific Surface Area

EIS: Electrochemical Impedance Spectroscopy

TAABF$_4$: Tetraalkylammonium tetrafluoroborate

Contents

Table of Contents

General Introduction

General Introduction

Climate change and dwindling fossil fuels are among the major challenges that our societies are currently facing.[1] The increasing demand for energy from growing populations and higher standards of living is resulting in rapid consumption of the limited fossil fuels. Additionally, the burning of fossil fuels for energy production also produces large amounts of toxic SO_x, NO_x gases along with other greenhouse gasses such as CO_2 and CH_4.[2] Although energy security is at the core of the issue, the impact of the energy policies extends into far reaching realms of environment, health, jobs, and economic costs. As a result, scientists, businesses and policy makers are working extensively towards developing clean and sustainable solutions for energy production from inexhaustible sources such as solar, wind, tidal, geothermal, etc. However, the intermittent nature of these sources requires efficient energy storage systems.

Energy is typically stored in the form of chemical, mechanical or thermal energy, but conversion of such energy into electricity incurs further losses. In this context, electrochemical devices offer great potential with their ability to store and deliver electrical energy with minimum losses to conversion.[3] Rechargeable batteries and electrochemical double layer capacitors are two main electrochemical devices that offer safe on-board energy storage. Batteries store electric charge in faradaic chemical reactions and offer high energy densities in the range of 50 – 200 Wh/kg.[1] In fact, these high energy densities of batteries have facilitated the exponential growth of portable electronics from the early 1990s to the present day. However, the kinetics of the faradaic reactions in batteries limit faster delivery/uptake of the energy and result in lower power densities (rate of energy consumption) of ~ 1 kW/Kg. The next generation of portable electronics and development of electric vehicles require devices that could offer both high energy and power densities.

Electrochemical double layer capacitors, also known as supercapacitors (SCs), store energy through non-faradaic electrolytic ion sorption on charged electrode surfaces.[4] This non-faradaic nature of the storage enables high power performance (15 kW/kg) and cycle life (>10^6 cycles), but suffers from low energy density (6 Wh/kg) as compared to batteries.[1] Hence, there is a huge interest in increasing the energy densities of supercapacitors. Higher energy densities could be achieved by using electrode materials that offer high electrochemical active surface

area and electrolytes with large voltage windows.[5] Porous carbons, such as activated carbons (ACs), are traditionally used as electrode materials due to their high surface areas and low costs.

Recently, various graphene derivatives (reduced graphene oxide (RGO), graphene hydrogels, etc.) have been proposed as potential electrode materials in SCs owing to their high electrical conductivities, large surface areas and mechanical flexibilities.[6] RGO, which is readily prepared from graphene oxide (GO), is extensively studied as a model graphene-like material. RGO displays good power capability but suffers from low capacitances as the reduced graphene sheets partially restack through π- π interactions.[7] Various three-dimensional (3D) architectures based on graphene (aerogels, films and fibers) are being evaluated to mitigate such restacking with a focus on tuning the material porosity.[8] Much of this current research in graphene derivatives is devoted to improving the porosity characteristics for higher surface areas, similar to the research on ACs. Surprisingly, little attention has been devoted to exploring the unique layered structures of graphene derivatives in SCs.

This thesis aims at achieving enhanced energy and power densities in supercapacitors using chemically functionalized graphene derivatives as electrodes. The specific idea is to explore the possibility of storing charges in between the layers of a graphene derivative. The naturally occurring graphitic stacking in graphene-derivatives has an inter-layer separation of 0.33 nm, which could be narrow for some ions in SCs. Hence, expanded layered structures of graphene derivatives were synthesized using alkyl diamines as spacers (pillars) and graphene oxide (GO) as a precursor. We speculated that such expanded layered structures could offer possible ion sorption sites through ion desolvation and confinement effects as earlier seen in ACs. We believed that this approach could be complementary to the 3D graphene architectures towards high energy densities in SCs, so we studied pillared 3D graphene assemblies.

The results obtained during the thesis are written in this document in the form scientific articles. The four articles based on this work are presented as four chapters (2nd-5th) with an additional detailed account of the specific objectives and conclusions obtained. Each article is presented in the format of the respective scientific journal with abstract, introduction, results, etc. Nevertheless, the supplementary information of each article is embedded into the chapter in the proper sections for ease of reading.

In **the first chapter** of this thesis, bibliographical background covering the following aspects is presented: basic principles of SCs, concepts for improved charge storage through design of cell elements, state-of-the-art electrode materials and electrolytes used in current SCs and their merits and demerits. Particular attention has been devoted to graphene-based material as this thesis work is mainly based on such materials. Charge storage mechanisms through desolvation and confinement in porous carbons are also presented from a fundamental point of view. Specific objectives of this thesis and the material design strategies adopted are discussed at the end.

The second chapter presents our initial approach towards synthesizing 3D graphene monoliths with varied inter-layer separation using short alkyl diamines (hydrazine (C=0), 1,2-diaminoethane (C=2), 1,4-diaminobutane (C=4)) as gel formation agents. Various characterization methods were used to analyze the physicochemical properties of the synthesized monoliths. Among the different monoliths produced, a highly conductive graphene hydrogel was obtained in a single-step reaction using hydrazine hydrate as the gelation agent. The synthesized material, when used as an electrode in 6 M KOH electrolyte, delivered excellent power capability (190 at 0.5 A/g and 123 F/g at 100 A/g) in SCs owing to its high electrical conductivity of 1140 S/m. This initial study using different diamines gave further insights and perspectives into the gel formation ability and reducing nature of various diamines.

The shorter diamines (C=2, 4) used in the previous chapter showed little or no changes in the layered structures of graphene compared to a directly reduced graphene oxide (using hydrazine hydrate). In **the third chapter** various pillared graphene materials were synthesized using longer diamines (C=5, 6, 8). The syntheses and associated characterization studies of the pillared materials are described in detail. X-ray diffraction patterns confirmed formation of expanded layered graphene structure that have varied inter-layer separation depending on alkyl chain length. A comprehensive study of ion sieving in SCs using various electrolyte ion sizes in an organic electrolyte has shown that ions could access the inter-layer galleries when the naked ion sizes are smaller than the inter-layer gallery height (defined by d-spacing).

Electrochemical impedance spectroscopic (EIS) analyses of the pillared materials under positive and negative electrode polarization are presented in **the fourth chapter**. Extremely

impeded ion transport dynamics were observed in the pillared graphene materials as the large number of pillars in between the layers sterically hinders the ion transport. This study gave important perspectives towards synthesis of pillared materials with favorable ion transport dynamics. Banking on the conclusions from the fourth chapter, **fifth chapter** presents pillared graphene materials with optimized number of pillars. The optimized materials have accessible surface areas and enhanced ion transport characteristics which resulted in both improved energy and power densities. A systematic lowering of the diamine pillars number of equivalents has improved ion access and transport to the adsorption sites. A 3D assembly (monolith) was also synthesized with low number of diamine pillars along with additional macro porosity. A simple drying procedure of this monolith allowed synthesis of the above material with high density (1.1 g/cm^3) which enabled high volumetric capacitances ~200 F/cm^3.

The results obtained in all the chapters and the overall thesis work are summarized in the **sixth chapter**. The perspectives gained from this thesis work for the field of energy storage and beyond are also discussed. **The seventh chapter** describes the materials and methods used for all syntheses and characterizations in this thesis. Extensive details about the SCs electrode fabrication and analysis in two, three-electrode SC devices are also presented. Finally, the electrochemical techniques used in this thesis are described in an annex.

References

(1)   Simon, P.; Gogotsi, Y. Materials for Electrochemical Capacitors. Nat. Mater. 2008, 7 (11), 845.

(2)   Rao, S.; Klimont, Z.; Smith, S. J.; Van Dingenen, R.; Dentener, F.; Bouwman, L.; Riahi, K.; Amann, M.; Bodirsky, B. L.; van Vuuren, D. P.; et al. Future Air Pollution in the Shared Socio-Economic Pathways. Glob. Environ. Change 2017, 42, 346–358.

(3)   Armand, M.; Tarascon, J.-M. Building Better Batteries. Nature 2008, 451, 652.

(4)   Conway, B. E. Electrochemical Supercapacitors - Scientific Fundamentals and Technological Applications; Springer International Publishing: NewYork, 1999.

(5)   Béguin, F.; Presser, V.; Balducci, A.; Frackowiak, E. Carbons and Electrolytes for Advanced Supercapacitors. Adv. Mater. 2014, 26 (14), 2219–2251.

(6)   Raccichini, R.; Varzi, A.; Passerini, S.; Scrosati, B. The Role of Graphene for Electrochemical Energy Storage. Nat. Mater. 2015, 14 (3), 271.

(7)   Stoller, M. D.; Park, S.; Zhu, Y.; An, J.; Ruoff, R. S. Graphene-Based Ultracapacitors. Nano Lett. 2008, 8 (10), 3498–3502.

(8)   Li, C.; Shi, G. Functional Gels Based on Chemically Modified Graphenes. Adv. Mater. 2014, 26 (24), 3992–4012.

CHAPTER I:
Bibliography

Chapter I. Bibliography

1. Supercapacitors

1.1 Interest in Supercapacitors

Climate change and depletion of fossil fuels are among the pressing challenges that require urgent and sustainable solutions. Release of greenhouse gasses such as CO_2 and CH_4 from using fossil fuels for electricity production and vehicular applications threaten to increase the global temperatures, rise the sea levels and cause extreme weather patterns.[1,2] Additionally, burning of fossil fuels also produces large amounts of toxic SO_x and NO_x gases leading to significant air pollution. Hence, scientists and policy makers are working extensively towards developing clean and sustainable energy solutions. Much effort has been put into studying renewable energy sources such as wind or solar to produce electricity for various applications. However, the intermittent nature of these resources requires intermediate energy storage systems that could store energy when available and deliver when required. Electrochemical energy storage systems offer great potential with their ability to store and deliver electrical energy with minimum losses to conversion.[3,4]
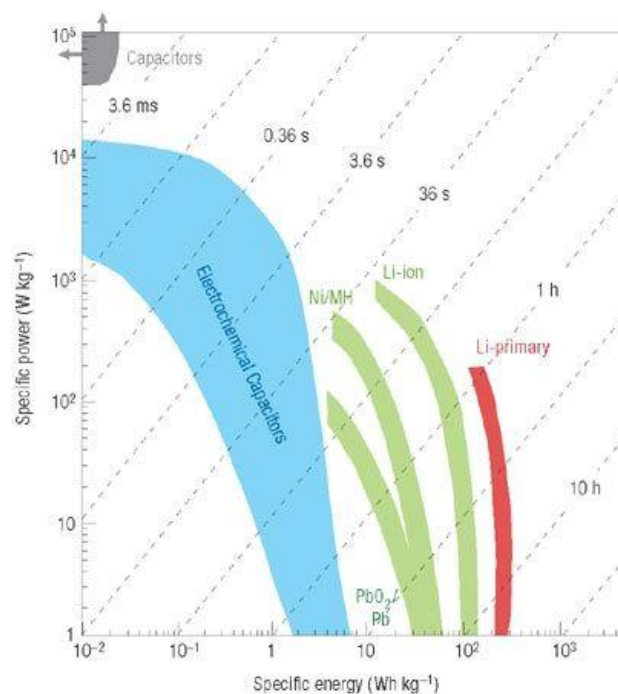
Figure I-1 Specific power versus specific energy plot, known as Ragone plot, for various electrochemical energy storage devices. Times shown are the time constants obtained by dividing the energy density by power density.[2]

10

Ragone plot, a plot of specific energy densities vs specific power densities, is commonly used to evaluate the performances of various types of energy storage systems.[3] Specific energy quantifies the amount of energy stored in the device whereas specific power evaluates the rate at which the energy could be delivered. Three main types of energy storage devices i.e., batteries, electrochemical capacitors (commonly known as supercapacitors (SCs)) and capacitors are shown with their respective specific power and energy densities (Figure I-1).[5] Capacitors store energy through charge separation on two metallic surfaces placed in a dielectric medium and offer the highest power densities but have the lowest energy densities.[6] These specific properties of capacitors enabled their extensive application in electrical circuits. Batteries offer highest energy densities and have facilitated the exponential growth of portable electronics from the early 1990s to the present day.[4] However, the kinetics of the faradaic reactions in batteries limit faster delivery/uptake of the energy and result in lower power densities. The next generation of portable electronics and development of electric vehicles requires devices that could offer both high energy and power densities.[3]

From the Ragone plot, SCs could be seen as intermediate between batteries and conventional capacitors. SCs store energy through reversible electrostatic adsorption of electrolytic ions on the charged electrode surfaces.[6] When a voltage is applied across the electrodes in SCs, the electrolytic ions of the opposite charge accumulate on the surface of each electrode. Energy is stored through charge separation between an electrode charge and the layer of electro-adsorbed ions. The non-faradaic nature of this charge storage enables rapid storage/delivery of the charge to/from the electrode-electrolyte interface and results in high power capabilities of ~ 15 kW/kg in SCs.[3] Additionally, this surface charge storage mechanism lets SCs sustain few millions of charge-discharge cycles with nominal losses in performances. However, as an undesired consequence, the non-faradaic charge storage also results in typically low energy densities of ~ 6 Wh/kg in SCs.[3] Batteries, on the other hand, store energy through reversible redox reactions in the electrodes and have high energy densities of ~ 200 Wh/kg but have low energy densities of 1 kW/kg.[4] The insertion or conversion mechanism associated with the faradaic charge storage process in the electrodes lead to expansion/degradation/pulverization of the electrode materials and result in limited cycling ability of few hundred cycles. Therefore, SCs can been seen as perfectly complementary devices to batteries in applications that require both high power and energy.[7] Table I-1

summarizes capacitors, rechargeable batteries and SCs with respect to their performance characteristics.

Characteristics	Capacitors	Supercapacitors (SCs)	Rechargeable Batteries
Storage Mechanism	Electrostatic	Electrostatic	Chemical
E (Wh/kg)	< 0.1	1 - 10	20 - 200
P (kW/kg)	>> 10	0.5 - 10	1 - 2
Cycle life (cycles)	>> 10^6	> 10^6	~ 1000
Charge-discharge time	10^{-6} - 10^{-3} s	10^{-3} – 1 s	1 – 10 h
Efficiency (fraction)	~ 1.00	0.85 - 0.95	0.70 - 0.85
Operating voltage (V_{max})	6 – 800 V	2.3 - 2.8 V	1.2 – 4.2 V
V_{max} determined by	Dielectric thickness	Electrode/electrolyte stability	Thermodynamics of the reactions
Self-discharge	Low	Moderate	Low
Operating Temperature	-20 to +100°C	-40 to +85°C	-20 to +65°C
Examples	Al, Ta oxide	Activated Carbons in $TEABF_4$/AN	Pb Acid, Li-ion, Ni-Cd and Ni-MH

Table I-1 Properties and characteristics of capacitors, supercapacitors and rechargeable batteries.

1.2 Basics of Supercapacitors

1.2.1 **Brief History**

The first capacitor, named as ''Leyden jar'' after the University of Leiden, was independently invented by Edward von Kleist and Pieter van Musschenbroek around 1745.[6] This rudimentary capacitor design involved charge storage on tin foils coated on the inner and outer walls of a glass jar filled with water. The inner tin foil in the jar is charged by an electrostatic generator by using a metallic rod/chain as the electrode contact (Figure I-2). Experimental studies on these jars by Benjamin Franklin led to conclusion that the charge is stored in the glass and not in the water. The mechanism of the electrical charge storage in capacitors was then studied and the first model of double layer capacitor was proposed by von Helmholtz in 1853.[8] Later in 1950s, General Electric and its engineer H. Becker used activated carbons with high specific surface area (SSA) as electrodes and developed a ''low voltage electrolytic capacitor with porous carbon electrodes''.[9]
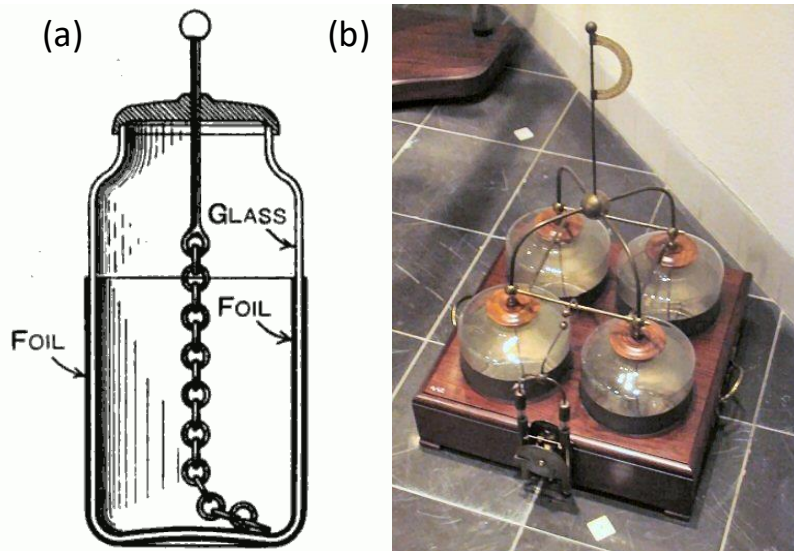
Figure I-2 Construction of the Leyden jar; (a) glass jar filled with water and coated with Tin on its interior and exterior surfaces. (b) A battery of four Leyden jars.[6]

In 1969, the SOHIO corporation patented and produced a double-layer capacitor porous carbon-paste electrode in sulfuric acid electrolyte separated by ion-permeable separator.[10,11] However, SOHIO did not commercialize the cells and licensed the technology to NEC (Japan). In 1971, NEC marketed the first supercapacitors in to provide backup power for computer memory.[12] Later Panasonic marketed its Goldcaps brand, which became a successful energy source for memory backup applications.[13] The first generation of SCs had relatively high internal resistance that limited the discharge current and hence were used for low current

applications. The first SC with low internal resistance was developed by PRI and were branded as PRI Ultracapacitor. In 1992, Maxwell laboratories took over PRI technology and named the devices as Boost Caps to signal their power performance.[14] Currently, SCs are widely used in various high power applications (see section 1.3). The commercial SCs use porous activated carbons as electrodes and solution of an organic salt dissolved in acetonitrile or propylene carbonate as electrolytes.

1.2.2 **Types of Supercapacitors**

SCs are largely classified into three different types depending on the charge storage mechanism at the electrode-electrolyte interface. (i) Electric double layer capacitors (EDLCs) are the pure form of SCs, which store energy in electric double layers formed at the electrode-electrolyte interface.[6] During charging and discharging of an EDLC no charge transfer occurs across the electrode-electrolyte interface. EDLCs are the most commonly available SCs and use activated carbons with high SSAs as electrode materials (Figure I-3a&c).[15–17] (ii) Another group of SCs is pseudo-capacitors that use electrode materials, which undergo fast redox reactions at the surfaces. This faradaic charge storage, called pseudo-capacitance, lead to much greater charge storage compared to EDLCs. Metal oxides such as RuO_2 and Fe_3O_4 and electronically conducting polymers are examples of such redox materials (Figure I-3 b&d).[18,19] Pseudo-capacitors differ from batteries with their fast sequence of reversible processes and electron transfer with minimum structural phase changes at the electrodes. Pseudo-
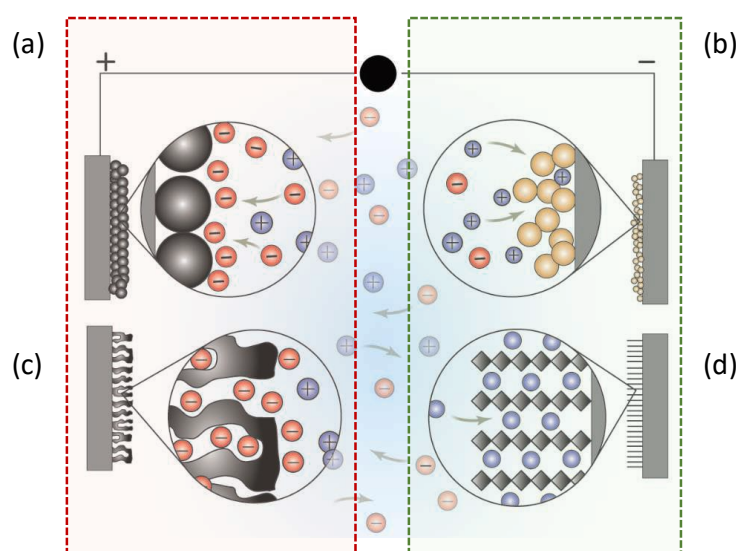
Figure I-3 Double-layer capacitance at electrodes comprising a) carbon particles or (b) porous carbon. The double layer shown here arises from adsorption of negative ions from the electrolyte on the positively charged electrode. Pseudo-capacitive mechanisms include (c) redox pseudo-capacitance, as occurs in hydrous RuO_2, and (d) intercalation pseudo-capacitance, where Li^+ ions are inserted into the host material.

capacitors could also have a minor EDLC component through ion sorption on surfaces and EDLCs could have pseudocapacitance contribution through reversible reaction of the surface functional groups in specific electrolytes. (iii) Hybrid capacitors were proposed in the recent years as a combination of a capacitive or pseudo-capacitive electrode with a battery electrode. This type of devices is expected to benefit from high power and high energy properties of capacitor and batteries. This thesis work focuses on the first type of SCs (EDLCs) using carbon-based materials in which charge is stored in electrical double layers.

1.2.3 **Applications of Supercapacitors**

The range of commercial applications of SCs is expanding and novel materials are being constantly developed and tested as potential electrodes. SCs mainly find applications in systems that require high power input for a short time (low energy) owing to their characteristics described earlier. SCs are used in hybrid electric, electric vehicles, trams and buses as reliable high-power sources under various climate conditions as viable competitors to high-power Li-ion batteries. SCs provide enhanced power during acceleration, capture breaking energy and offer low maintenance operation costs in the long term. Additionally, the growing popularity of the automatic start-stop technology further expands the need of SCs
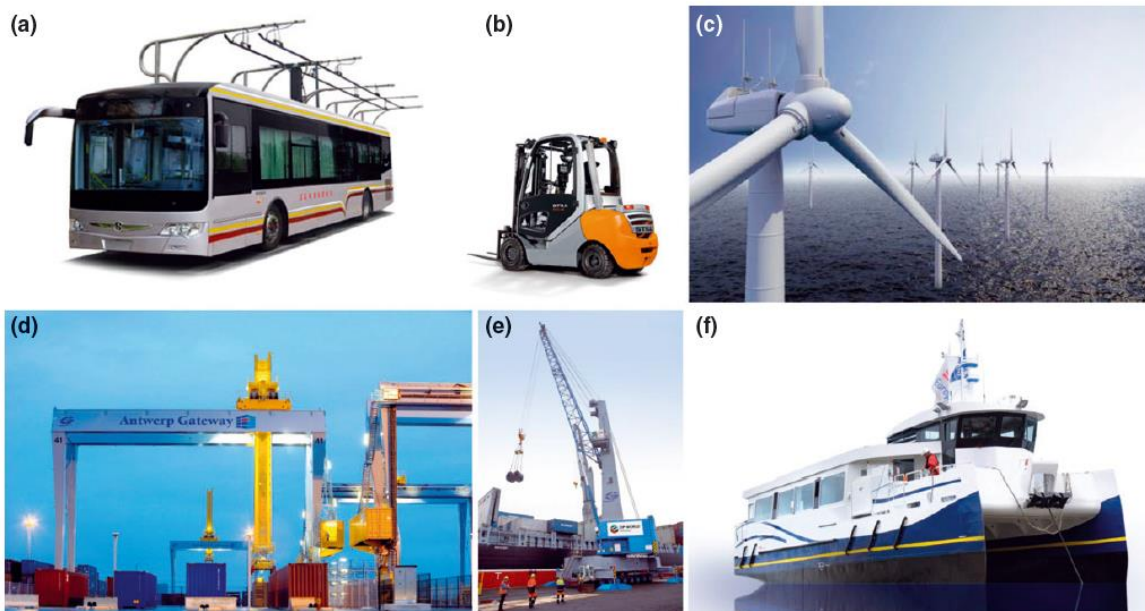
Figure I-4 Examples of SC applications in (a) electric bus (reproduced from Chinabuses.com), (b) forklift (reproduced from Still, Germany), (c) off-shore wind farms (reproduced from Gottwald, Germany), (d, e) industrial cranes and (f) electric ferries (reproduced from STX, South Korea).

with high-power capabilities. SC powered buses capable of charging at the regular stops are gaining popularity in China and Europe (Figure I-4).

SCs are most commonly used in industrial equipment including hybrid forklifts and hybrid cranes. The high power and good low operating temperature of SCs make them very viable for operation in forklifts that function in refrigerated warehouses. SCs are also viable for all-electric short distance ferries (5-20 min) or well-equipped military ships that have strong need for mobility and reliability. Uninterruptable power is critical to key applications where the cost of interruptions could be life/health threatening (ex. Hospitals, data centers, communication facilities etc.). Backup standby generators require few seconds to minutes to plug in. SCs could be used as backup power sources in such key applications. The backup power from SCs is also used to power wind turbine control systems that need to maximize the energy harvesting by controlling motor speed. SCs provide reliable supply in wind farms that are often in remote locations and have minimum maintenance costs.

1.3 Fundamentals of Electrical Double Layer Capacitors

In a conventional capacitor, two conductive metallic plates are separated by dielectric media such as glass, ceramics, paper or mica (Scheme I-1). Opposite charges are stored on the two metal plates (separated by a given distance d) by applying an external bias voltage. These opposite charges on the metallic plates are maintained by the insulating dielectric material and an electric field is thus developed between the two oppositely charged plates. The amount of charges stored (Q in Coulomb) is determined by the capacitance (C in Farads) and the voltage difference (V in volt) across the capacitor as defined in Equation I-1 .The ability of a capacitor to store energy in an electric field is quantified as ''capacitance''. Specifically, capacitance is described as the derivate of charge stored to the corresponding change in its electric potential. One Farad of capacitor signifies one Coulomb at a potential difference of one V. Capacitance depends on the geometry of the electrodes, permittivity of the dielectric material and the separation between the charged plates (Equation I-2). ε_o and ε are the permittivity of a vacuum ($8.85 * 10^{-12}$ F/m) and electrolyte dielectric constants respectively. A is the area of the plates and d is the distance of separation between the two plates.
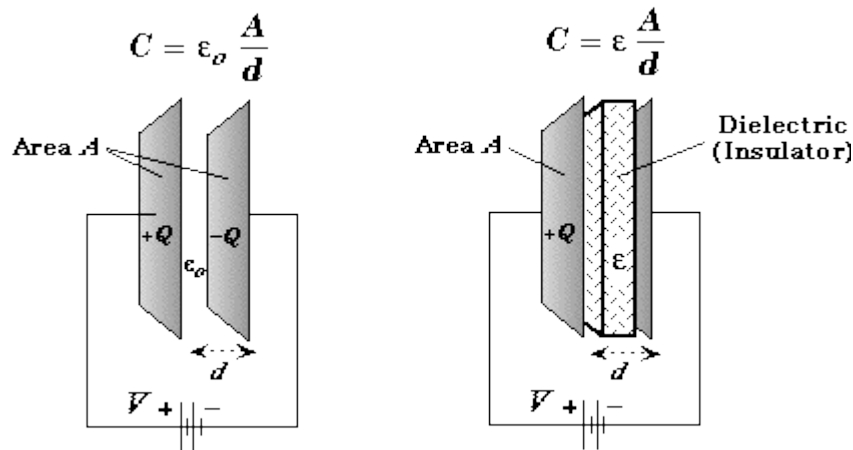
Scheme I-1 Schematic representation of a parallel plate capacitor

$$Q = C \cdot V$$

Equation I-1

$$C = \frac{\varepsilon_o \cdot \varepsilon \cdot A}{d}$$

Equation I-2

17

1.3.1 **Electric Double Layer Theory**

The basic charge storage mechanisms in EDLCs is similar to a parallel plate capacitor where the conductive plates are replaced with different active materials (ex. Porous carbons) and a polymeric separator immersed in electrolyte is used instead of the dielectric material. Electronic charges accumulate at positive and negative electrode surfaces when an external bias is applied. The cations and anions in the electrolyte move towards the oppositely charged electrode surfaces due to electrostatic attraction and accumulate as layers. The charge separation at the electrode-electrolyte interfaces is referred to as ''electric double layer'' (EDL) giving rise to the term electric double layer capacitor. The concept of EDL was first described and modeled by von Helmholtz in 1853 and this model states that two layers of opposite charges form at the electrode-electrolyte interface and are separated by an atomic distance d (Figure I-5a).[8] The potential near the electrode decreases when the distance (m) between the ions and the electrode increases. The Helmholtz double-layer (DL) could be regarded as an electric capacitor of capacitance C_H (Equation I-3) with an electrode surface area S (m^2). d is the effective thickness of the DL and is often approximated as the Debye length. Considering the very large SSA of the porous carbon electrodes and a Debye length < 1 nm, the resulting capacitance of DL's will be much higher than parallel plate capacitors.

$$C_H = \frac{\varepsilon_0 \cdot \varepsilon_r \cdot S}{d}$$

Equation I-3

The Helmholtz model does not consider several factors such as diffusion of ions in the solution and the interaction between dipole moment of the solvent and the electrode. Gouy in 1910 and Chapman in 1913 proposed a diffuse model of the EDL in which ions in the electrolyte (both cations and anions) are considered as both mobile and under influence of the electrostatic forces leading to formation of a diffuse layer (Figure I-5b).[20] The potential decreases exponentially across the diffuse layer into the bulk of the electrolyte. However, the Gouy-Chapman model overestimates the EDL capacitance as it treats ions as point charges. In 1924, Stern combined the Helmholtz model with the Gouy-Chapman model to explicitly recognize two regions of ion distribution; the inner region as a compact layer or Stern layer and the outer diffuse layer (Figure I-5c).[21] The inner compact layer consists of strongly adsorbed ions which are often solvated. Additionally, the diffuse layer consists specifically of

adsorbed ions and non-specifically adsorbed counter ions at both positive and negative electrode surfaces. These two layers are equivalent to two capacitors in series, C_H (Helmholtz layer) and C_D (diffusion layer) and the total capacitance of the electrode is given by C_{DL} (Equation I-4).

$$\frac{1}{C_{DL}} = \frac{1}{C_H} + \frac{1}{C_D}$$

Equation I-4
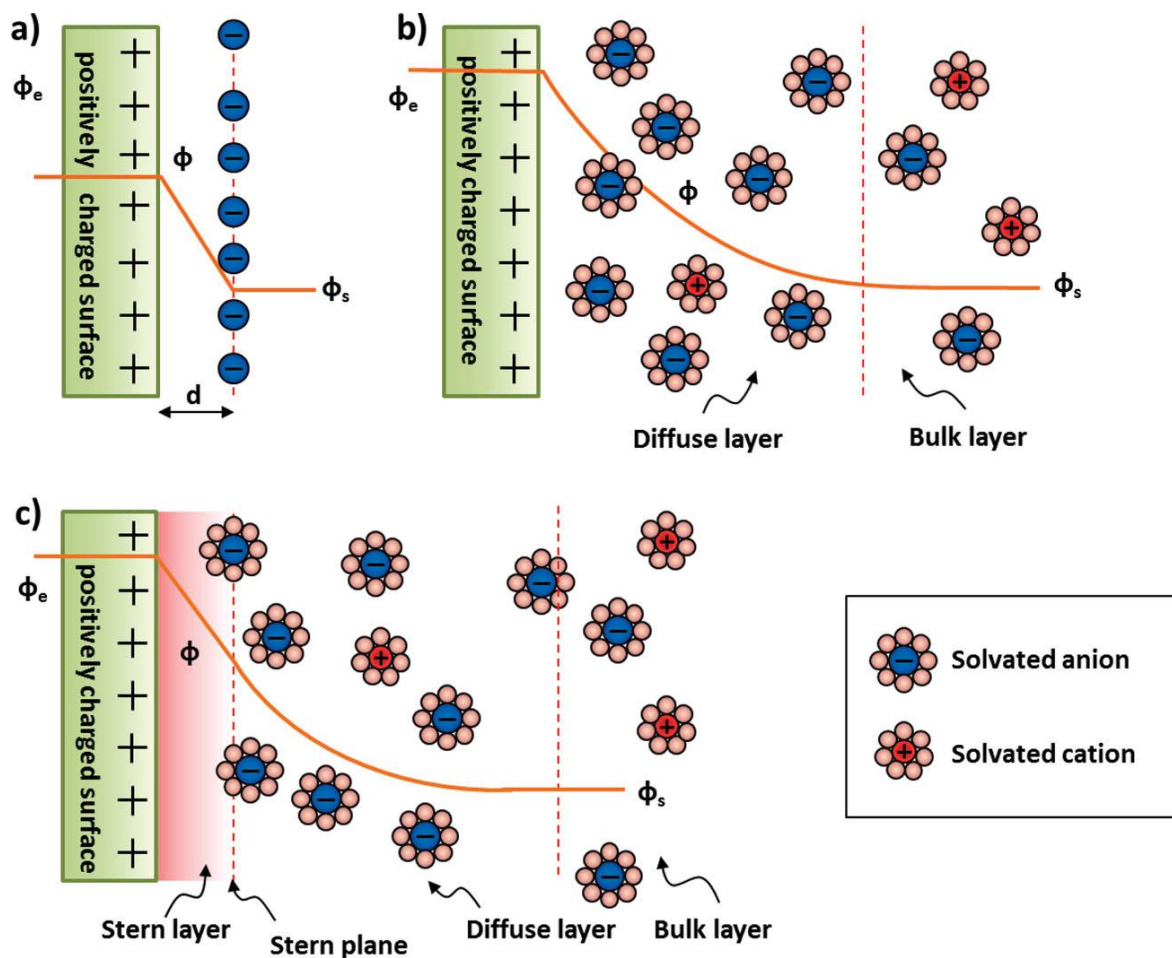
Figure I-5.(a) Helmholtz, (b) Gouy-Chapman, and (c) Stern model of the electrical double-layer formed at a positively charged electrode in an aqueous electrolyte. The electrical potential, φ, decreases when transitioning from the electrode, φ$_e$, to the bulk electrolyte infinite away from the electrode surface, φ$_s$. The Stern plane marks the distance of closest approach of the ions to the charged surface. Note the absence of charges/ions in the Stern layer. The diffuse layer starts in the range of 10 − 100 nm from the electrode surface.[17]

A traditional EDLC consists of two porous carbon electrodes in direct contact with the current collector and separated by a polymer film impregnated with an electrolyte solution (Scheme I-2). When a potential difference is applied between the two electrodes, electrons at the

negatively polarized electrode are balanced by an equal number of positive cations at the electrode/electrolyte interface, while the holes stored at the positively polarized electrode are electrically balanced by anions. Hence, a SC consisting of two electrodes is equivalent to two capacitors in series with additional solution resistance and the resulting capacitance (C) can then be expressed according to Equation I-5. C_+, C_- and C are capacitances of the positive electrode, negative electrode and the whole device respectively.
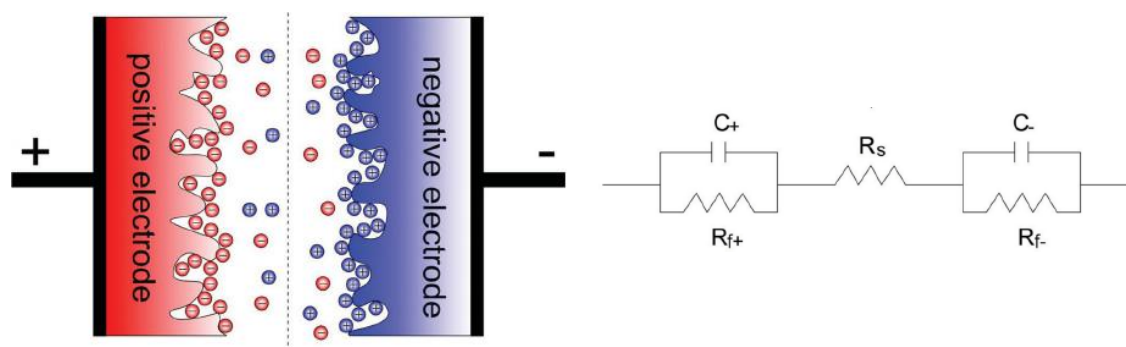
Scheme I-2 Schematic representation of a parallel plate capacitor and the equivalent circuit. [17]

$$\frac{1}{C} = \frac{1}{C_+} + \frac{1}{C_-}$$

Equation I-5

In order to compare the performances of various electrode materials, it has become a common practice in the literature to provide specific gravimetric capacitances of material relating to the capacitance of a single electrode (C_{SP}). Specific volumetric capacitances can also be used as a measure of the compactness of the materials. In case of a symmetric system with equal electrode masses, sizes and thicknesses, C_{SP} is given by Equation I-6, where m_{AM} is the total mass of the active materials in both electrodes.

The specific energy stored (Wh/kg) and the deliverable specific power (W/Kg) of a SC are represented by Equation I-7 & Equation I-8 Vmax is the maximum electrochemical stable window, ESR is the equivalent series resistance and m is the total mass of the SC. The ESR of EDLC corresponds to the sum of ionic resistances, electronic resistances and the interface resistance between electrodes and current collectors.

$$C_{SP} = \frac{4 \cdot C}{m_{AM}}$$

Equation I-6

$$E = \frac{C \cdot V_{max}^2}{2 \cdot m \cdot 3600}$$

Equation I-7

$$P = \frac{V_{max}^2}{4 \cdot ESR \cdot m}$$

Equation I-8

2. Cell Design Characteristics for SCs

SCs offer great power performance for various specific applications but suffer from low energy values for their application in large-scale applications like rechargeable batteries. Thus, the main challenge in the field of SCs has been to improve the energy densities and still maintain their high-power performances. Extensive research has been devoted towards finding new electrolytes and electrode materials that could offer such ideal performances.[17,22,23] The core strategies in this research arise directly from the specific energy and power equations described earlier.

Energy and power densities of SCs can be enhanced significantly by increasing the operational voltage window (V_{max}) of the SC as they depend on V_{max} through a square relationship (Equation I-7& Equation I-8). The maximum operational voltage of a SC is generally determined by the nature of the electrolyte. Electrolytes based on aqueous, organic and ionic liquid (IL) media all have different operational windows determined by the electrochemical stability of the solvents.[24] Specific electrolytic ions dissolved in the above solvents and the interactions with electrode surfaces could also determine the maximum possible operational window. While enhanced V_{max} is a positive attribute of a SC, the equivalent circuit resistance (ESR) is also an important parameter for determining the power of a SC. ESR is the sum of various types of resistances including the intrinsic resistance of the electrode material, electrolyte solution, mass transfer resistance of the ions and the contact resistance between current collector and the electrode material.[24] Among the various resistances, the resistance of the bulk electrolyte solution and the electrolyte inside the electrode pores dominate the overall ESR. Unfortunately, often there is a trade-off between the V_{max} and the ESR of a system. Aqueous electrolytes such as H_2SO_4 or KOH have high ionic conductivities but the operational voltage window is low. In contrast, organic and IL electrolytes offer high V_{max} but their ionic conductivities are at least one order lower than aqueous electrolytes.

The energy densities of pure double layer capacitors could be improved by increasing the surface area of the electrode that is accessible for electrochemical ion sorption (Equation I-2).[23,25] Thus, achieving higher electrochemically active surface area has been a well-defined and straightforward challenge. It was commonly assumed that increasing the overall specific surface area (SSA) of an electrode material would lead to enhanced electrochemical active

surface area (A).[17,26] Hence, over the past two decades, several materials with high surface areas have been analyzed for application as electrode materials in SCs.[22] In the early 2000s, fundamental understanding of ion sorption on carbons surfaces has revealed the importance of the size, shape and distribution of pores in a particular material.[27–29]

The energy densities of SCs could also be improved by using electrodes or electrolytes that offer additional attributes. The charge storage capability of an electrode material could be enhanced through addition of redox processes,[6] decreasing the distance (d) between ions and the carbon electrode surface and by modifying the permittivity of the EDL, which is mainly governed by the electrolyte.[30] Addition of redox reaction processes to an electrode material (pseudo-capacitance) is known to enhance the capacitance by nearly 10 fold as compared to double layer charge storage (ex. RuO_2). However, such an addition also results in problems that rechargeable batteries typically face: poor cycle life and power performances.[3] Nevertheless, pseudo-capacitance offer great potential as an intermediate between batteries and pure capacitors with mixed attributes.

Specific attributes and types of electrolytes and electrode materials suitable for SC applications are detailed briefly in the following section.

2.1 Electrolytes

An electrolyte solution typically consists of a salt dissolved in a solvent. Broadly, the ions in the electrolyte solution provide charge compensation to the electronic charges accumulated on each electrode in a SC. As the two electrodes are oppositely charged, electrolytic ions of the opposite charges adsorb on the electrode surfaces to form electrical double layers. Hence, an electrolyte provides an ionic conducting media and insulating to flow of electrical charges. Electrolytes such as those made with ionic liquids and solid-state polymers could differ from the traditional definition of salt + solvent (discussed in detail below). As electrolyte is a key component of the double layer charge storage process, it has to meet various key requirements to be considered as an ideal electrolyte.[30,31] An ideal electrolyte has: (a) a wide voltage window of stability; (b) a high ionic conductivity; (c) a wide operating temperature range; (d) low volatility and flammability; (e) chemical and electrochemical inertness to SC components; (f) low viscosity for low ESR; (g) environmentally friendly and (h) low synthesis costs. As it is difficult for an electrolyte to meet all these requirements, various types of electrolytes are developed and reported in the literature, each with respective merits and demerits.[30] The reported electrolytes are broadly classified into three classes based on the solvent present (Figure I-6).
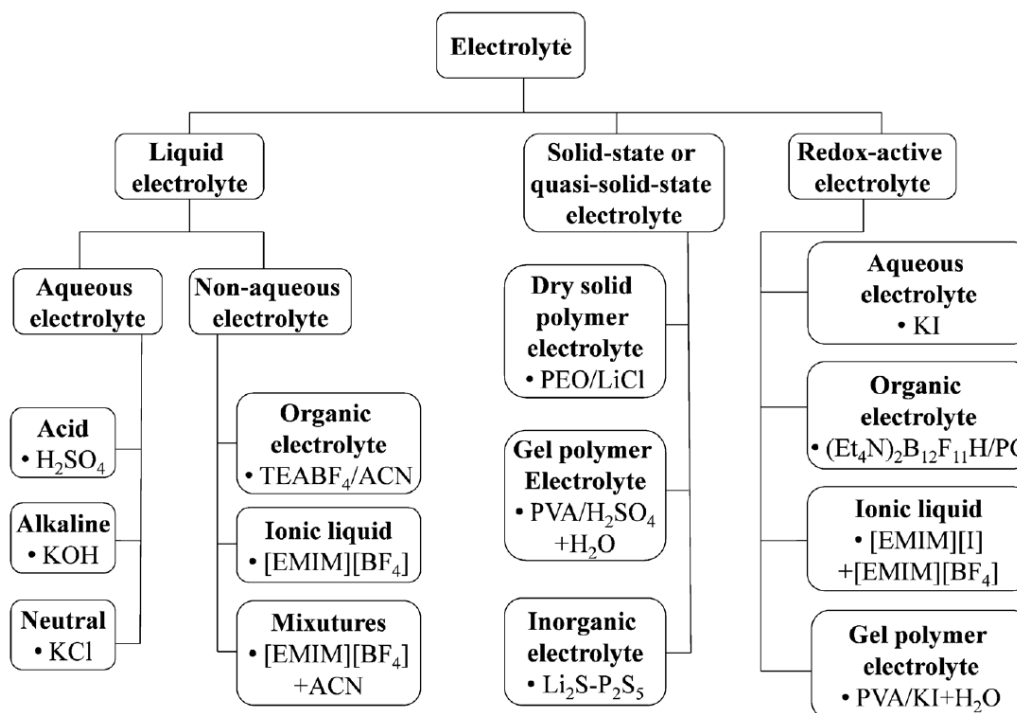
Figure I-6 Classification of electrolytes for SCs.[30]

2.1.1 **Aqueous Electrolytes**

Aqueous electrolytes are cost effective, safe, could be handled easily and greatly simplify the overall SC fabrication and assembly process. Comparatively, organic and IL electrolytes require complicated purification procedures and need a moisture-controlled atmosphere. Another unique advantage of aqueous electrolytes is their high ionic conductivities and correspondingly low ESR values, which lead to better power capabilities. For example, 1 M H_2SO_4 has about 0.8 S/cm conductivity at 25°C whereas that of 6 M KOH 0.6 S/cm at the same temperature. The major disadvantages of aqueous electrolytes are the limited maximum operating voltage window and operational temperature range. The voltage window of aqueous electrolytes is restricted by the decomposition of water. The hydrogen evolution generally limits negative potential at around 0 V vs. SHE and the oxygen evolution occur at 1.23 V, thus resulting SC has a cell voltage of about 1.23 V. To avoid gas evolution, the cell voltage of aqueous SCs, is commonly restricted to 1 V. Additionally, the temperature range of aqueous SCs is restricted by the boiling and freezing point of the electrolyte.

In general, aqueous electrolytes are grouped into acidic, alkaline and neutral solutions in which H_2SO_4, KOH and Na_2SO_4 are representatives and are the most frequently used electrolytes. The three types of electrolytes benefit from specific attributes. (i) Acidic and alkaline electrolytes support various pseudo-capacitive mechanisms and aid the overall charge storage.[32,33] (ii) Neutral electrolytes have lower H^+ and OH^- concentration compared to acidic and alkaline electrolytes, and enable higher stable voltage windows up to 2.2 V.[34] Specific demerits of the electrolytes include corrosive nature of acidic solutions towards current collectors and relatively low conductivities of neutral solution due to solubility issues. Despite all the merits and demerits, the low operating voltage windows of aqueous electrolytes has been the major hurdle towards commercial applications.

2.1.2 **Organic Electrolytes**

Although extensive academic studies have been focused on using aqueous electrolytes in SCs, organic electrolytes currently dominate the commercial applications owing to their high operational voltage window (~ 2.8 V).[30,31] Most organic electrolyte-based SCs use acetonitrile (AN) solvent while others employ propylene carbonate solvent (PC).[35] The increased voltage window provide significant improvements in energy and power densities. Additionally, the specific salts and solvents used in organic electrolytes enable desired performances in a wide

range of temperatures. Typical organic electrolytes for commercial SCs use conductive salts (ex. Tetraethylammonium tetrafluoroborate salt (TEABF$_4$)) dissolved in AN or PC,[36] it has been reported that the specific capacitance of a SC in 1 M TEABF$_4$/AN did not have any obvious changes when the temperature is decreased from 45 to -30°C (Figure I-7a). [37]

However, the high operational cell voltages lead to concerns of aging and degradation of cell performances.[38,39] Wide cell voltage could cause accelerated oxidation of electrode materials
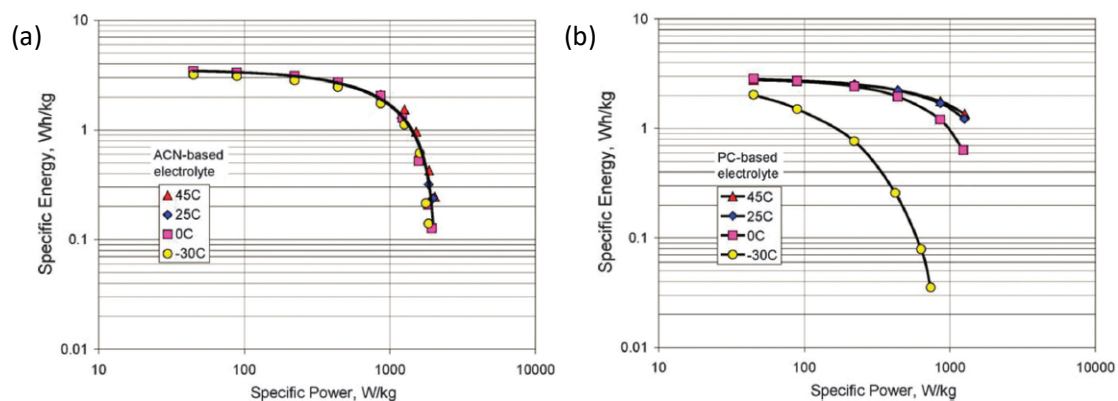
Figure I-7 Ragone plots for (a) AN and (b) PC based SCs at different temperatures.[37]

and intercalation of electrolytic ions into layered materials. Both such cases lead to irreversible changes in the electrode materials and cause performance degradation with time.[36] Other important issues regarding organic electrolytes include higher costs, lower specific capacitances and safety concerns related to flammability, volatility and toxicity.[40–44] Another drawback of organic electrolytes compared to aqueous electrolytes is their low ionic conductivities.[36] For example, the ionic conductivity of the most commonly used 1 M TEABF$_4$/AN is 0.06 S/cm, which is significantly lower than that of 1 M H$_2$SO$_4$ at 25°C (0.8 S/cm). Similar to aqueous electrolytes, the nature of salts and solvents in the electrolyte has a profound impact on the performances of SCs and needs optimization of various parameters. Specific tests of SCs performed by Kotz et al. gave very different responses when 1 M TEABF$_4$/PC was used instead of 1 M TEABF$_4$/AN.[42] The conducting salts in the electrolyte also have a profound impact on the V$_{max}$, thermal stability and the overall capacitances of SCs. Careful consideration should be given on the solubility, stability and conductivity of the individual salts. Figure I-8 shows an example demonstrating that there are optimum ion

concentration values for achieving maximum ionic conductivities in each electrolyte. TEABF$_4$ has limited solubility (up to 1 M) in PC whereas other salts show higher solubility above 2 M.[36]
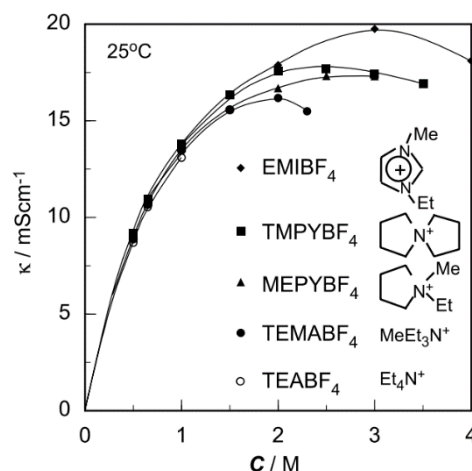
Figure I-8 Ionic conductivity as a function of quaternary ammonium tetrafluoroborate salt concentration in PC solvent.[36]

2.1.3 **Ionic Liquid based electrolytes**

Ionic liquids (IL) are generally defined as salts that are solely composed of ions with melting points below 100°C.[45] An IL generally has a large asymmetric organic cation and an inorganic or an organic anion, and this special combination of certain cations and anions contributes to a low vapor pressure.[46] The intrinsic energetics involved in the interactions between the anions and cations are typically measured by the surface tension of the ILs. ILs offer several potential advantages including high thermal, chemical and electrochemical stability, negligible volatility and non-flammability (certain ILs).[47] These positive attributes render ILs as safe for high-temperature applications (80°C or more). Moreover, the physical and chemical properties of ILs are highly tunable and offer excellent opportunity for optimization.[48] The major advantage of the IL electrolytes over organic and aqueous electrolytes is their high V$_{max}$ values of higher than 3 V.

Unfortunately, there are several main drawbacks with most ILs, such as high viscosity, low ionic conductivity and high costs, which can limit their practical use in SCs. Even for [EMIM][BF$_4$] electrolytes, which has relatively high ionic conductivity among common ILs, its conductivity (0.014 S/cm) is still much lower than that of organic or aqueous electrolytes. Both low conductivity and high viscosity of ILs can significantly increase ESR values and limit power performances in SCs. Additionally, specific capacitances of IL based SCs are significantly low, probably due to the high viscosities.[49]

2.1.4 **Solid or Quasi Solid-State Electrolytes**

Solid state electrolytes can serve as both ion conducting media and electrode separator. The rapid growing demand of power for portable electronics, printable electronics and flexible devices is the major driving force behind application of these electrolytes in SCs. The major advantage of such electrolytes are the simplification fabrication and packaging of leakage proof SC devices.[50–52] Currently, solid-state electrolytes are mainly based on various polymers and are classified as solid polymer, polyelectrolytes and gel polymer electrolytes. A solid polymer electrolyte is made of a polymer and a salt without any solvent. A gel polymer electrolyte consists in a polymer host (ex. Polyvinyl alcohol) and a liquid electrolyte (ex. H_2SO_4) and have the highest ionic conductivity among the three types of electrolytes.[50] Polyelectrolytes conduct ions through charged polymer chains.

Gel Polymer Electrolytes (GPEs) are currently the most extensively studied electrolytes for solid-state ES devices and they consist of a polymer matrix and an aqueous salt solution or an organic salt solution or an ionic liquid as the liquid electrolyte in the polymer host. Depending on the electrolyte constituent, the GPEs are called as Hydrogels, Organogels and Ionogels. Examples of GPEs include H_2SO_4 or KOH Poly(vinyl alcohol) as hydrogel, $LiClO_4$/DMF in Polyvinylpyrrolidone (PVP) as organogel and [BMIM][Cl] ionic liquid in PVP as ionogels Owing to the individual characteristics of the constituent liquid electrolyte (see previous sections), GPEs differ in properties such as thermal behavior, voltage window and environmental stability.

The main drawback of these electrolytes is their poor mechanical strength and narrow operational temperature range. Globally, solid electrolytes also suffer from limited contact surface area with electrode materials (especially for nanoporous materials), and lead to low specific capacitances and high ESR values.[51]

With the merits and demerits of each class of electrolytes explained above, a choice of the electrolyte for a SC system should be made by considering the nature of charge storage (EDLC/pseudo-capacitance) and operational conditions (temperature) and requirements (energy and power) of a SC.

2.2 Electrode Materials

As described in the previous section, energy densities of SCs could be increased by choosing materials with high electrochemically active surface area as electrodes. Additionally, high electrical conductivity of the electrode materials is essential to maintain low ESR and achieve high power performances. Hence, the choice of electrode materials for supercapacitors requires high specific surface area (SSA) and good electrical conductivity (~ 1 S/cm).

Carbons are one among the most abundantly available and structurally diverse materials, making them the preferred choice of electrode materials in SCs.[53] Abundantly available organic materials, such as food waste, are particularly attractive as natural sources for the production of carbon materials. Carbon materials also have desired attributes such as low cost, variety of form (powders, fibers, aerogels, and monoliths), ease of process ability, relatively inert electrochemistry and controllable porosity. Activated carbons (ACs) are the most commonly used porous carbons used in the commercial SCs owing to their high specific surface areas (SSA) and costs.[54,55]

 The specific surface area of an electrode material is an important parameter for ion sorption but other aspects such as pore sizes, shapes and their connectivity are also crucial for enhanced electrochemically active area.[56] The International Union of Pure and Applied Chemistry (IUPAC) defines pores according to their sizes as micropores (< 2 nm), mesopores (2-50 nm) and macropores (> 50 nm).[57] The broad consensus on the role of different pores in SCs is that the micropores provide ion sorption sites, mesopores act as channels for electrolytes ions to the sites and the macropores act as electrolyte buffers. Thus, an inter play between different types of pores is crucial.[58]

Material	Carbon onions	Carbon nanotubes	Graphene	Activated carbon	Carbide derived carbon	Templated carbon
Dimensionality	0-D	1-D	2-D	3-D	3-D	3-D
Conductivity	High	High	High	Low	Moderate	Low
Volumetric Capacitance	Low	Low	Moderate	High	High	Low
Cost	High	High	Moderate	Low	Moderate	High
Structure						
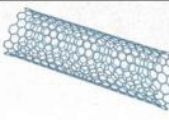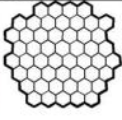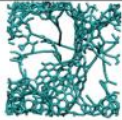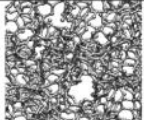
Table I-2 Various dimensions of carbon materials and their specific properties.[56]

Different forms of carbons materials are known to offer varied porosity characteristics (pore shapes, size distributions, volume), diverse physical and chemical properties (Table 1.2). Onion-like carbons, carbon nanotubes (CNTs), graphene, ACs, Carbide-derived carbons (CDCs) and templated carbons are carbons with different dimensional arrangement in space that have been investigated for next generation SCs with potentially high energy and power densities. In this section, different carbon materials are briefly summarized and discussed with respect to their synthesis methods, characteristic structures and electrochemical performances in SCs.

2.2.1 **Onion-Like Carbon**

Onion-Like Carbon (OLC), also called as carbon onions or multi-walled fullerenes, consist concentric spherical graphitic sheets.[59,60] It can be mass produced either by arc-discharge or by annealing diamond nanoparticles in an inert atmosphere at temperatures above 1200°C (Figure I-9a & b). OLC have moderately high BET SSA of 400-600 m^2/g with relatively low cost and high conductivity for applications in SCs (~ 4 S/cm).[61] OLCs have open surface structure and are free of micropores with particle size ranges from 5 to 15 nm.[62] Since all the surface area is fully ion accessible without ion transport limitation like in a microporous network, OLCs presents high power capability (Figure I-9c). Micro-supercapacitors based on these OLCs showed impressive rate capability (up to 200 V/s) and relaxation time constant (26 ms). Yet the low SSA of this material gives a poor energy performance and low capacitance (~ 30 F/g) in 1.5 M TEABF$_4$/AN electrolyte and make them suitable for micro-supercapacitor applications with low energy demands.[63]
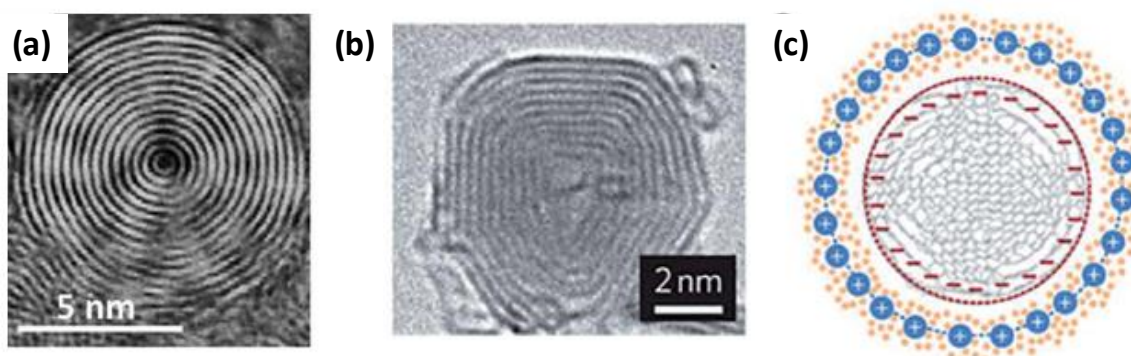
Figure I-9 TEM images of OLC produced by (a) arc discharge method[60] and (b) annealing nano-diamond powders at 1800°C.[63] (c) Schematic representation of the ion sorption on the external surface of OLC.

2.2.2 **Carbon Nanotubes**

Carbon nanotubes are one dimensional carbon materials with cylindrical structure commonly grown via catalyst-assisted chemical vapor deposition (CVD) techniques using hydrocarbon-based precursors such as methane, acetylene etc.[64] CNTs consist either of one rolled-up graphene (single-walled CNT) or of several co-axial ones (multi-walled CNT) (Figure I-10). CNTs are characterized by their superior electrical conductivity, excellent thermal and mechanical stability and are suitable for application in SCs. Current trend is to grow CNTs vertically on conductive substrate to allow a direct contact between the current collector and the CNTs.[65] Such assemblies facilitate low contact resistances (correspondingly low ESR) and easier ion accessibility form bulk electrolyte to the CNT surfaces. Similar to OLCs, CNTs have an exohedral surface with moderate SSA 120-500 m^2/g (single wall CNTs have up to 1000 m^2/g) and result in moderate gravimetric capacitances of 50-90 F/g.[64] The low CNT material density and moderate SSAs result in low volumetric capacitance and energy densities of SCs. Nevertheless, the high electrical conductivity and open porosity of CNTs can allow fast ion transport and power performances in SCs. Research has been undertaken to improve the energy density of CNTs by increasing their specific surface area via chemical activation (KOH activation). However, a proper balance between porosity and conductivity must be achieved in order to have both high capacitance and good rate performance. Another way to improve energy densities of CNTs is by decorating them with a thin layer of pseudo-capacitive materials on the surface as the tubular structures of CNTs also make them a good host for additional active materials.[66] In spite of having excellent properties, the limited surface area, high production costs and purity issues still hinder commercial application of CNTs. Additionally, the health and safety aspects of CNT fibers (probable carcinogenic agents) hinder their use in SCs.
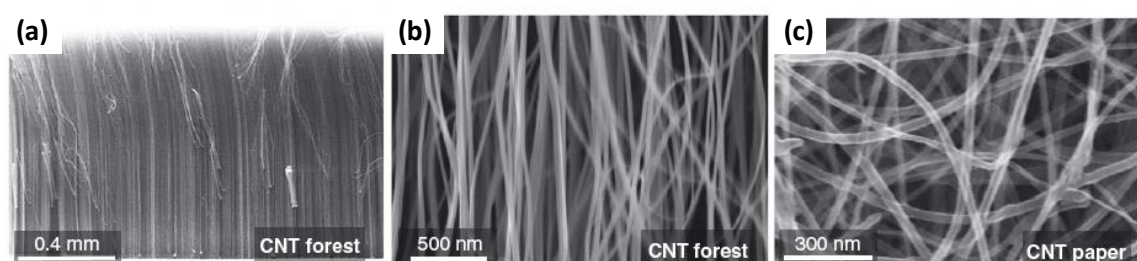
Figure I-10 SEM image of (a & b) vertically aligned CNT and (c) CNT paper.[64]

2.2.3 **Various 3-D Carbons**

Activated Carbons (3-D) Structure

ACs are non- graphitized forms of carbons that are unable to restack even after treatment at 3000°C.[3] The textural entanglement of ACs is explained by presence of structural fragments resembling fullerenes with pentagons and non-hexagonal rings, giving rise to curvatures.[22] ACs are the most widely used electrode materials in SCs due to their large surface area, relatively good electrical properties and moderate costs of synthesis.[53] ACs are generally produced from thermal and/or chemical activation of various types of carbonaceous materials (e.g. wood, coal, nutshell, etc.).[67] Thermal activation usually involves treatment of carbon precursors at high temperature (from 700 to 1200°C) in the presence of oxidizing gases such as steam and CO_2. Chemical activation is usually carried out at relatively lower temperatures (from 400 to 700°C) with activating agents like phosphoric acid, potassium hydroxide and sodium hydroxide.[68] Depending on the activation methods as well as the carbon precursors used, ACs possessing various physicochemical properties with very high surface areas of 3000 m^2/g are produced. The porous morphology of ACs have a broad distribution of micro, meso and macropores.[69] Despite their high surface areas, in general, specific capacitance values ranging from 150-300 F/g and up to 150 F/g are observed in aqueous and organic electrolytes respectively.[3] It was suggested that for carbons with high SSA, the pore walls might become too thin to provide complete charge screening of the ions in the pores.[70]

Currently, ACs are applied as electrodes in commercial SCs restricted only to a certain niche markets due to their limited energy storage and rate capabilities.[71] The specific surface area is an important parameter for ion sorption but other aspects such as pore sizes, shapes and their connectivity are also crucial for enhanced electrochemically active area.[72] Furthermore, excessive activation will lead to larger pore volume and results in the drawbacks of low material density and conductivity.[17] In addition, high surface areas may increase the risk of decomposition of the electrolyte at dangling bond positions.[73] Therefore, designing ACs to have narrow pore size distribution (accessible to electrolyte ions) with an interconnected pore structure would benefit the energy density of SCs without deteriorating their power density.[74]

Templated Carbons (3-D)

Templating method offers another effective way to produce nanostructured carbons with well controlled narrow pore size distributions, ordered pore structures, large specific surface areas and an interconnected pore network (Figure I-11).[75] These unique properties make them suitable for applications in SCs. In general, templated carbons are prepared by infiltration of a carbon precursor into the pores of a template, followed by a carbonization treatment and finally the removal of the template to leave behind a porous carbon structure. Various carbon structures with well-controlled micropores, mesopores and/or macropores produced from different types of template and carbon precursors have been studied for supercapacitor applications.[76,77]
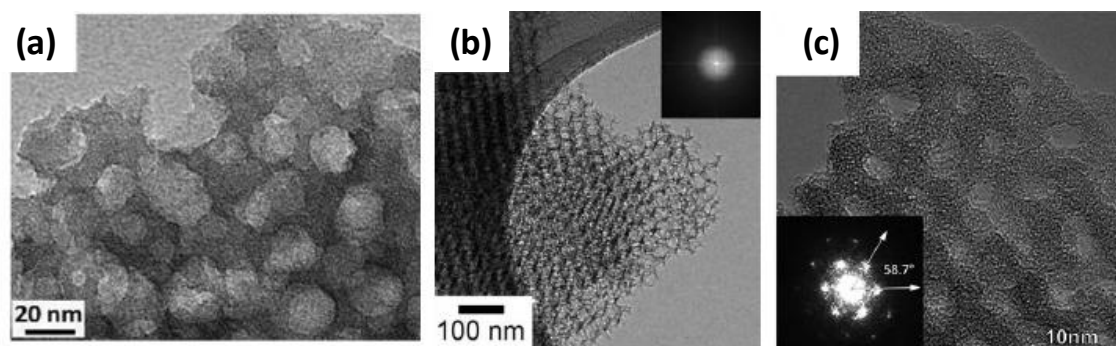
Figure I-11 TEM images of different template-synthesized porous carbons.[76,77]

A functionalized microporous carbon material was obtained by using zeolite Y as a template and the resultant carbon material possessed a high gravimetric capacitance of about 120-340 F/g in aqueous electrolyte and 60-150 F/g in organic electrolytes with good cyclability (over 10000 cycles).[78] Compared to ACs with disordered micropores and broad in-pore size distribution, the templated microporous carbons with a narrow pore size distribution, well adapted pore size to the electrolyte ions and the ordered straight pore channels are better for use as high-energy-density electrode materials. Relatively high cost of production of the sacrificial templates is the main drawback of the templated carbons.[22] Development of a simple, economical and environmentally benign template route would be advantageous for their future application. Despite the cost, templated carbons are a model class of materials which could provide valuable information about the effect of pore size, pore shape, channel structures and other parameters on the ion diffusion and charge storage in SCs.

Carbide derived carbons (3-D)

Carbon produced from extraction of metals from metal carbides is commonly known as carbide derived carbon (CDC).[73] Metal atoms from various carbides are etched out using treatments in supercritical water or halogens to produce carbon coatings, powders, fibers and membranes.[79] The carbon structure of CDC is found to contain various structures such as carbon onions, graphene, CNT and simple amorphous carbon (Figure I-12). CDC with disordered carbon structure is the most attractive candidate for SCs and is generally produced by treatment of carbides in a chlorine gas. By selecting different carbide precursors (ex. TiC) and changing the chlorination temperature, a range of CDCs with fine control of average pore sizes have been prepared and studied in SCs. CDCs possess high SSAs ranging from 1000 – 3000 m^2/g and tuneable pore structures with sub-nanometer accuracy, thus making them the best candidates for fundamental EDL studies.
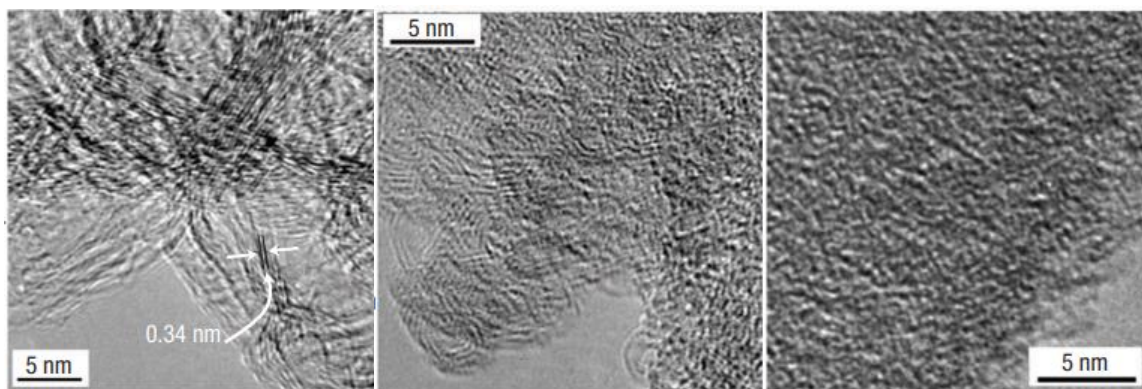
Figure I-12 TEM images of CDC showing evolution of the carbon structure with temperature: (a) 300 °C, (b) 700 °C and (c) 1200 °C

The specific capacity of CDC in aqueous electrolyte is moderately high. Depending on the precursor and the chlorination conditions, capacitances in the range of 100-220 F/g are observed.[80,81] The specific capacitance in organic electrolytes is slightly lower than in aqueous with values from 70-160 F/g. CDC are also synthesized as fibers and through template assisted technique for enhanced power characteristics. Overall, CDCs offer a model class of materials that offer finely tuned porosity characteristics for fundamental studies on electrolyte ion sizes and pore sizes. In fact, CDCs with ultra-micropores and narrow pore size distribution have helped in understanding the role of pores that are smaller than the solvated electrolyte ions in ion sorption (described in section 3).

2.3 Graphene-based Materials for SCs

Graphene, a one-atom thick layer of sp2 C atoms arranged in a honeycomb lattice structure, is among the various carbonaceous materials that are under study for this type of electrochemical storage.[82] Graphene segments are considered to be the building blocks of many others regularly structured carbons (graphite and CNTs) and various irregular porous carbons with distorted structures (ACs, carbide derived carbons (CDC)).[83] The specific capacitances of graphene vary in a broad range. Owing to the unique sheet arrangement of carbon atoms through sp2 bond renders several impressive properties to graphene. Graphene has a high electron mobility (> 150,000 cm^2/V.s), mechanical flexibility (> 100 stronger than steel) and remarkable theoretical surface area of 2630 m^2/g and is an ideal candidate for SCs.[84] Theoretical predictions assign that a high gravimetric capacitance of 550 F/g could be obtained if both surfaces of graphene were used for charge storage.[85] However, later studies have revealed that a single sheet of graphene may be too thin to provide complete charge screening of ions on both sides and some reduction to the theoretical predictions is expected.[86]

2.3.1 Production Methods of Graphene

The methods adopted for graphene production (Scheme I-3) play a crucial role in determining the properties of the final graphene-based material.[71] Limited scalability and high production costs of production methods such as mechanical exfoliation,[82] synthesis on silicon carbide (SiC)[87] and bottom-up synthesis from organic precursors restrict the use of graphene to fundamental research.[88] Likewise, chemical vapor deposition (CVD) of hydrocarbons, although a well-established technique in industry, seems unsuitable for mass-production of graphene for electrochemical energy storage because of its high cost and rather low yield.[87] The other two methods that are widely employed for the bulk production of graphene are liquid-phase exfoliation, and reduction of graphene oxide. In liquid-phase exfoliation, pristine or expanded graphite particles, obtained by thermal expansion of graphite intercalation compounds, are dispersed in a solvent and exfoliated using external driving forces.[89–91] An external driving force such as ultra-sonication, electric field or shearing forces induce the exfoliation of graphite into high quality graphene sheets. Unfortunately, low yields of this process leaves a considerable amount of unexfoliated graphite.[91]
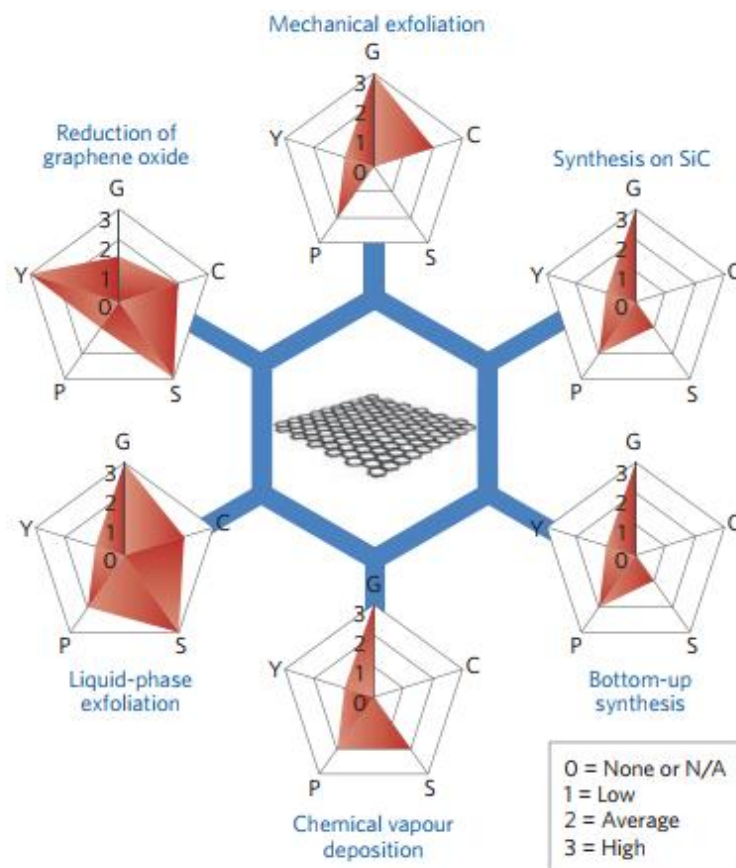
Scheme I-3 Schematic of most common graphene production methods. Each method is evaluated with graphene quality (G), cost (C), scalability (S), purity (P) and yield (Y) of the overall process.[71]

The most commonly used bulk scale synthesis method is from graphene oxide (GO), a highly defective form of graphene with a disrupted sp2-bonding network (Scheme I-4).[84] GO is produced by strong oxidation of pristine graphite followed by stirring or ultra-sonication in liquid media to ensure the exfoliation of the oxidized graphene oxide sheets. Hummers and Offeman's method of oxidation[92] (among others such as of Tour's[93] and Brodie's[94]) is widely used to obtain the initial graphite oxide which are then exfoliated under different optimized conditions. Unfortunately, GO has very poor electrical conductivity as the sp2 C atoms conjugated network of the graphene sheets is disrupted with formation of various oxygen containing functional groups such as alcohols, epoxides and other carbonyls.[84] Hence, the sp2 network must be restored through reduction in order to be useful for electrochemical energy storage applications. Chemical, thermal and electrochemical processes are commonly employed for this purpose to eventually produce reduced graphene oxide.[95–99] Despite the low-to medium quality of the obtained material due to the presence of both intrinsic defects

36

(edges and deformations) and extrinsic defects (O and H-containing groups), GO allows production of bulk quantities of graphene-based materials with high yield and contained costs.
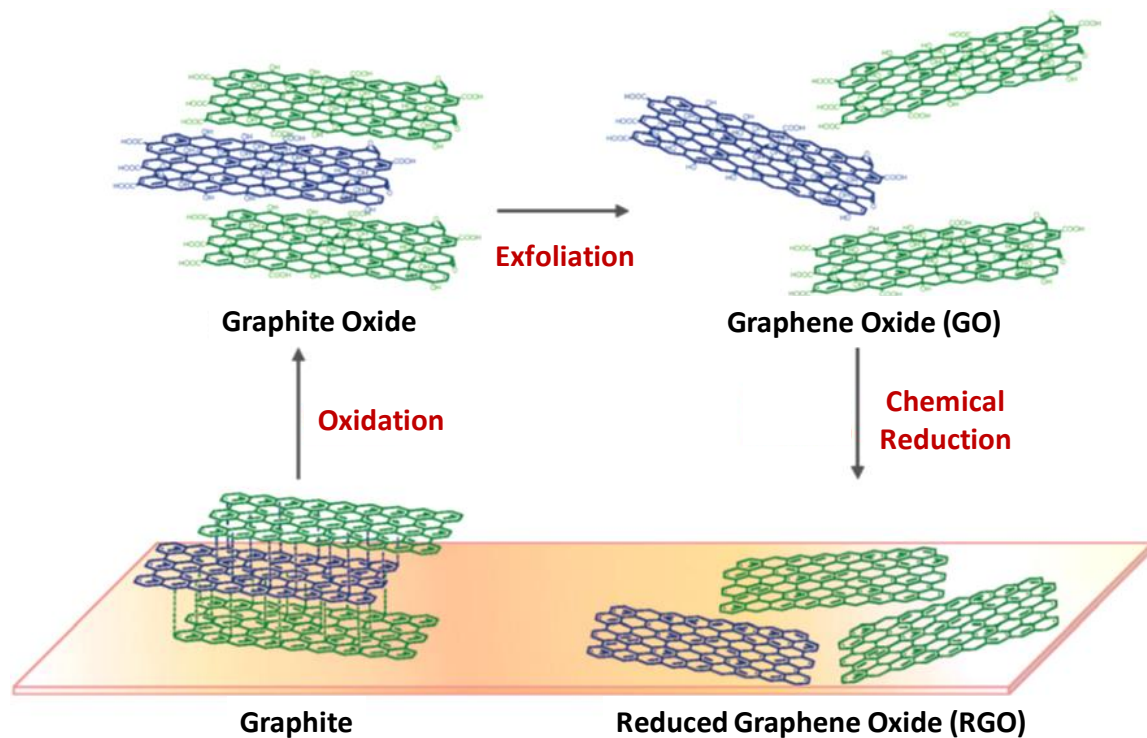
Scheme I-4 The general synthesis protocol for the synthesis of GO from graphite.
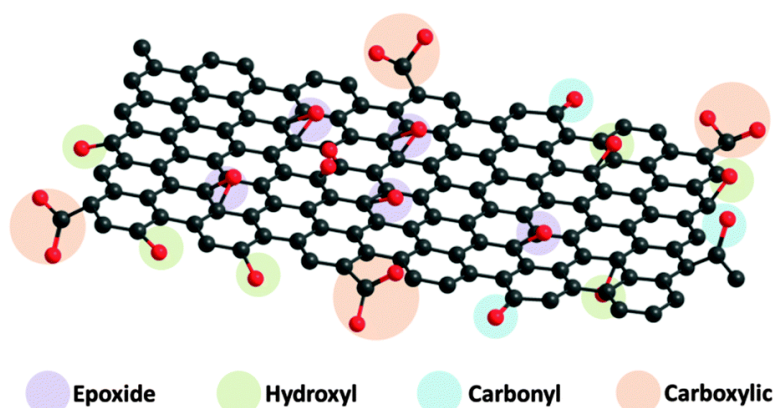
Figure I-13 The chemical structures of graphene and GO.

The chemical structure of GO was extensively studied in the 1990s using X-ray diffraction (XRD), Fourier-transform infrared spectroscopy (FT-IR)[96], X-ray photoelectron spectroscopy (XPS)[96], electron-spin resonance (EPR)[100] and nuclear magnetic resonance (NMR)[101] spectroscopies. Among the several models proposed to describe GO[101], Lerf-Klinowski's model[102] is generally regarded as the most appropriate model (Figure I-13). In this model, GO

is characterized with randomly distributed oxygen-containing functional groups and it is believed that the epoxy and hydroxyl groups lie above and below each layer whereas the carboxylic groups are on the edges. Thanks to its surface functionalities, GO offers abundant chemical tunability for various applications.

2.3.2 **Graphene-based 2D materials**

In the context of SCs, graphene-based materials that were synthesized through reduction of GO, were analyzed as close graphene-like materials. These graphene-like materials contain two dimensionally arranged graphene sheets as electrodes in SCs.[103] One of the first studies of graphene for SCs was reported by thermal exfoliation of graphene oxide (GO) (Figure I-14a).[104] This processing resulted in well-developed porosity and high BET SSA of 920 m^2/g. When tested in SCs using 1 M H_2SO_4 electrolyte, specific capacitance of 100-120 F/g were observed. This value was better than OLC and CNTs but was inferior to the more common ACs. An alternative method for graphene synthesis was proposed by reducing graphene oxide sheets in water with hydrazine hydrate (Figure I-14b).[103] The synthesized reduced graphene oxide (RGO) has graphite structures with 15-20 μm size particles exhibiting moderately high SSA of 700 m^2/g. RGO provides specific capacitance of 130 and 100 F/g in aqueous and organic electrolytes, respectively.[103] The low specific capacitances were due to the formation
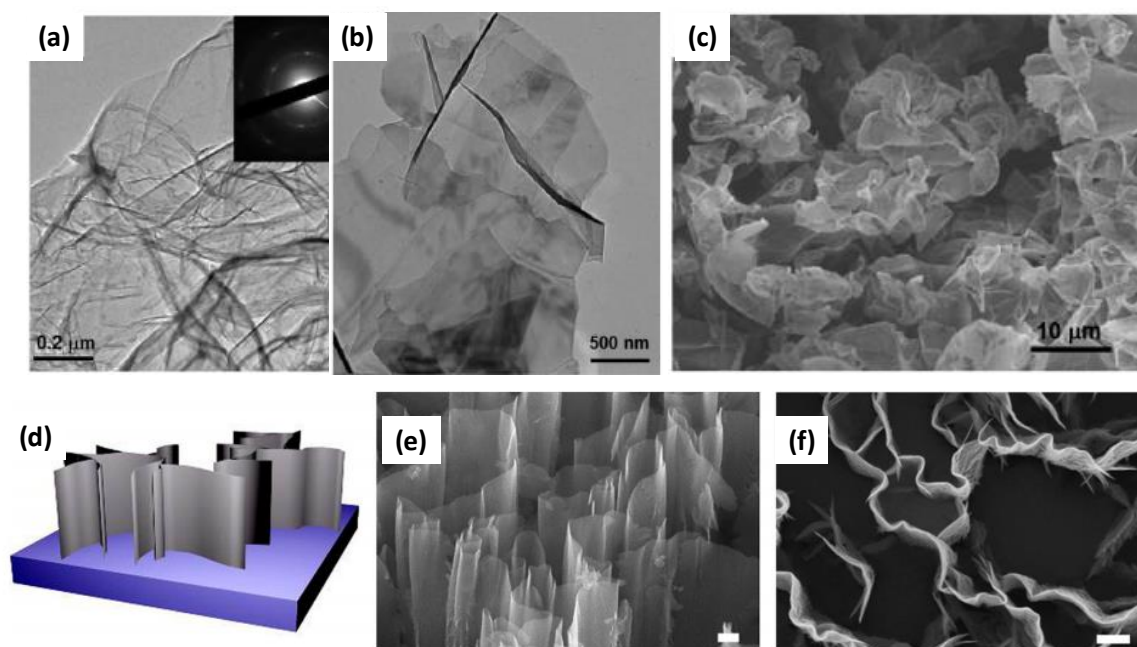
Figure I-14 TEM images of (a) thermally exfoliated graphene oxide and (b) chemically reduced graphene oxide. (c) SEM image of curved graphene sheets. (d) Schematic of vertically aligned graphene and its corresponding (e & f) SEM images at a scale of 100 nm.[103,106]

of stacked graphene sheets during reduction to strong π- π interactions. This restacking of graphene sheets during chemical reduction of GO has encouraged other methods of graphene synthesis.

Curved graphene[105], partially reduced graphene[98] and *in situ* electrochemical reduction of GO[90] are proposed as few such strategies to avoid the restacking of graphene sheets (Figure I-14c). Another interesting strategy is to grow vertically aligned graphene sheets on a carbon cloth through CVD techniques (Figure I-14d-f).[106] 2D graphene nanosheets are grown perpendicularly to the substrates to construct an interconnected array structure by using gaseous carbon sources. The synthesized films offered great porosity, large surface area, high conductivity, and good mechanical stability. However, the height of such films is usually less than 1 μm and lead to low capacitances in SCs (1.8 mF/cm^2). A reliable and reproducible synthesis in large scale with low cost has been the challenge for the strategies discussed here. Recently 3D architectures based on graphene derivatives have been proposed as potential candidates with limited restacking and offering a 3D microporous network that can be synthesized at large scales.[74] The next section describes the various proposed structures in more detail.

2.3.3 **Graphene-based 3D structures**

Reduced graphene oxide (RGO) has been extensively studied as a graphene-like material that can be synthesized in bulk quantities for SCs applications.[96] However, the two-dimensional structure and amphiphilicity of the reduced graphene oxide sheets make them restack easily into aggregates, which greatly reduces their accessible surface area, and thereby deteriorates their performance in SCs. Fortunately, the individual 2D graphene oxide sheets could be integrated into 3D macroporous sponges or monoliths.[74] The 3D structures thus obtained limit graphitic stacking and offer several merits. (i) Interconnected graphene sheets can form a conductive and robust macroporous network, which facilitates ion and electron transfer inside the electrodes. (ii) The porous graphene structure with large SSA can increase the contact interface between the electrode and the electrolyte and decrease the diffusion resistance. (iii) Binder-free and metal current collector free electrodes could be fabricated from the pieces of monoliths for flexible SCs (iv) Without the addition of inactive binders and current collectors, the overall device capacitances can be greatly improved.

3D structures such as monoliths, films and foams are commonly synthesized using self-assembly techniques. A gel is usually defined as a non-fluid colloidal or polymer network expanded throughout its whole volume by a fluid. If the fluid is water and the network component is a polymer, it is referred to as a hydrogel. If the hydrogel is mechanically strong, it can result in formation of a monolith like a block of sponge. The monoliths normally take the shape of the container used for the synthesis and thus could be synthesized in various shapes. Typically, the polymer layers assemble at the water-air interface and gradually take the shape of the container.

GO is akin to a 2D amphiphilic polymer with presence of both hydrophilic and hydrophobic segments. The 2D laminated sheet morphology and the conjugated domains on the sheets could enable contact points and facilitate formation of a network. Indeed, GO sheets can self-assemble through van der Waals interaction or hydrogen bonding by subtly adjusting the hydrophilic/hydrophobic balances (Scheme I-5). A self-assembled gel through such non-covalent interaction would generally have little or no changes to the oxygen functionalities on the sheets. Several synthetic polymers (ex. Poly (ethylene oxide), Poly (vinyl pyrrolidone), etc.)[107] were found to be effective promoters of gel formation of GO through non-covalent hydrogen bonds. Further studies have found that amino acids,[108] nucleosides, polyamines,[109] multivalent cations (Ca^{2+}, Mg^{2+})[110] could also form GO gels by balancing the inherent electrostatic repulsion and hydrophobic interactions between GO sheets. Despite all the interesting synthesis procedures, GO gels are insulators and are not suitable for applications in SCs. The synthesized gels should be electrically conducting for high power SCs applications. Moreover, the synthesized gels should be mechanically strong for easier fabrication and long-term cycling in SCs.
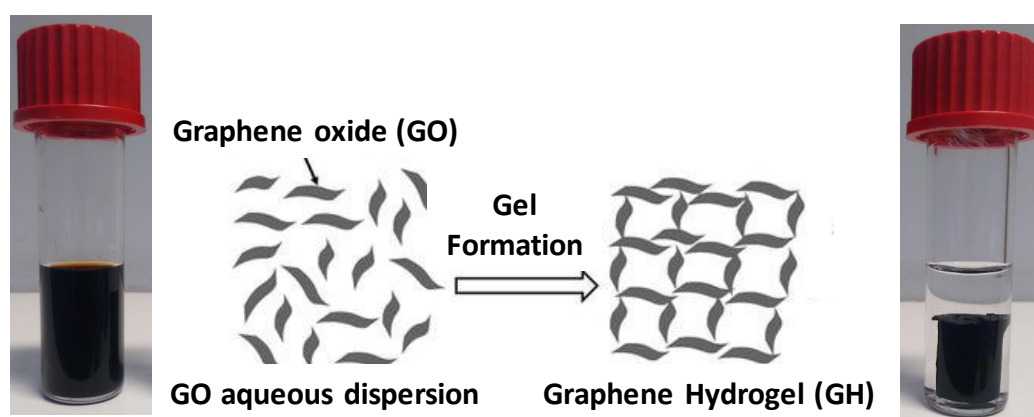
Scheme I-5 Schematic representation of hydrogel formation from an aqueous GO solution.

The-assembly of GO sheets could also be achieved through either controlled chemical reduction or by covalent reactions of a guest molecule with the surface oxygen functionalities.[111] The monoliths thus formed usually have interconnected 3D porous networks with pore diameters ranging from sub-micrometer to several micrometers and their pore walls consist of few layers of stacked RGO sheets.[112] Additionally, monoliths synthesized in this method usually have suitable mechanical strength and can be cut into pieces for electrodes without any binders or support materials. Such monoliths ease the electrode fabrication process and are of great interest for SCs.
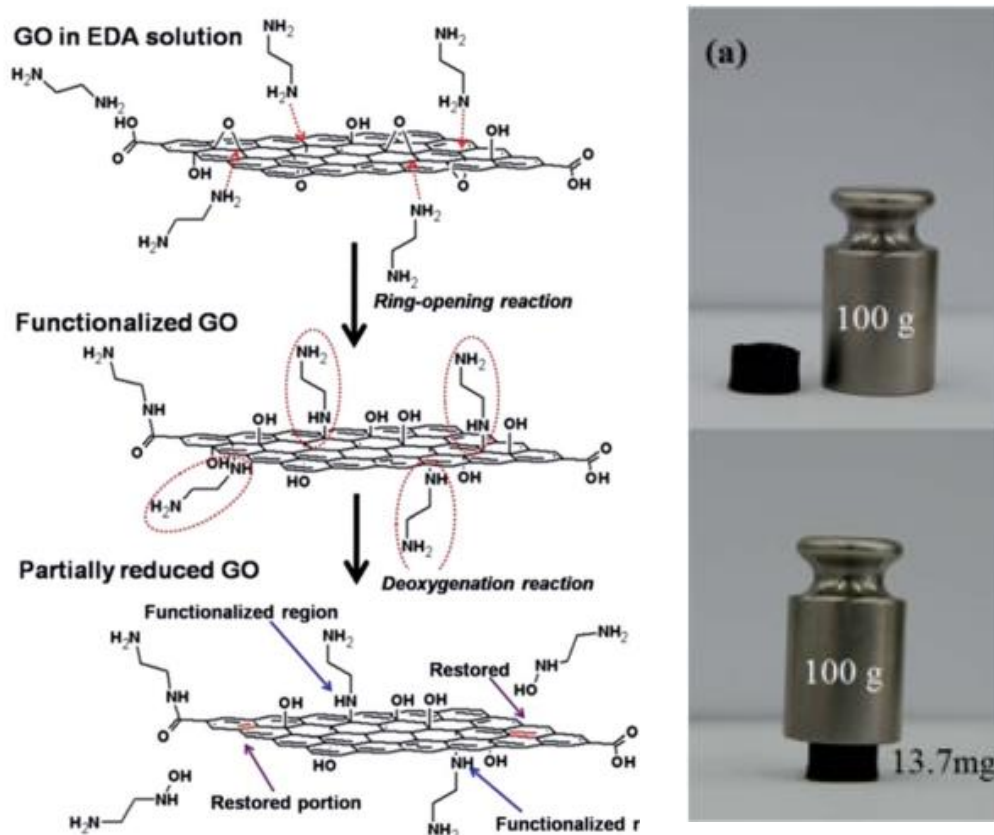
Figure I-15 (a) Schematic illustration of mechanism of ethylene diamine (EDA)-mediated functionalization and reduction of GO. (b) Digital images showing the strength of EDA functionalized gel.[113]

Alkyl diamines have been proposed as bi-functional linkers that could cross-link GO sheets through covalent interactions and concomitant reduction form a hydrogel (Figure I-15).[113–115] The rich surface chemistry of GO allows covalent bonding of sheets with an alkyl diamine. Additionally, alkyl diamines are partially reducing in nature and cause simultaneous gel formation through partial reduction of GO sheets. However, the partial reduction is

insufficient for their application in SCs and thus, an additional step of chemical reduction (hydrazine hydrate) is performed on the synthesized gels.[116]

Later studies have reported RGO hydrogels in a one-step procedure by hydrothermal reduction of GO suspensions (Figure I-16).[117] The supercritical water formed under autoclave (180°C sealed autoclave) facilitated simultaneous reduction and gel formation. This approach resulted in a high conducting and mechanically flexible gel, which needed no post-treatment for removing residual chemical reductants. The synthesized gel showed high capacitance of 220 F/g in SCs using aqueous electrolytes.
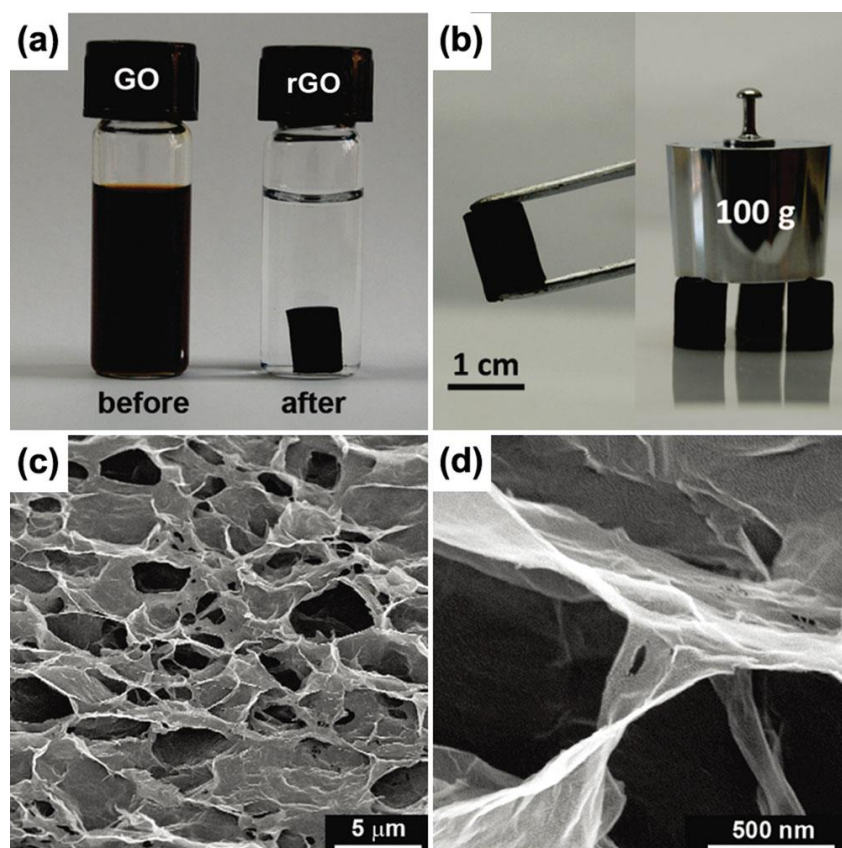
Figure I-16 Hydrothermal treatment of graphene oxide leads to (a, b) RGO hydrogels. The SEM images of show the interconnected 3D network.[117]

The hydrogels are characterized by their very low material density of ~ 0.02 g/cm^3 and thus have very low volumetric capacitances of < 10 F/cm^3. In addition to the 3D graphene structures discussed here, ACs and templated carbons also suffer from low volumetric densities in SCs. In the recent years, important breakthroughs have been made in improving the material densities of various 3D carbon materials for better volumetric performances.[118–120] Densifying

the pores is currently done in two ways; mechanical compression[121] and capillary compression.[122]

2.3.4 **Mechanical Compression**

Mechanical compression is a straightforward way of improving the material densities (Scheme I-6). When put under pressure, materials undergo an irreversible compression of the large empty spaces that are in the size range of micrometers. Ruoff and co-workers employed simple mechanical compression to densify activated microwave exfoliated graphene oxide (aMEGO).[123] After compression with a force of 25 T, the density of the aMEGO sample increased to 0.75 g cm^3 with a SSA of 707 m^2/g compared to that of the uncompressed sample (0.34 g cm^3), leading to a significant improvement in the volumetric capacitance from 54 to 110 F/cm^3 in an organic electrolyte. As another example, Xu and co-workers reported a 3D free-standing holey graphene framework (HGF) film with a hierarchical porous structure and efficient ion transport shortcuts and a high packing density through mechanical compression of the hydrothermally synthesized HGF (Figure I-17).[121] The compressed HGF films exhibited a specific surface area of 810 m^2/g, close to that of the uncompressed HGFs 830 m^2/g. With a large ion-accessible surface area, efficient electron and ion transport pathways as well as a high packing density, the compressed HGF films could deliver a gravimetric capacitance of 298 F/g and a volumetric capacitance of 212 F/cm^3 in an organic electrolyte. This method of mechanically compressing carbon materials can be easily employed in large-scale commercial applications. However, this method generally requires high pressure and specific equipment.
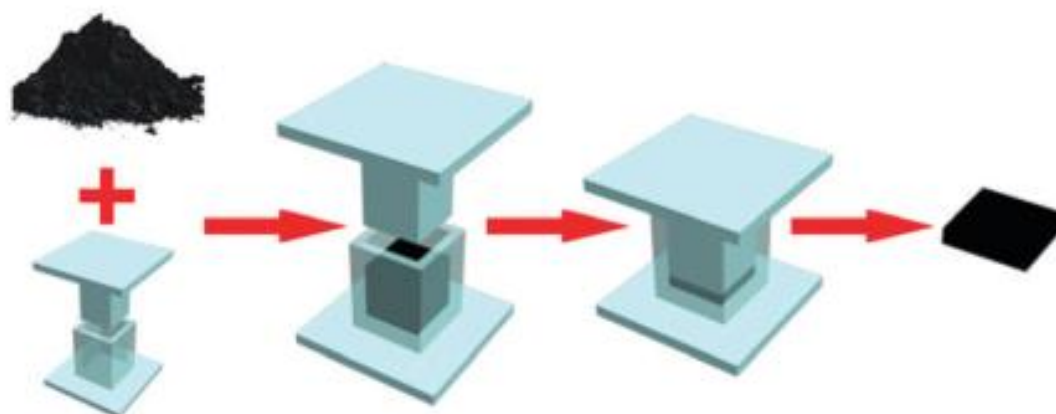
Scheme I-6 Schematic illustration of mechanical compression of various 3D graphene materials
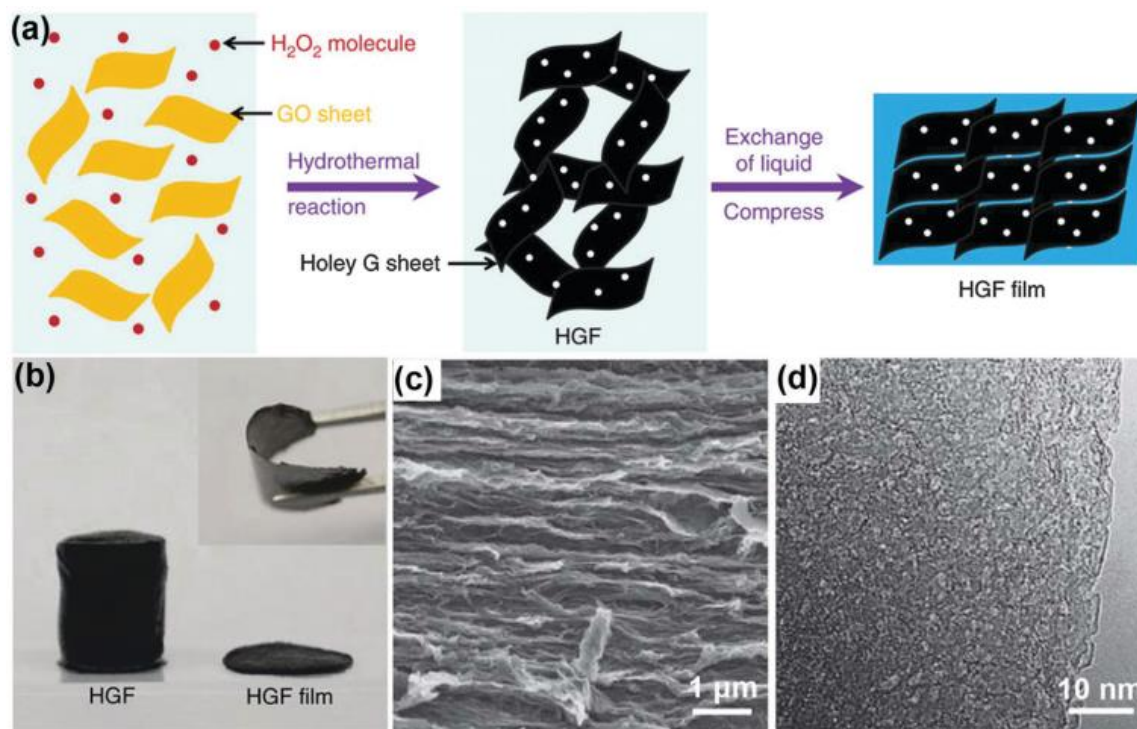
Figure I-17(a) Schematic representation of the synthesis of holey graphene framework (HGF) with its (b) digital pictures before and after compression. (c,d) Transmission electron microscopy images show the holes in the graphene sheets.[121]

2.3.5 **Capillary Compression**

Unlike mechanical compression, which relies on an external force, compression by capillary pressure through evaporation of solvents is a novel and effective liquid-mediated method to increase the packing density of carbon materials. Porous yet densely packed carbon electrodes with a high ion accessible surface area and low ion transport resistance are crucial to high-density electrochemical capacitive energy storage devices. Researchers have independently reported evaporation of solvents to densify chemically modified graphene (CMG) films and graphene hydrogels in 2013 (Scheme I-7).[118,122] CMG films were put in a mixture of volatile and non-volatile solvents and later densified by capillary pressure during a controlled removal of volatile solvent trapped in the gel. By changing the ratio of volatile and non-volatile liquids, the packing density of the CMG flexible film was increased in a controlled manner from 0.13 to 1.33 g/cm^3. This simple technique has resulted in exceptional volumetric values of 260 and 250 F/cm^3 in aqueous and organic electrolytes respectively.

Another simultaneous report on graphene hydrogels has used a simplified strategy of drying the hydrogels under ambient conditions and achieved an improvement in density from 0.02 g/cm^3 to 1.58 g/cm^3 (Scheme I-8). Conventionally, hydrogels are freeze-dried in order to retain

the microporous structure whereas, in this report, researchers shrink the gels using simple ambient drying technique. During the evaporation process, water exerts a ''pulling force'' on the graphene layers and results in the shrinkage of the macroporous network as there is strong interaction between water and graphene nanosheets. The robust but elastic macroporous network of flexible graphene nanosheets shrinks but retains a porous structure inherited from the parent hydrogel. Thus, the final form of dried gel consists of curved and very compactly packed graphene nanosheets. The resulting gel delivered highest double-layer capacitances of 374 F/cm^3 in an aqueous electrolyte.
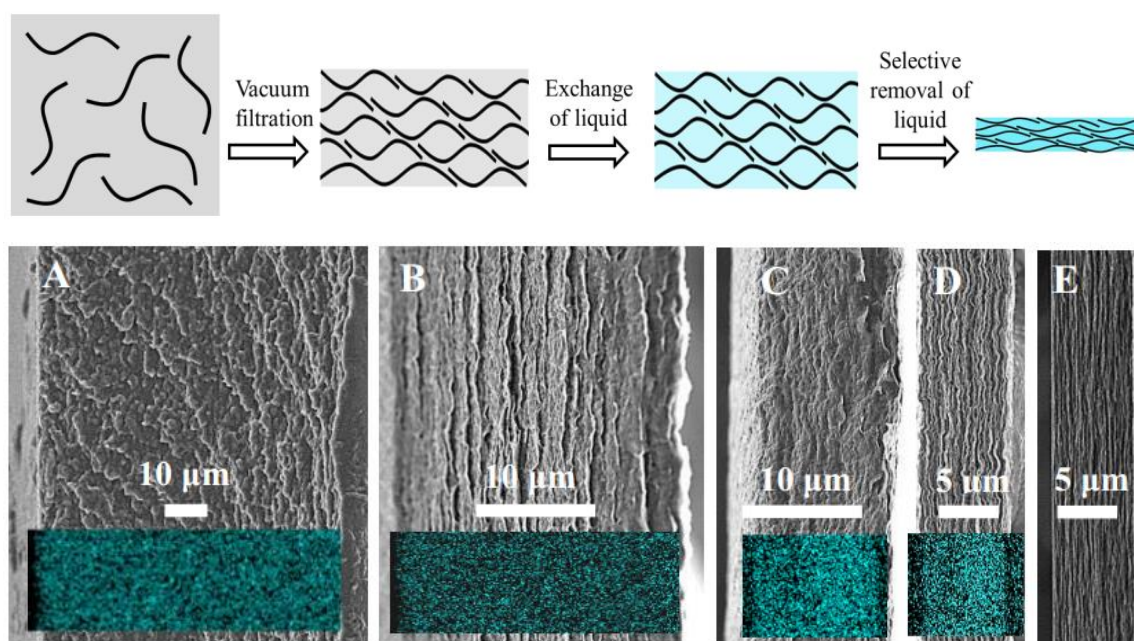
Scheme I-7 Schematic representation of the capillary compression of a chemically modified graphene film. Densities of the films were increased from 0.13 to 1.33 g/cm^3 in a controlled fashion.[118]

In summary, macroporous architectures of graphene (sponges, films, gels) have showed great potential for SCs applications with a conductive and robust network, which facilitates ion and electron transfer inside the electrodes. However, despite limiting the restacking of graphene sheets as compared to RGO, various 3D architectures of graphene still have significant restacking and do not offer the full potential of graphene.
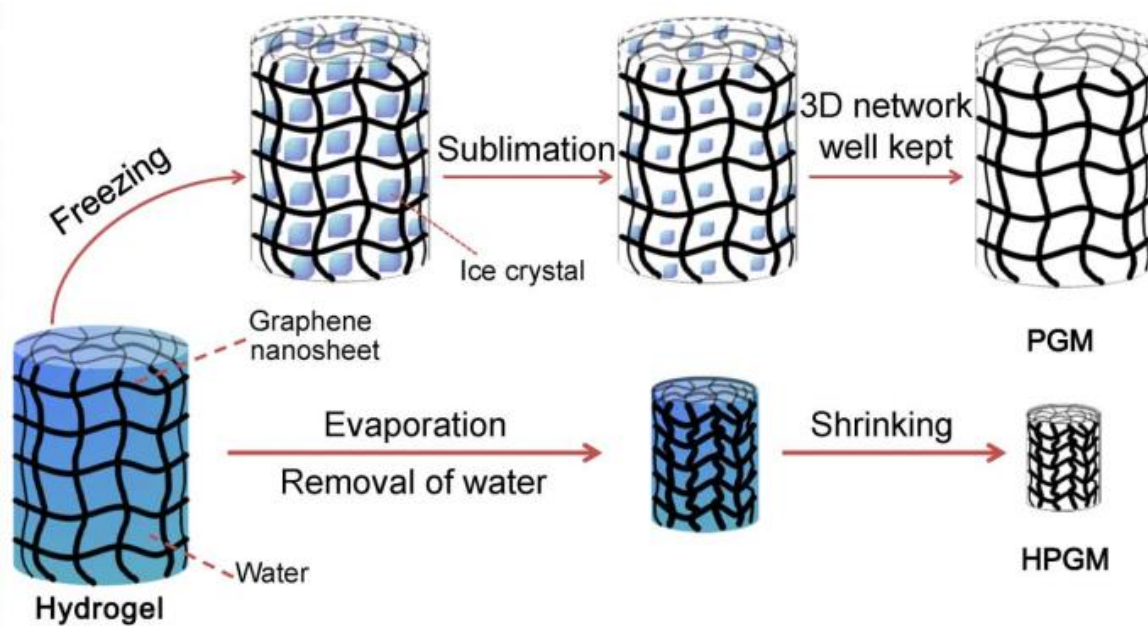
Scheme I-8 Schematic representation of the two types of drying process used for hydrogels. Freeze drying retains most of the 3D network as such, whereas, gradual evaporation of water shrinks the gels.[122]

3. Role of Pore Sizes on Charge Storage

As described in the previous section, energy densities of SCs could be increased by choosing materials with high electrochemically active surface area as electrodes. Initially, it was assumed that the SSA of a material obtained from gas sorption analyses (using Brunauer-Emmett-Teller (BET) method) is the same as the electrochemically active surface area of charge storage.[124] Early studies trying to correlate SC performances to porosity of electrodes suggested a linear dependence between specific capacitance and the SSA. Typically, there is a general correlation for small SSA values, but the capacitance becomes almost constant for values higher than 1200 – 1500 m^2/g. The BET method often overestimates the SSA for carbons therefore, density functional theory (DFT) method was applied to estimate SSA and showed a slightly better correlation, but there is still a plateau for values higher than 1500 m^2/g.[26] It was later understood that other porosity characteristics such as pore shapes, sizes and their distribution also have a strong influence on capacitance properties.[16]

The relationship between pore sizes and electrolytic ion sizes on charge storage has been extensively studied over the years. Studies have suggested that the electrolytic ions enter pores with their solvation shells owing to large solvation energy of the ions.[125] Thus, considering that the solvated ion sizes for organic electrolytes is larger than 1 nm, pores in the range of 2-5 nm were thought as best suited for ion sorption.[55,126,127] Essentially, mesoporous carbons with narrow pore size distributions were considered as materials with optimum charge storage in carbon materials. However, considerable effort in synthesizing mesoporous carbons using template techniques have only led to minor improvements.[128] Capacitances of 100-120 and 150-200 F/g were obtained in organic and aqueous electrolytes respectively.[129–131] In the early 2000s, few researchers have independently observed high capacitances with carbons containing large amounts of micropores.[55,125] One particular study had found a linear relationship between capacitance and microporous volume in the materials and raised several questions about the existing understanding of ion sorption at the time.[55]

3.1 Ion Sorption in Micropores

The difficulty in studying the individual effects of SSA, pore size, porosity and pore size distribution on the capacitive charge storage is mainly due to poor synthesis control on carbon pore characteristics.[17] New developments in synthesis of CDCs with sub-nanometer level

control of average sizes has opened up opportunities for analysis in SCs.[79,132] CDCs have a narrow pore-size distribution with a mean value that is tunable with better than 0.05 nm accuracy in the range of 0.5 to 3 nm and a SSA up to 2000 m^2/g, which make them attractive candidates for studying porosity in supercapacitor applications. This precise control of materials in the range of the sizes similar to the solvated electrolytic ions gave several insights into the contribution of micropores.
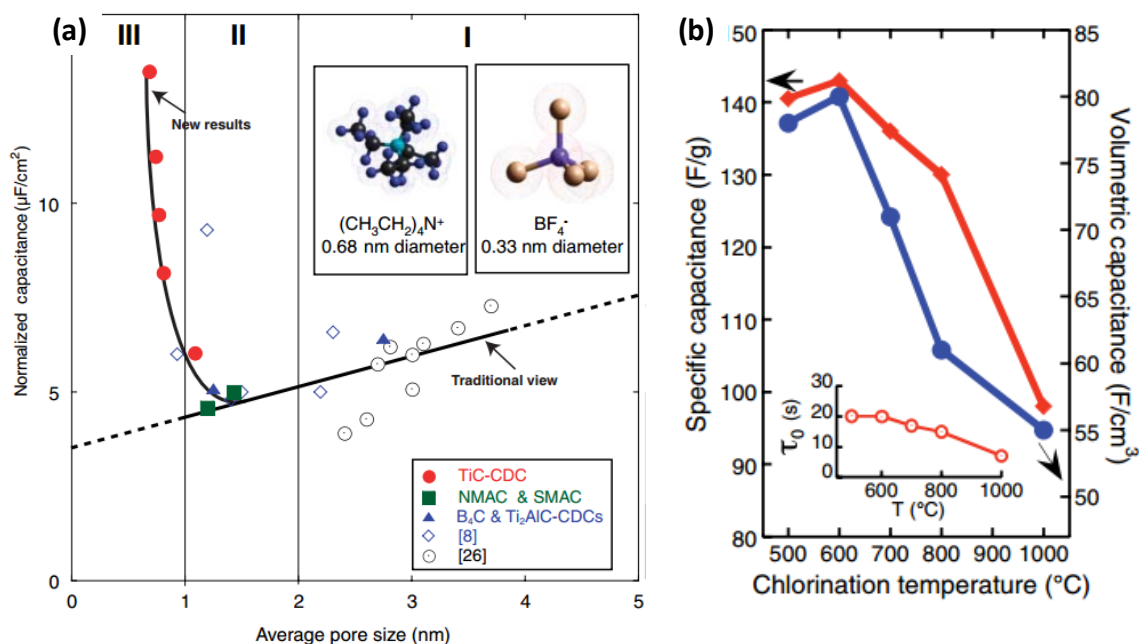
Figure I-18 Electrochemical behaviour of TiC-CDC synthesized in the range of 500- to 1000°C. (a) Plot of specific capacitance normalized by BET SSA for the carbons in this study and in two other studies with identical electrolytes. The normalized capacitance decreased with decreasing pore size until a critical value was reached, unlike the traditional view, which assumed that capacitance continually decreased. (b) Gravimetric and volumetric capacitances of the materials with respect to synthesis temperature.[125]

Chmiola et al. have used Titanium carbide-derived carbons (TiC-CDC) with average pore sizes ranging from 0.68 to 1.1 nm in SCs with $TEABF_4$ in acetonitrile as electrolyte (Figure I-18).[125] In contrast to the existing understanding, huge increases in capacitances were seen when pore sizes go below the solvated ion size (1 nm). The obtained results were normalized with the BET SSA to highlight the effect of pore size and compared with the traditional expectations. It was proposed that the solvated ions (1.3 nm) partially lose their solvation spheres to squeeze in the confined micropores. Such confinement would reduce the distance between ion center and the carbon surface resulting in an increased capacitance. The gravimetric capacitances increased from 100 to 140 F/g while reducing the pore sizes from 1.1 to 0.68 nm. Several other

studies have supported this size effect and signaled towards new fundamental understanding of the role of micropores.[133,134]

Further studies using the same system (TEABF$_4$/AN) were conducted in a three-electrode configuration to investigate the cation and anion behavior separately (Figure I-19).[126] The tested cation (TEA$^+$) is in the same size range as the pore sizes of TIC-CDC whereas BF$_4^-$ is smaller compared to all the pores. Results confirmed that both cations and anions are at least partially desolvated and the maximum capacitances or both the ions occur at different pore sizes. Moreover, anions exhibit higher capacitances than cations in all the pore sizes and indicate different effective ion sizes.
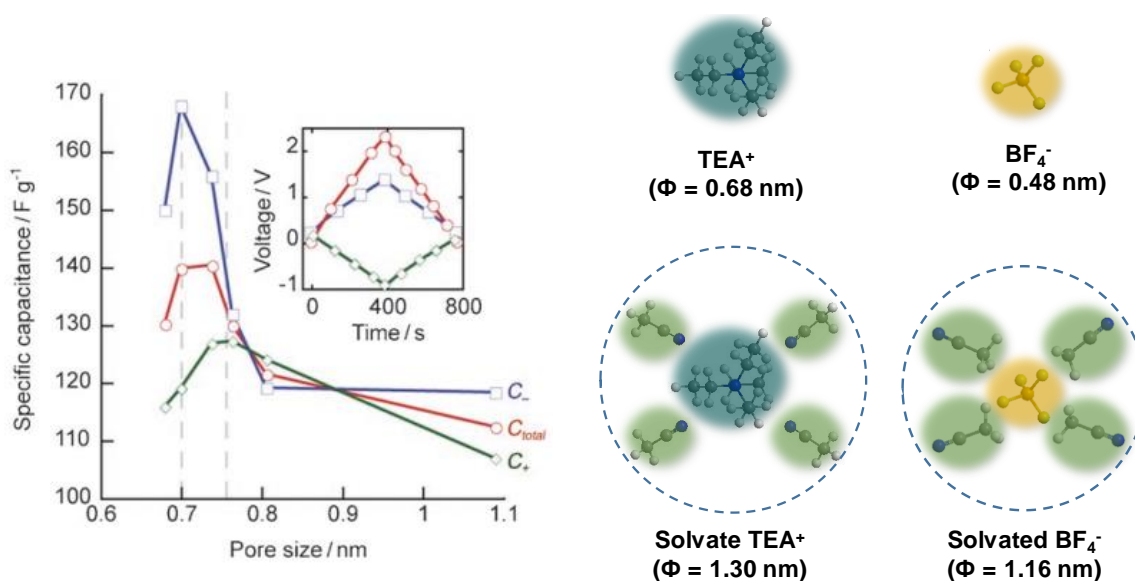
Figure I-19 Gravimetric capacitances of CDCs of various pore sizes under positive and negative polarization using 1 M TEABF$_4$/AN electrolyte. The calculated sizes of solvated and desolvated TEA$^+$ cation and BF$_4^-$ anion are show on the right.[126]

Subsequent studies on pore vs ion size relationship were done using cavity microelectrode (CME) by cyclic voltammetry and electrochemical impedance spectroscopy measurements in TEABF$_4$/AN.[135] As compared to conventional electrodes, microelectrodes have very less real electrochemical interface area and the ohmic drop arising from the bulk of the electrolytes is negligible, enabling use of scan rates of few volts per second. From CV measurements in AN, ideal rectangular curves were observed for CDC with 1 nm pore size, despite the solvated ion sizes of TEA$^+$ and BF$_4^-$ being larger than 1 nm.[136] A gradual decrease in pore sizes from 1 nm to 0.68 nm has shown reduction in cation adsorption (in the negative polarization vs. open circuit voltage (OCV)) but the anion adsorption (in the positive polarization vs. OCV) remained

unchanged. The pore size of the CDCs below which a reduction in current is observed for the cations is considered as the effective size of the cation in the pores. Thus, the effective size of the TEA$^+$ cation was found to be in between 0.76 – 1.0 nm. Similarly, the effective size of anions was deduced to be < 0.68 nm. Similar experiments were later performed using TEABF$_4$ in propylene carbonate (PC) solvent and the effective sizes from the CVs were found to be larger than those in AN (0.75 nm - anion and > 1 nm - cation).[137] These results highlighted the impact of nature of the solvent and the ion-solvent interaction on ion sorption and confirmed that the ions move in and out of micro pores with a partial degree of desolvation.[138]

3.2 Ion Desovlation in Micropores

Although the observation of partial desolvation in small micropores (< 1 nm) is definitive, the quantitative information about the extent of desolvation was not available through CV studies. Levi and Aurbach have pioneered the use of electrochemical quartz crystal microbalance (EQCM) in porous carbons to study the changes in ion population as a function of charge accumulated on the electrode (Figure I-20).[139–141] EQCM is composed with a thin piezoelectric quartz crystal sandwiched between two metal electrodes used to create an alternating electric field across the crystal, causing vibrational motion of the crystal at its resonating frequency. This resonating frequency is sensitive to the electrode mass deposited on the crystal. The shift in the quartz resonating frequency can be converted into the mass change on the quartz crystal during the electrochemical processes. EQCM studies were performed on CDC (1 nm) using 1-ethyl-3-methyl-imidazolium cation (EMI) and bis(trifluoromethylsulfonyl)imide anion (TFSI) in AN solvent.[142] A solvation number between
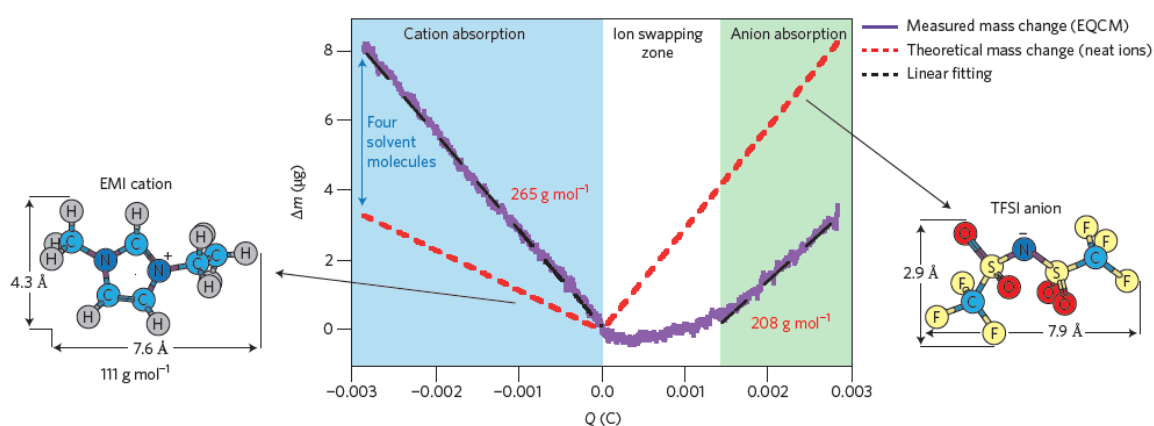
Figure I-20 EQCM curve showing the mass change with respect to accumulated charge on the CDCs electrodes in EMITFSI/AN electrolyte. The difference in the predicted mass change due to a completely desolvated ion allows calculation of the extent of partial desolvation.[142]

three and four was calculated for EMI cation in the pores compared to eight solvent molecules in the bulk electrolyte. These results clearly indicated the partial desolvation of ions when accessing small pores.

Additional studies were performed using ionic liquid electrolytes to analyze the pore sizes in a solvent free environment. CDCs with different pore sized were tested in neat EMI-TFSI ionic liquid and the highest capacitances were observed for pore sizes around 0.7 nm, close to long dimensions of cation and anions.[143] Thus, from the material point of view, it was suggested that adapting electrode pore sizes to electrolyte ion sizes is an efficient way of charge storage.

3.3 Hierarchical Porosity

Reports have suggested that if an electrode material contains only micropores, it would lengthen ion diffusion distances from the bulk electrolyte. This would lead to large IR drop and small accessible surface area at high currents and result in poor power performance.[58,134,144] On the other hand, it has been proposed that the presence of small mesopores (2-10 nm) can accelerate the kinetic process of the ion transport in the electrodes and improve power performance. A report on designing carbon materials with hierarchical porous structure with a combination of macro, meso and micropores has provided interesting insights into the role of various pores (Figure I-21).[145,146] The 3D hierarchical porous texture combined macroporous cores, mesoporous walls, and micropores. Electrochemical studies using aqueous and organic electrolytes offered high power performance and provided further understanding about the roles of different pores in charge storage.[58] The macroporous cores act as ion-buffering reservoirs and mesoporous provided low-resistant ion transport pathways. The micropores are the ion sorption sites that enable the charge accommodation in the electrodes during charge-discharge of a SC. Following this report, a new trend of electrode materials with focus on fabricating hierarchical micro-architecture was established.[58]

However, all porous carbons display a certain pore size distribution rather than just "one" pore size, which is characterized by with an average pore size. Synthesis of carbon materials with precisely tuned pores and narrow pore distributions is still hard and unfortunately, reliable determination of the pore sizes with gas sorption has been challenging as well.[147] Reliable determination of PSDs from gas adsorption studies remains a difficulty, as the density functional theory-based approaches require prior knowledge of the pore geometry and heat

of adsorption of the material. To that end, combinations of characterization and modelling techniques using small-angle X-ray and neutron scattering are being developed in complementarity to gas sorption analyses.[83,148–150]
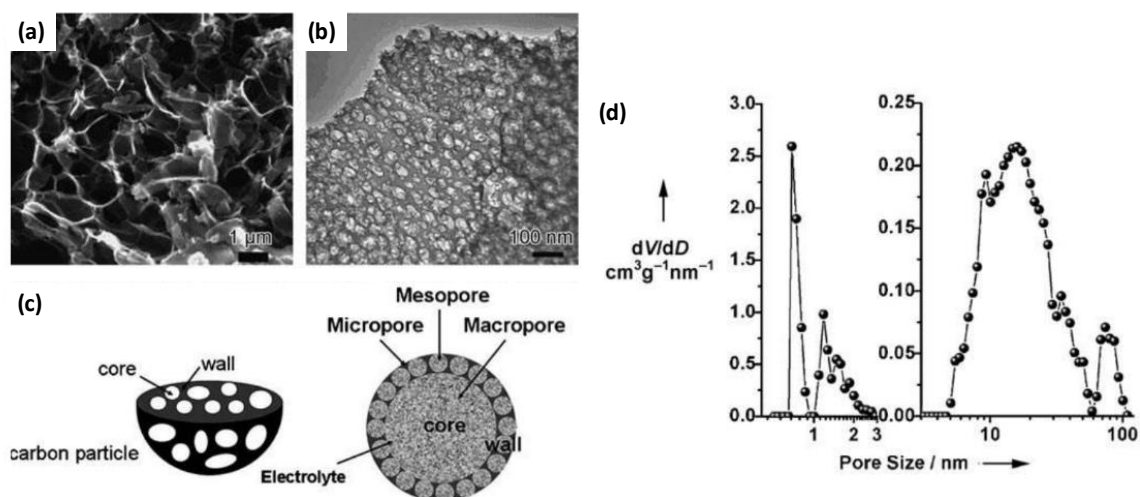
Figure I-21 (a) SEM image of the macroporous cores and (b) TEM image of the mesoporous walls of the 3-dimensional (3D) hierarchical porous carbon material. (c) Schematic representation and the (d) pore size distributions of the 3D hierarchical porous structure.[58]

4. Context & Objectives

4.1 Current Theme of Graphene Research for SCs

As discussed earlier, graphene-based materials have recently emerged as promising electrode materials for SCs owing to their high surface areas, electrical conductivities and mechanical flexibilities.[71] In the last few years, new developments in the synthesis of graphene-like materials have spurred their potential as candidates for SCs with high energy and power performances.[103] This thesis work is devoted towards designing and developing novel graphene-based architectures for SCs.

Since the first application of chemically reduced graphene oxide as electrode material for SCs, the problem of graphitic-stacking and the corresponding low electrochemical active surface areas in SCs has been well acknowledged in the scientific community. Researchers have since proposed macroporous 3D networks (hydro/aero gels, foams) to have higher active surface areas and interconnected porous structures for SCs.[74] The 3D architectures of the materials have limited the graphitic restacking and provided multiple ion transport pathways in SCs with considerable success. Various forms of graphene-based 3D structures with varied porous structures are proposed in the literature (in previous section). Much of the current research in graphene derivatives is devoted to optimizing the morphology with a focus on the inter-particular porosity, similar to the research on ACs.[74]

4.2 Our Proposed Theme of Graphene Research for SCs

Graphene-based materials differ from ACs with an ordered layered structure compared to the disordered and curved sheets in ACs (Scheme I-9a & b). Surprisingly, little attention has been devoted towards exploring the unique layered structures of the graphene-based materials. Although the natural graphitic spacing of 0.33 nm, defined as the intrinsic intra-particular pore, could be narrow for some ions in SCs, graphene derivatives are known to potentially exhibit expanded layered structures (extrinsic intra-particular pores) (Scheme I-9c). Expanded layered structures could be obtained by intercalating a molecule of interest in between the graphene layers and the inter-layer separation (d-spacing) could be precisely tuned by controlling the length or dimensions of the intercalant.[151] We speculate that the expanded layered structures in graphene-based materials could offer additional ion sorption sites and

yield maximum electrochemical active surface area. Moreover, the desolvation and confinement effects earlier seen in ACs could also be worth investigating in the expanded layers and as it could result in further efficient charge storage in graphene materials. Fortunately, the d-spacing of such structures could be readily evidenced through X-ray diffraction (XRD) analyses and thus an informed choice could be made to choose electrolytes with suitable ion sizes for SCs.
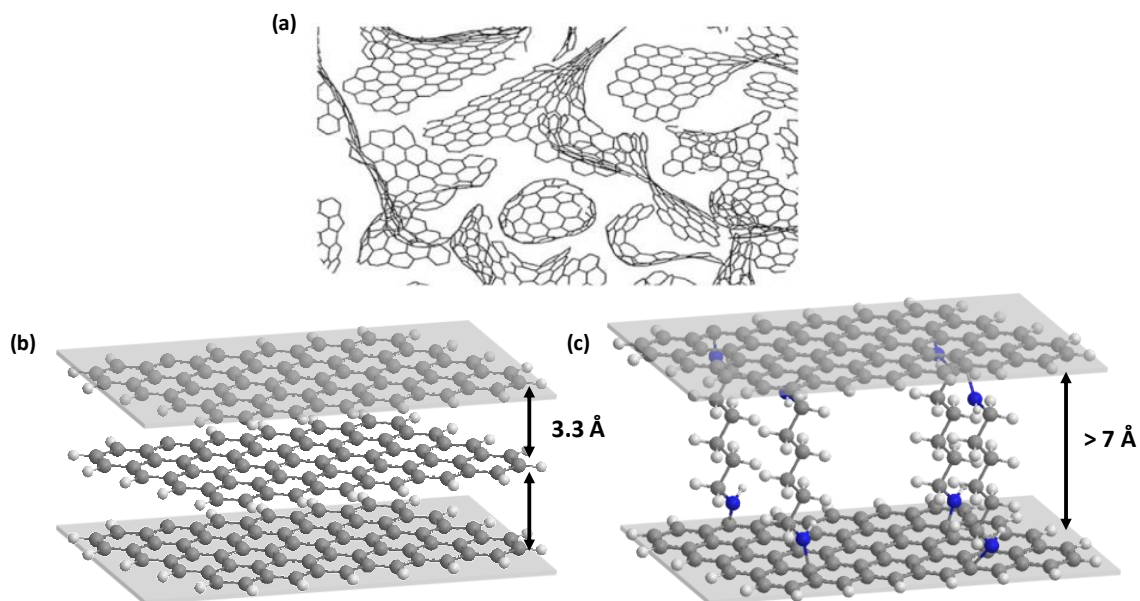
Scheme I-9 Schematic representation of the structures in (a) ACs, (b) graphite and the proposed (c) expanded layered structures.

4.3 Recent Reports in the Proposed Theme

Recently, few reports have attempted to describe the synthesis of graphene materials with expanded layered structures using organic molecules as pillars.[152,153] The described pillared graphene materials were then studied in SCs. Considerable improvements in charge storage were seen when a pillar is incorporated but the improved performances could not be directly related to changes in d-spacing. Instead, only the changes in the micro porosity of the material upon insertion of a pillar were identified as the reason behind the gains in capacitance values. Moreover, no evidence of the electrolytic ions entering the inter-layer galleries was observed.

Another specific fundamental study employed controlled electrochemical exfoliation of graphene oxide in propylene carbonate to tune the inter-layer separation (Figure I-22).[154] A combination of exfoliation and in-situ XRD analysis were used to study the relation between the inter-layer separation and the capacitance values. The exfoliated graphene oxide (GO)

films showed enhanced capacitances when d-spacing matches the desolvated ion sizes. This in situ study offered the first proof of concept for role of d-spacing in SCs. However, the insulating nature of GO and low capacitances values of ~ 1 F/g require significant improvements.
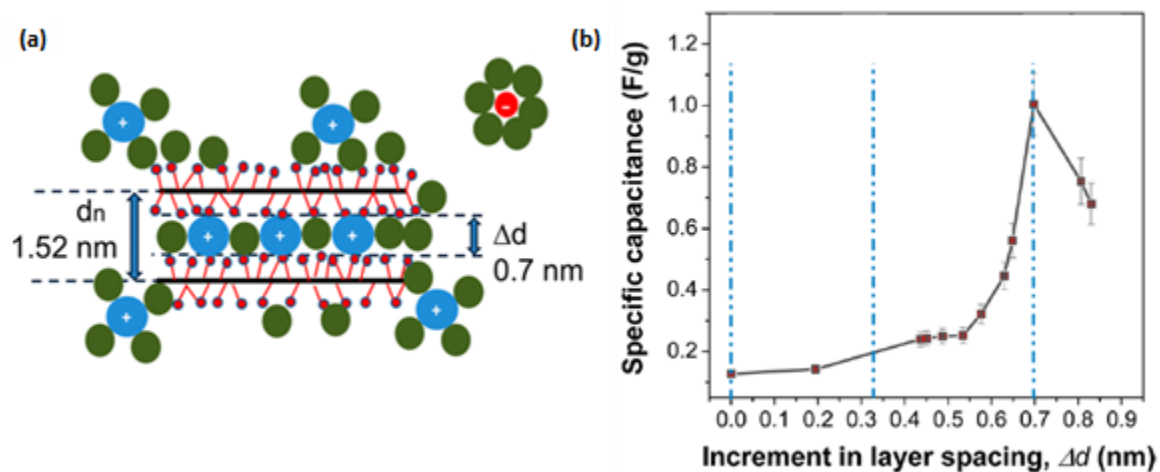
Figure I-22 (a) Expanded graphene oxide structure obtained through gradual exfoliation caused by insertion of propylene carbonate solvent molecules. (b) Highest capacitances were obtained when the d-spacing matched the electrolytic ion size (TEA+ - 0.68 nm).[154]

4.4 Synthesis of Ion Accessible Inter-Layer Graphene Galleries

The broad objective of this thesis is to develop graphene-based materials with high energy and power densities for SCs. The main challenge in using graphene for SCs applications has been the low electrochemical active surface areas due to restacking. The specific objective of this thesis is to synthesize and analyze 3D graphene materials that have 3D arrangement at the nanoscale and macroscale for SC applications. A continuous arrangement of the 2D graphene sheets with an intercalant leads to formation of a 3D arrangement at the nanoscale. Further incorporation of the individual intercalated stacks into an interconnected network leads to 3D structures at the macroscopic scale. A graphene-based material with such properties would enjoy the benefits of high surface areas from the expanded layered structures at the nanoscale and have favorable electrical and ion transport pathways from the interconnected macroporous networks. Ideally, such graphene materials would have the following characteristics:

➢ An intercalant should act as pillar and hold the sheets together at a specific distance

➢ The expanded layered structures should be stable and display a long charge-discharge cycle life in SCs

➢ A precise control over the d-spacing of the graphene materials is essential to optimize its application in SCs with suitable electrolyte ion sizes

➢ The synthesized inter-layer galleries should not be sterically blocked to ensure a facile ion transport

➢ The macroporous network should have high electrical and ionic conductivities in SCs

4.5 Proposed Methodology

4.5.1 Methods to Obtain Pillared Graphene Materials

As described above, we are interested in graphene-based materials that have expanded layered structures with a precise d-spacing and are durable during the long cycling life of SCs. An intercalant that can act as pillar and hold the sheets together at a specific distance could serve the purpose. Hence, a bi-functional intercalant that could covalently crosslink two sheets of GO together is essential. Continuous crosslinking of sheets turns the individual 2D sheets into a 3D pillared graphene structure at the nanoscale. Further incorporation of the

individual pillared stacks into an interconnected network could lead to 3D structures at the macroscopic scale.

In order to synthesize pillared graphene materials, we propose to use small organic molecules (with low molecular weight) that have reactive functional groups at both ends to covalently crosslink the GO sheets. Studies on pillared materials for H_2 storage have shown that bulky aromatic rings in the pillar could sterically render the galleries as closed.[155,156] Additionally, pillar molecules with aromatic rings have a greater tendency to stack on the graphene layers through π-π interactions. These are probably the reasons why earlier studies on aromatic pillars for SCs have not shown contributions from the inter-layer galleries. With this knowledge, instead, we propose to use alkyl diamines with varied alkyl chain lengths as pillars to synthesize a class of pillared graphene materials with varied inter-layer separation Scheme I-10). Alkyl diamines are partially reducing in nature and thus they cause simultaneous crosslinking and partial reduction of GO sheets. However, SC applications require high electrical conductivity from the electrode materials and thus the pillared materials are further reduced in a chemical reduction process.

Graphene oxide

Alkyl diamine

Pillared graphene material

Pillared graphene sheets
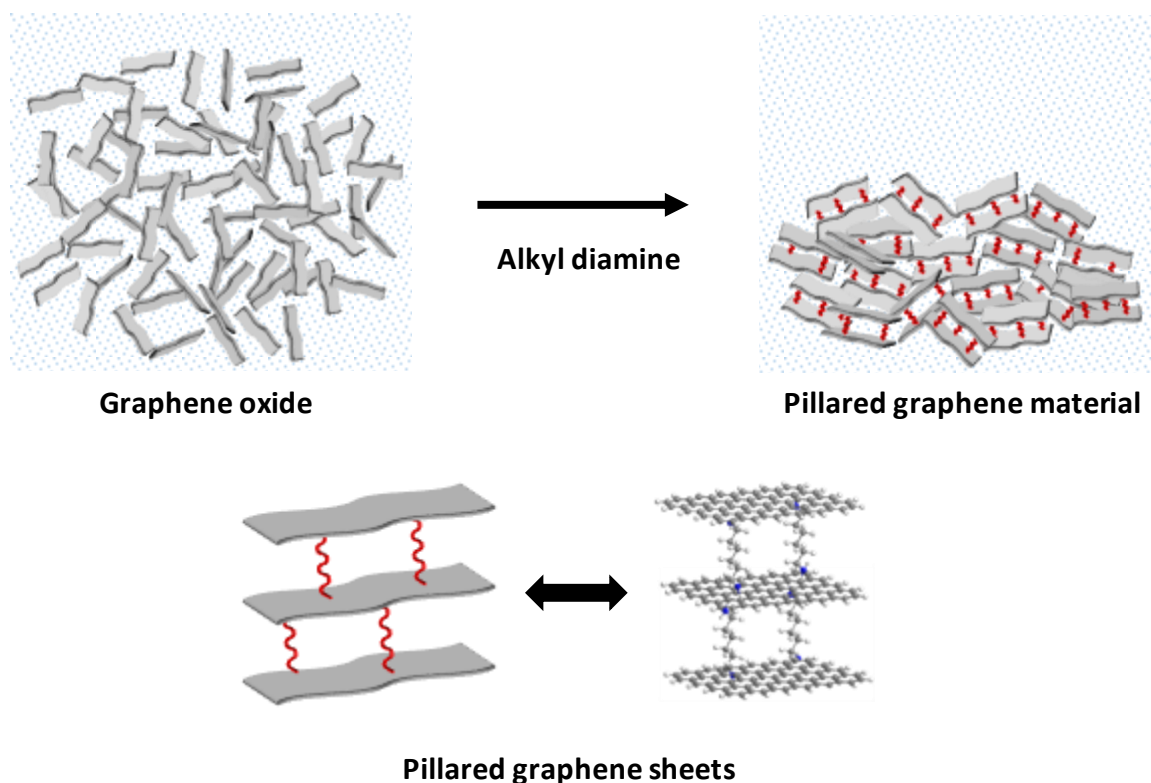
Scheme I-10 Schematic showing the formation if desired pillared graphene material from GO.

4.5.2 **Methods to Obtain Macroporous Networks**

As described earlier, alkyl diamines such as 1,2-diaminoethane or 1,4-diaminobutane are known to form monoliths from the GO solutions when appropriate synthesis conditions are used.[157] In parallel, treatment of GO under hydrothermal conditions is also known to form monoliths in a simple one-step process.[117] In this thesis, we analyze various synthesis conditions to prepare monoliths with simultaneous nanoscale pillaring of the graphene sheets (Scheme I-11).

At first, we try direct monolith formation with various diamines (as reported in the literature) and then we propose to use hydrothermal reaction conditions.

Graphene oxide   **Alkyl diamine**   **Pillared graphene hydrogel**
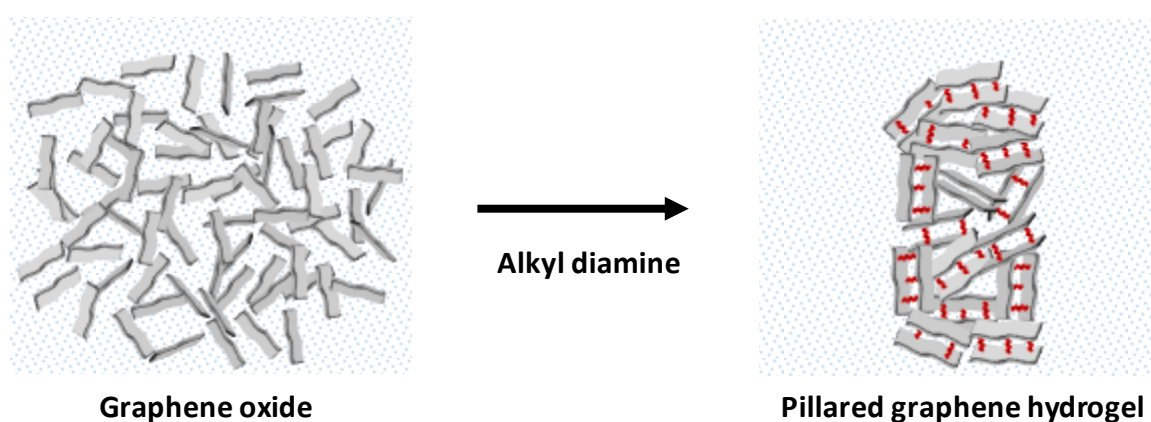
Scheme I-11 Schematic showing the formation if desired pillared graphene hydrogel from GO.

4.5.3 **Electrochemical Analysis Protocols in SCs**

Once a graphene-based material is synthesized with required attributes, its possible interest as an electrode material for SC applications is tested through a preliminary study of ion sieving (selection of ions based on sizes) to ensure that the electrolytic ions enter the inter-layer graphene galleries. Later, with the feedback from the ion sieving, graphene materials would be further optimized with the right choice of ion size and d-spacing for enhanced performances in SCs.

Additionally, the proposed pillared graphene materials could be of broader interest for fundamental understanding of ion sorption in SCs. The synthesized materials could be a model class of materials that could enable a study on ion desolvation and confinement effects seen in ACs and CDCs. Earlier studies on ACs and CDCs in the last decade have identified and gained rich understanding of the ion desolvation and sorption in the ultra-micro pores that are smaller than the fully solvated electrolyte ions. Nevertheless, the distribution of pores in such

materials and a reliable determination of the porosity characteristics using gas sorption analysis have been a considerable challenge. Graphene-based materials with expanded layered structures could alleviate this problem through precise tuning and facile determination of the d-spacing through XRD analyses. These inter-layer graphene galleries could be studied as analogous to an ultra-micro pore in CDCs, although with different shape, and enhance further understanding of ion sorption.

5. References

(1)   Rao, S.; Klimont, Z.; Smith, S. J.; Van Dingenen, R.; Dentener, F.; Bouwman, L.; Riahi, K.; Amann, M.; Bodirsky, B. L.; van Vuuren, D. P.; et al. Future Air Pollution in the Shared Socio-Economic Pathways. *Glob. Environ. Change* **2017**, *42*, 346–358.

(2)   Aricò, A. S.; Bruce, P.; Scrosati, B.; Tarascon, J.-M.; Schalkwijk, W. van. Nanostructured Materials for Advanced Energy Conversion and Storage Devices. *Nat. Mater.* **2005**, *4* (5), 366–377.

(3)   Simon, P.; Gogotsi, Y. Materials for Electrochemical Capacitors. *Nat Mater* **2008**, *7* (11), 845–854.

(4)   Armand, M.; Tarascon, J.-M. Building Better Batteries. *Nature* **2008**, *451*, 652.

(5)   Winter, M.; Brodd, R. J. What Are Batteries, Fuel Cells, and Supercapacitors? *Chem. Rev.* **2004**, *104* (10), 4245–4270.

(6)   Conway, B. E. *Electrochemical Supercapacitors - Scientific Fundamentals and Technological Applications*; Springer International Publishing: NewYork, 1999.

(7)   Miller, J. R.; Simon, P. Electrochemical Capacitors for Energy Management. *Science* **2008**, *321* (5889), 651.

(8)   Helmholtz, H. Ueber Einige Gesetze Der Vertheilung Elektrischer Ströme in Körperlichen Leitern Mit Anwendung Auf Die Thierisch-Elektrischen Versuche. *Ann. Phys.* **1853**, *165* (6), 211–233.

(9)   Becker, H. I. Low Voltage Electrolytic Capacitor. *US2800616 A* **1957**.

(10)   Rightmire, R. A. Electrical Energy Storage Apparatus. *US3288641 A* **1966**.

(11)   Boos, D. L. Electrolytic Capacitor Having Carbon Paste Electrodes. *US3536963 A* **1970**.

(12)   Schindall,J. The Charge of the Ultra-Capacitors The link for the article is given below https://spectrum.ieee.org/transportation/advanced-cars/the-charge-of-the-ultra-capacitors.

(13)   Electric Double Layer Capacitors (Gold Capacitor) Technical Guide | Industrial Devices & Solutions | Panasonic https://industrial.panasonic.com/ww/ds/library/EDLC_TechnicalGuide.

(14)   WaybackMachine- The link for the article is given below
         https://web.archive.org/web/20141222044332/http://services.eng.uts.edu.au.

(15)   Pandolfo, A. G.; Hollenkamp, A. F. Carbon Properties and Their Role in Supercapacitors. *J. Power Sources* **2006**, *157* (1), 11–27.

(16)   Frackowiak, E. Carbon Materials for Supercapacitor Application. *Phys. Chem. Chem. Phys.* **2007**, *9* (15), 1774–1785.

(17)   Béguin, F.; Presser, V.; Balducci, A.; Frackowiak, E. Carbons and Electrolytes for Advanced Supercapacitors. *Adv. Mater.* **2014**, *26* (14), 2219–2251.

(18)   Zheng, J. P.; Jow, T. R. A New Charge Storage Mechanism for Electrochemical Capacitors. *J. Electrochem. Soc.* **1995**, *142* (1), L6–L8.

(19)   Fan, Z.; Yan, J.; Wei, T.; Zhi, L.; Ning, G.; Li, T.; Wei, F. Asymmetric Supercapacitors Based on Graphene/MnO2 and Activated Carbon Nanofiber Electrodes with High Power and Energy Density. *Adv. Funct. Mater.* **2011**, *21* (12), 2366–2375.

(20)   Gouy, M. Sur la constitution de la charge électrique à la surface d'un électrolyte. *J. Phys. Théorique Appliquée* **1910**, *9* (1), 457–468.

(21)   ZUR THEORIE DER ELEKTROLYTISCHEN DOPPELSCHICHT - Stern - 1924 - Zeitschrift F&252;r Elektrochemie Und Angewandte Physikalische Chemie - Wiley Online Library.

(22)   Gu, W.; Yushin, G. Review of Nanostructured Carbon Materials for Electrochemical Capacitor Applications: Advantages and Limitations of Activated Carbon, Carbide-Derived Carbon, Zeolite-Templated Carbon, Carbon Aerogels, Carbon Nanotubes, Onion-like Carbon, and Graphene. *Wiley Interdiscip. Rev. Energy Environ.* **2014**, *3* (5), 424–473.

(23)   Zhang, L. L.; Zhao, X. S. Carbon-Based Materials as Supercapacitor Electrodes. *Chem. Soc. Rev.* **2009**, *38* (9), 2520–2531.

(24)   Wang, G.; Zhang, L.; Zhang, J. A Review of Electrode Materials for Electrochemical Supercapacitors. *Chem. Soc. Rev.* **2012**, *41* (2), 797–828.

(25)   Zhu, Y.; Murali, S.; Stoller, M. D.; Ganesh, K. J.; Cai, W.; Ferreira, P. J.; Pirkle, A.; Wallace, R. M.; Cychosz, K. A.; Thommes, M.; et al. Carbon-Based Supercapacitors Produced by Activation of Graphene. *Science* **2011**, *332* (6037), 1537–1541.

(26)   Barbieri, O.; Hahn, M.; Herzog, A.; Kötz, R. Capacitance Limits of High Surface Area Activated Carbons for Double Layer Capacitors. *Carbon* **2005**, *43* (6), 1303–1310.

(27)   Salanne, M.; Rotenberg, B.; Naoi, K.; Kaneko, K.; Taberna, P.-L.; Grey, C. P.; Dunn, B.; Simon, P. Efficient Storage Mechanisms for Building Better Supercapacitors. *Nat. Energy* **2016**, *1*, 16070.

(28)   Lozano-Castelló, D.; Cazorla-Amorós, D.; Linares-Solano, A.; Shiraishi, S.; Kurihara, H.; Oya, A. Influence of Pore Structure and Surface Chemistry on Electric Double Layer Capacitance in Non-Aqueous Electrolyte. *Carbon* **2003**, *41* (9), 1765–1775.

(29)   Raymundo-Piñero, E.; Kierzek, K.; Machnikowski, J.; Béguin, F. Relationship between the Nanoporous Texture of Activated Carbons and Their Capacitance Properties in Different Electrolytes. *Carbon* **2006**, *44* (12), 2498–2507.

(30)   Zhong, C.; Deng, Y.; Hu, W.; Qiao, J.; Zhang, L.; Zhang, J. A Review of Electrolyte Materials and Compositions for Electrochemical Supercapacitors. *Chem. Soc. Rev.* **2015**, *44* (21), 7484–7539.

(31)   Ue, M.; Ida, K.; Mori, S. Electrochemical Properties of Organic Liquid Electrolytes Based on Quaternary Onium Salts for Electrical Double-Layer Capacitors. *J. Electrochem. Soc.* **1994**, *141* (11), 2989–2996.

(32)   Jiménez-Cordero, D.; Heras, F.; Gilarranz, M. A.; Raymundo-Piñero, E. Grape Seed Carbons for Studying the Influence of Texture on Supercapacitor Behaviour in Aqueous Electrolytes. *Carbon* **2014**, *71*, 127–138.

(33)   Zhang, X.; Wang, X.; Jiang, L.; Wu, H.; Wu, C.; Su, J. Effect of Aqueous Electrolytes on the Electrochemical Behaviors of Supercapacitors Based on Hierarchically Porous Carbons. *J. Power Sources* **2012**, *216*, 290–296.

(34)   Fic, K.; Lota, G.; Meller, M.; Frackowiak, E. Novel Insight into Neutral Medium as Electrolyte for High-Voltage Supercapacitors. *Energy Environ. Sci.* **2012**, *5* (2), 5842–5850.

(35)   Arulepp, M.; Permann, L.; Leis, J.; Perkson, A.; Rumma, K.; Jänes, A.; Lust, E. Influence of the Solvent Properties on the Characteristics of a Double Layer Capacitor. *J. Power Sources* **2004**, *133* (2), 320–328.

(36)   Ue, M. Chemical Capacitors and Quaternary Ammonium Salts. *Electrochemistry* **2007**, *75* (8), 565–572.

(37)   Liu, P.; Verbrugge, M.; Soukiazian, S. Influence of Temperature and Electrolyte on the Performance of Activated-Carbon Supercapacitors. *J. Power Sources* **2006**, *156* (2), 712–718.

(38)   Francke, R.; Cericola, D.; Kötz, R.; Weingarth, D.; Waldvogel, S. R. Novel Electrolytes for Electrochemical Double Layer Capacitors Based on 1,1,1,3,3,3-Hexafluoropropan-2-Ol. *Electrochimica Acta* **2012**, *62*, 372–380.

(39)   Perricone, E.; Chamas, M.; Cointeaux, L.; Leprêtre, J.-C.; Judeinstein, P.; Azais, P.; Béguin, F.; Alloin, F. Investigation of Methoxypropionitrile as Co-Solvent for Ethylene Carbonate Based Electrolyte in Supercapacitors. A Safe and Wide Temperature Range Electrolyte. *Electrochimica Acta* **2013**, *93*, 1–7.

(40)   Ishimoto, S.; Asakawa, Y.; Shinya, M.; Naoi, K. Degradation Responses of Activated-Carbon-Based EDLCs for Higher Voltage Operation and Their Factors. *J. Electrochem. Soc.* **2009**, *156* (7), A563–A571.

(41)   Hardwick, L. J.; Hahn, M.; Ruch, P.; Holzapfel, M.; Scheifele, W.; Buqa, H.; Krumeich, F.; Novák, P.; Kötz, R. An in Situ Raman Study of the Intercalation of Supercapacitor-Type Electrolyte into Microcrystalline Graphite. *Electrochimica Acta* **2006**, *52* (2), 675–680.

(42)   Kötz, R.; Hahn, M.; Gallay, R. Temperature Behavior and Impedance Fundamentals of Supercapacitors. *J. Power Sources* **2006**, *154* (2), 550–555.

(43)   Brandon, E. J.; West, W. C.; Smart, M. C.; Whitcanack, L. D.; Plett, G. A. Extending the Low Temperature Operational Limit of Double-Layer Capacitors. *J. Power Sources* **2007**, *170* (1), 225–232.

(44)   Vaquero, S.; Díaz, R.; Anderson, M.; Palma, J.; Marcilla, R. Insights into the Influence of Pore Size Distribution and Surface Functionalities in the Behaviour of Carbon Supercapacitors. *Electrochimica Acta* **2012**, *86*, 241–247.

(45)   Galiński, M.; Lewandowski, A.; Stępniak, I. Ionic Liquids as Electrolytes. *Electrochimica Acta* **2006**, *51* (26), 5567–5580.

(46)   Armand, M.; Endres, F.; MacFarlane, D. R.; Ohno, H.; Scrosati, B. Ionic-Liquid Materials for the Electrochemical Challenges of the Future. *Nat. Mater.* **2009**, *8* (8), 621–629.

(47)   Zhou, Z.-B.; Matsumoto, H.; Tatsumi, K. Low-Melting, Low-Viscous, Hydrophobic Ionic Liquids: 1-Alkyl(Alkyl Ether)-3-Methylimidazolium Perfluoroalkyltrifluoroborate. *Chem. – Eur. J.* **2004**, *10* (24), 6581–6591.

(48)   Huddleston, J. G.; Visser, A. E.; Reichert, W. M.; Willauer, H. D.; Broker, G. A.; Rogers, R. D. Characterization and Comparison of Hydrophilic and Hydrophobic Room Temperature Ionic Liquids Incorporating the Imidazolium Cation. *Green Chem.* **2001**, *3* (4), 156–164.

(49)   Cui, W.; Du, F.; Zhao, J.; Zhang, W.; Yang, Y.; Xie, X.; Mai, Y.-W. Improving Thermal Conductivity While Retaining High Electrical Resistivity of Epoxy Composites by Incorporating Silica-Coated Multi-Walled Carbon Nanotubes. *Carbon* **2011**, *49* (2), 495–500.

(50)   Łatoszyńska, A. A.; Żukowska, G. Z.; Rutkowska, I. A.; Taberna, P.-L.; Simon, P.; Kulesza, P. J.; Wieczorek, W. Non-Aqueous Gel Polymer Electrolyte with Phosphoric Acid Ester and Its Application for Quasi Solid-State Supercapacitors. *J. Power Sources* **2015**, *274*, 1147–1154.

(51)   Fan, L.-Q.; Zhong, J.; Wu, J.-H.; Lin, J.-M.; Huang, Y.-F. Improving the Energy Density of Quasi-Solid-State Electric Double-Layer Capacitors by Introducing Redox Additives into Gel Polymer Electrolytes. *J. Mater. Chem. A* **2014**, *2* (24), 9011–9014.

(52)   Verma, M. L.; Minakshi, M.; Singh, N. K. Synthesis and Characterization of Solid Polymer Electrolyte Based on Activated Carbon for Solid State Capacitor. *Electrochimica Acta* **2014**, *137*, 497–503.

(53)   Zhai, Y.; Dou, Y.; Zhao, D.; Fulvio, P. F.; Mayes, R. T.; Dai, S. Carbon Materials for Chemical Capacitive Energy Storage. *Adv. Mater.* **2011**, *23* (42), 4828–4850.

(54)   Alonso, A.; Ruiz, V.; Blanco, C.; Santamaría, R.; Granda, M.; Menéndez, R.; de Jager, S. G. E. Activated Carbon Produced from Sasol-Lurgi Gasifier Pitch and Its Application as Electrodes in Supercapacitors. *Carbon* **2006**, *44* (3), 441–446.

(55)   Raymundo-Piñero, E.; Kierzek, K.; Machnikowski, J.; Béguin, F. Relationship between the Nanoporous Texture of Activated Carbons and Their Capacitance Properties in Different Electrolytes. *Carbon* **2006**, *44* (12), 2498–2507.

(56)   Simon, P.; Gogotsi, Y. Capacitive Energy Storage in Nanostructured Carbon–Electrolyte Systems. *Acc. Chem. Res.* **2013**, *46* (5), 1094–1103.

(57)   Sing, K. S. W. Reporting Physisorption Data for Gas/Solid Systems with Special Reference to the Determination of Surface Area and Porosity (Recommendations 1984). *Pure Appl. Chem.* **1985**, *57* (4), 603–619.

(58)   Wang, D.-W.; Li, F.; Liu, M.; Lu, G. Q.; Cheng, H.-M. 3D Aperiodic Hierarchical Porous Graphitic Carbon Material for High-Rate Electrochemical Capacitive Energy Storage. *Angew. Chem. Int. Ed.* **2008**, *47* (2), 373–376.

(59)   McDonough, J. K.; Gogotsi, Y. Carbon Onions: Synthesis and Electrochemical Applications. *Electrochem. Soc. Interface* **2013**, *22* (3), 61–66.

(60)   Alexandrou, I.; Wang, H.; Sano, N.; Amaratunga, G. a. J. Structure of Carbon Onions and Nanotubes Formed by Arc in Liquids. *J. Chem. Phys.* **2003**, *120* (2), 1055–1058.

(61)   Portet, C.; Yushin, G.; Gogotsi, Y. Electrochemical Performance of Carbon Onions, Nanodiamonds, Carbon Black and Multiwalled Nanotubes in Electrical Double Layer Capacitors. *Carbon* **2007**, *45* (13), 2511–2518.

(62)   Gao, Y.; Zhou, Y. S.; Qian, M.; He, X. N.; Redepenning, J.; Goodman, P.; Li, H. M.; Jiang, L.; Lu, Y. F. Chemical Activation of Carbon Nano-Onions for High-Rate Supercapacitor Electrodes. *Carbon* **2013**, *51* (1), 52–58.

(63)   Pech, D.; Brunet, M.; Durou, H.; Huang, P.; Mochalin, V.; Gogotsi, Y.; Taberna, P.-L.; Simon, P. Ultrahigh-Power Micrometre-Sized Supercapacitors Based on Onion-like Carbon. *Nat. Nanotechnol.* **2010**, *5* (9), 651–654.

(64)   Evanoff, K.; Khan, J.; Balandin, A. A.; Magasinski, A.; Ready, W. J.; Fuller, T. F.; Yushin, G. Towards Ultrathick Battery Electrodes: Aligned Carbon Nanotube – Enabled Architecture. *Adv. Mater.* **2012**, *24* (4), 533–537.

(65)   Zhang, H.; Cao, G.; Yang, Y.; Gu, Z. Comparison Between Electrochemical Properties of Aligned Carbon Nanotube Array and Entangled Carbon Nanotube Electrodes. *J. Electrochem. Soc.* **2008**, *155* (2), K19–K22.

(66)   Boukhalfa, S.; Evanoff, K.; Yushin, G. Atomic Layer Deposition of Vanadium Oxide on Carbon Nanotubes for High-Power Supercapacitor Electrodes. *Energy Environ. Sci.* **2012**, *5* (5), 6872–6879.

(67)   Sevilla, M.; Mokaya, R. Energy Storage Applications of Activated Carbons: Supercapacitors and Hydrogen Storage. *Energy Environ. Sci.* **2014**, *7* (4), 1250–1280.

(68)   Wu, F.-C.; Tseng, R.-L.; Hu, C.-C.; Wang, C.-C. Effects of Pore Structure and Electrolyte on the Capacitive Characteristics of Steam- and KOH-Activated Carbons for Supercapacitors. *J. Power Sources* **2005**, *144* (1), 302–309.

(69)   San Miguel, Guillermo; Fowler, G. D.; Sollars, C. J. A Study of the Characteristics of Activated Carbons Produced by Steam and Carbon Dioxide Activation of Waste Tyre Rubber. *Carbon* **2003**, *41* (5), 1009–1016.

(70)   Stoller, M. D.; Magnuson, C. W.; Zhu, Y.; Murali, S.; Suk, J. W.; Piner, R.; Ruoff, R. S. Interfacial Capacitance of Single Layer Graphene. *Energy Environ. Sci.* **2011**, *4* (11), 4685–4689.

(71)   Raccichini, R.; Varzi, A.; Passerini, S.; Scrosati, B. The Role of Graphene for Electrochemical Energy Storage. *Nat. Mater.* **2015**, *14* (3), 271–279.

(72)   Salanne, M.; Rotenberg, B.; Naoi, K.; Kaneko, K.; Taberna, P.-L.; Grey, C. P.; Dunn, B.; Simon, P. Efficient Storage Mechanisms for Building Better Supercapacitors. *Nat. Energy* **2016**, *1*, 16070.

(73)   Presser, V.; Zhang, L.; Niu, J. J.; McDonough, J.; Perez, C.; Fong, H.; Gogotsi, Y. Flexible Nano-Felts of Carbide-Derived Carbon with Ultra-High Power Handling Capability. *Adv. Energy Mater.* **2011**, *1* (3), 423–430.

(74)   Li, C.; Shi, G. Functional Gels Based on Chemically Modified Graphenes. *Adv. Mater.* **2014**, *26* (24), 3992–4012.

(75)   Zhao, X. S.; Su, F.; Yan, Q.; Guo, W.; Bao, X. Y.; Lv, L.; Zhou, Z. Templating Methods for Preparation of Porous Structures. *J. Mater. Chem.* **2006**, *16* (7), 637–648.

(76)   Vu, A.; Li, X.; Phillips, J.; Han, A.; Smyrl, W. H.; Bühlmann, P.; Stein, A. Three-Dimensionally Ordered Mesoporous (3DOm) Carbon Materials as Electrodes for Electrochemical Double-Layer Capacitors with Ionic Liquid Electrolytes. *Chem. Mater.* **2013**, *25* (21), 4137–4148.

(77)   Karthik, M.; Redondo, E.; Goikolea, E.; Roddatis, V.; Doppiu, S.; Mysyk, R. Effect of Mesopore Ordering in Otherwise Similar Micro/Mesoporous Carbons on the High-Rate Performance of Electric Double-Layer Capacitors. *J. Phys. Chem. C* **2014**, *118* (48), 27715–27720.

(78)   Nishihara, H.; Itoi, H.; Kogure, T.; Hou, P.-X.; Touhara, H.; Okino, F.; Kyotani, T. Investigation of the Ion Storage/Transfer Behavior in an Electrical Double-Layer Capacitor by Using Ordered Microporous Carbons as Model Materials. *Chem. – Eur. J.* **2009**, *15* (21), 5355–5363.

(79)   Dash, R.; Chmiola, J.; Yushin, G.; Gogotsi, Y.; Laudisio, G.; Singer, J.; Fischer, J.; Kucheyev, S. Titanium Carbide Derived Nanoporous Carbon for Energy-Related Applications. *Carbon* **2006**, *44* (12), 2489–2497.

(80)   Korenblit, Y.; Rose, M.; Kockrick, E.; Borchardt, L.; Kvit, A.; Kaskel, S.; Yushin, G. High-Rate Electrochemical Capacitors Based on Ordered Mesoporous Silicon Carbide-Derived Carbon. *ACS Nano* **2010**, *4* (3), 1337–1344.

(81)   Rose, M.; Korenblit, Y.; Kockrick, E.; Borchardt, L.; Oschatz, M.; Kaskel, S.; Yushin, G. Hierarchical Micro- and Mesoporous Carbide-Derived Carbon as a High-Performance Electrode Material in Supercapacitors. *Small* **2011**, *7* (8), 1108–1117.

(82)   Novoselov, K. S.; Geim, A. K.; Morozov, S. V.; Jiang, D.; Zhang, Y.; Dubonos, S. V.; Grigorieva, I. V.; Firsov, A. A. Electric Field Effect in Atomically Thin Carbon Films. *Science* **2004**, *306* (5696), 666–669.

(83)   Bonaccorso, F.; Colombo, L.; Yu, G.; Stoller, M.; Tozzini, V.; Ferrari, A. C.; Ruoff, R. S.; Pellegrini, V. Graphene, Related Two-Dimensional Crystals, and Hybrid Systems for Energy Conversion and Storage. *Science* **2015**, *347* (6217), 1246501.

(84)   Zhu, Y.; Murali, S.; Cai, W.; Li, X.; Suk, J. W.; Potts, J. R.; Ruoff, R. S. Graphene and Graphene Oxide: Synthesis, Properties, and Applications. *Adv. Mater.* **2010**, *22* (35), 3906–3924.

(85)   Liu, C.; Yu, Z.; Neff, D.; Zhamu, A.; Jang, B. Z. Graphene-Based Supercapacitor with an Ultrahigh Energy Density. *Nano Lett.* **2010**, *10* (12), 4863–4868.

(86)   Xia, J.; Chen, F.; Li, J.; Tao, N. Measurement of the Quantum Capacitance of Graphene. *Nat Nano* **2009**, *4* (8), 505–509.

(87)   Novoselov, K. S.; Fal'ko, V. I.; Colombo, L.; Gellert, P. R.; Schwab, M. G.; Kim, K. A Roadmap for Graphene. *Nature* **2012**, *490* (7419), 192–200.

(88)   Cai, J.; Ruffieux, P.; Jaafar, R.; Bieri, M.; Braun, T.; Blankenburg, S.; Muoth, M.; Seitsonen, A. P.; Saleh, M.; Feng, X.; et al. Atomically Precise Bottom-up Fabrication of Graphene Nanoribbons. *Nature* **2010**, *466* (7305), 470–473.

(89)   Cai, M.; Thorpe, D.; Adamson, D. H.; Schniepp, H. C. Methods of Graphite Exfoliation. *J. Mater. Chem.* **2012**, *22* (48), 24992–25002.

(90)   Wei, D.; Grande, L.; Chundi, V.; White, R.; Bower, C.; Andrew, P.; Ryhänen, T. Graphene from Electrochemical Exfoliation and Its Direct Applications in Enhanced Energy Storage Devices. *Chem. Commun.* **2012**, *48* (9), 1239–1241.

(91)   Paton, K. R.; Varrla, E.; Backes, C.; Smith, R. J.; Khan, U.; O'Neill, A.; Boland, C.; Lotya, M.; Istrate, O. M.; King, P.; et al. Scalable Production of Large Quantities of Defect-Free Few-Layer Graphene by Shear Exfoliation in Liquids. *Nat. Mater.* **2014**, *13* (6), 624–630.

(92)   Hummers, W. S.; Offeman, R. E. Preparation of Graphitic Oxide. *J. Am. Chem. Soc.* **1958**, *80* (6), 1339–1339.

(93)   Marcano, D. C.; Kosynkin, D. V.; Berlin, J. M.; Sinitskii, A.; Sun, Z.; Slesarev, A.; Alemany, L. B.; Lu, W.; Tour, J. M. Improved Synthesis of Graphene Oxide. *ACS Nano* **2010**, *4* (8), 4806–4814.

(94)   Botas, C.; Álvarez, P.; Blanco, P.; Granda, M.; Blanco, C.; Santamaría, R.; Romasanta, L. J.; Verdejo, R.; López-Manchado, M. A.; Menéndez, R. Graphene Materials with Different Structures Prepared from the Same Graphite by the Hummers and Brodie Methods. *Carbon* **2013**, *65*, 156–164.

(95)   Zhu, Y.; Stoller, M. D.; Cai, W.; Velamakanni, A.; Piner, R. D.; Chen, D.; Ruoff, R. S. Exfoliation of Graphite Oxide in Propylene Carbonate and Thermal Reduction of the Resulting Graphene Oxide Platelets. *ACS Nano* **2010**, *4* (2), 1227–1233.

(96)   Stankovich, S.; Dikin, D. A.; Piner, R. D.; Kohlhaas, K. A.; Kleinhammes, A.; Jia, Y.; Wu, Y.; Nguyen, S. T.; Ruoff, R. S. Synthesis of Graphene-Based Nanosheets via Chemical Reduction of Exfoliated Graphite Oxide. *Carbon* **2007**, *45* (7), 1558–1565.

(97)   Toh, S. Y.; Loh, K. S.; Kamarudin, S. K.; Daud, W. R. W. Graphene Production via Electrochemical Reduction of Graphene Oxide: Synthesis and Characterisation. *Chem. Eng. J.* **2014**, *251*, 422–434.

(98)   Hantel, M. M.; Kaspar, T.; Nesper, R.; Wokaun, A.; Kötz, R. Partially Reduced Graphite Oxide for Supercapacitor Electrodes: Effect of Graphene Layer Spacing and Huge Specific Capacitance. *Electrochem. Commun.* **2011**, *13* (1), 90–92.

(99)   Chua, C. K.; Pumera, M. Chemical Reduction of Graphene Oxide: A Synthetic Chemistry Viewpoint. *Chem. Soc. Rev.* **2013**, *43* (1), 291–312.

(100) Ashok Kumar, N.; Gambarelli, S.; Duclairoir, F.; Bidan, G.; Dubois, L. Synthesis of High Quality Reduced Graphene Oxide Nanosheets Free of Paramagnetic Metallic Impurities. *J. Mater. Chem. A* **2013**, *1* (8), 2789–2794.

(101) Cai, W.; Piner, R. D.; Stadermann, F. J.; Park, S.; Shaibat, M. A.; Ishii, Y.; Yang, D.; Velamakanni, A.; An, S. J.; Stoller, M.; et al. Synthesis and Solid-State NMR Structural Characterization of 13C-Labeled Graphite Oxide. *Science* **2008**, *321* (5897), 1815–1817.

(102) Lerf, A.; He, H.; Forster, M.; Klinowski, J. Structure of Graphite Oxide Revisited. *J. Phys. Chem. B* **1998**, *102* (23), 4477–4482.

(103) Stoller, M. D.; Park, S.; Zhu, Y.; An, J.; Ruoff, R. S. Graphene-Based Ultracapacitors. *Nano Lett.* **2008**, *8* (10), 3498–3502.

(104) Vivekchand, S. R. C.; Rout, C. S.; Subrahmanyam, K. S.; Govindaraj, A.; Rao, C. N. R. Graphene-Based Electrochemical Supercapacitors. *J. Chem. Sci.* **2008**, *120* (1), 9–13.

(105) Wang, H.; Wang, Y.; Hu, Z.; Wang, X. Cutting and Unzipping Multiwalled Carbon Nanotubes into Curved Graphene Nanosheets and Their Enhanced Supercapacitor Performance. *ACS Appl. Mater. Interfaces* **2012**, *4* (12), 6827–6834.

(106) Zhang, Z.; Lee, C.-S.; Zhang, W. Vertically Aligned Graphene Nanosheet Arrays: Synthesis, Properties and Applications in Electrochemical Energy Conversion and Storage. *Adv. Energy Mater.* **2017**, *7* (23), 1700678.

(107) Bai, H.; Li, C.; Wang, X.; Shi, G. On the Gelation of Graphene Oxide. *J. Phys. Chem. C* **2011**, *115* (13), 5545–5551.

(108) Lei, Z.; Zhang, J.; Zhang, L. L.; Kumar, N. A.; Zhao, X. S. Functionalization of Chemically Derived Graphene for Improving Its Electrocapacitive Energy Storage Properties. *Energy Environ. Sci.* **2016**, *9* (6), 1891–1930.

(109) Chen, Y.; Chen, L.; Bai, H.; Li, L. Graphene Oxide-Chitosan Composite Hydrogels as Broad-Spectrum Adsorbents for Water Purification. *J. Mater. Chem. A* **2013**, *1* (6), 1992–2001.

(110) Park, S.; Lee, K.-S.; Bozoklu, G.; Cai, W.; Nguyen, S. T.; Ruoff, R. S. Graphene Oxide Papers Modified by Divalent Ions—Enhancing Mechanical Properties via Chemical Cross-Linking. *ACS Nano* **2008**, *2* (3), 572–578.

(111) Adhikari, B.; Biswas, A.; Banerjee, A. Graphene Oxide-Based Hydrogels to Make Metal Nanoparticle-Containing Reduced Graphene Oxide-Based Functional Hybrid Hydrogels. *ACS Appl. Mater. Interfaces* **2012**, *4* (10), 5472–5482.

(112) Xu, Y.; Shi, G.; Duan, X. Self-Assembled Three-Dimensional Graphene Macrostructures: Synthesis and Applications in Supercapacitors. *Acc. Chem. Res.* **2015**, *48* (6), 1666–1675.

(113) Hu, H.; Zhao, Z.; Wan, W.; Gogotsi, Y.; Qiu, J. Ultralight and Highly Compressible Graphene Aerogels. *Adv. Mater.* **2013**, *25* (15), 2219–2223.

(114) Che, J.; Shen, L.; Xiao, Y. A New Approach to Fabricate Graphene Nanosheets in Organic Medium: Combination of Reduction and Dispersion. *J. Mater. Chem.* **2010**, *20* (9), 1722–1727.

(115) Zhang, X.; Sui, Z.; Xu, B.; Yue, S.; Luo, Y.; Zhan, W.; Liu, B. Mechanically Strong and Highly Conductive Graphene Aerogel and Its Use as Electrodes for Electrochemical Power Sources. *J. Mater. Chem.* **2011**, *21* (18), 6494–6497.

(116) Zhang, L.; Shi, G. Preparation of Highly Conductive Graphene Hydrogels for Fabricating Supercapacitors with High Rate Capability. *J. Phys. Chem. C* **2011**, *115* (34), 17206–17212.

(117) Xu, Y.; Sheng, K.; Li, C.; Shi, G. Self-Assembled Graphene Hydrogel via a One-Step Hydrothermal Process. *ACS Nano* **2010**, *4* (7), 4324–4330.

(118) Tao, Y.; Xie, X.; Lv, W.; Tang, D.-M.; Kong, D.; Huang, Z.; Nishihara, H.; Ishii, T.; Li, B.; Golberg, D.; et al. Towards Ultrahigh Volumetric Capacitance: Graphene Derived Highly Dense but Porous Carbons for Supercapacitors. *Sci. Rep.* **2013**, *3*.

(119) Zhang, C.; Lv, W.; Tao, Y.; Yang, Q.-H. Towards Superior Volumetric Performance: Design and Preparation of Novel Carbon Materials for Energy Storage. *Energy Environ. Sci.* **2015**, *8* (5), 1390–1403.

(120) Wang, Q.; Yan, J.; Fan, Z. Carbon Materials for High Volumetric Performance Supercapacitors: Design, Progress, Challenges and Opportunities. *Energy Environ. Sci.* **2016**, *9* (3), 729–762.

(121) Xu, Y.; Lin, Z.; Zhong, X.; Huang, X.; Weiss, N. O.; Huang, Y.; Duan, X. Holey Graphene Frameworks for Highly Efficient Capacitive Energy Storage. *Nat. Commun.* **2014**, *5*, 4554.

(122) Yang, X.; Cheng, C.; Wang, Y.; Qiu, L.; Li, D. Liquid-Mediated Dense Integration of Graphene Materials for Compact Capacitive Energy Storage. *Science* **2013**, *341* (6145), 534–537.

(123) Kim, T.; Jung, G.; Yoo, S.; Suh, K. S.; Ruoff, R. S. Activated Graphene-Based Carbons as Supercapacitor Electrodes with Macro- and Mesopores. *ACS Nano* **2013**, *7* (8), 6899–6905.

(124) Brunauer, S.; Emmett, P. H.; Teller, E. Adsorption of Gases in Multimolecular Layers. *J. Am. Chem. Soc.* **1938**, *60* (2), 309–319.

(125) Chmiola, J.; Yushin, G.; Gogotsi, Y.; Portet, C.; Simon, P.; Taberna, P. L. Anomalous Increase in Carbon Capacitance at Pore Sizes Less Than 1 Nanometer. *Science* **2006**, *313* (5794), 1760–1763.

(126) Largeot, C.; Portet, C.; Chmiola, J.; Taberna, P.-L.; Gogotsi, Y.; Simon, P. Relation between the Ion Size and Pore Size for an Electric Double-Layer Capacitor. *J. Am. Chem. Soc.* **2008**, *130* (9), 2730–2731.

(127) Salitra, G.; Soffer, A.; Eliad, L.; Cohen, Y.; Aurbach, D. Carbon Electrodes for Double-Layer Capacitors I. Relations Between Ion and Pore Dimensions. *J. Electrochem. Soc.* **2000**, *147* (7), 2486–2493.

(128) Kota, M.; Yu, X.; Yeon, S.-H.; Cheong, H.-W.; Park, H. S. Ice-Templated Three Dimensional Nitrogen Doped Graphene for Enhanced Supercapacitor Performance. *J. Power Sources* **2016**, *303*, 372–378.

(129) Fernández, J. A.; Morishita, T.; Toyoda, M.; Inagaki, M.; Stoeckli, F.; Centeno, T. A. Performance of Mesoporous Carbons Derived from Poly(Vinyl Alcohol) in Electrochemical Capacitors. *J. Power Sources* **2008**, *175* (1), 675–679.

(130) Álvarez, S.; Blanco-López, M. C.; Miranda-Ordieres, A. J.; Fuertes, A. B.; Centeno, T. A. Electrochemical Capacitor Performance of Mesoporous Carbons Obtained by Templating Technique. *Carbon* **2005**, *43* (4), 866–870.

(131) Sevilla, M.; Álvarez, S.; Centeno, T. A.; Fuertes, A. B.; Stoeckli, F. Performance of Templated Mesoporous Carbons in Supercapacitors. *Electrochimica Acta* **2007**, *52* (9), 3207–3215.

(132) Gogotsi, Y.; Dash, R. K.; Yushin, G.; Yildirim, T.; Laudisio, G.; Fischer, J. E. Tailoring of Nanoscale Porosity in Carbide-Derived Carbons for Hydrogen Storage. *J. Am. Chem. Soc.* **2005**, *127* (46), 16006–16007.

(133) Vix-Guterl, C.; Frackowiak, E.; Jurewicz, K.; Friebe, M.; Parmentier, J.; Béguin, F. Electrochemical Energy Storage in Ordered Porous Carbon Materials. *Carbon* **2005**, *43* (6), 1293–1302.

(134) Leis, J.; Arulepp, M.; Kuura, A.; Lätt, M.; Lust, E. Electrical Double-Layer Characteristics of Novel Carbide-Derived Carbon Materials. *Carbon* **2006**, *44* (11), 2122–2129.

(135) Lin, R.; Huang, P.; Ségalini, J.; Largeot, C.; Taberna, P. L.; Chmiola, J.; Gogotsi, Y.; Simon, P. Solvent Effect on the Ion Adsorption from Ionic Liquid Electrolyte into Sub-Nanometer Carbon Pores. *Electrochimica Acta* **2009**, *54* (27), 7025–7032.

(136) Kim, Y.-J.; Masutzawa, Y.; Ozaki, S.; Endo, M.; Dresselhaus, M. S. PVDC-Based Carbon Material by Chemical Activation and Its Application to Nonaqueous EDLC. *J. Electrochem. Soc.* **2004**, *151* (6), E199–E205.

(137) Segalini, J.; Daffos, B.; Taberna, P. L.; Gogotsi, Y.; Simon, P. Qualitative Electrochemical Impedance Spectroscopy Study of Ion Transport into Sub-Nanometer Carbon Pores in Electrochemical Double Layer Capacitor Electrodes. *Electrochimica Acta* **2010**, *55* (25), 7489–7494.

(138) Pean, C.; Daffos, B.; Rotenberg, B.; Levitz, P.; Haefele, M.; Taberna, P.-L.; Simon, P.; Salanne, M. Confinement, Desolvation, And Electrosorption Effects on the Diffusion of Ions in Nanoporous Carbon Electrodes. *J. Am. Chem. Soc.* **2015**, *137* (39), 12627–12632.

(139) Levi, M. D.; Salitra, G.; Levy, N.; Aurbach, D.; Maier, J. Application of a Quartz-Crystal Microbalance to Measure Ionic Fluxes in Microporous Carbons for Energy Storage. *Nat. Mater.* **2009**, *8* (11), 872–875.

(140) Levi, M. D.; Levy, N.; Sigalov, S.; Salitra, G.; Aurbach, D.; Maier, J. Electrochemical Quartz Crystal Microbalance (EQCM) Studies of Ions and Solvents Insertion into Highly Porous Activated Carbons. *J. Am. Chem. Soc.* **2010**, *132* (38), 13220–13222.

(141) Levi, M. D.; Sigalov, S.; Aurbach, D.; Daikhin, L. In Situ Electrochemical Quartz Crystal Admittance Methodology for Tracking Compositional and Mechanical Changes in Porous Carbon Electrodes. *J. Phys. Chem. C* **2013**, *117* (29), 14876–14889.

(142) Tsai, W.-Y.; Taberna, P.-L.; Simon, P. Electrochemical Quartz Crystal Microbalance (EQCM) Study of Ion Dynamics in Nanoporous Carbons. *J. Am. Chem. Soc.* **2014**, *136* (24), 8722–8728.

(143) Chmiola, J.; Largeot, C.; Taberna, P.-L.; Simon, P.; Gogotsi, Y. Desolvation of Ions in Subnanometer Pores and Its Effect on Capacitance and Double-Layer Theory. *Angew. Chem. Int. Ed.* **2008**, *47* (18), 3392–3395.

(144) Huang, J.; Sumpter, B. G.; Meunier, V. A Universal Model for Nanoporous Carbon Supercapacitors Applicable to Diverse Pore Regimes, Carbon Materials, and Electrolytes. *Chem. – Eur. J.* **2008**, *14* (22), 6614–6626.

(145) Stein, A.; Rudisill, S. G.; Petkovich, N. D. Perspective on the Influence of Interactions Between Hard and Soft Templates and Precursors on Morphology of Hierarchically Structured Porous Materials. *Chem. Mater.* **2014**, *26* (1), 259–276.

(146) Wang, Q.; Yan, J.; Wang, Y.; Wei, T.; Zhang, M.; Jing, X.; Fan, Z. Three-Dimensional Flower-like and Hierarchical Porous Carbon Materials as High-Rate Performance Electrodes for Supercapacitors. *Carbon* **2014**, *67*, 119–127.

(147) Kondrat, S.; Pérez, C. R.; Presser, V.; Gogotsi, Y.; Kornyshev, A. A. Effect of Pore Size and Its Dispersity on the Energy Storage in Nanoporous Supercapacitors. *Energy Environ. Sci.* **2012**, *5* (4), 6474–6479.

(148) Palmer, J. C.; Llobet, A.; Yeon, S.-H.; Fischer, J. E.; Shi, Y.; Gogotsi, Y.; Gubbins, K. E. Modeling the Structural Evolution of Carbide-Derived Carbons Using Quenched Molecular Dynamics. *Carbon* **2010**, *48* (4), 1116–1123.

(149) Boukhalfa, S.; Gordon, D.; He, L.; Melnichenko, Y. B.; Nitta, N.; Magasinski, A.; Yushin, G. In Situ Small Angle Neutron Scattering Revealing Ion Sorption in Microporous Carbon Electrical Double Layer Capacitors. *ACS Nano* **2014**, *8* (3), 2495–2503.

(150) Griffin, J. M.; Forse, A. C.; Tsai, W.-Y.; Taberna, P.-L.; Simon, P.; Grey, C. P. *In Situ* NMR and Electrochemical Quartz Crystal Microbalance Techniques Reveal the Structure of the Electrical Double Layer in Supercapacitors. *Nat. Mater.* **2015**, *14* (8), 812.

(151) Herrera-Alonso, M.; Abdala, A. A.; McAllister, M. J.; Aksay, I. A.; Prud'homme, R. K. Intercalation and Stitching of Graphite Oxide with Diaminoalkanes. *Langmuir* **2007**, *23* (21), 10644–10649.

(152) Yuan, K.; Xu, Y.; Uihlein, J.; Brunklaus, G.; Shi, L.; Heiderhoff, R.; Que, M.; Forster, M.; Chassé, T.; Pichler, T.; et al. Straightforward Generation of Pillared, Microporous Graphene Frameworks for Use in Supercapacitors. *Adv. Mater.* **2015**, *27* (42), 6714–6721.

(153) Lee, K.; Yoon, Y.; Cho, Y.; Lee, S. M.; Shin, Y.; Lee, H.; Lee, H. Tunable Sub-Nanopores of Graphene Flake Interlayers with Conductive Molecular Linkers for Supercapacitors. *ACS Nano* **2016**, *10* (7), 6799–6807.

(154) Galhena, D. T. L.; Bayer, B. C.; Hofmann, S.; Amaratunga, G. A. J. Understanding Capacitance Variation in Sub-Nanometer Pores by in Situ Tuning of Interlayer Constrictions. *ACS Nano* **2016**, *10* (1), 747–754.

(155) Burress, J. W.; Gadipelli, S.; Ford, J.; Simmons, J. M.; Zhou, W.; Yildirim, T. Graphene Oxide Framework Materials: Theoretical Predictions and Experimental Results. *Angew. Chem. Int. Ed.* **2010**, *49* (47), 8902–8904.

(156) Srinivas, G.; Burress, J. W.; Ford, J.; Yildirim, T. Porous Graphene Oxide Frameworks: Synthesis and Gas Sorption Properties. *J. Mater. Chem.* **2011**, *21* (30), 11323–11329.

(157) Luan, V. H.; Tien, H. N.; Hoa, L. T.; Hien, N. T. M.; Oh, E.-S.; Chung, J.; Kim, E. J.; Choi, W. M.; Kong, B.-S.; Hur, S. H. Synthesis of a Highly Conductive and Large Surface Area Graphene Oxide Hydrogel and Its Use in a Supercapacitor. *J. Mater. Chem. A* **2013**, *1* (2), 208–211.

CHAPTER II:
Study of Graphene Hydrogels Self-Assembled with Short Alkyl Diamines

Chapter II. Study of Graphene Hydrogels Self-Assembled with Short Alkyl Diamines

1. Objectives & Approach

As discussed in chapter I, we started out to synthesize graphene monoliths using alkyl diamines as gel formation agents. In this way, we expected to achieve materials that have both the nanoscale pillaring of the graphene sheets and the interconnected macroporous network of a hydrogel. Reports in the literature have described monolith formation from GO solution using short alkyl diamines such as 1,2-diaminoethane or 1,4-diaminobutane as excellent gel formation agents through covalent linkages.[23,24] However, the obtained monoliths still had several oxygen functional groups on the GO sheets and thus, had poor electrical conductivities. Alkyl diamines are partially reducing in nature but the reaction with GO does not ensure high electrical conductivities required for SC applications. Hence, another reaction step of chemical reduction of the monoliths is generally performed using a strong reducing agent, such as hydrazine hydrate.

We wondered if hydrazine, being the smallest possible diamine and strong reducing agent, could form a monolith with very high conductivity in a direct process. An earlier report attempted to prepare monoliths of reduced GO by using various reducing agents such as $NaHSO_3$, Na_2S, HI and hydrazine hydrate as gel formation agents. Except hydrazine hydrate, all the three reducing agents formed monoliths and led the authors to conclude that the residual nitrogen in hydrazine hydrate may prevent monolith formation. Eventually, later reports with 1,2-diaminoethane and 1,4-diaminobutane proved otherwise with monoliths containing 4-5 % atomic concentration of nitrogen. Hence, we attempted to try and optimize the reaction conditions of GO and hydrazine hydrate for a successful monolith formation.

Overall, we performed a preliminary focused study using three different diamines i.e. hydrazine hydrate (the smallest diamine), 1,2-diaminoethane and 1,4-diaminobutane (the first two smallest alkyl diamines) (Scheme II-1). We expected to understand their gel formation capacity, pillaring ability, electrical conductivities and the virtues of their macroporous network for SCs. Reduced graphene oxide with a 2D arrangement, was also synthesized, as a control material to the synthesized monoliths. Electrochemical measurements were performed using an aqueous electrolyte (6 M KOH). Since the gels were

prepared in aqueous media, they enabled a facile assembly into aqueous electrolytes without much processing during the electrode fabrication.

Short Alkyl diamines
n = 0, 2 and 4

No Stirring

Graphene oxide

Pillared graphene hydrogel

$H_2N—NH_2$

$H_2N\diagup\diagdown NH_2$

$H_2N\diagup\diagdown\diagup NH_2$

Hydrazine hydrate (GH-HD)

1,2-diaminoethane (GH-ED)

1,4-diaminobutane (GH-DB)
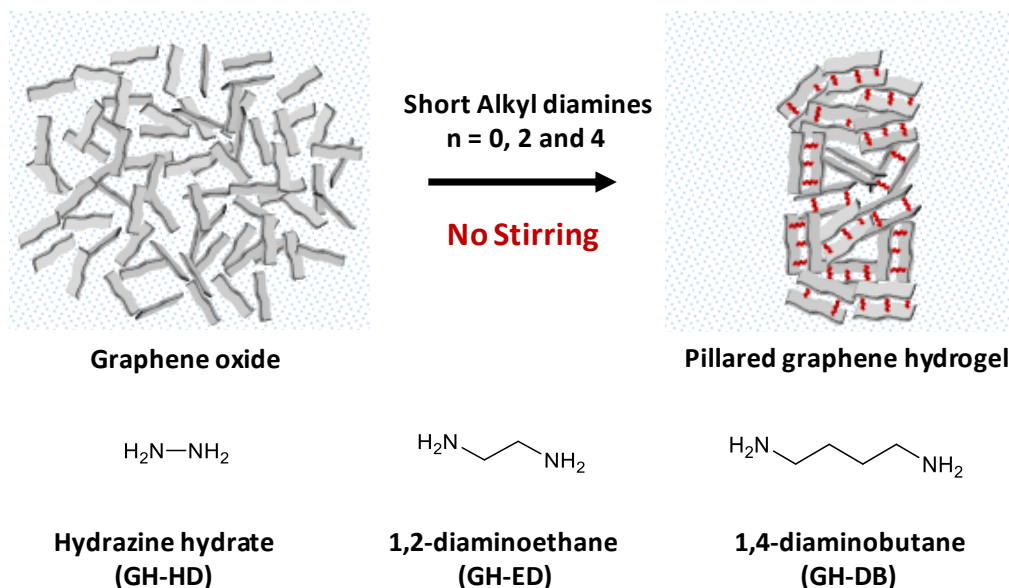
Scheme II-1 Schematic representation of the expected monolith formation using three different diamines. The gels synthesized using hydrazine hydrate, 1,2-diaminoethane and 1,4-diaminobutnae were named as GH-HD, GH-ED and GH-DB respectively. Reaction was done without magnetic stirring to facilitate the growth of a monolith.

The results obtained from the above study were published as an article in the Journal of Power Sources in 2017 (https://doi.org/10.1016/j.jpowsour.2017.06.033). The knowledge and the perspectives gained form the materials for the broader interest of this thesis are described at the end of this article.

Based on the material properties and electrochemical results of the gels synthesized, an article was written with a specific projection for publication. The article focuses on the ability to synthesize highly reduced graphene monoliths in a one- step process using hydrazine hydrate, overturning the earlier suggestion in the literature. In addition, a comparison of the physicochemical and electrochemical responses of the gels made with three diamines was also made throughout the article. The article is presented below in the same format as it appears in the journal. FD and HB conceptualized the idea and designed experiments. HB performed experiments, analysed data and conceived the manuscript. YC helped with GO preparation, AB helped with XPS analyses and BD performed gas sorption experiments. HB and FD compiled the work and wrote the manuscript. All authors have discussed the results and contributed to the final manuscript.

One-Step Synthesis of Highly Reduced Graphene Hydrogels for High Power Supercapacitor Applications

Harish Banda[†], David Aradilla[†], Anass Benayad[§], Yves Chenavier[†], Barbara Daffos,[± ‡] Lionel Dubois[†] and Florence Duclairoir[†]*

[†] University Grenoble Alpes, INAC-SyMMES, F-38000 Grenoble, France.

CEA, INAC-SyMMES, 17 rue des Martyrs, F-38000 Grenoble, France.

[§]CEA-LITEN, MINATEC, 17 rue des martyrs, F-38000 Grenoble, France

[±]CIRIMAT, Université de Toulouse, CNRS, INPT, UPS, 31062 Toulouse, cedex 9, France

[‡]Réseau sur le Stockage Electrochimique de l'Energie (RS2E), FR CNRS 3459, France

*Corresponding authors: florence.duclairoir@cea.fr
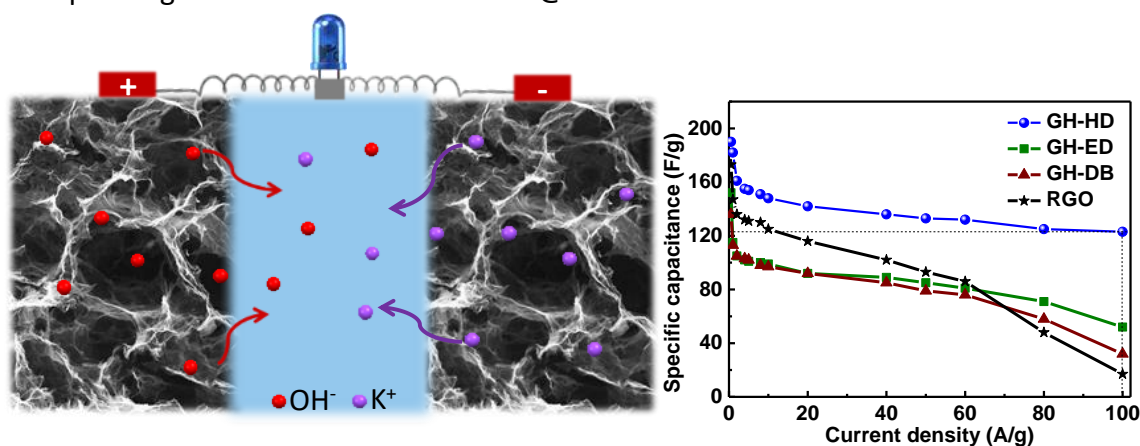
Abstract

Graphene hydrogels with high electrical conductivity were prepared by a one-step process using hydrazine hydrate as gel assembly agent (GH-HD). Conventional two-step process of gel formation and further reduction to prepare highly conducting gels was replaced by a single step involving equivalent amount of hydrazine. Optimized graphene oxide concentration was established to facilitate such monolith formation. Extensive characterization and control studies enabled understanding of the material properties and gel formation mechanism. The synthesized gel shows a high electrical conductivity of 1141 S/m. The supercapacitor based on GH-HD delivers a high specific capacitance of 190 F/g at a current density of 0.5 A/g and 123 F/g at very high current density of 100 A/g. Furthermore, excellent power capability and cyclic stability were also 3D macroporous morphology of GH-HD makes it ideal for high rate supercapacitor applications.

2. Introduction

Supercapacitors (SCs) based on electrochemical double layer capacitance have attracted great interest as electrochemical energy storage devices in the last decade [1,2]. Successful elaboration of SCs promise a wide range of applications in electric vehicles, memory back-up devices and large industrial equipment. While high power capability and long cycle-life of SC have been the driving force for this extensive scientific research, inferior energy densities compared to batteries has been a major shortcoming [3,4]. Considerable efforts on materials design have been made in attaining superior energy densities without compromising the power capability and cycle-life [5]. Graphene, a one-atom thick layer of graphite, is among the various carbonaceous materials that are under study for this type of electrochemical storage. Graphene with its high electrical conductivity, mechanical flexibility and remarkable theoretical surface area of 2630 m^2/g is an ideal candidate for SC [6]. It is noteworthy that theoretically a high gravimetric capacitance of 550 F/g could be obtained if both surfaces of graphene were used for charge storage [7]. While synthesis of pristine graphene for practical applications is challenging, Ruoff et al. have pioneered the bulk synthesis of reduced graphene oxide (RGO) as a graphene-like material [8,9]. This synthesis pathway is based on the oxidation of graphite powder to exfoliated graphene oxide (GO) that is subsequently reduced into RGO [8]. When tested in a SC, RGO demonstrated good power capability in both aqueous and organic electrolytes [10]. However, low specific capacitances of 130 and 99 F/g respectively were achieved owing to limited exposition of graphene sheets to the electrolyte. This unexpectedly lower accessible surface area was explained by the restacking of individual hydrophobic graphene sheets due to strong π- π interactions [10].

Later, Shi *et al.* have first developed self-assembled graphene hydrogels (GHs) from aqueous graphene oxide (GO) solutions [11-13]. This assembly is achieved through careful modulation of the hydrophobic/hydrophilic balances in the GO solution through either non-covalent or covalent interactions [14-22]. Two interesting monolith assembly methods are the hydrothermal treatment of a graphene oxide solution, and the bridging of graphene oxide sheets by reaction with diamine [12, 23-26]. The first method can be considered as non-covalently based as the monolith formation is triggered by the GO sheets reduction under supercritical conditions followed by their physical cross-linking [12]. The second method concerns the reactivity of the

75

terminal amines of an organic diamine structuring agent with the oxygen functionalities on the graphene oxide sheets [25]. The amine groups react with the electropositive carbons on graphene oxide and a covalent C-N bond is thus formed. Each diamine molecule could react twice and can thus bridge two graphene sheets together. In this method, the concomitant reducing nature of the diamine also plays a role in the monolith formation [25]. The covalent bond formation and the concomitant reduction of GO occur at a varied degree depending on the diamine used. It was shown that the assembly of 2D sheets into 3D monolith limits restacking of the layers, creates a unique macro porous network with pore diameters ranging from sub-micrometers to several micrometers that enables unobstructed transport of the electrolyte, and yield a 3D percolating network [17]. Hence, these GH have been tested in SC systems and indeed showed excellent electrochemical performances [27].

In the case of the hydrothermally synthesized GH, discharge capacitance of 200 F/g was achieved at a low current density of 0.3 A/g with good cycle-life [12]. However, a great decrease in specific capacitance was observed upon increasing the current densities owing to low electrical conductivity. Nevertheless, a subsequent hydrazine-reduction of this gel allowed better capacitances at high current densities (222 F/g at 1 A/g) [28]. Similar enhancement in power performances is also reported with hydrazine treatment of 1,2-diaminoethane assisted GHs. These examples from literature emphasize that an additional reduction step of the monolith is essential to achieve the highest SC performances explained by a higher electrical conductivity of the percolating network [23-25, 28, 29].

Interestingly, depending on the nature of the reducing agent and the reaction parameters, chemical reduction of GO in itself has been identified as an efficient gel assembly method. For example, reducing agents such as ascorbic acid, $NaHSO_3$, Na_2S and HI were proposed as assembly initiators to form high conducting gels in varying shapes [30]. Surprisingly, hydrazine hydrate, an excellent reducing agent, which originally instigated the development of RGO and was also used to further reduce the assembled gels, was shown to be ineffective for monolith assembly under specific conditions.[30] Yan et. al. have suggested that the presence of residual nitrogen in the gel may prevent monolith formation with hydrazine [30]. However, now it is well known that nitrogen doped gels are indeed possible [23, 24-26]. Hence, successful demonstration of a monolith using hydrazine is conceivable and promises an excellent conducting GH for high power supercapacitors.

Herein, we demonstrate that the graphene monolith assembly using hydrazine monohydrate is indeed feasible. A simple one-step synthesis process under optimized reaction conditions enables exceptionally conducting gels (GH-HD) with excellent power capabilities. Furthermore, instead of large quantities of hydrazine monohydrate as reported earlier, a molar equivalent of reagent corresponding to GO is used. For comparison and better understanding of the mechanisms involved, GH with other longer chain diamines such as 1,2-diaminoethane (GH-ED) and 1,4-diaminobutane (GH-DB) have also been synthesized (Scheme II-2). The synthesized GH-HD demonstrates a high capacitance of 190 F/g at a current density of 0.5 A/g and a remarkable cyclic stability over 2000 cycles at 10 A/g. Moreover, a high capacitance of 123 F/g could be retained at a very high current density of 100 A/g. Although gravimetric capacitances were conventionally used as the evaluation criterion of a SC, volumetric capacitance is considered to be a crucial measure for portable applications with limited space [31-36]. By adopting a simple drying technique [31], we could double the volumetric capacitance of 110 F/cm^3 for freeze dried GH-HD to 257 F/cm^3 at 0.5 A/g.

3. Results & Discussion

In this study, the graphene monolith assembly is obtained by reacting GO solution with a diamine structuring agent at 80°C for 24 h under no stirring condition (Scheme II-2). Concentration of the GO solution and molar equivalents of the diamine used are two important parameters in the gel formation. An earlier report describing the effort to synthesize GH with 1.5 mg/mL GO and 41 mmol/L of hydrazine showed that it was unsuccessful [30]. In this work a series of control experiments were performed to identify if a monolith could be assembled for specific values of GO concentration and diamine equivalents (details in Materials & Methods). It was evidenced that for optimized concentrations of 5 mg/mL GO and 3.7 µl hydrazine monohydrate for 1 mg of GO respectively, a GH-HD monolith could be successfully formed. This finding certainly differs from what was observed in the literature. This can be explained by the higher GO concentration used in this work which promotes enhanced cross-linking between the GO sheets and gel formation [24]. GH-ED and GH-DB were also synthesized using these optimized parameters to allow clear physical and electrochemical property comparisons of the gels. The physical and chemical properties of GHs were characterized by FT-IR, TGA, XRD, XPS and conductivity measurements. SEM analysis was performed to analyze the expected 3D assembly of the systems.
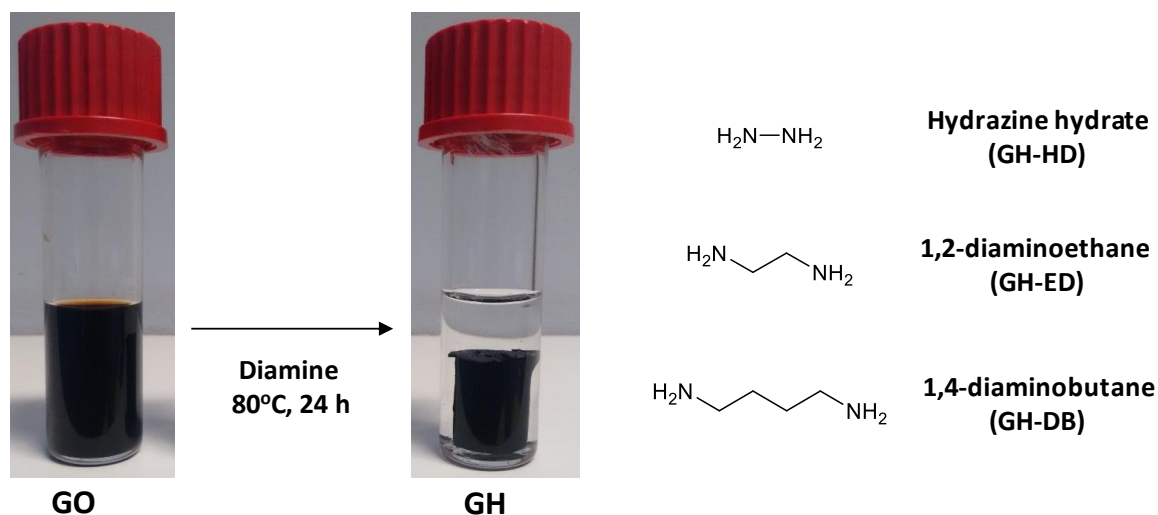
Scheme II-2 Schematic of the gel formation process with different diamines used.

Figure II-1a shows the comparison of the FT-IR spectra recorded for graphene oxide and each of the gels assembled. The GO FT-IR spectra displays intense adsorption peaks at ~ 3400, 1728 and 1620 cm^{-1} corresponding respectively to OH, C=O and C=C stretching modes which is in

accordance with the high degree of oxidation of the starting material. Upon gel assembly with diamines, the broad and intense band at 3700-3200 cm^{-1} is replaced by a relatively weak band at 3400 cm^{-1}. The carbonyl signature at 1728 cm^{-1} disappears while two new bands assigned to N-H of primary amines and aliphatic C-N at 1568 and 1200 cm^{-1} respectively appear [25]. These modifications in spectra upon gel assembly can be explained by the reduction of oxygen containing function (chemical reduction) and by the diamine reaction with GO. While GH-ED and GH-DB show presence of primary amine from respective diamines with intense bands at 1568 cm^{-1}, this band is much less intense for GH-HD suggesting that the gel formation mechanism with hydrazine could be different with other longer diamines.
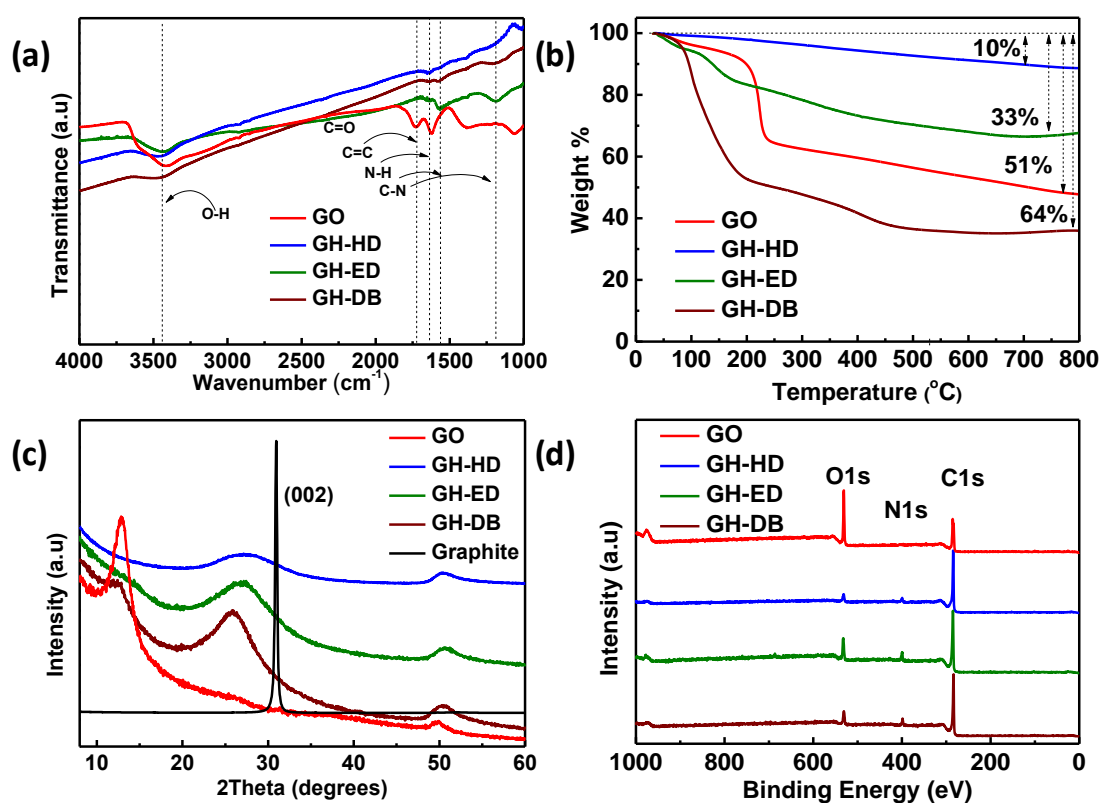
Figure II-1(a) FT-IR spectra from the raw data, (b) TGA response under N$_2$ atmosphere, (c) XRD patterns and (d) XPS survey scans of GO and GHs.

Thermal degradation responses of GO and GHs were analyzed with TGA analysis (Figure II-1b). GO shows a typical two step degradation profile corresponding to loss of moisture at around 100°C and decomposition of labile oxygen functionalities at ~ 220°C [38]. The synthesized gels show varied decomposition profiles depending on the nature of the diamine. On one hand, GH-ED and GH-DB show a gradual weight loss from 180-350°C, similar to that of GO. This loss is explained by the presence of residual oxygen functionalities in these gels. Further, a

significant weight loss could be noted around the boiling points of respective diamines (116 and 158°C) suggesting the removal of labile diamines. From these thermograms it can be deduced that these gels are not fully reduced and that the reaction with 1,2-diaminoethane and 1,4-diaminoethane successfully occurred. On the other hand, GH-HD thermogram does not indicate any significant weight loss throughout the heating range indicating lack of any labile diamine or oxygen functionalities. Thus, GH-HD demonstrates a high degree of reduction and a graphite-like thermal behavior. As hinted by the IR study, the lack of amine loss in this gel highlights a different gel formation mechanism when longer diamines were used.

Figure II-1c displays the XRD patterns of GO and freeze-dried gels. The pattern for GO depicts a relatively sharp peak at 2θ = 12.9° corresponding to 7.94 Å of inter-layer spacing indicating high oxidation of the starting material. The synthesized GH-HD exhibits a broad peak around 2θ = 27.5°, corresponding to the graphitic (002) orientation and an inter-graphene sheet distance of 3.76 Å. This value is very close to that of graphite itself (3.36 Å), evidencing a high degree of reduction of GH-HD. GH-ED and GH-DB diffractograms display a (002) peak shifted very slightly to lower 2θ corresponding to interlayer spacing of 3.82 and 4.01 Å respectively. The gel formation with diamines results in removal of oxygen functional groups from the surface of GO sheets and thus partially restores the stacking as evidenced by the (002) peak shift. Among the three diamines, GH-HD shows a near graphite-like behavior with an inter-layer spacing of 3.76 Å highlighting better degree of reduction than the other gels. Notably, GH-ED shows a broad bump around 14° whereas GH-DB shows a short peak around 12°. This could be probably due to the insertion of alkyl diamines between the GO sheets.

Further, XPS was performed to analyze the surface chemical composition of GO and GHs. Figure II-1d shows survey spectra of different samples with presence of the same elements i.e. C, O and N. It is visible that depending on the samples the relative elemental concentrations vary. For example, on the GO spectra, the intensity of the O peak is higher than that of the C peak, whereas for the gels this ratio is inversed and the C peak intensity becomes higher. This evolution shows that GO is highly oxidized compared to the gels that all show a spectra indicative of a sample reduction. It is also visible that upon gel formation an additional N 1s peak appeared at ~399 eV giving evidence of a reaction between graphene and the diamine used for the gel structuration.

To compare the samples further, HR XPS spectra were recorded on C, O and N for each sample. As can be seen on Figure II-2a, after deconvolution, the high resolution C1s core-level spectra of GO shows four characteristic peaks at 284.6, 285.9, 286.5 and 288.3 eV corresponding to C=C/C-C, C-OH, epoxy/alkoxy and carbonyl groups respectively [8]. For the synthesized gels, the C1s HR XPS spectra display significant decrease in the intensities of the signals arising from C in an oxidized environment (C=O, C-OH, O-C-O) and a new peak attributed to C-N bond appears at 285.6 eV (Figure II-2b, c&d for GH-HD, GH-ED and GH-DB respectively) [25]. These findings confirm the removal of oxygen groups upon the conversion of GO to GHs due to chemical reduction and assert the reaction between GO and the diamine structuring agent. Further, restoration of the conjugation is also typically seen through π-π* signal that occurs beyond 290 eV. Such a signal could be clearly spotted in GH-HD again confirming the reduction of GO.
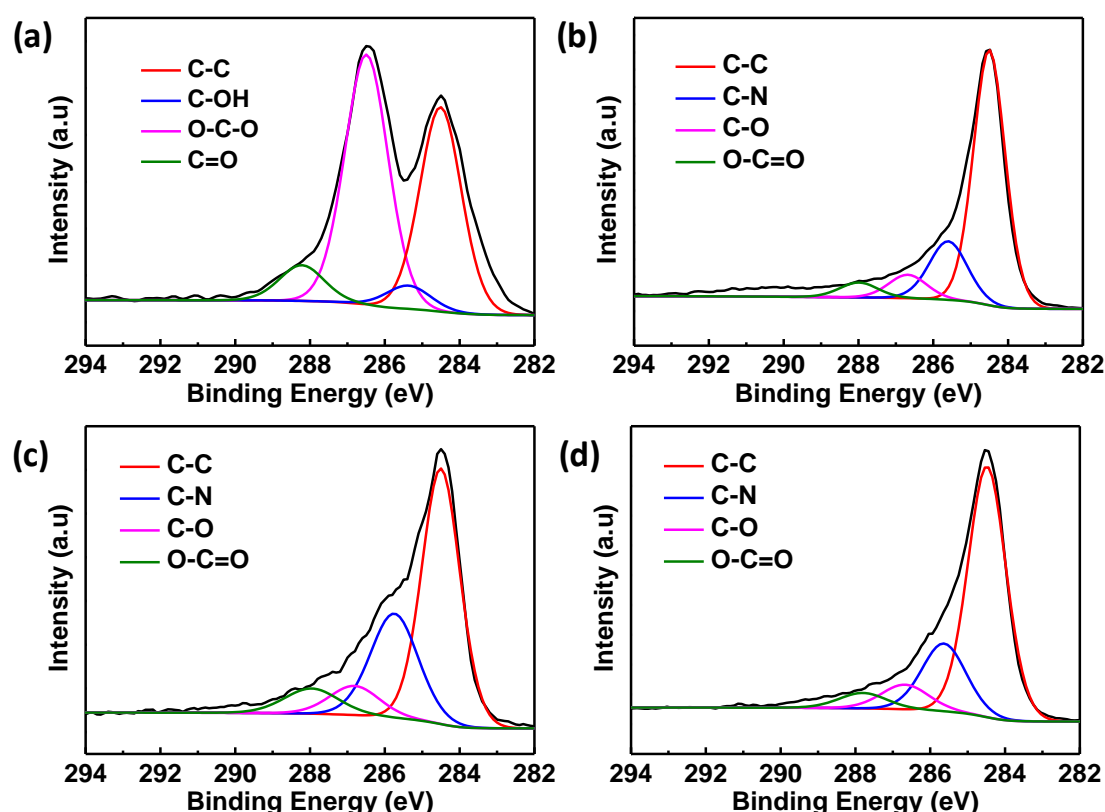
Figure II-2 Deconvoluted C 1s HR XPS spectra of (a) GO, (b) GH-HD, (c) GH-ED and (d) GH-DB For each material, the high resolution (HR) C1s spectra was deconvoluted into 4 components: C-C (284.6 eV), C-N (285.6 eV), C-O (286.6 eV) and O-C=O (287.9 eV). The same deconvolution parameters were applied to each spectrum.

The reactivity between GO and the diamine structuring agent was further addressed by observing the N1s HR XPS spectra for various gels (Figure II-3a). The N1s signal for GH-HD is

centered at higher binding energy of ~400 eV compared to (~399 eV) of GH-ED and GH-DB, showing variation in N environment. Based on reference studies, the N 1s spectra was deconvoluted into pyridinic (398.2 eV), amine (399.2 eV), pyrrolic (400.2 eV) and graphitic (401.5 eV) components (Figure II-3b, c, d for GH-HD, GH-ED and GH-DB respectively) [25,29].
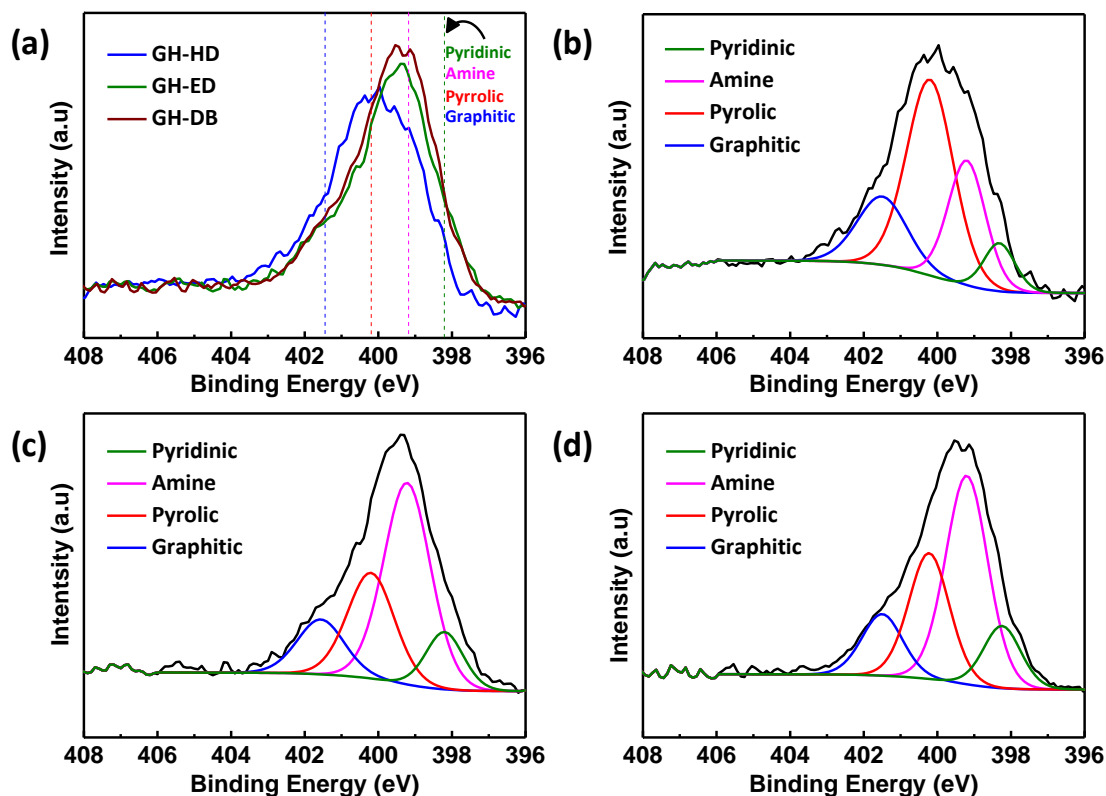
Figure II-3 N 1s high resolution XPS spectra of the three gels shown as (a) an overlap and individually (b) GH-HD, (c) GH-ED and (d) GH-DB. For each gel, the HR N1s spectra was deconvoluted into 4 components: Pyridinic (398.2 eV), amine (399.2 eV), pyrrolic (400.2 eV) and graphitic (401.5 eV).

As evoked in the literature, these components arise from different types of Ns resulting from various possible mechanisms: the amines react covalently with the GO to form amine linkages on graphene sheets. Intramolecular rearrangements with these amine linkages can cause insertion of pyridinic/pyrrolic/graphitic components into the graphene sheet (Figure II-4).[29] An analysis of the relative intensities of all N components in the three gels is displayed in Figure II-5. The N atomic concentration in GH-HD (4%) is lower than that for both GH-ED and GH-DB (~ 6%) (Table II-1). Approximately, 50% the nitrogen present in GH-ED and GH-DB corresponds to amine whereas only 25% corresponds to amine N in GH-HD (Figure II-5b). For GH-HD the main N component is pyrrolic. This differentiation may arise from different gel formation mechanisms between GO and hydrazine and GO and ED or DB. As an extension, GH-HD, even with lower N content, could present different material properties compared to GH-ED and GH-

DB. For example, it is known that addition of graphitic nitrogen into graphene materials improves the electrical conductivity and presence of pyridinic nitrogen and pyrrolic nitrogen under basic conditions boost electrochemical capacitances [29, 39].

Pyridinic   Amine   Pyrrolic   Graphitic
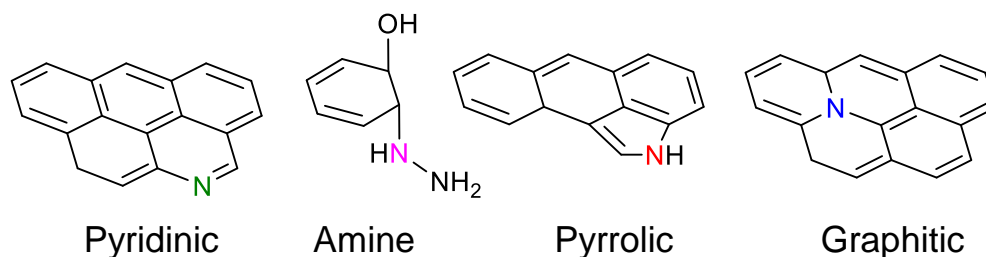
Figure II-4 Representation of the different possible N chemical environment/Proposed reaction mechanisms
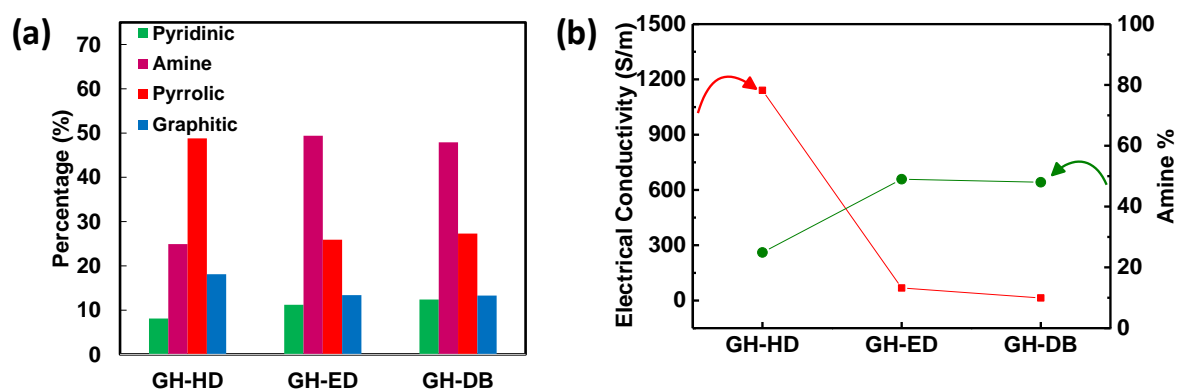
Figure II-5 (a) A histogram showing the percentages of different N environments in the gels and (b) electrical conductivities of the gels shown with corresponding amine contents from XPS analysis.

Conventionally C/O ratios are analyzed as a measure of the degree of reduction of graphene materials [28]. However, carbons coming from the 1,2-diaminoethane and 1,4-diaminobutane alkyl chains are added into the C content, hence, the C/O ratios obtained herein should be interpreted with caution. The obtained elemental compositions and C/O ratios of the gels are listed in Table II-1.

	C (%)	O (%)	N (%)	C/O	σ (S/m)	C_{wt} (F/g) at 0.5 A/g	C_{wt} (F/g) at 100 A/g
GH-HD	90.4	5.4	4.2	16.7	1141	190	123
GH-ED	82.4	10.7	6.8	7.1	68	152	51
GH-DB	85.4	8.5	6.2	10.7	14	136	32

Table II-1 Elemental composition and C/O ratios obtained from XPS, electrical conductivity (σ) and discharge capacitances in F/g (C_{wt}) at different rates of GHs.

GH-HD, GH-ED and GH-DB show C/O ratios of 16.7, 7.1 and 10.7 respectively while GO demonstrates 2.6. These values further demonstrate the reduction of GO during gel formation with diamines. The C/O ratio observed for GH-HD here is greatest among the hydrazine reduction of the GO [8, 9]. Repeated experiments confirm this value and investigations are under way to clearly understand the merits of the current procedure over previous reduction protocols. Furthermore, the values obtained by GH-DB and GH-ED may not be a correct representation of the order of degree of reduction as greater number of alkyl carbons are added into GH-DB than GH-ED. Electrical conductivity measurements were performed on each freeze-dried gel. From Figure II-5b, it is clear that GH-HD has nearly two-fold greater conductivity (1141 S/m) compared to that of GH-ED (68 S/m) and GH-DB (14 S/m) indicating a higher reduction extent for GH-HD.
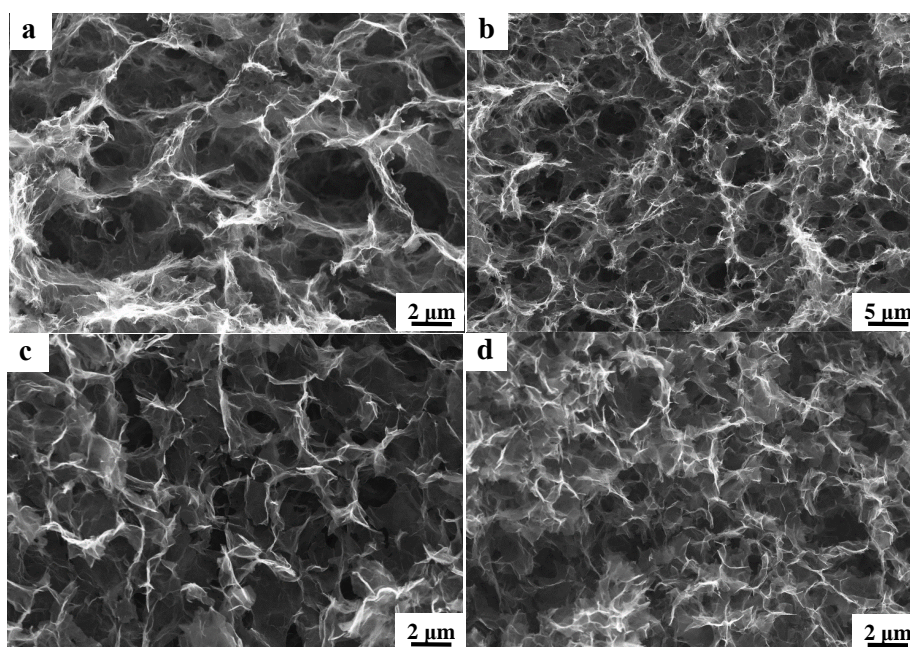
Figure II-6 Scanning electron microscopy images of the 3D frameworks in (a&b) GH-HD, (c) GH-ED and (d) GH-DB.

Scanning electron microscopic images (Figure II-6) show that well-developed extensive 3D porous networks are achieved for the gels. GH-HD is characterized by macropore diameters of several micrometers (Figure II-6a&b); whereas GH-ED and GH-DB have smaller pore volumes than GH-HD with pore diameters in sub micrometer range. Interestingly, GH-ED has larger pores than GH-DB as also seen in an earlier study of diamines with different chain lengths [23]. The specific surface areas for the gels were obtained through methylene blue (MB) dye adsorption studies. MB adsorption is extensively used to quantify the solvated surface

area of a material in which any possible restacking of graphene layers is prevented by avoiding freeze drying technique [40,33,34]. GH-HD shows high specific surface area (SSA) of 1433 m^2/g whereas GH-ED and GH-DB have 677 and 335 m^2/g respectively. GH-HD demonstrates a porous morphology (Figure II-6a&b) that is similar to the hydrothermally synthesized gels which were found to have a SSA of 1030 and 1560 m^2/g [33]. On the other hand, despite the propensity of lyophilization to reduce the SSA through graphene layer restacking, surface area from gas sorption studies of fully freeze-dried samples can be helpful. Additionally, SSA values from gas sorption make it easier to compare these samples to other monoliths described in the literature.
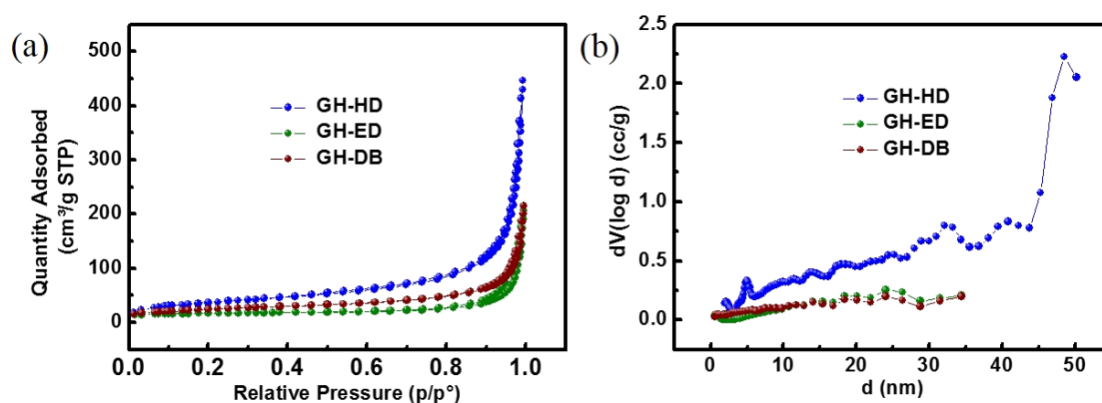
Figure II-7.(a) N$_2$ gas sorption isotherms and the corresponding (b) pore size distributions of the synthesized gels calculated by using quenched solid density functional theory (QSDFT) method.

For GH-HD a 130 m^2/g SSA with a mean pore size of 25 nm is determined while for GH-ED and GH-DB the SSA are respectively 85 and 80 m^2/g with mean pore sizes of 17 and 13 nm (Figure II-7). Hence, the trend obtained with MB adsorption is also observed here confirming that GH-HD monolith presents a higher surface area. It is noteworthy that the PSD also shows that GH-HD displays macroporosity as evidenced in SEM. For GH-ED gel that can be directly compared to literature data, the SSA obtained is half of what was described earlier [24]; however, both the values remain in the same range and this difference can be explained by variation in 1,2-diaminoethane concentration used leading to different graphene assembly structures. When compared to the precursor of holey graphene foam obtained by the hydrothermal route, GH-HD displays a lower SSA; however, despite being prepared following different methods and using different initial GO concentration, both SSA remain in the same magnitude range [33]. Again this morphological characterization tend to prove that while the three structuring agent are diamines, they do not react identically with GO leading to GH with different properties (proposed mechanisms in Scheme II-3 and Scheme II-4).

As evoked before, gel formation with hydrazine occurs mainly through reduction of oxygenated functionalities on the GO sheets; this high reduction degree is confirmed with XPS, TGA and conductivity measurements. In this case the reduced graphene oxide sheets cross-link through π–π stacking resulting in 3D framework with entrapped water (Scheme II-3).[12] For 1,2-diaminoethane and 1,2-diaminoethane structuring agents, the nature of the reaction is more covalent and the amine functions will react with C in an oxidized environment. The reductive power of these two amines compared to hydrazine are lower explaining that this reduction-based gel formation path is not favored (Scheme II-4). In this case, the 3D assembly is triggered by covalent cross-linking leading to structures with smaller pore volumes. This gel comparison therefore shows that in a one-step process by selecting a diamine that remains short and display a high reductive power, a gel with interestingly high conductivity and porosity can be formed. It is noteworthy that the GH-HD conductivity and porosity fall in the same range than of that of the further reduced hydrothermally synthesized gel [12].
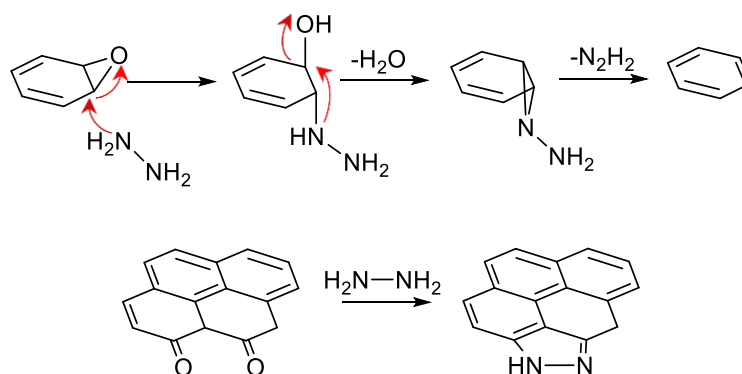
Scheme II-3 Possible major reaction pathways between hydrazine and oxygen functionalities on GO.
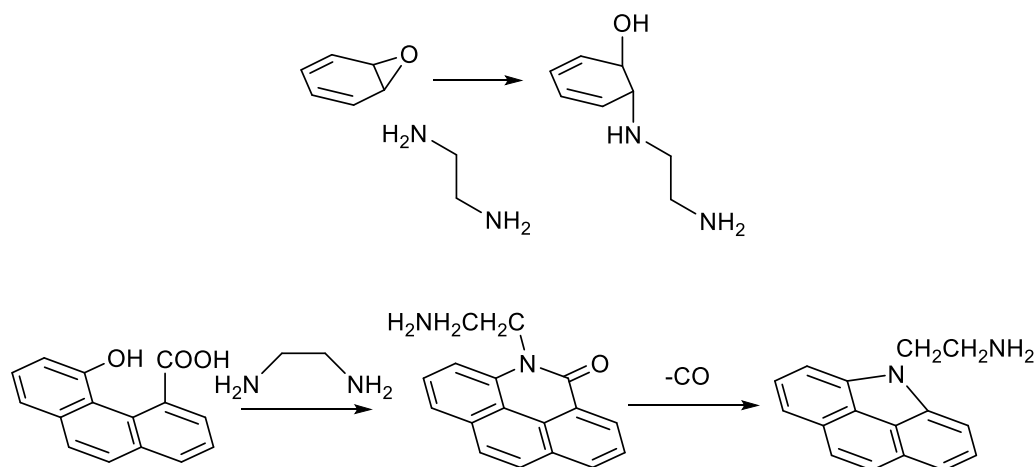
Scheme II-4 Possible major reaction pathways between 1,2-diaminoethane and oxygen functionalities on GO. Similar mechanisms could be expected for 1,4-diaminobutane.

3.1 Electrochemical Studies on GHs

GHs synthesized with different diamine chain lengths were tested in a two-electrode supercapacitor configuration with aqueous potassium hydroxide (6 M) as electrolyte. Since the gels were prepared in aqueous media, they enable facile assembly into aqueous electrolyte without much processing. Slices of gels were assembled symmetrically without any conductive additives or binding agents. CV, galvanostatic charge-discharge at different current densities and EIS were performed to evaluate the electrochemical performances. CV curves were obtained in the potential range of 0-1 V at relatively low and high scan rates of 100 mV/s and 1000 mV/s. At a lower scan rate all three gels show rectangular curves with little deformation suggesting mainly electrochemical double layer capacitance (EDLC) mechanism with good charge propagation at the electrode-electrolyte interface (Figure II-8a). Upon increasing the scan rate from 100 mV/s to 1000 mV/s, the CV curves of GH-HD and GH-ED retain a nearly rectangular shape while that of GH-DB distorts into narrow and oblique rectangle (Figure II-8b). Charge storage mechanism which involves adsorption-desorption of the ionic species at the electrode surfaces depends on the time scales of the electrochemical processes. High scan rates or charge-discharge current densities may not allow sufficient time for double layer formation and thus could result in such resistive behavior. Notably, GH-HD offers greater current densities compared to the other two gels at both scan rates. These results suggest better ion transport characteristics and higher ion accessible surface areas in GH-HD.

The slight distortion in the CVs at 100 mv/s could possibly be due to redox activity of the nitrogen and oxygen content in the synthesized gels. Three electrodes configuration allows to study the individual electrode response and could give additional information over the two-electrode measurements. Hence, CVs were obtained at 100 mv/s scan rates for all the gels in the voltage range of -0.9 V to 0.1 V vs. standard calomel electrode (Figure II-9b). 3-electrodes CVs of the three gels show similarly slightly distorted rectangular shape and confirm the contribution of pseudo capacitance from N and O functionalities [29]. Among the three gels, GH-HD demonstrates more intense redox peaks (-0.6 V vs. SCE) than GH-ED and GH-DB. Good electrical conductivity of the material for better electron transport to and from the redox active sites and higher redox active N content explain the more intense pseudo capacitance peaks in the case of GH-HD with high capacitance values if 248 F/g.
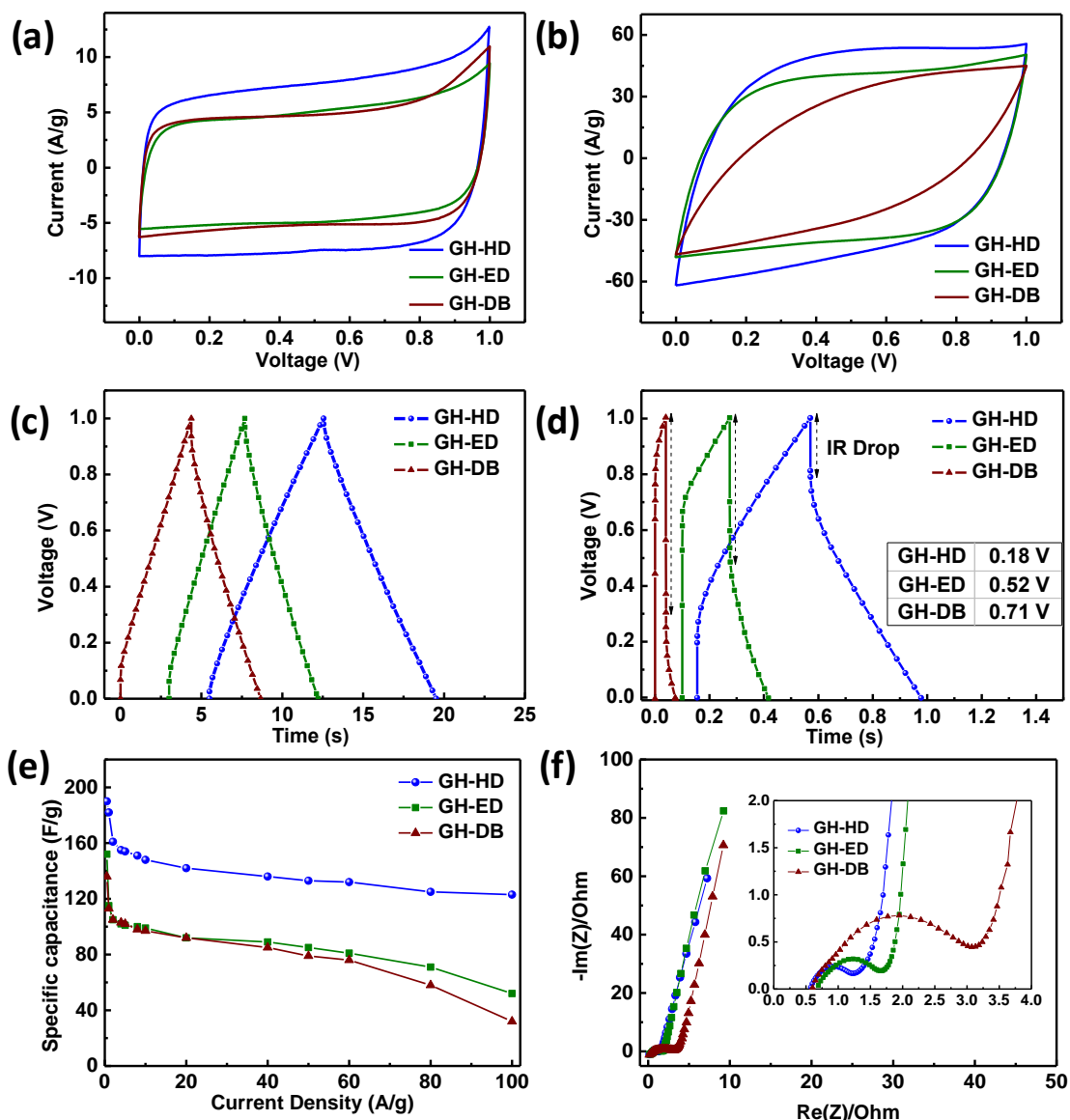
Figure II-8 Cyclic voltammograms of gels obtained at scan rates of (a) 100 mV/s and (b) 1000 mV/s in the voltage range of 0-1 V; galvanostatic charge-discharge voltage profiles of the gels obtained at current densities of (c) 10 A/g and (d) 100 A/g; (e) rate capability and (f) Nyquist plot obtained from frequency response of the gels from 400 kHz to 40 mHz. Inset shows a magnified plot with frequency response at high frequencies.
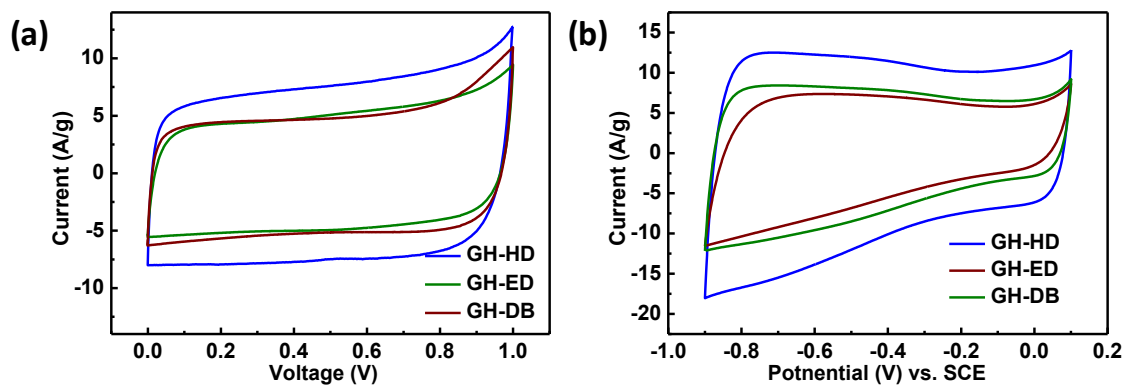
Figure II-9 CVs of gels obtained at 100 mV/s in (a) two-electrode and (b) three-electrode set-up.

Table II-2 compares the three-electrode electrochemical performance of GH-HD with different materials in the literature.

Material (Synthesis procedure)	Scan rate/ Current density	Specific Capacity (F/g)
Thermal exfoliation of GO	2 mV/s	183
Chemical reduction of GO	10 mV/s	122
Nitrogen doped graphene	1 A/g	110
GH-HD	10 mV/s	248

Table II-2 Comparison of GH-HD with various graphene materials when tested in aqueous electrolytes using three-electrode system.

Galvanostatic charge-discharge cycling of gels was performed at high current densities of 10 A/g and 100 A/g. At 10 A/g, symmetrical charge-discharge curves (Figure II-8c) could be seen for all the gels in agreement with the major EDLC behavior observed in the CV curves. GH-ED and GH-DB suffer from a slight internal resistance (IR) drop of 0.04 V and 0.06 V respectively, whereas GH-HD has no drop-in voltage. The voltage drop caused by IR of the electrodes is more significant when cycling is done at high current densities. When cycled at a very high current density of 100 A/g, GH-ED and GH-DB show an asymmetric voltage profile with huge IR drops of 0.52 V and 0.71 V respectively (Figure II-8d). Similar IR drops were observed in literature when cycled at high current density of 100 A/g [28]. GH-HD retains a nearly symmetric behavior with an IR drop value of 0.18 V. This can be understood from the high electrical conductivity of GH-HD (1141 S/m) as compared to GH-ED (68 S/m) and GH-DB (14 S/m). High electrical conductivity of GH-HD ensures lower IR drops and energy loss as heat, enabling better rate performance.

Material (Synthesis procedure)	Scan rate/ Current density	Specific Capacity (F/g)
GHG, Hydrothermal treatment	20 mV/s	152
GHG, ethylenediamine hydrothermal treatment	20 A/g	120
GHG, L- glutathione	10 A/g	95
GHG film, Ascorbic acid hydrothermal treatment	1 A/g	185
GHG film, Hydrazine and ammonia treatment	1 A/g	215
GHG, Hydrothermal & hydrazine treatment	1 A/g	205
GHG, Ethylene diamine & hydrazine treatment	1 A/g	144, 191, 220
Laser Scribed Graphene	1 A/g	201
Chemically modified graphene	1.33 A/g	135
Commercial activated carbon	1 A/g	160
Chemically converted graphene	10 A/g	146
GH-HD	0.5 A/g 100 A/g	190 123

Table II-3 Comparison of GH-HD with various graphene hydrogels reports studied in aqueous electrolytes using a two-electrode configuration. References are given at the end of the chapter.

Gravimetric capacitances of cycling at 0.5 A/g and 100 A/g are obtained by calculating the slope of the discharge curves and are listed in Table II-3. Figure II-8e shows the power capability of GHs in a range of current densities from 0.5 A/g to 100 A/g. GH-HD delivers 190 F/g at 0.5 A/g, which is similar to that of hydrothermally synthesized gels (200 F/g at 0.3 A/g). GH-ED and GH-DB deliver capacitances of 152 F/g and 136 F/g under same conditions. At a high current density of 100 A/g, GH-HD offers discharge capacitance of 123 F/g whereas GH-ED and GH-DB yield poor discharge capacitances of 51 F/g and 32 F/g respectively. The superior performance of GH-HD compared to GH-ED and GH-DB is attributed to multiple factors. Firstly, GH-HD has a greater wet-state surface area of 1433 m^2/g whereas GH-ED and GH-DB have 677 and 335 m^2/g respectively. Also, the excellent electronic conductivity of GH-HD enables fast charge transfer at the electrode-electrolyte interface and allows better rate

performance. The extensive 3D networks with large pore volumes facilitate fast ion transfer to the electrode interface. Moreover, the lower percentage of amine N in GH-HD than other gels results in greater pseudo capacitive contribution by redox active N components. As a result of increased electrolyte access to electrode surface, higher conductivity and greater pseudo capacitive contributions, enhanced electrochemical capacitances are observed in GH-HD.

Charge and ion-transfers inside the highly conductive and porous GH-HD have been shown to be at the origin of its good SC electrochemical performances. An EIS study has therefore been performed to analyze these factors more directly Figure II-8f. Indeed, this technique offers the frequency response from 400 kHz to 40 mHz yielding a Nyquist plot with real and imaginary components of impedance X and Y axes respectively, and each region of the plot will give direct evidence of a specific process. First, an arc at high frequency region is ascribed to charge transfer resistance, the 45° slope of Warburg impedance in intermediate frequency range is related to ion diffusion and finally the nearly vertical line at higher frequency shows the capacitive behavior of the system. GH-HD exhibits the smallest semi-circle diameter and its charge-transfer resistance (R_{CT}) was deduced to be 0.62 Ω compared to 1 Ω for GH-ED and 2.46 Ω of GH-DB. Also, the shorter Warburg impedance region for GH-HD indicates the most efficient ion transfer among the three gels. These two findings corroborate the positive impact of the superior electrical conductivity and porosity of GH-HD on electrode charge-transfer and ion-diffusion.

The electrochemical data recorded in this work (GH-HD and GH-ED) are positioned on a Ragone plot with comparative values of GHs prepared through various reduction methods in the literature (Figure II-10a) [41, 42]. When cycled at a at a high current density of 100 A/g, with a sub-second discharge time of 0.4s, GH-HD offers a high-power density 38 kW/kg while delivering an energy density of 4.3 Wh/kg. The observed values are on par with the best reported energy and power densities in aqueous electrolytes. GH-HD outperforms GHs synthesized through reduction of GO by hydrothermal treatment [12], thermal treatment [41] and L-glutathione [42]. Also, GH-HD performs better than both GH-ED and ethylenediamine assisted gel obtained with an extra step of hydrazine reduction as reported in the literature [24]. Table II-3 compares the electrochemical performance of GH-HD with various reports on carbon materials for supercapacitors in the literature. The electrochemical performances

achieved with GH-HD are high and fall in the range of values obtained for hydrothermal gel further reduced by hydrazine, which display a power density of 30 kW/kg and energy density of 5.7 Wh/kg at 100 A/g [28].
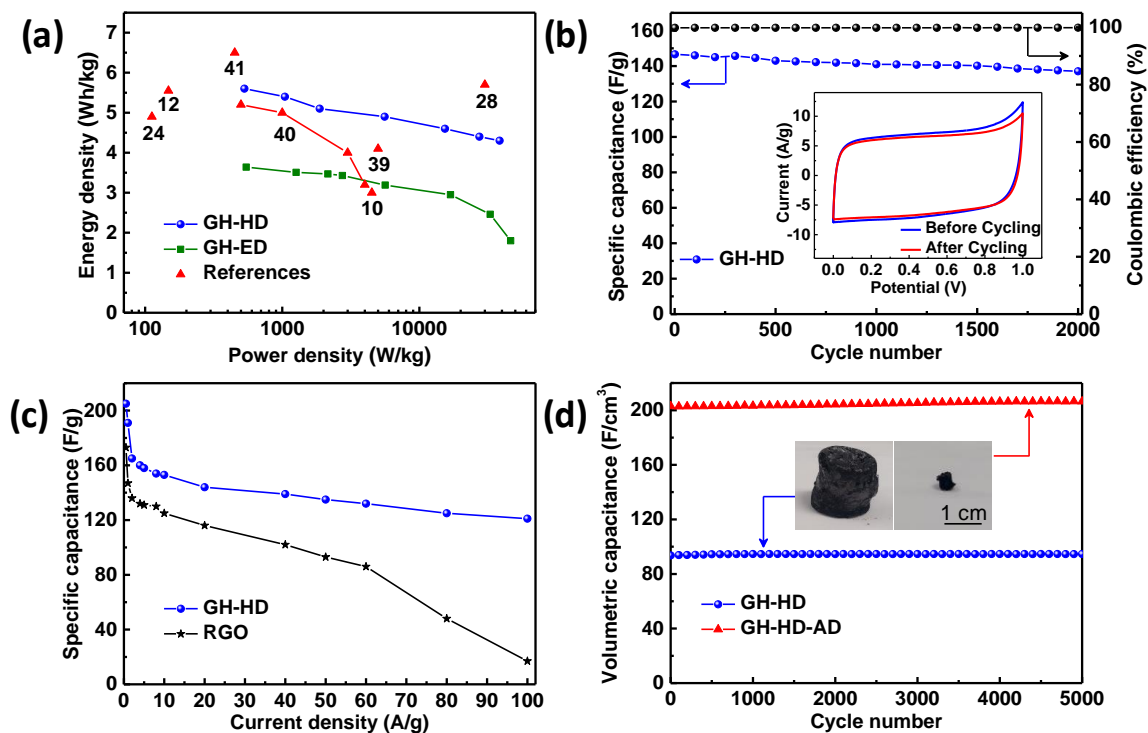
Figure II-10 (a) Ragone plot showing a comparison of energy and power densities of GH-HD and GH-ED with references from literature based on graphene-based materials obtained by various reduction techniques; (b) cyclic stability of GH-HD obtained at high current density of 10 A/g; Inset shows CVs at a scan rate of 100 mV/s for GH-HD before the 1st and after the 2000th charge-discharge cycle; (c) rate capability of GH-HD and RGO; (d) cyclic stability of GH-HD and densified GH-HD-AD obtained at a current density of 2 A/g.

The cycling study recorded at a higher rate of 10 A/g showed 93% retention of discharge capacitance after 2000 cycles (Figure II-10b). The observed cyclic stability is better than the 90% capacitance retention reported at an intermediate 4 A/g after 2000 cycles for the hydrazine-reduced hydrothermal gel. These results further demonstrate the merits of GH-HD which is obtained by a simple one-step process involving equivalent amount of hydrazine. Currently, we are devoted towards achieving higher energy densities by benefiting from large stable voltage ranges of non-aqueous electrolytes. Preliminary results using 1M tetraethylammonium tetrafluoroborate/ Acetonitrile (TEABF$_4$/ACN) as the electrolyte also show better performance for GH-HD among the synthesized gels (Figure II-11).
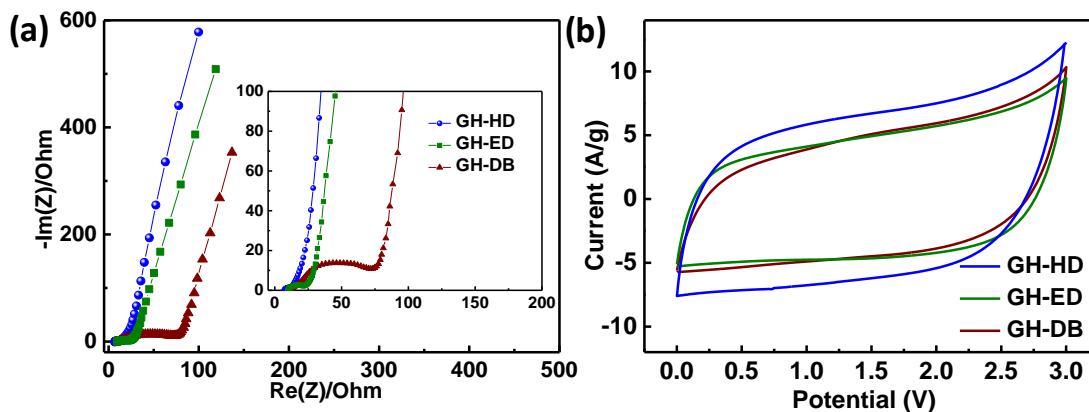
Figure II-11 (a) Nyquist plot obtained from frequency response of the gels from 400 kHz to 40 mHz. Inset shows a magnified plot with frequency response at high frequencies. (b) Cyclic voltammograms of gels obtained at a scan rate of 100 mV/s in 1M TEABF₄/ACN.

The synthesized RGO was characterized with high electrical conductivity and stacked morphology of the reduced graphene oxide sheets. We believed that a study of the electrochemical performance of this highly conducting RGO compared to GH-HD would help us critically analyze the implications of 3D porous networks in SC performances. For this purpose, we performed a controlled study by synthesizing RGO under similar reaction conditions as for GH-HD with continuous stirring (details in Materials and Methods). Four probe measurements showed an improved electrical conductivity of 1832 S/m compared to GH-HD (1141 S/m) as can be understood by greater extent of reduction under homogenized reaction media. CV of RGO shows an ideal EDLC behavior at 100 mV/s but distorts into an oblique shape at a high scan rate of 1000 mV/s (Figure II-12). Power capability study from 0.5 A/g to 100 A/g shows a similar performance of RGO to that of GH-HD at lower rates but a huge drop is noticed with increasing currents (Figure II-10c). Despite being a better electrical conductor, RGO shows poorer electrochemical performance than GH-HD at higher currents. This can be explained by the difference in porosity characteristics (Figure II-13). While, RGO performs well at lower current densities, the compact porous structure prevents seamless ion transport at higher densities. The extensive porous network in GH-HD enables excellent ion accessibility to the electrode-electrolyte interface even at higher currents. From these observations, it can be concluded that, 3D interconnected porous network, along with good electrical conductivity, is an equally important factor in enabling a high-power capability of a SCs.

Finally, considering the importance of good volumetric capacitances for SC applications with limited space, we synthesized a dense GH-HD gel by following a simple drying procedure. After gel assembly with hydrazine, GH-HD was densified from a packing density of 0.58 g/cm^3 to 1.56 g/cm^3 by drying it under ambient conditions. The gradual removal of water molecules from the inter layer spaces shrinks the gel to nearly a tenth of its original size. Figure II-10d shows the cyclic stability of GH-HD and its densified counterpart (GH-HD-AD) at a current density of 2 A/g. The volumetric capacitances of GH-HD could be noted to increase by a factor of two. GH-HD-AD delivers gravimetric and volumetric discharge capacitances of 130 F/g and 200 F/cm^3 respectively at a high current density of 2 A/g.
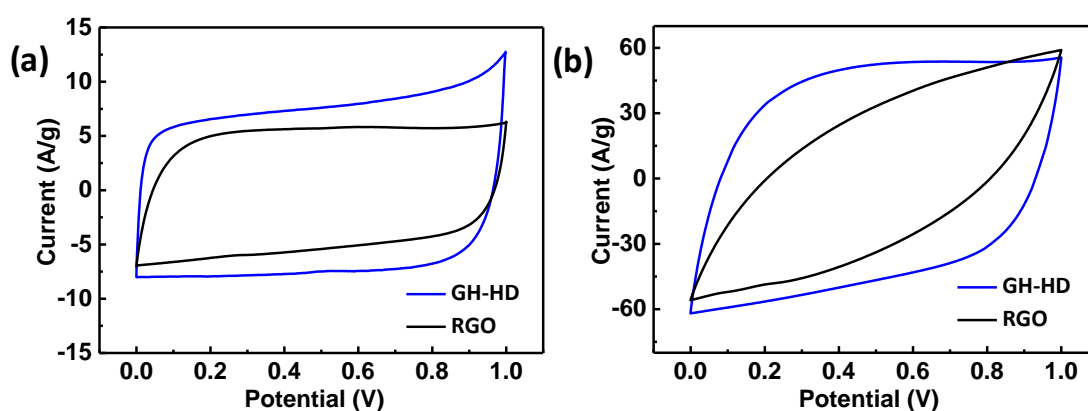
Figure II-12 Cyclic voltammograms of GH-HD and RGO obtained at scan rates of (a) 100 mV/s and (b) 1000 mV/s in the voltage range of 0-1 V. GH-HD and RGO electrochemical responses were studied by cyclic voltammetry at different scan rate. The CVs recorded at 1000 mV/s are particularly representative of the best behaviour of GH-HD attributed to a porosity better suited to ion exchanges.
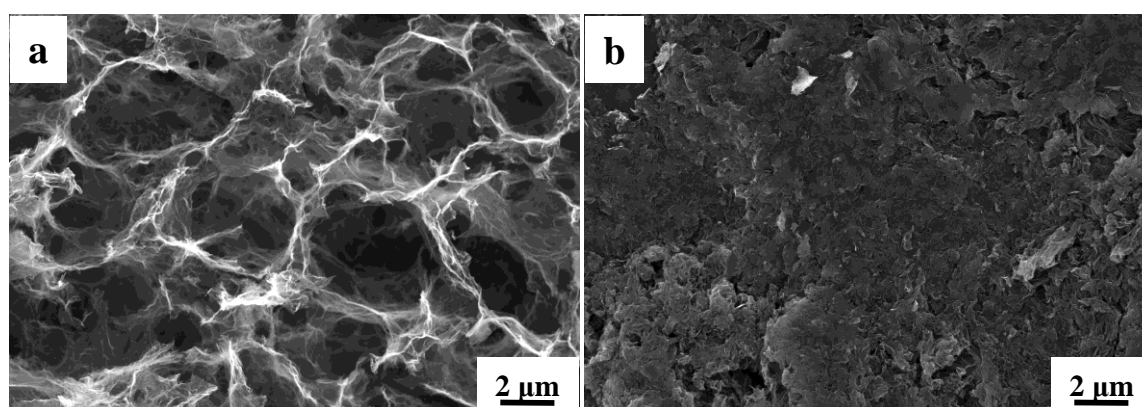
Figure II-13 Scanning electron microscopy images of the 3D framework in (a) GH-HD and compact morphology in (b) RGO. The inner morphologies of GH-HD and RGO were observed by SEM. Both materials display very different porosity as RGO appears very compact while GH-HD is more porous.

94

4. Conclusions

GH-HD was prepared as highly conducting monolith using a simple one-step synthesis process. An optimization study of the reaction conditions enabled such a hydrogel assembly. GH-ED and GH-DB based on longer diamines were also synthesized to analyze different mechanisms and their implications. Hydrazine, being a strong reducing agent, promotes gel formation via assembly of reduced GO through non-covalent interactions such as π - π interactions. When tested in aqueous SC, GH-HD with a low charge transfer resistance of 0.62 Ω and excellent 3D macroporous network, offered high rate performance. An excellent cycling stability with 93 % capacitance retention was noted after cycling for 2000 cycles at a high current density of 10 A/g and full capacitance was observed when cycled at lower rate of 2 A/g over 5000 cycles. Furthermore, at a very high current density of 100 A/g discharge capacitance of 123 F/g could be achieved. Extensive 3D porous networks along with high electrical conductivity were evidenced as the major factors behind such performances. The control study performed in this work to understand the interplay between electrical conductivity and porosity in electrochemical performances allows us to design superior materials for SCs. The simple one-step synthesis procedure under atmospheric conditions to obtain highly reduced GHs could enable the development of low cost and high-power performance SCs.

5. Further Conclusions & Perspectives

In the context of the thesis, besides providing a route to highly reduced graphene monolith, this preliminary study gave a lot of information about the gel formation ability, pillaring ability and electrical conductivities of the hydrogels synthesized by the three diamines. All the three diamines showed ability to form monoliths with interconnected porous networks as seen from SEM images. The synthesized gels have gradually lower electrical conductivities with increasing alkyl chain length of the diamine.

One particular aspect of great interest to us was the pillaring ability and the mechanism involved in the gel formation when different diamines were used. Through different characterization techniques, such as FT-IR, TGA and XRD, GH-HD showed that the hydrazine hydrate reduces the GO sheets but does not covalently react with the oxygen functionalities. GH-HD showed nearly no presence of primary amines in FT-IR, had no weight loss corresponding to loss of hydrazine molecule in TGA and had no peak at lower 2θ values in XRD that may arise from intercalation of hydrazine between the GO sheets. These observations could probably be explained by the short length of hydrazine molecule. Holding two large GO sheets together at such a short distance may not be energetically favorable and thus only reduction of GO was seen in GH-HD. On the other hand, GH-ED and GH-DB show a clear presence of alkyl diamine in FT-IR, TGA and XPS. Additionally, the XRD patterns at lower angles (10-15°) show presence of broad peaks with very low intensity in GH-ED and GH-DB. Based on these characterization data, we proposed a different reaction mechanism for reaction of 1,2-diaminoethane and 1,4-diaminobutane with GO wherein, simultaneous covalent linking and chemical reduction of GO sheets occur.

Nevertheless, the XRD diffraction plots showed peaks at lower angles with much higher intensity in GH-DB compared to that of GH-ED and to that of no peak in GH-HD. This led us to believe that, from hydrazine hydrate to 1,4-diaminobutane, the decrease in reduction ability and the favorable longer alkyl chain lengths may have favored the covalent cross-linking process over the chemical reduction (Scheme II-5). Another point of view could be that the longer diamines may enable formation of repetitive cross-linking of GO sheets to form larger crystallites and thus have XRD peaks with higher intensities. In any case, the observed peak

for GH-DB is still broad and not well-defined to perform fundamental analysis of ion-sieving using electrolyte ions of particular size.
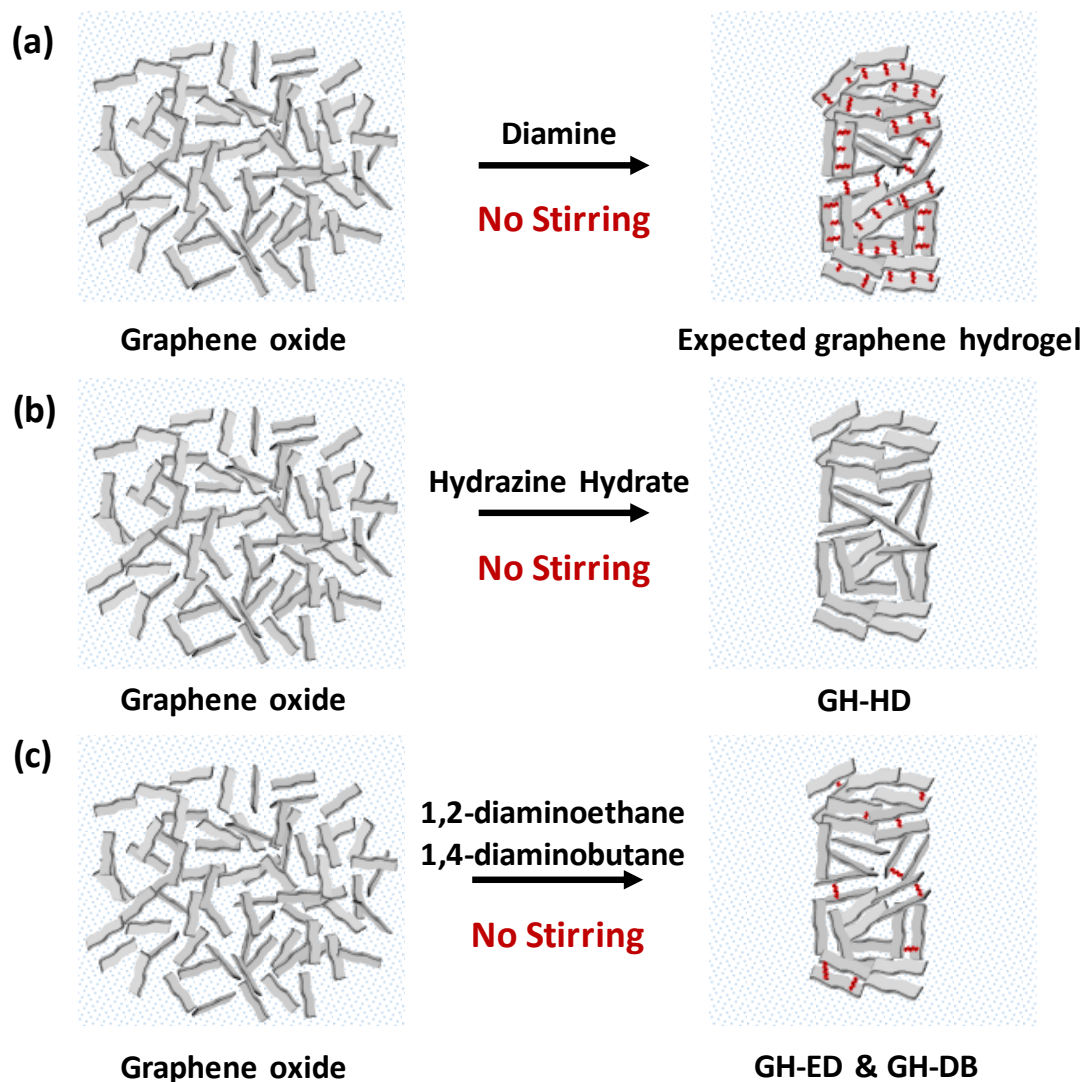
Scheme II-5 Schematic representation of (a) the desired graphene hydrogel as compared to(b) GH-HD and (c) GH-ED/GH-DB.

Thus, the two important perspectives from this study to take ahead into this thesis were. (i) Longer alkyl diamines should be tested to enable a better cross-linking that can also be well characterized using X-ray analyses. (ii) Additional chemical reduction of the gels is necessary for better electrical conductivity in SCs.

6. References

[1] G. Wang, L. Zhang, J. Zhang, A review of electrode materials for electrochemical supercapacitors, Chem. Soc. Rev. 41 (2012) 797-828.

[2] P. Simon, Y. Gogotsi, Materials for electrochemical capacitors, Nat. Mater. 7 (2008) 845-854.

[3] A. Burke, R&D Considerations for the performance and application of electrochemical capacitors. Electrochim. Acta 53 (2007) 1083-1091.

[4] J. R. Miller, P. Simon, Electrochemical capacitors for energy management, Science 321 (2008) 651-652.

[5] L. L. Zhang, X. S. Zhao, Carbon-based materials as supercapacitor electrodes, Chem. Soc. Rev. 38 (2009) 2520-2531.

[6] Y. Zhu, S. Murali, W. Cai, X. Li, J. W. Suk, J. R. Potts, R. S. Ruoff, Graphene and graphene oxide: Synthesis, properties, and applications. Adv. Mater. 22 (2010) 3906–3924.

[7] J. Xia, F. Chen, J. Li, N. Tao, Measurement of the quantum capacitance of graphene. Nat. Nano 4 (2009) 505-509.

[8] S. Stankovich, D. A. Dikin, R. D. Piner, K. A. Kohlhass, A. Kleinhammes, Y. Jia, Y. Wu, S. T. Nguyen, R. S. Ruoff, Synthesis of graphene-based nanosheets via chemical reduction of exfoliated graphite oxide. Carbon 45 (2007) 1558–1565.

[9] D. Li, M. B. Muller, S. Gilje, R. B. Kaner, G. G. Wallace, Processable aqueous dispersions of graphene nanosheets. Nat. Nano 3 (2008) 101–105.

[10] M. D. Stoller, S. Park, Y. Zhu, J. An, R. S. Ruoff, Graphene-based ultracapacitors, Nano Lett. 8 (2008) 3498-3502.

[11] H. Bai, C. Li, X. Wang, G. A. Shi, A pH-sensitive graphene oxide composite hydrogel, Chem. Commun. 46 (2010) 2376-2378.

[12] Y. Xu, K. Sheng, C. Li, G. Shi, Self-assembled graphene hydrogel via a one-step hydrothermal process, ACS Nano 4 (2010) 4324-4330.

[13] Y. Xu, Q. Wu, Y. Sun, H. Bai, G. Shi, Three-dimensional self-assembly of graphene oxide and DNA into multifunctional hydrogels, ACS Nano 4 (2010) 7358-7362.

[14] C. Li, G. Shi, Functional gels based on chemically modified graphenes, Adv. Mater. 26 (2014) 3992-4012.

[15] H. Bai, C. Li, X. Wang, G. Shi, On the gelation of graphene oxide, J. Phys. Chem. C 115 (2011) 5545-5551.

[16] P. M. Sudeep, T. N. Narayanan, A. Ganesan, M. M. Shaijumon, H. Yang, S. Ozden, P. K. Patra, M. Pasquali, R. Vajtai, S. Ganguli, A. K. Roy, M. R. Anantharaman, P. M. Ajayan, Covalently interconnected three-dimensional graphene oxide solids, ACS Nano 7 (2013) 7034-7040.

[17] Z. Lei, J. Zhang, L. L. Zhang, N. A. Kumar, X. S. Zhao, Functionalization of chemically derived graphene for improving its electrocapacitive energy storage properties, Energy Environ. Sci. 9 (2016) 1891-1930.

[18] Y. Chen, L. Chen, H. Bai, L. Li, Graphene oxide-chitosan composite hydrogels as broad-spectrum adsorbents for water purification, J. Mater. Chem. A 1 (2013) 1992-2001.

[19] S. Park, K.-S. Lee, G. Bozoklu, W. Cai, S. T. Nguyen, R. S. Ruoff, Graphene oxide papers modified by divalent ions-enhancing mechanical properties via chemical cross-linking, ACS Nano 2 (2008) 572-578.

[20] B. Adhikari, A. Biswas, A. Banerjee, Graphene oxide-based hydrogels to make metal nanoparticle-containing reduced graphene oxide-based functional hybrid hydrogels, ACS Appl. Mater. Interfaces 4 (2012) 5472-5482.

[21] B. Adhikari, A. Biswas, A. Banerjee, Graphene oxide-based supramolecular hydrogels for making nanohybrid systems with Au nanoparticles, Langmuir 28 (2012) 1460-1469.

[22] Y. Xu, G. Shi, X. Duan, Self-assembled three-dimensional graphene macrostructures: Synthesis and applications in supercapacitors, Acc. Chem. Res. 48 (2015) 1666-1675.

[23] P. Chen, J.-J. Yang, S.-S. Li, Z. Wang, T.-Y. Xiao, Y.-H. Qian, S.-H. Yu, Hydrothermal synthesis of macroscopic nitrogen-doped graphene hydrogels for ultrafast supercapacitor, Nano Energy 2 (2013) 249-256.

[24] V. H. Luan, H. N. Tien, L. T. Hoa, N. T. M. Hien, E.-S. Oh, J. Chung, E. J. Kim, W. M. Choi, B.-S. Kong, S. H. Hur, Synthesis of a highly conductive and large surface area graphene oxide hydrogel and its use in a supercapacitor, J. Mater. Chem. A 1 (2013) 208-211.

[25] H. Hu, Z. Zhao, W. Wan, Y. Gogotsi, J. Qiu, Ultralight and highly compressible aerogels, Adv. Mater. 25 (2013) 2219-2223.

[26] J. Che, L. Shen, Y. Xiao, A new approach to fabricate graphene nanosheets in organic medium: Combination of reduction and dispersion. J. Mater. Chem. 20 (2010) 1722-1727.

[27] X. Zhang, Z. Sui, B. Xu, S. Yue, Y. Luo, W. Zhan, B. Liu, Mechanically strong and highly conductive graphene aerogel and its use as electrodes for electrochemical power sources, J. Mater. Chem. 21 (2011) 6494-6497.

[28] L. Zhang, G. Shi, Preparation of highly conductive graphene hydrogels for fabricating supercapacitors with high rate capability, J. Phys. Chem. C 115 (2011) 17206-17212.

[29] H.-L. Guo, P. Su, X. Kang, S.-K. Ning, Synthesis and characterization of nitrogen-doped graphene hydrogels by hydrothermal route with urea as reducing-doping agents, J. Mater. Chem. A 1 (2013) 2248-2255.

[30] W. Chen, L. Yan, In situ self-assembly of mild chemical reduction graphene for three-dimensional architectures, Nanoscale 3 (2011) 3132-3137.

[31] Y. Tao, X. Xie, W. Lu, D.-M. Tang, D. Kong, Z. Huang, H. Nishihara, T. Ishii, B. Li, D. Golberg, F. Kang, T. Kyotani, Q.-H. Yang, Towards ultrahigh volumetric capacitance: Graphene derived highly dense but porous carbons for supercapacitors, Sci. Rep. 3 (2013) 2975.

[32] Y. Gogotsi, P. Simon, True performance metrics in electrochemical energy storage, Science 334 (2011) 917-918.

[33] Y. Xu, Z. Lin, X. Zhong, X. Huang, N. O. Weiss, Y. Huang, X. Duan, Holey graphene frameworks for highly efficient capacitive energy storage, Nat. Commun. 5 (2014) 4554.

[34] X. Yang, C. Cheng, Y. Wang, L. Qiu, D. Li, Liquid-mediated dense integration of graphene materials for compact capacitive energy storage, Science 341 (2013) 534-537.

[35] X. Feng, N. Chen, Y. Zhang, Z. Yan, X. Liu, Y. Ma, Q. Shen, L. Wang, W. Huang, The self-assembly of shape controlled functionalized graphene-MnO_2 composites for application as supercapacitors, J. Mater. Chem. A 2 (2014) 9178-9184.

[36] X. Feng, N. Chen, J. Zhou, Y. Li, Z. Huang, L. Zhang, Y. Ma, L. Wang, X. Yan, Facile synthesis of shape-controlled graphene-polyaniline composites for high performance supercapacitor electrode materials, New J. Chem. 39 (2015) 2261-2268.

[37] W. S. Hummers, R. E. Offeman, Preparation of graphitic oxide, J. Am. Chem. Soc. 80 (1958) 1339.

[38] B. Song, C. Sizemore, L. Li, X. Huang, Z. Lin, K. Moon, C.-P. Wong, Triethanolamine functionalized graphene-based composites for high performance supercapacitors, J. Mater. Chem. A 3 (2015) 21789-21796.

[39] H. M. Jeong, J. W. Lee, W. H. Shin, Y. J. Choi, H. J. Shin, J. K. Kang, J. W. Choi, Nitrogen-doped graphene for high-performance ultracapacitors and the importance of nitrogen-doped sites at basal planes, Nano Lett. 11 (2011) 2472-2477.

[40] C. Pelekani, V. L. Snoeyink, Competitive adsorption between atrazine and methylene blue on activated carbon: The importance of pore size distribution, Carbon 38 (2000) 1423-1436.

[41] Q. Du, M. Zheng, L. Zhang, Y. Wang, J. Chen, L. Xue, W. Dai, G. Ji, J. Cao, Preparation of functionalized graphene sheets by a low-temperature thermal exfoliation approach and their electrochemical supercapacitive behaviors, Electrochim. Acta, 55 (2010) 3897-3903.

[42] H. Gao, F. Xiao, C. B. Ching, H. Duan, High performance asymmetric supercapacitor based on graphene hydrogel and nanostructured MnO_2, ACS Appl. Mater. Interfaces 4 (2012) 2801-2810.

[43] Y. Wang, Z. Shi, Y. Huang, Y. Ma, C. Wang, M. Chen, Y. Chen, Supercapacitor devices based on graphene materials, J. Phys. Chem. C 113 (2009) 13103-1310.

CHAPTER III:

Study of Graphene Materials with Longer Alkyl Diamines as Pillars

Chapter III. Study of Graphene Materials with Long Alkyl Diamines as Pillars

1. Objectives & Approach

Learning from the conclusions of the previous chapter, work in this chapter focuses on synthesizing graphene hydrogels with longer alkyl diamines and possibly obtain a pillared graphene material with well-defined inter-layer separation (d-spacing). We aim to evaluate the possible layered structures in graphene derivatives as analogous to pores for charge storage. 1,5-Diaminopentane, 1,6-Diaminohexane and 1,8-Diaminooctane were chosen as the series of longer alkyl diamines (with 5, 6 and 8 Cs). Unlike the short diamines (C = 2, 4), addition of these longer alkyl diamines into aqueous GO solutions have resulted in immediate formation of coagulated gel like structures. Earlier report using such alkyl diamines has suggested that the poor solubility of the longer alkyl chains in aqueous GO solution may be the reason behind such coagulation.[32] It was suggested that the longer alkyl diamines (C = 5, 6, 8) could be dissolved in ethanol and used to react with GO.[32] However, addition of a new solvent to the aqueous GO solution would alter the ability of GO sheets to self-assemble into a monolith. While GO self-assembly in aqueous media is well-studied in the literature,[25] its behavior in co-solvents has not been explored extensively. At this point in the thesis, our primary focus was to study the ability of alkyl diamines to show pillaring (nanoscale assembly) of GO sheets. Hence, we chose to react ethanol solutions of diamines with aqueous solutions and address the formation of monolith (macroscale assembly) at a later stage. Since monolith formation was not a concern at the moment for this study, the reaction mixtures were continuously stirred throughout for homogeneity.

Another important observation from the study on short diamines was that the larger diamines are poor reducing agents, which result in low electrical conductivity of the synthesized materials. To address this issue, we proposed to perform an additional step of chemical reduction using hydrazine hydrate after the first reaction with alkyl diamines. However, reports in the literature make contradictory suggestions that such a step of chemical reduction might remove the alkyl diamines that are incorporated on GO sheets in the first step. Nevertheless, we chose to perform this two-step process of reaction with alkyl diamines and hydrazine hydrate (Scheme III-1).

The graphene-based materials obtained after the first reaction of GO with alkyl diamines are named as pillared graphene materials and abbreviated as 5 P, 6 P and 8 P depending on the alkyl diamine used. The materials obtained after the reduction of 5 P, 6 P and 8 Ps with hydrazine hydrate were named as reduced pillared graphene materials and abbreviated as 5 RP, 6 RP and 8 RP depending on the alkyl diamine used in the first step. Reduced graphene oxide was also synthesized as a control material by direct reduction of GO with hydrazine hydrate.

1. Alkyl diamine

2. Hydrazine hydrate
Continuous Stirring

Graphene oxide

Pillared graphene material

1,5-Diaminopentane

1,6-Diaminohexane

1,8-Diaminooctane
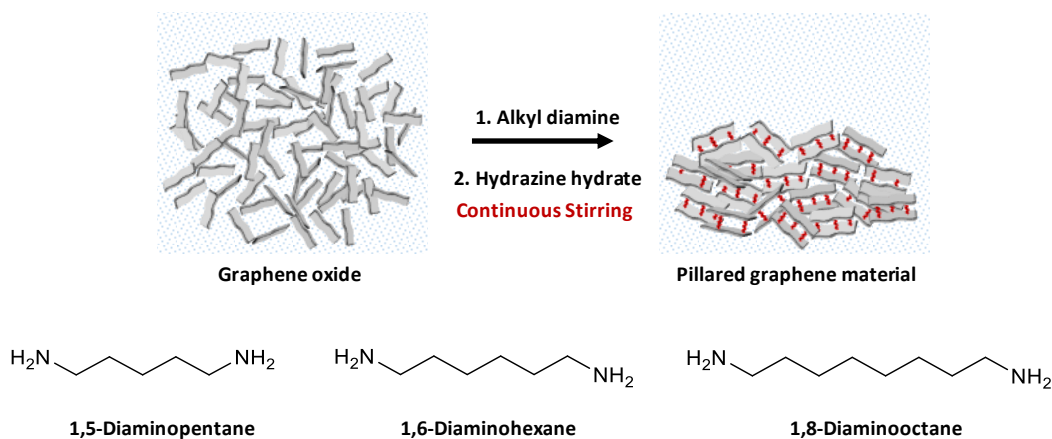
Scheme III-1 Schematic representation of the synthesis of pillared graphene materials.

The synthesized materials were characterized with various physicochemical characterization techniques and X-Ray diffraction analysis gave direct evidence of incorporation of diamines in between the GO sheets and allowed to quantify the inter-graphene sheet distance. Elaborate electrochemical analyses were performed on the materials in three-electrode cell-configuration to check if the synthesized pillared graphene screen ions based on ion sizes. This ion sieving study was performed by using a range of electrolytes with varying ion sizes. 1 M tetralkylammonium tetrafluoroborate (TAABF$_4$) salt solutions in acetonitrile with constant anion size and varying cation sizes; ethyl (TEA$^+$ - 0.68 nm), propyl (TPA$^+$ - 0.76 nm), butyl (TBA$^+$ - 0.82 nm), hexyl (THA$^+$ - 0.95 nm) were used as electrolytes.

The results obtained from the study were published as an article in the journal ''*Chemistry of Materials*'' (https://pubs.acs.org/doi/abs/10.1021/acs.chemmater.8b00759). The knowledge and the future perspectives gained from the article are described at the end of this article. FD and HB conceptualized the idea. HB performed experiments, and analysed data. YC, BD and SP helped with GO synthesis, BET and XRD analyses respectively. PS, OC, PLT and LD aided with analysis. HB and FD compiled the work and wrote the manuscript with inputs from all authors.

Ion Sieving Effects in Chemically Tuned Pillared Graphene Materials for Electrochemical Capacitors

Harish Banda,[†*] Barbara Daffos,[¶,‡] Sandy Périé,[†] Yves Chenavier,[†] Lionel Dubois,[†] David Aradilla,[†] Stéphanie Pouget,[†] Patrice Simon,[¶,‡] Olivier Crosnier,[§] Pierre-Louis Taberna[¶,‡] and Florence Duclairoir[†*]

† Univ. Grenoble Alpes, CEA, CNRS, INAC, SyMMES, Grenoble, 38000, France.

‡ CIRIMAT, Université de Toulouse, CNRS, INPT, UPS, 31062 Toulouse, France.

§ Institut des matériaux Jean Rouxel (IMN), Univ. de Nantes, CNRS, Nantes, 44300, France.

¶ Réseau sur le Stockage Electrochimique de l'Energie (RS2E), FR CNRS, 3459, France.

5 RP (d: 0.78 nm)

TBA⁺ (0.82 nm), BF₄⁻ (0.48 nm)
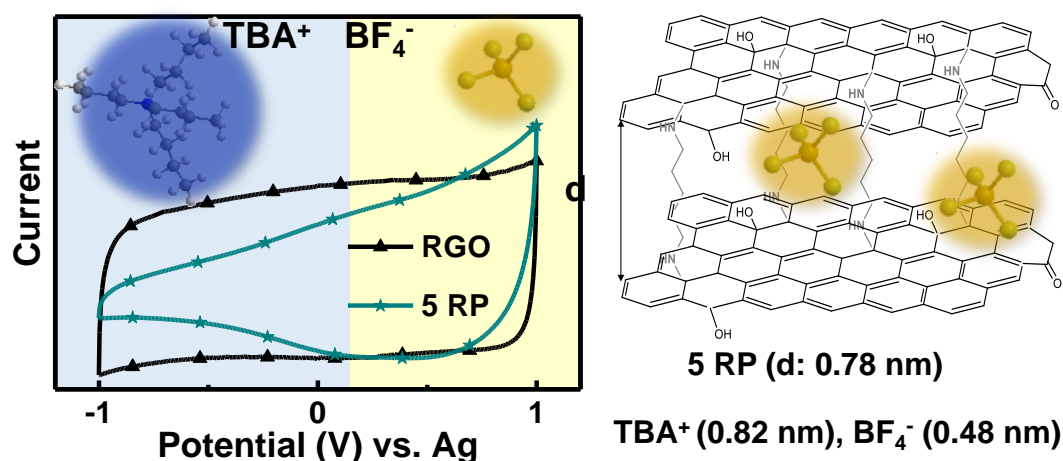
Abstract

Supercapacitors offer high power densities but require further improvements in energy densities for wide-spread commercial applications. In additional to the conventional strategy of using high surface area materials to enhance energy storage, recently, matching electrolyte ion sizes to material pore sizes is shown to be particularly effective. However, synthesis and characterization of materials with precise pore sizes remains challenging. Herein, we propose to evaluate the layered structures in graphene derivatives as analogous to pores and study the possibility of ion sieving. A class of pillared based graphene materials with suitable inter-layer separation were synthesized, readily characterized by x-ray diffraction, and tested in various electrolytes. Electrochemical results show that the inter-layer galleries could indeed sieve electrolyte ions based on size constrictions: ions with smaller naked sizes than the inter-

layer separation access the galleries whereas the larger ions are restricted. These first observations of ion-sieving in pillared graphene-based materials enable efficient charge storage through optimization of the d-spacing/ion size couple.

2. Introduction

Electrical double-layer capacitors, commonly known as supercapacitors (SCs), store energy through reversible adsorption of electrolytic ions on the charged electrode surfaces.[1] The non-faradaic nature of this charge storage enables supercapacitors to offer high power densities and long cycle life.[2] As an undesired consequence, the non-faradaic charge storage also results in typically low energy densities in SCs.[3] Hence, porous carbon materials (eg. activated carbons (ACs), templated carbons) with high specific surface areas (SSA) and good electrical conductivities are typically studied as electrode materials for improved energy densities.[4,5] However, the traditional beliefs about the high surface area of the material as the unique strategy for maximized charge storage needed reconsideration when complementary storage mechanisms were discovered in nanopores (< 1 nm).[6] Following the work by Aurbach et al. on selective electrosorption of ions based on size (ion sieving)[7], researchers have reported the capacitance contribution from these nanopores in SCs.[8,9] Extensive work on carbide-derived carbons (CDCs)[10] and ACs has since revealed that the nanopores offer more efficient charge storage by confining the electrolytic ions and thereby restricting excessive charge screening by solvent molecules.[4,11] These studies also revealed that the ions access such narrow pores by shedding a part of their solvation spheres.[12,13] Recent studies using electrochemical quartz crystal microbalance (EQCM)[14] and nuclear magnetic resonance (NMR) techniques have quantitatively confirmed such desolvation.[15,16]

Several reports have since studied charge storage in nanopores and proposed that the maximum specific capacitances are obtained when ion sizes and pore sizes match.[17,18] Particularly, it was also shown that a narrow pore size distribution (PSDs) of a carbon material is essential for such observations.[19] However, only a few carbons, such as CDCs and some ACs, display narrow PSDs.[4] Furthermore, reliable determination of PSDs from gas adsorption studies still remains a difficulty as the density functional theory based approaches require prior knowledge of the pore geometry and heat of adsorption of the material.[4] To that end, combinations of characterization and modeling techniques using NMR and small-angle X-ray scattering are being used to allow unambiguous pore size and geometry determination.[20-22] In parallel, research on graphene derivatives for SCs has shown potential owing to their high surface areas, electrical conductivities and mechanical flexibilities.[23,24] However, in the context

of material porosity for charge storage, much of the current research in graphene derivatives is devoted to improving the morphology with a focus on inter-particular porosity[25], similar to the research on ACs. Surprisingly, little attention has been devoted towards exploring the unique layered structures of graphene derivatives in SCs. Although the natural graphitic spacing of 0.33 nm, defined as intrinsic intra-particular pore, could be narrow for some ions in SCs, graphene derivatives are known to exhibit expanded layered structures, (extrinsic intra-particular pores).[26] These expanded layered structures could be precisely tuned and the d-spacing values describing inter-layer distances could readily be evaluated using X-ray diffraction (XRD). Recent study on electrochemically exfoliated graphene oxide (GO) films showed enhanced capacitances when the d-spacing matches the ion sizes. This *in situ* study offers a proof of concept for impact of d-spacing in SCs but the low capacitance values of ~ 1 F g^{-1} mandate further improvements.[27] Few other reports have studied pillared graphene materials in SCs but the enhanced performances could only be related to improved hierarchical porosity.[28,29]

In this context, herein, we study the electrosorption of ions in pillared graphene materials with varied inter-layer distances. An analysis of such materials would test the possibility of ion sieving and, thereby, ion confinement in the inter-layer galleries for an efficient charge storage. A class of materials using GO as precursor and alkyl diamines as covalent pillars were synthesized and then chemically reduced to yield suitable electrical and morphological characteristics for SCs. XRD patterns of the synthesized materials gave evidence of the expanded structures with determination of the respective d-spacing values. Extensive electrochemical characterization was performed in SCs using electrolytes containing constant anion but varied cation sizes. The observed electrochemical responses clearly show limitations in ion adsorption based on size constrictions and a direct correlation between d-spacing values and ion sizes was noted. These first results of ion sieving in pillared graphene materials could help us readily design and develop materials for optimized charge storage in SCs.

3. Materials & Characterization

3.1 Material Design

GO has long been studied as a perfect precursor for various graphene-like materials, thanks to its surface functionalities that offer abundant chemical tunability.[30] GO is characterized with randomly distributed oxygen-containing functional groups and it is believed that the epoxy and hydroxyl groups lie above and below each layer whereas the carboxylic groups are on the edges.[31] This rich surface chemistry allows covalent bonding of GO sheets with an organic linker. Particularly, a bi-functional linker bearing its reactive functions at both ends is used to cross-link two sheets together.[32] For example, alkyl diamines, very reactive towards epoxide groups, have been shown to be effective in forming pillared materials with tunable inter-layer distances.[32,33] Hence, we use diamines with varied alkyl chain lengths (C = 5, 6 and 8) to obtain the necessary d-spacing values for this study. GO is electrically insulating and reaction with the alkyl diamines couldn't ensure high enough electrical conductivities of these pillared materials.[34] The obtained materials are thus chemically reduced using hydrazine to synthesize reduced pillared materials (RPs). Depending on the diamine used in the first step, RPs are named as 5 RP (1,5-diaminopentane), 6 RP (1,6-diaminohexane) and 8 RP (1,8-diaminooctane) (Scheme III-2). As a control, reduced graphene oxide (RGO) is also made by direct reduction of GO. Notably, as the GO precursor is not specifically treated to obtain single GO sheets, it is likely that each graphene layer in the synthesized materials consist few sheets rather than a single graphene sheet.
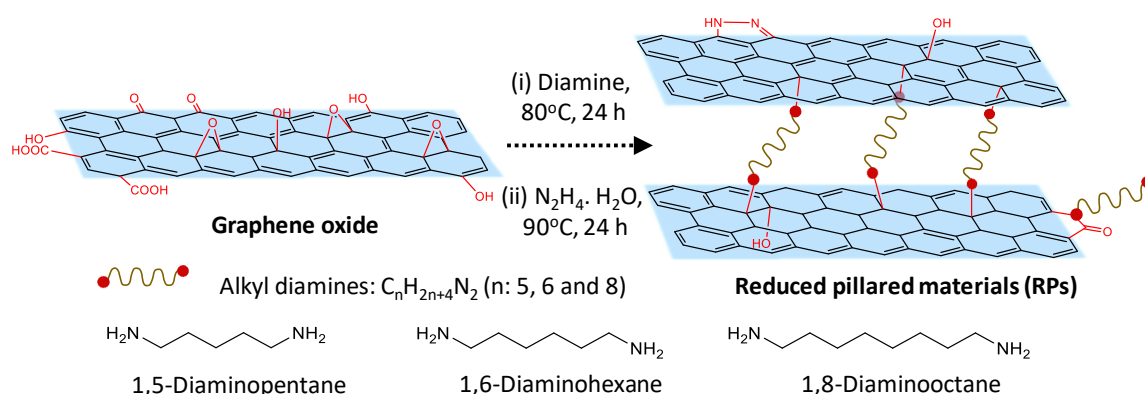
Scheme III-2 Schematic representation for the synthesis of RPs. For simplicity, the materials are depicted with single graphene sheets.

3.2 Characterization

The physicochemical properties of the synthesized materials were characterized using various techniques and the porosity characteristics were analyzed using scanning electron microscopy (SEM) and gas sorption studies. The thermal degradation responses of the materials were obtained using thermogravimetric analysis (TGA) and are shown in Figure III-1a. Consistent with previous reports[30,35], GO displays a two-step weight loss profile with the first removal of the adsorbed water occurring below 100°C and an abrupt weight loss around 200°C corresponding to decomposition of surface oxygen functional groups. Additionally, a steady loss beyond 200°C is also seen owing to gradual removal of stable functionalities. Upon reacting GO with hydrazine, the abrupt weight loss and moisture removal are no longer seen, suggesting an efficient chemical reduction. Synthesized with a two-step process, RPs also show no removal of moisture or oxygen functionalities but exhibit a gradual weight loss between 300-500°C. Such gradual weight losses at temperatures above the boiling points of the respective diamines are attributed to the removal of non-labile diamine species.[35] Hence, TGA shows presence of diamine linkers and an absence of labile oxygen functional groups in RPs. Furthermore, a careful analysis of the weight losses identifies similar diamine grafting densities in all the three RPs (Table III-1).
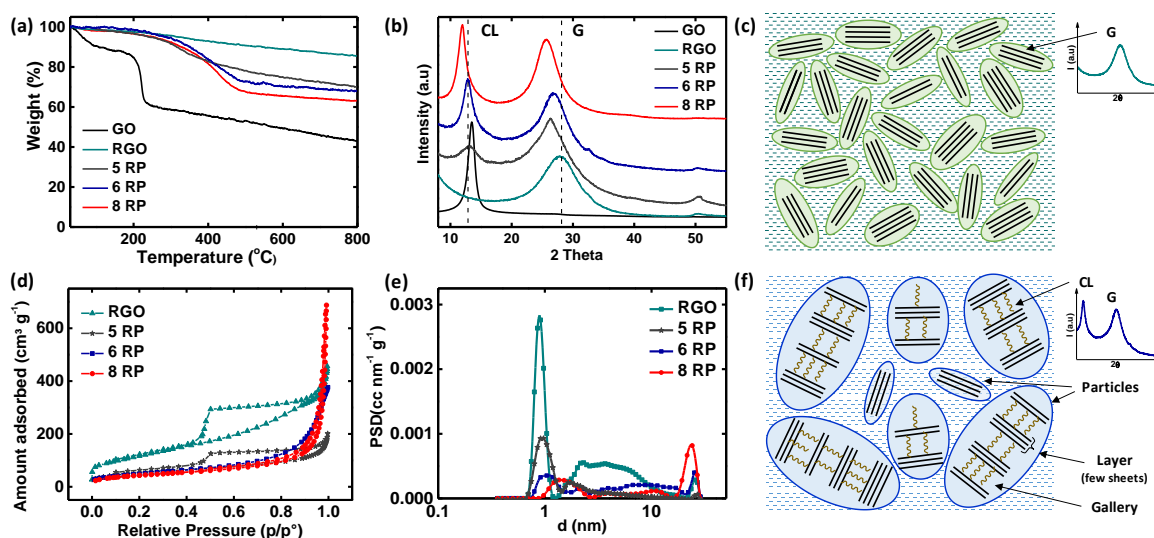
Figure III-1 (a) Thermal gravimetric analyses (5o°C/min) under N_2 atmosphere and (b) X-Ray diffraction patterns of the synthesized materials. The two different regions in XRD are attributed to graphitic (G) and cross-linked (CL) domains. (c) RGO is schematically represented with G domain and, (f) 6 RP is shown with both G and CL domains. (d) N_2 sorption isotherms recorded at 77 K and (e) pore size distributions calculated using non-local density functional theory for RGO and RPs.

Material	TGA Analyses			XPS - Elemental Composition			XRD Analyses		BET Analyses
	Wt. loss (%)[a]	Wt. loss with RGO as Ref.[b]	Grafting density[c]	C %	O %	N %	d (Å) G	d (Å) CL	Specific Surface Area (m^2.g^{-1})
GO	43	-	-	74.7	25.3	-	-	7.6	
RGO	14	-	-	91.2	4.5	4.3	3.7	-	330
5 RP	31	17	0.16	86.5	8.0	5.3	3.9	7.8	138
6 RP	33	19	0.15	86.8	7.6	5.4	3.9	8.0	130
8 RP	37	23	0.16	86.8	7.6	5.5	4.0	8.6	108

Table III-1 Thermal gravimetric weight loss values, elemental composition values from X-ray photoelectron spectroscopy and d-spacing obtained from X-ray diffraction spectra for the synthesized materials. The grafting densities of the diamines in different RPs were calculated by normalizing TGA weight losses with respect to RGO and dividing by the respective diamine molecular weights. [a]Weight losses at 800°C were used for this calculation assuming that all the diamines in RPs would be degraded by this temperature. [b]Weight losses in RPs normalized with RGO as baseline. [c]Adjusted weight loss of RPs were divided by the respective diamine molecular weights for a comparison of the amounts of diamine.

X-ray photoelectron spectroscopy (XPS) was performed to analyze the surface elemental composition of the synthesized materials. The survey spectra of the materials indicate presence of C, N and O elements with GO showing significantly higher O and lower N intensities compared to others (Figure III-2a). High resolution C 1s spectra of the materials show two main peaks at 284.5 and 286.5 eV for GO whereas RGO and RPs have a single main peak at 284.5 eV (Figure III-2b). The observed C 1s signals were deconvoluted and assigned as C=C/C-C (284.5 eV), C-OH (285.9 eV), alkoxy/epoxy (286.5 eV) and carbonyl components (288.3 eV) based on earlier reports (Figure III-3).[30] GO exhibits a highly oxidized nature with
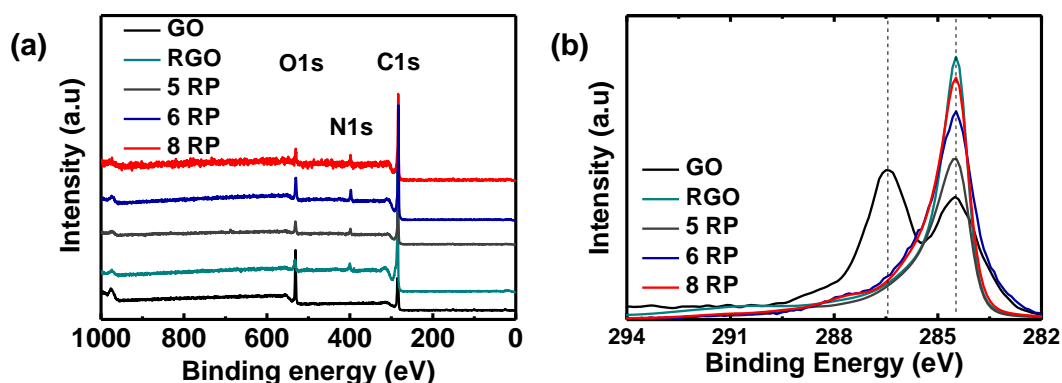
Figure III-2 X-ray photoelectron (a) survey scans and (b) C 1s high-resolution spectra of GO, RGO and RPs. The spectra indicate presence of C, N and O elements in the materials with GO showing significantly higher O intensities compared to others.

presence of various oxygen containing functional groups and the predominant peak corresponding to alkoxy-epoxy groups (Figure III-3a). Whereas, RGO and RPs show significant decrease in oxygen functionalities and the predominant peak is assigned to C=C/C-C carbons (Figure III-3b-e). In addition, a new peak at 285.6 eV corresponding to C-N was observed.
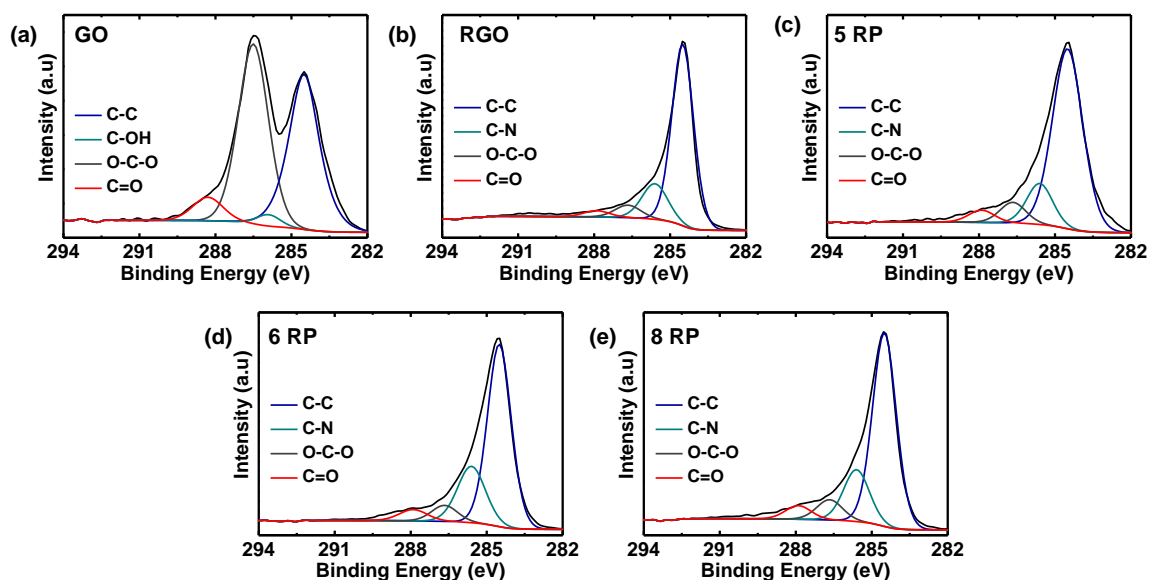
Figure III-3 C 1s high-resolution X-ray photoelectron spectra of (a) GO, (b) RGO, (c) 5 RP, (d) 6 RP and (e) 8 RPs. The signals from C atoms in different chemical environments are deconvoluted as C-C/C=C (284.5 eV), C-N (285.6 eV), C-OH (285.9 eV), epoxy/alkoxy (286.5 eV) and carbonyl groups (288.3 eV).

The surface elemental compositions obtained from survey spectra show a decrease in O content from 26% in GO to 4-8% in RGO and RPs with an additional incorporation of 4-6% N (Table III-1). These observations indicate efficient reduction of oxygen functionalities and incorporation of N groups into RGO and RPs. High resolution N 1s spectra reveal a very weak signal for GO and clear peaks, with varied positions, for RGO and RPs (Figure III-4). Deconvolution of N spectra could explain this shift in peak positions and the differences in N content between RGO and RPs. As evoked in the literature, the diamines could react and form covalent linkages with GO, resulting in amine N (399.2 eV), and instigate further internal rearrangements forming pyridinic (398.2 eV), pyrrolic (400.2 eV) and graphitic N (401.5 eV) components.[35] RGO shows a typical abundance of N in pyrrolic and graphitic rings owing to the strong reducing nature of hydrazine. Whereas, RPs have a major contribution from amine N, owing to the incorporation of diamines, and thus show a shift in the peak position compared to RGO. These results reaffirm the presence of covalently linked diamines in RPs as also seen from TGA.
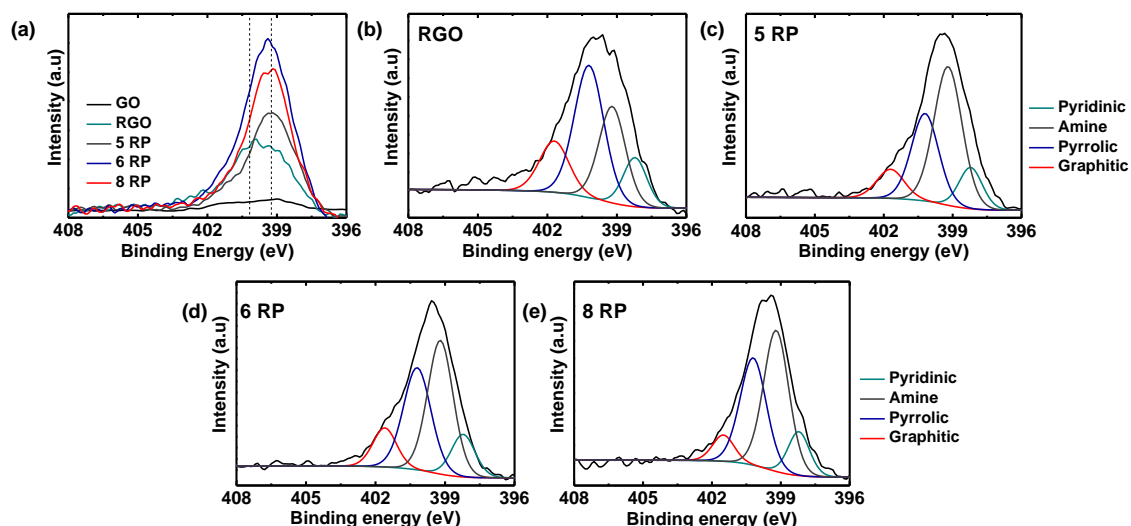
Figure III-4 N 1s high-resolution X-ray photoelectron spectra of GO, RGO and RPs. Deconvolutions of high-resolution N 1s signal into pyridinic (398.2 eV), amine (399.2 eV), pyrrolic (400.2 eV), and graphitic (401.5 eV) components for (b) RGO, (c) 5 RP (d) 6 RP and (e) 8 RP.

XRD patterns were obtained to directly analyze the layered structures of the synthesized materials (Figure III-1b). Freeze-dried GO shows a sharp peak at 13.5° related to a d-spacing of 7.6 Å, indicating a high degree of oxidation in the starting material. RGO displays a broad peak at 28° corresponding to a graphite-like pattern (002), suggesting partial re-stacking of graphene sheets due to the removal of oxygen functionalities during chemical reduction. Synthesized in a two-step process, RPs exhibit diffraction patterns with two distinct peaks around 25-27° and 11-13° each. The broad peaks at higher angles correspond to graphite-like partial re-stacking and indicate a reduction degree close to that of RGO. The relatively sharper peaks at lower angles show gradual increase in d-spacing from 7.8 Å (5 RP), 8.0 Å (6 RP) to 8.6 Å (8 RP) with increasing lengths of diamines used. Earlier studies have attributed these peaks to the expanded layered structures caused by intercalation of diamines in between the graphene layers.[32] Although the d-spacing values relate to the diamines used, an exact prediction of d-spacing based on alkyl chain lengths is difficult to obtain as it requires knowledge about local orientation and conformation of diamines.[32] Additionally, the increased d-spacing values demonstrate intercalation of the linker between the graphene layers, but do not confirm their covalent cross-linking. Swelling experiments were proposed in the literature as an indirect way to analyze the cross-linking of the graphene layers.[32,33] If the RPs were covalently linked by the diamine, they should resist swelling by solvents. XRD patterns of 8 RP after soaking overnight in ethanol-water solution remain unchanged and

confirm that the intercalated diamine indeed covalently cross-links the layers (Figure III-5a) as already hinted by TGA and XPS. In a parallel test with GO (Figure III-5b), visible swelling and shift in XRD peak positions is seen just after few minutes in solvent and thus highlighting the lack of cross-linking.
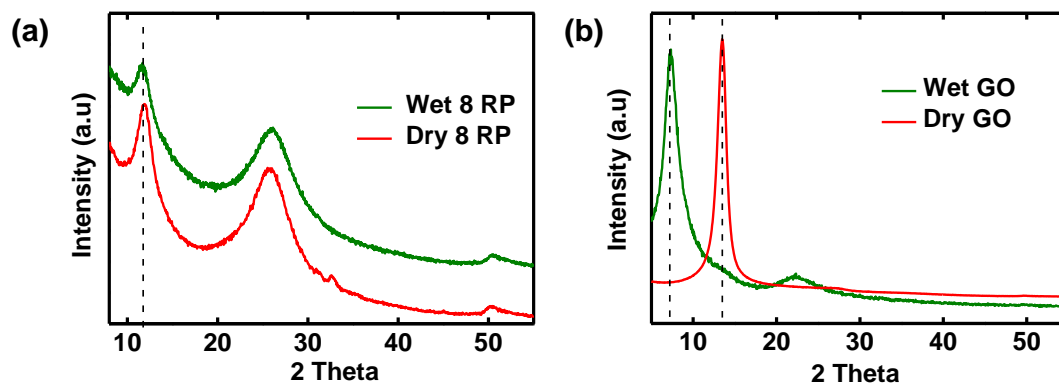
Figure III-5 (a) X-Ray diffraction spectra of 8 RP before and after soaking in 80% ethanol-water solution for overnight, (b) X-Ray diffraction spectra of GO before and after soaking in 80% ethanol-water solution for 5 minutes. Even after soaking overnight in ethanol-water solution, XRD pattern of 8 RP remains unchanged confirming that the presence of covalent crosslinks between the sheets. Visible swelling and shift in XRD peak positions is seen in GO after just few minutes in solvent and thus highlighting the lack of cross-linking.

To summarize, the synthesized materials could possess two different domains corresponding to graphitic-like (G) and cross-linked (CL) arrangements. The G domains are attributed to partially stacked graphene sheets with d-spacing of ~ 3.5 - 4.0 Å whereas, CL domains relate to cross-linked graphene layers and are characterized with d-spacing values of 7.8 - 8.6 Å. RGO, synthesized as a control material, only has the G stacking of the sheets (Figure III-1c) whereas, RPs have both G and CL domains co-existing in a random manner (Figure III-1f). Additionally, the CL peaks in RPs could be seen to become narrow from 5 RP to 8 RP with larger diamines used (Figure III-1b). These sharper peaks with increased alkyl chain lengths probably arise from improved flexibilities of diamines, which enable formation of larger particles. Hence, the CL peaks in XRD patterns evidence formation of expanded layered structures and also suggest varied particle sizes between RPs.

SEM images show porous morphology for RGO and RPs without any obvious differences (Figure III-6). The observed morphologies were then analyzed by N_2 sorption isotherms recorded at 77 K and the SSA and PSDs were obtained using 2D non-local density functional theory (NLDFT)[36,37] (details in materials and methods). The synthesized materials exhibit type II adsorption-desorption behavior with a hysteresis loop indicating presence of micro and mesopores (Figure III-1d).29 RGO has the highest SSA of 330 $m^2.g^{-1}$ whereas RPs display lower
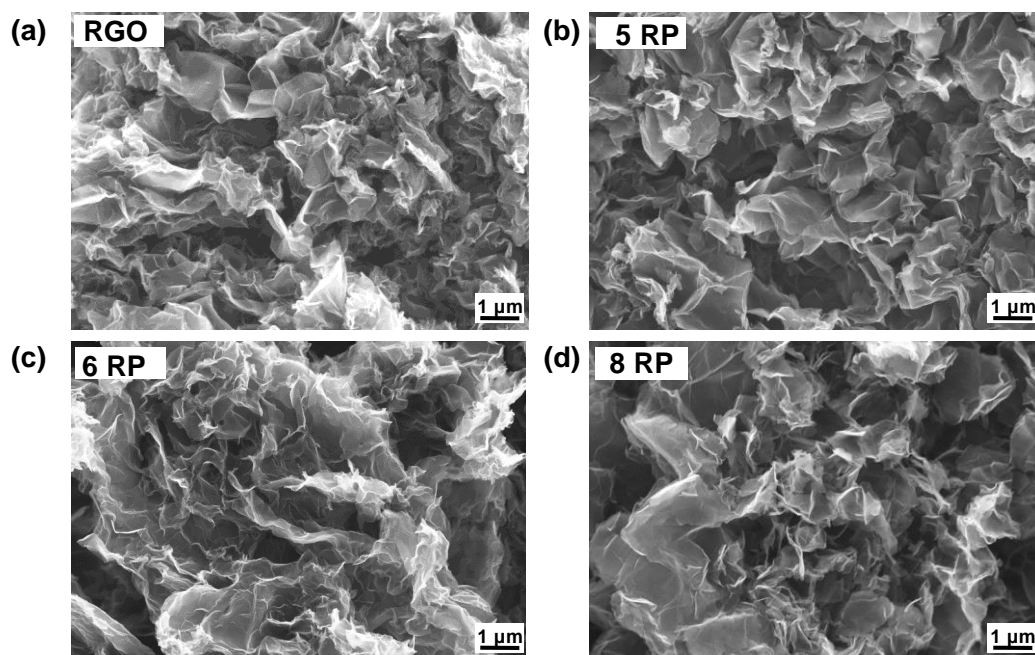
Figure III-6 Scanning electron microscopy images of (a) RGO, (b) 5 RP, (c) 6 RP and (d) 8 RP.

SSA values with de-creasing values from 138 $m^2.g^{-1}$ in 5-RP to 130 $m^2.g^{-1}$ in 6-RP and 108 $m^2.g^{-1}$ in 8-RP (Table III-1). The observed lower surface areas in RPs compared to RGO are attributed to two plausible reasons; (i) diamines increase the overall inactive weight of RPs and (ii) the diamine pillars may sterically hinder the gas sorption and the inter-layer gallery pores are rendered as closed pores.[38] If the inter-layer galleries indeed act as closed pores, surfaces of the graphene layers in the CL arrangement would be inaccessible and result in such lower SSA values. The calculated PSDs shows significant contribution from micro pores and presence of mesopores in RGO whereas the PSDs for RPs vary with diamines used (Figure III-1e). All RPs possess both types of pores but with increasing chain lengths the micro pore content decreases and the mesopores increase. This could be explained by the XRD patterns which suggested larger particle sizes in RPs with larger diamines to result in such mesoporosity.

The above characterization techniques describe RPs as reduced, covalently linked and morphologically suitable for application in SCs. TGA, XRD and XPS showed presence of diamines while the swelling experiments provide evidence for the cross-linking. SEM and gas sorption analyses attribute a porous morphology to RPs and the PSD curves indicate predominant presence of pores > 1 nm with little or no contribution from smaller pores. The dearth of such nanopores highlights RPs as ideal materials to study the distinct impact of inter-

layer galleries on SCs performances. Furthermore, the cross-linked galleries have d-spacing values in the range of sizes of common electrolyte ions offering a good template for SC studies.

4. Electrochemical studies

The ion sieving behavior of these reduced pillared graphene materials was studied in SCs by using a range of electrolytes with varying ion sizes. 1 M tetralkylammonium tetrafluoroborate (TAABF$_4$) salt solutions in acetonitrile with constant anion size and varying cation sizes; ethyl (TEA$^+$ - 0.68 nm), propyl (TPA$^+$ - 0.76 nm), butyl (TBA$^+$ - 0.82 nm), hexyl (THA$^+$ - 0.95 nm) were used as electrolytes. A three-electrode configuration in SCs was adapted to study the individual electrode responses. Cyclic voltammograms (CVs) were acquired by scanning the cells from open-circuit potential (OCV ~ 0.1 V) to positive and negative terminal potentials separately to record the distinct anion and cation sorption responses. For ease of comparison, all CVs are normalized with the respective currents at 0.1 V vs. Ag and the curves are de-noted with their respective d-spacing values; 5 RP – 0.78 nm, 6 RP – 0.80 nm and 8 RP – 0.86 nm.

Figure III-7 shows the CVs obtained for RGO and RPs in various TAABF$_4$ electrolytes at a scan rate of 20 mV.s^{-1} in the potential range from -1.0 to 0.1 V vs. Ag. These scans from OCV to negative potentials mainly relate to the adsorption/desorption responses of TAA$^+$ cations. When tested with TEABF$_4$ electrolyte (Figure III-7a), all the materials showed nearly rectangular curves with no specific features suggesting an ideal double layer charge storage mechanism. Upon using a slightly larger cation with TPABF$_4$ electrolyte (Figure III-7b), the CV curves of the materials remain comparable except for 5 RP, which indicates a slight reduction in current at the negative terminal potential. Moving to an even larger cation in TBABF$_4$, both 5 RP and 6 RP show a steep reduction in current at lower potentials whereas 8 RP remains mostly unchanged (Figure III-7c). Finally, when the largest cation is tested using THABF$_4$, all the RPs display significantly decreased currents (Figure III-7d). Moreover, the asymmetric shapes of CVs indicate that these limitations in currents at negative terminal potentials are not consequences of poor electrical or ionic conductivities. In turn, the behavior of RGO remains nearly unchanged regardless of the electrolyte used. The above data clearly suggests an explicit dependence of electrochemical responses from RPs based on the size of cations used. This tunable ion accessibility in RPs highlights them as sufficiently rigid layered structures which can restrict ions that are larger than d-spacing. As already evidenced by TGA,

XPS and XRD, covalent interaction between graphene and diamines is likely to be responsible for this electrochemical behavior.
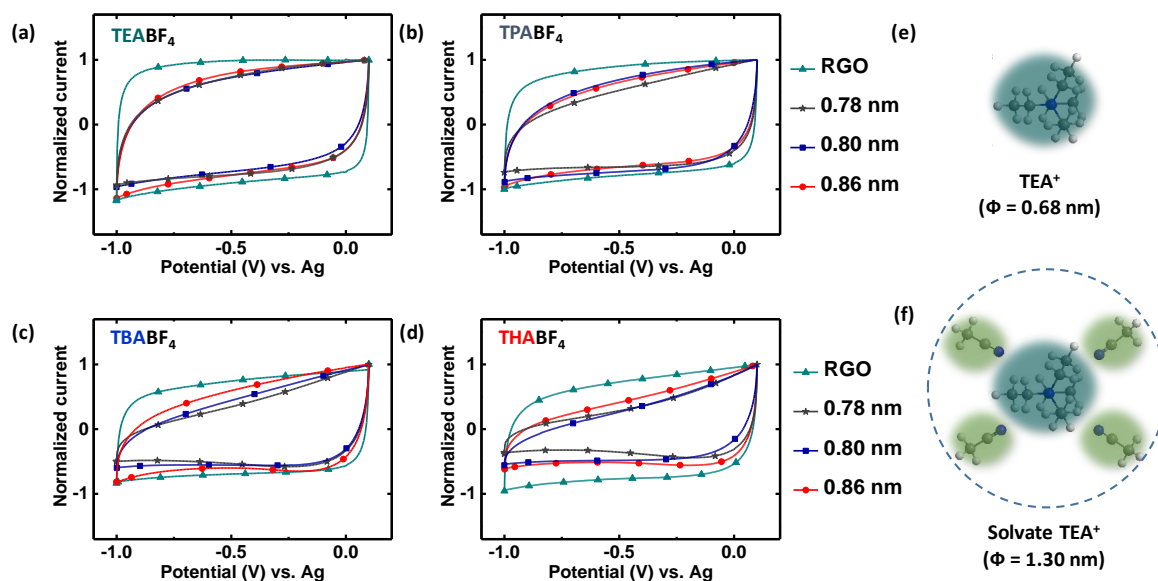
Figure III-7 Normalized CVs of RGO and RPs obtained at a scan rate of 20 mV.s⁻¹ in the voltage range of 0.1 V to -1.0 V vs. Ag using 1 M solutions of (a) TEABF₄ (Φ= 0.68 nm), (b) TPABF₄ (Φ= 0.76 nm), (c) TBABF₄ (Φ= 0.82 nm), and (d) THABF₄ (Φ= 0.95 nm) in acetonitrile as electrolytes. (e) and (f) show the naked and solvated TEA⁺ species and their diameters respectively. The chosen voltage window maintains negative polarization in the materials and ensures adsorption and desorption of mainly the cation.

Studies on CDCs have noted such reduction in currents i.e. the limitations in ion adsorption, when the naked electrolyte ions are larger than the average pore sizes.[11] In the current study, though we observe similar ion limitation, gas sorption results have indicated dearth of pores that are smaller than the cations tested. However, as evoked earlier, the gas sorption studies may deem the inter-layer gallery pores in RPs as closed pores which, nevertheless, could be accessible to ion adsorption under polarization. Hence, the d-spacing values of RPs were directly compared with the naked ion sizes by plotting the electrochemical data as responses for each material (Figure III-8). 5 RP, with a d-spacing of 0.78 nm, shows a regular CV in TEA⁺ (0.68 nm) but an increasing limitation in ion adsorption is seen from TPA⁺ (0.76 nm) to THA⁺ (0.95 nm) (Figure III-8a). 6 RP is characterized with a d-spacing of 0.80 nm and it allows TEA⁺ or TPA⁺ but limits TBA⁺ and THA⁺ cations (Figure III-8b). 8 RP behaves similarly by limiting THA⁺ that is larger than its d-spacing of 0.86 nm (Figure III-8c). These observations clearly show that the cations are limited in RPs when the naked ion sizes are larger than the inter-layer distances. Conversely, the cations enter the gallery pores of RPs when their naked ion sizes are smaller (Figure III-7e). Meanwhile RGO shows no limitations indicating that ion adsorption

occurs only in the inter-particular porosity (Figure III-8a). Additionally, RGO shows perfect rectangular curves compared to RPs probably due to its superior electrical and ionic conductivities owing to lack of diamine residues.[35]

Figure III-8 Normalized CVs of (a) RGO (b) 5 RP (d = 0.78 nm), (c) 6 RP (d = 0.80 nm) and (d) 8 RP (d = 0.86 nm) obtained using various 1 M TAABF₄ / acetonitrile electrolytes at a scan rate of 20 mV.s⁻¹ in the voltage range of -1.0 V to 0.1 V vs. Ag. RGO lacks nanopores or cross-linked interlayer galleries and hence does not show any specific limitation to TAA⁺ cations.

The electrosorption behavior of BF_4^- anions was analyzed by performing CVs in the positive voltage window from 0.1 V to 1.0 V vs. Ag (Figure III-9). Unlike the behavior under negative polarization, RGO and RPs both show nearly rectangular curves in all the electrolytes indicating no limitation for BF_4^- anion. CVs were then recorded in the full potential window of -1.0 to 1.0 V vs. Ag and were shown to correspond to the behavior of each material in different electrolytes (Figure III-10). RGO shows identical half curves on both sides of the OCV, suggesting no specific difference for TAA⁺ or BF_4^- adsorption (Figure III-10a). RPs also display identical half curves when both naked ion sizes are smaller than the d-spacing values but if the cation size is larger, a clear distinction could be seen between the two halves of a CV. For instance, 6 RP shows ideal CV curve with TEABF₄ but distinct anion and cation adsorption are seen in TBABF₄ and THABF₄ electrolytes (Figure III-10c). The naked BF_4^- anion is smaller than the cross-linked galleries in RPs (Figure III-9e) and is not limited, whereas the TAA⁺ cations vary in size from 0.68 nm to 0.95 nm and their adsorptions are limited based by size constrictions.

Hence, these observations confirm that the inter-layer galleries in pillared graphene materials indeed sieve ions based on sizes. Furthermore, the durability of the diamine pillars was tested by cycling 8 RP in THABF$_4$ electrolyte (Figure III-11). CVs at 50th and 500th cycles show identical limitation for THA$^+$ cations and the XRD patterns for the electrode before and after cycling remains similar (Figure III-11b&c). Particularly, the presence of the CL peak at around 12° before and after cycling confirms the retention of the pillars. Beside the characterization conducted on the material, these electrochemical analyses performed under the influence of polarization are an additional proof for the successful covalent anchoring of the diamine on graphene. Otherwise, if the diamines were rather held with non-covalent interactions, polarization of the electrodes during cycling would lead to their release and to a structural change.
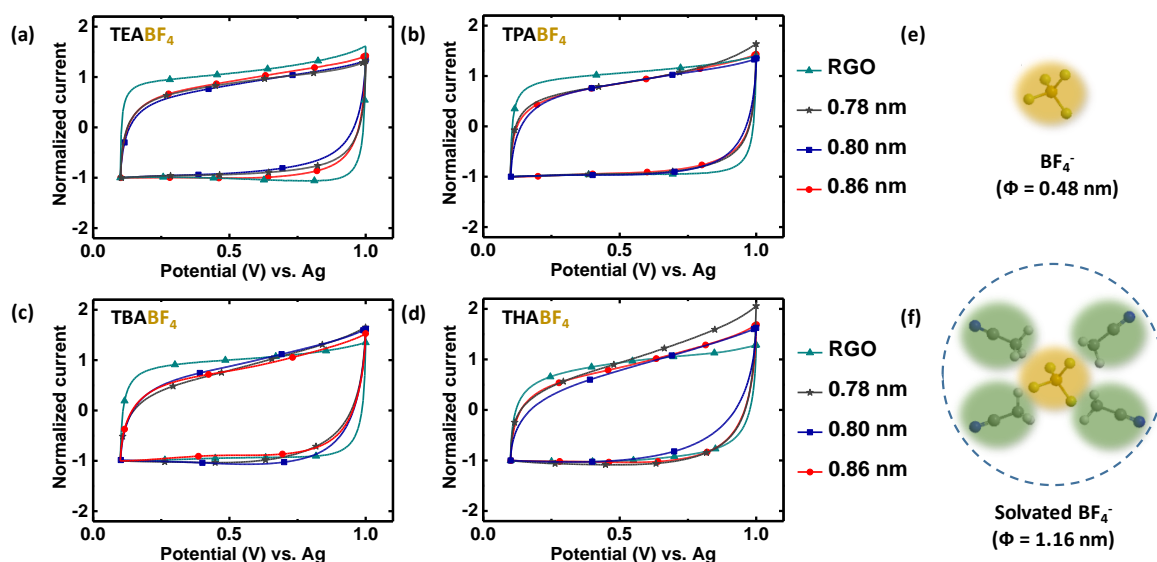
Figure III-9 Normalized CVs of RGO and RPs obtained at a scan rate of 20 mV.s^{-1} in the voltage range of 0.1 V to 1.0 V vs. Ag using 1 M solutions of (a) TEABF$_4$ (b) TPABF$_4$, (c) TBABF$_4$, and (d) THABF$_4$ in acetonitrile as electrolytes. (e) and (f) show the naked and solvated BF$_4^-$ species and their diameters respectively. The chosen voltage window maintains positive polarization in the materials and ensures adsorption and desorption of mainly the anion.

The direct relation between the naked ions and the d-spacing values of RPs raises interesting aspects about the ion adsorption in gallery pores. Typically, an ion exists as a solvated species in a solution and the solvation number, thus the solvated radii, depends on its interactions with the solvent.[11] In the current study, all the solvated TAA$^+$ (TEA$^+$ - 1.30 nm) and BF$_4^-$ ions (BF$_4^-$ - 1.16 nm) are larger than the inter-layer distances in RPs and thus they could only access the gallery pores by partially shedding their solvation shells (Figure III-7f & Figure III-9f). In fact, earlier work on porous carbons have shown that the solvated electrolyte ions indeed

enter smaller pores as partially desolvated ions.[15] Herein we speculate a similar partial desolvation for ions in the gallery pores of RPs. However, advanced characterization using

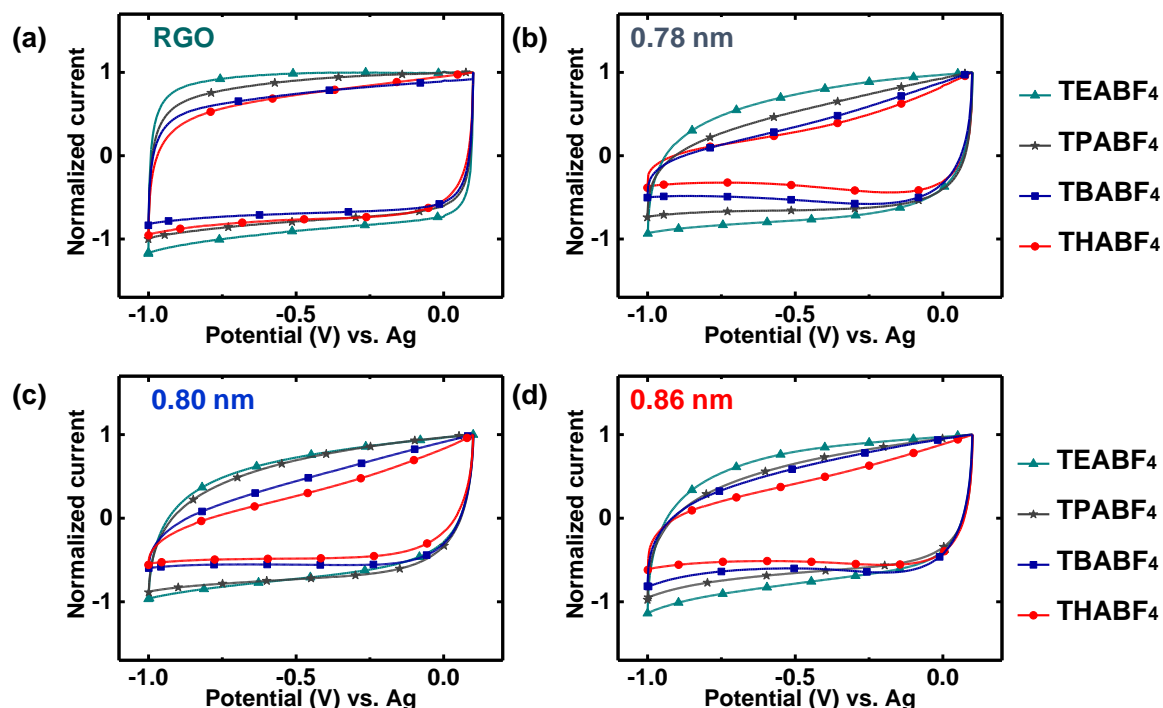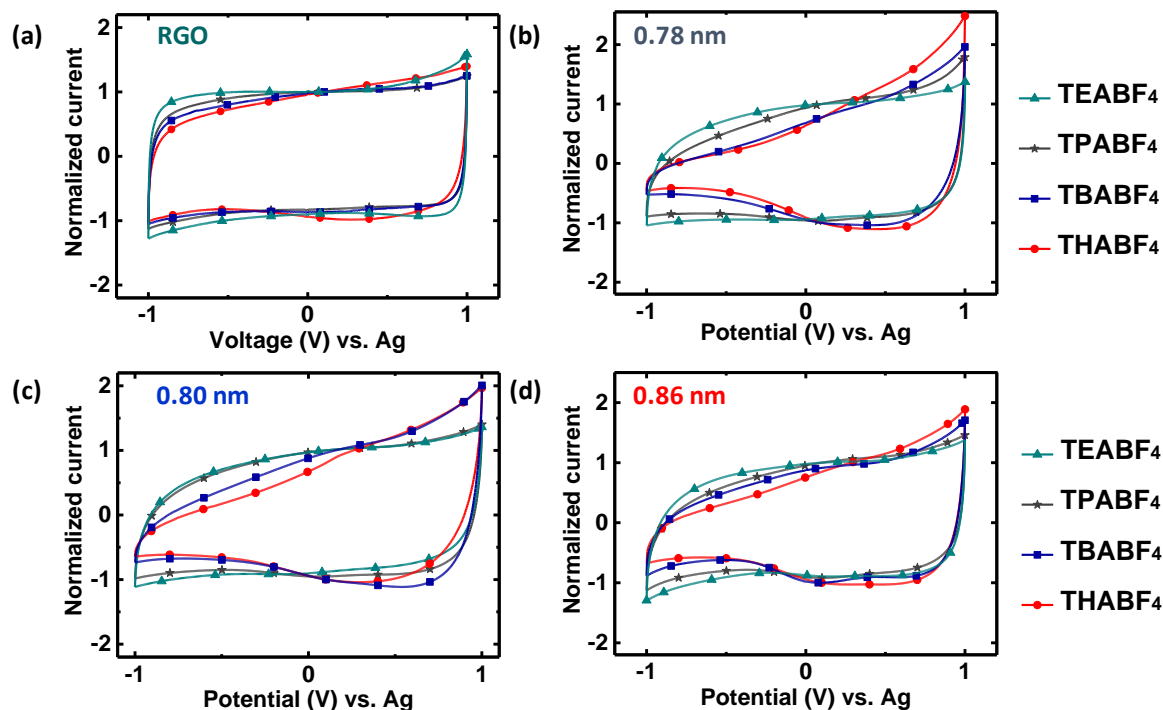*Figure III-10 Normalized CVs of (a) RGO (b) 5 RP (d = 0.78 nm), (c) 6 RP (d = 0.80 nm) and (d) 8 RP (d = 0.86 nm) obtained using various 1 M TAABF4 / AN electrolytes at a scan rate of 20 mV.s-1 in the voltage range of -1.0 V to 1.0 V vs. Ag. RGO lacks pores or inter-layer galleries spacing below 1 nm and hence doesn't show any specific limitation to TAA+ cations.*

EQCM and NMR techniques are required to quantitatively confirm this partial desolvation.

Specific capacitances of RPs were calculated for both the anion and cation adsorption from CVs at 20 mV.s^{-1} (Figure III-12). For the cation adsorption, RGO exhibits close capacitance values around 100 F.g^{-1} in all the four electrolytes underlining similar accessible electrochemical surface areas (Figure III-12a). In turn, RPs show comparable capacitances around 120 F.g-1 in TEABF$_4$ and exhibit lower capacitances when the cations could no longer be adsorbed in the gallery pores. For instance, 5 RP performs similar to the other RPs in TEABF$_4$ but exhibits a steep decline in capacitances from TPABF$_4$ to fractional values in THABF$_4$. 6 RP and 8 RP, possess larger d-spacing values and thus show a decline starting with TBABF$_4$ and THABF$_4$ respectively. Notably, even with this ion limitation in RPs, some charge will always be stored rather than none as the inter-particular pores and the bulk porosity in the materials are still accessible for ion sorption. For the anion adsorption, RGO shows similar capacitance values of about 100 F.g^{-1} in the four electrolytes (Figure III-12b). Since the anions are not

limited, RPs also exhibit close values in each electrolyte with a general trend of lower capacitances from TEABF$_4$ to THABF$_4$ electrolytes. Furthermore, the specific capacitances obtained in the full voltage window of -1.0 to 1.0 V vs. Ag mirror the results seen for cations (Figure III-13). RPs, with one third of SSAs compared to RGO, exhibit capacitances of about 130 F.g^{-1} in TEABF$_4$, close to that of RGO, and emphasize that the gas sorption analyses do not probe inter-layer gallery pores in RPs and hence underestimate the overall electrochemically active surface area available. In other electrolytes, RPs exhibit a decline in capacitances from TPABF$_4$ to THABF$_4$ as the cation limitation becomes increasingly substantial. The overall lower capacitances of RPs compared to RGO could also arise from a couple of reasons; the incorporated alkyl chains contribute to 20% increase of weight in RPs, and RPs possess lower inter-particular micro pore volume compared to RGO.
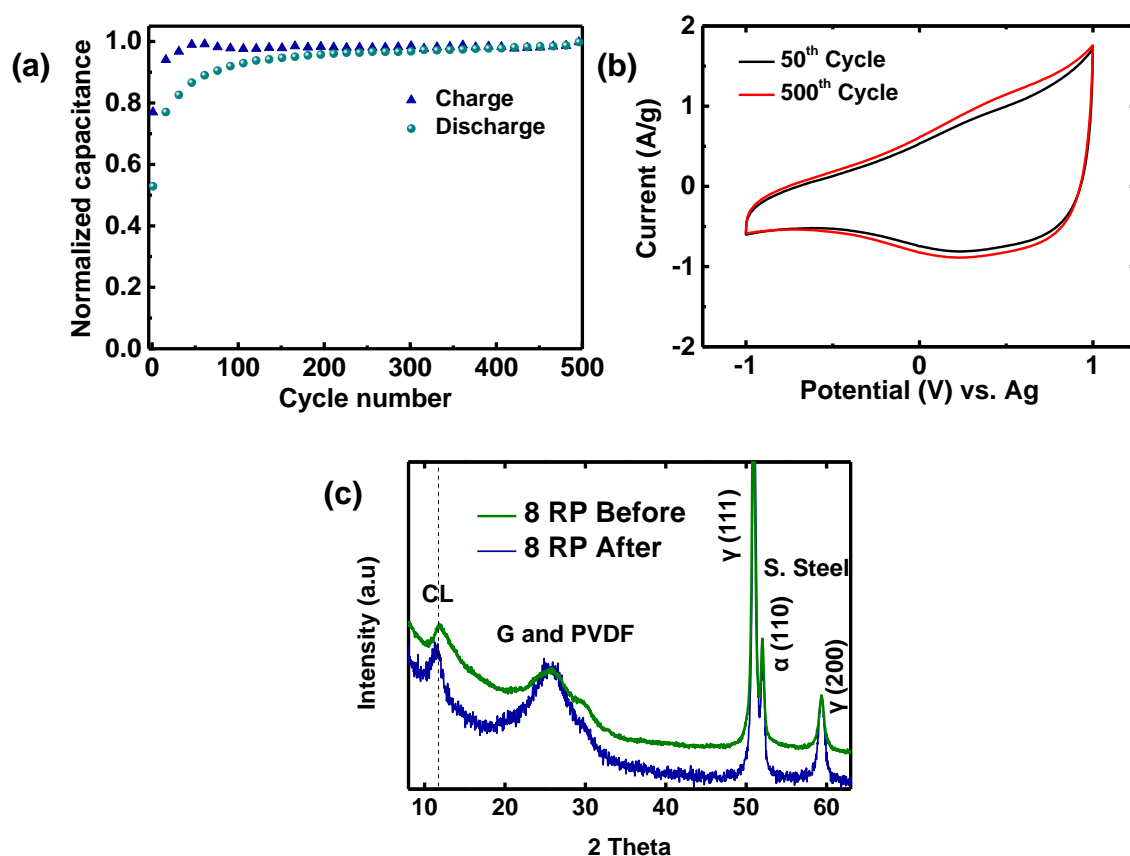
Figure III-11 (a) Normalized charge-discharge capacitances of 5RP obtained from CVs in 1M THABF$_4$/AN at 50 mV.s^{-1} scan rate in the potential range of -1 to 1 V vs. Ag over 500 cycles. (b) CV curves for the 50th and the 500th cycles. (c) Ex-situ XRD patterns of 8 RP electrode before and after 500 CV cycles at 50 mV.s^{-1} scan rate in the potential range of -1 to 1 V vs. Ag. Peaks corresponding to PVDF binder and stainless-steel current collector are seen in the electrode and the cross-linking (CL) peak in 8 RP is retained after 500 CV cycles.
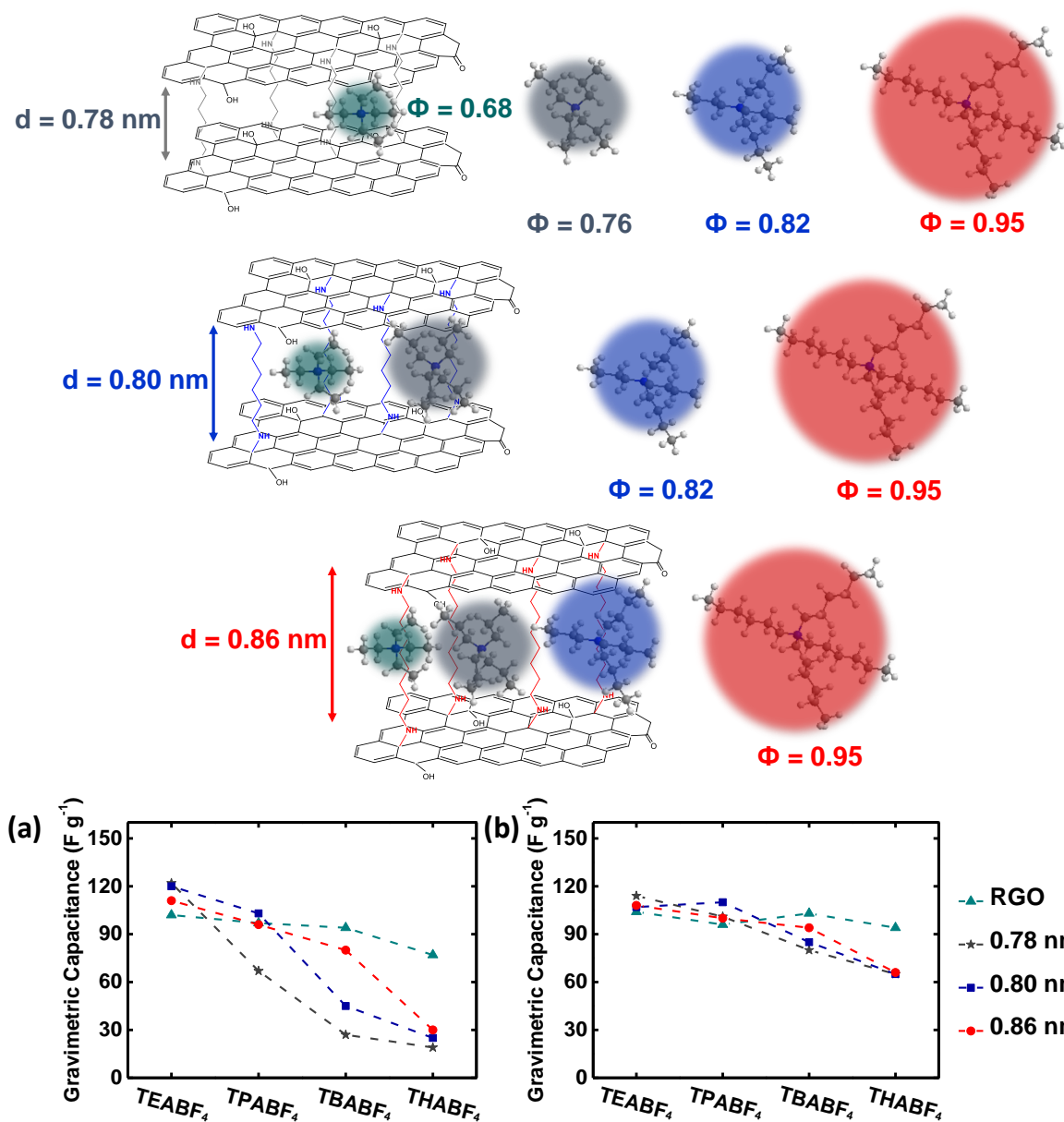
Figure III-12 Schematic representation showing limitation of TAA+ cations into RPs based on size constrictions. For simplicity, RPs are shown as individual graphene sheets cross-linked together instead of layers of graphene sheets bridged together. Specific capacitances are calculated from CVs at 20 mV.s⁻¹ for the cells tested in the voltage range of (a) -1.0 V to 0.1 V vs. Ag and (b) 0.1 V to 1.0 V vs. Ag. Dotted lines are added in the plots as a guide to the eye.

This study brings to light the possibility of using pillared graphene materials as reference materials for ion sieving and electrochemical adsorption in the inter-layer gallery pores of structured graphene materials. The combination of XRD, gas sorption and electrochemical analyses allowed to identify the electrochemically active porosity in these systems. Although the observed capacitances already occur in the range of RGO and the current literature[40, 41]

(Table III-2), pillared materials offer tremendous scope for improvements in both power and energy densities. Strategies such as using RPs that are synthesized with a low density of pillars could improve ionic diffusion and simultaneously ensure both higher power and energy densities. Additionally, conventional strategy of developing hierarchical porosity in addition to the inter-layer galleries could also enhance ion accessibility and charge storage.
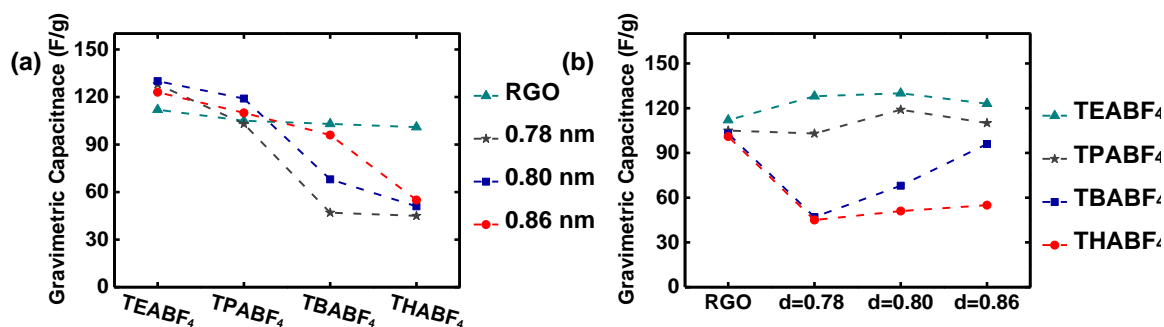
Figure III-13 Specific capacitances are calculated from CVs at 20 mV.s⁻¹ for the cells tested in the voltage range of -1.0 V to 1.0 V vs. Ag. Values are shown with (a) variation in the electrolyte and (b) change in the material.

Material	Electrolyte	Specific Capacitance (F/g) (Conditions)	Reference
Commercial activated carbon	-	80~120	3
Carbide derived carbon	EMIMTFSI	160 (0.3 A/g)	4
Chemically reduced graphene	TEABF$_4$/AN	99 (1.3 A/g)	5
Activated graphene	EMIMBF$_4$	231 (1 A/g)	6
a-MEGO	BMIMIBF$_4$/AN	165 (1 A/g)	7
5 RP (This work)	**TEABF$_4$/AN**	**130 (20 mV s⁻¹)** **154 (1 A/g)**	-

Table III-2.Comparison between the performances of various carbons found in the literature.

5. Conclusion

A class of reduced pillared graphene materials with tunable inter-layer galleries were readily synthesized using alkyl diamines as cross-links. A family of tetraalkylammonium tetrafluoroborate salts with constant anion and varying cation sizes in acetonitrile were used as electrolytes in SCs. The observed electrochemical responses for RGO show no ion specific limitation suggesting that the ion sorption occurs only in the inter-particular porosity. Whereas, RPs show limitations based on size constrictions indicating that the ions mainly adsorb in the inter-layer gallery pores. Ions are limited if their naked sizes are larger than the d-spacing of RP and thus show that the inter-layer galleries sieve ions based on sizes. This direct correlation between naked ion size and the gallery spacing suggests partial desolvation of the electrolyte ions during adsorption. Further experiments using different solvents and characterization techniques are being analyzed to understand this desolvation. These first results of ion sieving in pillared graphene materials could help us readily design and develop strategies for optimized charge storage in SCs.

6. Further Conclusions & perspectives

This extensive study performed on reduced pillared graphene materials (RPs) synthesized using three different alkyl diamines has shown that the alkyl diamines could indeed facilitate pillaring of graphene sheets and allow precise tuning of the d-spacing. XRD analyses allowed a direct characterization of the newly formed cross-linked galleries (CL) with direct determination of their d-spacing values. Additionally, the relative shapes and intensities of the CL peaks among various RPs has shown that with increasingly longer diamines the CL peaks get sharper and more intense. This observation along with the pore size distributions of the RPs have suggested that increasing length of the alkyl diamine may facilitate repetitive cross-linking of GO sheets with diamines and result in larger crystallite sizes. This observation was also noted in the previous chapter among the GH-ED and GH-DB synthesized with 1,2-diaminoethane and 1,4-diaminobutane. Overall, choosing longer alkyl diamines over the shorter ones from the previous chapter has provided the materials with required architecture.

The well-defined d-spacing values of RPs (0.78 – 0.86 nm) have allowed electrochemical ion sieving analyses with a class of $TAABF_4$ electrolytes that offer varying cation sizes (0.68 - 0.95 nm) and a constant anion size (0.48 nm). Cyclic voltammograms performed under positive and negative polarizations (with respect to OCV) showed a definitive evidence of ion sieving in these pillared graphene materials. This first observation that the electrolyte ions can enter the inter-layer graphene galleries has thus showed great potential of the pillared graphene materials for enhanced charge storage in SCs. Despite the promising fundamental observations of ions entering the galleries, the specific capacitances calculated from RPs were only marginally better than that of RGO which has extensive restacking with no pillared structures. 5 RP exhibited a charge storage of 130 $F.g^{-1}$ at 20 $mV.s^{-1}$ whereas RGO stored ~ 110 $F.g^{-1}$ in a 1 M $TEABF_4$/AN electrolyte. The expectations of significantly higher charge sorption capabilities from the newly synthesized pillared graphene galleries in RPs were not realized in these values.

Studies on pillared graphene materials in the field of gas storage have proposed that a dense filling of the inter-layer galleries with pillar molecules may render the galleries as closed pores for gas molecules. We speculated that the density of alkyl diamine pillars in RPs may also have a similar impact on their charge sorption capabilities. We believed that further understanding

of the ion transport dynamics in these RPs may evaluate our presumptions and provide perspectives to improve the capacitance values. Hence, we study the impedance responses of the materials from this chapter in the next two chapters.

Another important factor that governs the overall charge storage capability of a material is its porosity characteristics. In the previous chapter, a comparative study of GH-HD and RGO has shown the merits of a 3D interconnected porous network. The synthesis of GH-HD and RGO differed just with the magnetic stirring during the reaction: RGO is continuously stirred whereas GH-HD is left unstirred to form a monolith. The SEM images obtained for the two materials show the differences in their porosities (Figure III-14a&d). Also, the material density of GH-HD (0.02 g/cm^3) is significantly lower than that of RGO (0.5 g/cm^3). A comparison of the SEM images of GH-ED and GH-DB with their respective stirred counterparts (2 RP and 4 RP) have also showed different porosities (Figure III-14). GH-HD monolith showed higher capacitance (by 30 %) and a superior power capability compared to RGO that is more like a 2D material. In the current study, RPs are synthesized using a continuous stirring during the reaction and thus, do not form the monoliths.
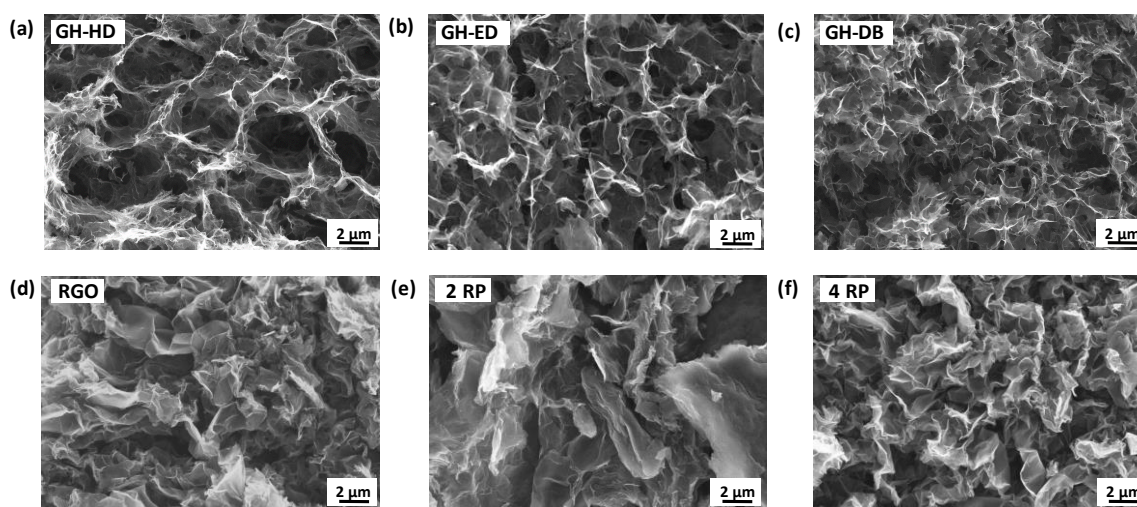
Figure III-14 Scanning electron microscopy images of monoliths synthesized using (a) hydrazine hydrate, (b) 1,2-diaminoethane and (c) 1,4-diaminobutane. A continuous stirring during the reaction led to powder like materials under same conditions. SEM images are shown for (d) RGO, (e) 2 RP and (f) 4 RP

Overall, this chapter raises few important questions about the materials properties of the synthesized pillared materials and their role in SCs. Few questions include; What is the role of diamine pillar density towards ion sorption in the galleries? How does the presence of pillars in the inter-layer galleries affect the ion transport in RPs? How durable are the pillared

graphene structures for long term cycling in SCs and what is the nature of the interaction between diamines and graphene sheets. In the next two chapters we tried to answer these questions.

7. References

(1)   Conway, B.E. Electrochemical Supercapacitors - Scientific Fundamentals and Technological Applications, Springer, 1999.

(2)   Simon, P.; Gogotsi, Y. Materials for Electrochemical Capacitors. Nat Mater 2008, 7, 845–854.

(3)   Burke, A. R&D Considerations for the Performance and Application of Electrochemical Capacitors. Electrochim. Acta 2007, 53, 1083–1091.

(4)   Béguin, F.; Presser, V.; Balducci, A.; Frackowiak, E. Carbons and Electrolytes for Advanced Supercapacitors. Adv. Mater. 2014, 26, 2219–2251.

(5)   Zhang, L. L.; Zhao, X. S. Carbon-Based Materials as Supercapacitor Electrodes. Chem. Soc. Rev. 2009, 38, 2520–2531.

(6)   Chmiola, J.; Yushin, G.; Gogotsi, Y.; Portet, C.; Simon, P.; Taberna, P. L. Anomalous Increase in Carbon Capacitance at Pore Sizes Less Than 1 Nanometer. Science 2006, 313, 1760–1763.

(7)   Eliad, L.; Salitra, G.; Soffer, A.; Aurbach, D. Ion Sieving Effects in the Electrical Double Layer of Porous Carbon Electrodes: Estimating Effective Ion Size in Electrolytic Solutions. J. Phys. Chem. B 2001, 105, 6880–6887.

(8)   Vix-Guterl, C.; Frackowiak, E.; Jurewicz, K.; Friebe, M.; Parmentier, J.; Béguin, F. Electrochemical Energy Storage in Or-dered Porous Carbon Materials. Carbon 2005, 43, 1293–1302.

(9)   Largeot, C.; Portet, C.; Chmiola, J.; Taberna, P.-L.; Gogotsi, Y.; Simon, P. Relation between the Ion Size and Pore Size for an Electric Double-Layer Capacitor. J. Am. Chem. Soc. 2008, 130, 2730–2731.

(10)   Presser, V.; Heon, M.; Gogotsi, Y. Carbide-Derived Carbons – From Porous Networks to Nanotubes and Graphene. Adv. Funct. Mater. 2011, 21, 810–833.

(11)   Chmiola, J.; Largeot, C.; Taberna, P.-L.; Simon, P.; Gogotsi, Y. Desolvation of Ions in Subnanometer Pores and Its Effect on Capacitance and Double-Layer Theory. Angew. Chem. Int. Ed. 2008, 47, 3392–3395.

(12)   Merlet, C.; Rotenberg, B.; Madden, P. A.; Taberna, P.-L.; Simon, P.; Gogotsi, Y.; Salanne, M. On the Molecular Origin of Supercapacitance in Nanoporous Carbon Electrodes. Nat. Mater. 2012, 11, 306-310.

(13)   Merlet, C.; Péan, C.; Rotenberg, B.; Madden, P. A.; Daffos, B.; Taberna, P.-L.; Simon, P.; Salanne, M. Highly Confined Ions Store Charge More Efficiently in Supercapacitors. Nat. Commun. 2013, 4, 3701-3707.

(14)   Levi, M. D.; Salitra, G.; Levy, N.; Aurbach, D.; Maier, J. Application of a Quartz-Crystal Microbalance to Measure Ionic Fluxes in Microporous Carbons for Energy Storage. Nat. Mater. 2009, 8, 872–875.

(15)   Tsai, W.-Y.; Taberna, P.-L.; Simon, P. Electrochemical Quartz Crystal Microbalance (EQCM) Study of Ion Dynamics in Nanoporous Carbons. J. Am. Chem. Soc. 2014, 136, 8722–8728.

(16)   Griffin, J. M.; Forse, A. C.; Tsai, W.-Y.; Taberna, P.-L.; Simon, P.; Grey, C. P. In Situ NMR and Electrochemical Quartz Crystal Microbalance Techniques Reveal the Structure of the Electri-cal Double Layer in Supercapacitors. Nat. Mater. 2015, 14, 812-819.

(17)   Zhou, J.; Li, Z.; Xing, W.; Shen, H.; Bi, X.; Zhu, T.; Qiu, Z.; Zhuo, S. A New Approach to Tuning Carbon Ultramicropore Size at Sub-Angstrom Level for Maximizing Specific Capacitance and CO2 Uptake. Adv. Funct. Mater. 2016, 26, 7955–7964.

(18)   Salanne, M.; Rotenberg, B.; Naoi, K.; Kaneko, K.; Taberna, P.-L.; Grey, C. P.; Dunn, B.; Simon, P. Efficient Storage Mechanisms for Building Better Supercapacitors. Nat. Energy 2016, 1, 16070.

(19)   Kondrat, S.; Pérez, C. R.; Presser, V.; Gogotsi, Y.; Kornyshev, A. A. Effect of Pore Size and Its Dispersity on the Energy Storage in Nanoporous Supercapacitors. Energy Environ. Sci. 2012, 5, 6474–6479.

(20)   Palmer, J. C.; Llobet, A.; Yeon, S.-H.; Fischer, J. E.; Shi, Y.; Gogotsi, Y.; Gubbins, K. E. Modeling the Structural Evolution of Carbide-Derived Carbons Using Quenched Molecular Dynamics. Carbon 2010, 48, 1116–1123.

(21)   Boukhalfa, S.; Gordon, D.; He, L.; Melnichenko, Y. B.; Nitta, N.; Magasinski, A.; Yushin, G. In Situ Small Angle Neutron Scattering Revealing Ion Sorption in Microporous Carbon Electrical Double Layer Capacitors. ACS Nano 2014, 8, 2495–2503.

(22)   Bañuelos, J. L.; Feng, G.; Fulvio, P. F.; Li, S.; Rother, G.; Dai, S.; Cummings, P. T.; Wesolowski, D. J. Densification of Ionic Liquid Molecules within a Hierarchical Nanoporous Carbon Structure Revealed by Small-Angle Scattering and Molecular Dynamics Simulation. Chem. Mater. 2014, 26, 1144–1153.

(23)   Raccichini, R.; Varzi, A.; Passerini, S.; Scrosati, B. The Role of Graphene for Electrochemical Energy Storage. Nat. Mater. 2015, 14, 271–279.

(24)   Stoller, M. D.; Park, S.; Zhu, Y.; An, J.; Ruoff, R. S. Graphene-Based Ultracapacitors. Nano Lett. 2008, 8, 3498–3502.

(25)   Li, C.; Shi, G. Functional Gels Based on Chemically Modified Graphenes. Adv. Mater. 2014, 26, 3992–4012.

(26)   Inagaki.M; Kang, F, Materials Science and Engineering of Carbon - 1st Edition, Butterworth-Heinemann, 2016.

(27)   Galhena, D. T. L.; Bayer, B. C.; Hofmann, S.; Amaratunga, G. A. J. Understanding Capacitance Variation in Sub-Nanometer Pores by in Situ Tuning of Interlayer Constrictions. ACS Nano 2016, 10, 747–754.

(28)   Lee, K.; Yoon, Y.; Cho, Y.; Lee, S. M.; Shin, Y.; Lee, H.; Lee, H. Tunable Sub-Nanopores of Graphene Flake Interlayers with Conductive Molecular Linkers for Supercapacitors. ACS Nano 2016, 10, 6799–6807.

(29)   Yuan, K.; Xu, Y.; Uihlein, J.; Brunklaus, G.; Shi, L.; Heiderhoff, R.; Que, M.; Forster, M.; Chassé, T.; Pichler, T.; et al. Straightforward Generation of Pillared, Microporous Graphene Frameworks for Use in Supercapacitors. Adv. Mater. 2015, 27, 6714–6721.

(30)   Stankovich, S.; Dikin, D. A.; Piner, R. D.; Kohlhaas, K. A.; Kleinhammes, A.; Jia, Y.; Wu, Y.; Nguyen, S. T.; Ruoff, R. S. Synthe-sis of Graphene-Based Nanosheets via Chemical Reduction of Exfoliated Graphite Oxide. Carbon 2007, 45, 1558–1565.

(31)   R. Dreyer, D.; Park, S.; W. Bielawski, C.; S. Ruoff, R. The Chemistry of Graphene Oxide. Chem. Soc. Rev. 2010, 39, 228–240.

(32)   Herrera-Alonso, M.; Abdala, A. A.; McAllister, M. J.; Aksay, I. A.; Prud'homme, R. K. Intercalation and Stitching of Graphite Oxide with Diaminoalkanes. Langmuir 2007, 23, 10644–10649.

(33)   Hung, W.-S.; Tsou, C.-H.; De Guzman, M.; An, Q.-F.; Liu, Y.-L.; Zhang, Y.-M.; Hu, C.-C.; Lee, K.-R.; Lai, J.-Y. Cross-Linking with Diamine Monomers To Prepare Composite Graphene Oxide-Framework Membranes with Varying d-Spacing. Chem. Mater. 2014, 26, 2983–2990.

(34)   Li, D.; Muller, M. B.; Gilje, S.; Kaner, R. B.; Wallace, G. G. Processable Aqueous Dispersions of Graphene Nanosheets. Nat Nano 2008, 3, 101–105.

(35)   Banda, H.; Aradilla, D.; Benayad, A.; Chenavier, Y.; Daf-fos, B.; Dubois, L.; Duclairoir, F. One-Step Synthesis of Highly Reduced Graphene Hydrogels for High Power Supercapacitor Applications. J. Power Sources 2017, 360, 538–547.

(36)   Brunauer, S.; Emmett, P. H.; Teller, E. Adsorption of Gases in Multimolecular Layers. J. Am. Chem. Soc. 1938, 60, 309–319.

(37)   Jagiello, J.; Olivier, J. P. 2D-NLDFT Adsorption Models for Carbon Slit-Shaped Pores with Surface Energetical Heterogeneity and Geometrical Corrugation. Carbon 2013, 55, 70–80.

(38)   Srinivas, G.; Burress, J. W.; Ford, J.; Yildirim, T. Porous Graphene Oxide Frameworks: Synthesis and Gas Sorption Proper-ties. J. Mater. Chem. 2011, 21, 11323–11329.

(39)   Ue, M. Mobility and Ionic Association of Lithium and Quaternary Ammonium Salts in Propylene Carbonate and Γ-Butyrolactone. J. Electrochem. Soc. 1994, 141, 3336–3342.

(40)   Zhang, L.; Zhang, F.; Yang, X.; Long, G.; Wu, Y.; Zhang, T.; Leng, K.; Huang, Y.; Ma, Y.; Yu, A.; et al. Porous 3D Graphene-Based Bulk Materials with Exceptional High Surface Area and Excel-lent Conductivity for Supercapacitors. Sci. Rep. 2013, 3, 1408.

(41)   Zhu, Y.; Murali, S.; Stoller, M. D.; Ganesh, K. J.; Cai, W.; Ferreira, P. J.; Pirkle, A.; Wallace, R. M.; Cychosz, K. A.; Thommes, M.; et al. Carbon-Based Supercapacitors Produced by Activation of Graphene. Science 2011, 332, 1537–1541.

(42)   Hummers, W. S.; Offeman, R. E. Preparation of Graphitic Oxide. J. Am. Chem. Soc. 1958, 80, 1339–1339.

(43)   Ashok Kumar, N.; Gambarelli, S.; Duclairoir, F.; Bidan, G.; Dubois, L. Synthesis of High Quality Reduced Graphene Oxide Nanosheets Free of Paramagnetic Metallic Impurities. J. Mater. Chem. A 2013, 1, 2789–2794.

CHAPTER IV:

Electrochemical Impedance Analysis of Ion-Sieving in Pillared Graphene Materials

Chapter IV. Electrochemical Impedance Analysis of Ion Transport in Pillared Graphene Materials

1. Objectives & Approach

In the previous chapter, successful elaboration of reduced pillared graphene materials (RPs) and their ion sieving capabilities in SCs were described. Electrochemical analysis of RPs in three electrode SC cells through cyclic voltammetry showed limitations in cation adsorption when the cation sizes were larger than the inter-layer gallery heights, characterized by the d-spacing values. In other words, ions entered the inter-layer galleries when they are smaller than d-spacing values and were restricted when larger. However, despite this direct observation of the ion sorption inside the galleries, the calculated specific capacitances were only marginally better for RPs than that obtained for RGO that displays are-stacked structure.

In order to further characterize the materials in the electrochemical cells and to understand the origin of the lower-than-expected specific capacitances, we proposed to study the ion transport behavior in the synthesized RPs. Hence, we performed electrochemical impedance analysis of 5 and 6 RPs using the same class of TAABF$_4$/AN electrolytes. The frequency responses were obtained under positive and negative polarizations with respect to open circuit voltage in order to observe distinct cation and anion behavior. RGO was also studied as a control material under the same conditions. We believed that the comparison with RGO would give a definitive understanding of differences in ion transport.

As discussed in the previous chapters, the global objective of this thesis was to synthesize and study pillared graphene materials with an interconnected macroporous structure. We expect the pillared nano structures to contribute towards ion sorption while the interconnected porosity would facilitate ion access to the sites. The comparison of the power capabilities of GH-HD and RGO in chapter II emphasized the important role of porosity in SCs. In chapter III we achieved successful pillaring of graphene materials but the synthesized RPs do not self-assemble into monoliths. Thus, while looking out for self-assembly techniques, we found that hydrothermal treatment of GO is an effective one-step process to obtain such monoliths.

Herein, we have attempted to synthesize a pillared graphene hydrogel (GH) through a one-step hydrothermal treatment of the GO-alkyl diamine mixture (Scheme IV-1). Electrochemical

impedance analyses were also performed on the synthesized GHs and were then compared to RPs. The comparison of GHs to RPs, wherein both the materials have pillared architectures but differ in the porous characteristics, was expected to describe the role of porosity in the SC performances of pillared graphene materials.

The results obtained in this chapter were written as an article and are currently under review at the journal of "*Electrochimica Acta*". The broader insights and perspectives obtained from the article are discussed at the end of this chapter.

FD and HB conceptualized the idea and designed the work. HB and SP performed experiments, analysed data and conceived the manuscript. BD performed gas sorption experiments. PLT proposed Imaginary C and Real Impedance Plots. LD, OC, PS and PLT aided with data analysis FD and HB complied the work and wrote the manuscript. All authors have discussed the results and contributed to the final manuscript.
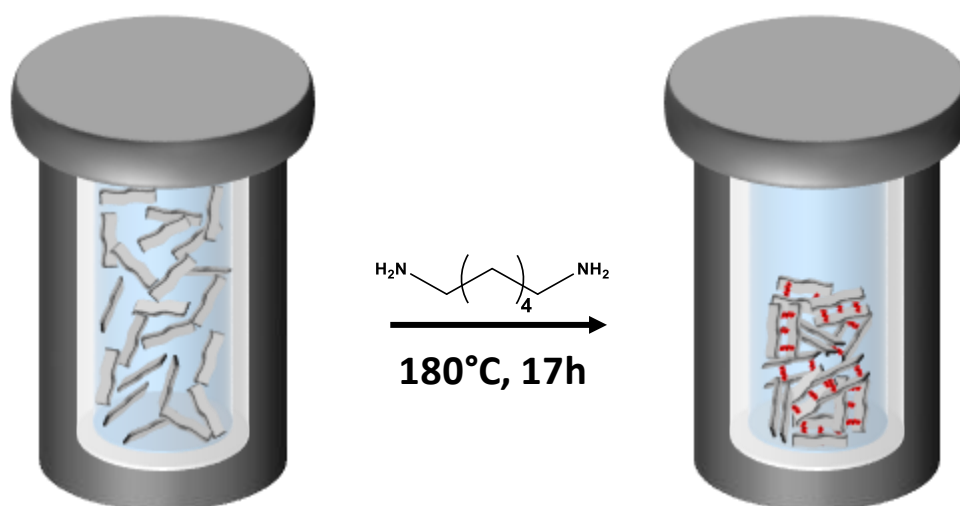
Scheme IV-1 Schematic representation of the synthesis of pillared graphene hydrogel in an autoclave.

Investigation of ion transport in chemically tuned pillared graphene materials through electrochemical impedance analyses

Harish Banda[†], Sandy Périé[†], Barbara Daffos[¶‡], Lionel Dubois[†], Olivier Crosnier[¶§], Patrice Simon[¶‡], Pierre-Louis Taberna[¶‡*] and Florence Duclairoir[†*]

[†] Univ. Grenoble Alpes, CEA, CNRS, INAC, SyMMES, Grenoble, 38000, France.

[‡] CIRIMAT, Université Toulouse, CNRS, INPT, UPS, 31062 Toulouse, France.

[§] Institut des matériaux Jean Rouxel (IMN), Université Nantes, CNRS, Nantes, 44300, France.

[¶] Réseau sur le Stockage Electrochimique de l'Energie (RS2E), FR CNRS, 3459, France.

* Email : florence.duclairor@cea.fr

External graphene surfaces (RGO)   **Densely filled galleries (RPs)**
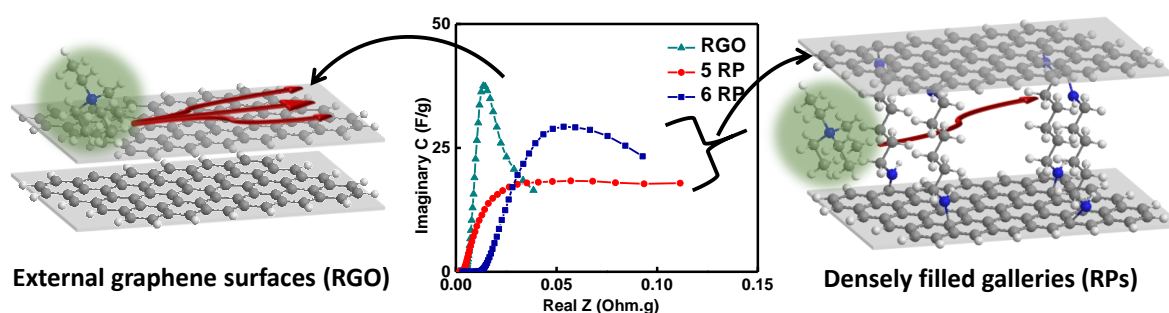
Abstract

Chemically tuned pillared graphene structures show ability to limit restacking of graphene sheets for electrochemical energy storage in SCs. A comprehensive electrochemical characterization using various ion sizes allowed identification of ion-sieving in the cross-linked galleries of reduced pillared graphene materials (RPs). The access to the cross-linked galleries, which provide additional ion sorption sites, offered slightly increased capacitances in RPs compared to completely restacked sheets in reduced graphene oxide (RGO). We performed electrochemical impedance analyses on RPs and RGO to understand the ion transport inside the cross-linked graphene galleries. RGO adsorbs ions in the inter-particle micro/mesopores and the ion access to such sites from the bulk electrolyte occurs with relative ease. RPs sieve ions into their inter-layer gallery pores based on effective ion sizes and the ion transport

process is resistive compared to RGO. A control study using 3D pillared graphene hydrogel with improved macro porosity assigns this resistive behavior and the moderate capacitances to limited ion access to the active sites due to excess number of pillars. The obtained results on the ion transport dynamics between graphene layers provide perspectives towards further optimization of these graphene materials for SCs.

2. Introduction

Supercapacitors (SCs) or electrochemical-double layer capacitors are electrochemical energy storage devices able to deliver high power densities with excellent cycle life.[1,2] These characteristics are made possible by the charge storage process involving a charge separation at the electrode-electrolyte interface *via* fast adsorption of electrolytic ions at the electrode surface. However, these systems are also characterized by limited energy densities and thus are widely studied as complementary to batteries.[3] To improve the energy densities, researchers are working on new systems with porous carbons, or the development of pseudocapacitive materials with additional faradaic processes, or hybrid systems that operate between batteries and SCs. [4–6]

Among various carbons, activated carbons (ACs) have been widely studied for SCs applications owing to their high specific surface areas (SSA) and low material costs.[4] Interest in ACs also lies in their tunable porous structures that allowed analysis of the impact of pore sizes on specific capacitances. [7,8] These studies revealed that in addition to high surface areas, matching pore sizes to electrolytic ion sizes also enable high capacitances.[9–11] Extensive analyses on ion-sieving in these pores have discovered that the high capacitances are a result of a partial desolvation and confinement of ions in these pores. [12–14] Among other carbon derivatives tested, graphene has been studied as an electrode material candidate.[15–17] The derived-research paths have mainly focused on tuning graphene sample porosity,[18,19] for example, by creating holes inside the graphene sheets, or by forming graphene aerogels displaying porosities adapted for efficient electrolyte ion transfer. [20] In parallel, many research paths involve the use of graphene as a support for a faradaic or non-faradaic component to improve the overall capacity of the system. [21]

Recently, our group proposed pillared graphene structures with organic molecules pillars to prevent the significant restacking of graphene sheets during chemical reduction. We predict that such pillared structures would offer higher specific capacitances with more electrochemical active sites available for ion sorption. Hence an interesting class of materials with varied inter-graphene layer separation (d-spacing) were readily synthesized by varying the size of the pillar (alkyl diamine) used.[22–24] In the course of related electrochemical studies, ion-sieving behavior was observed in these graphene-derived materials.[22] A clear dependency

between d-spacing of the inter-layer galleries and electrolytic ion sizes was noted: ions with sizes smaller than d-spacing can access gallery pores whereas larger ions cannot access the surface area inside the galleries.[22] The cross-linked galleries in these materials sieve ions based on their size and hence demonstrate a potential for enhanced capacitances through optimization of d-spacing/ion size couple.[25] While this phenomenon has been clearly identified and explained using cyclic voltammetry (CV) experiments, additional electrochemical impedance spectroscopy (EIS) studies are presented in this paper with further insights on the electrolytic ion transport in between the graphene layers. This analysis of ion dynamics inside the graphene galleries gives new perspectives and is of direct interest towards optimizing graphene materials for SCs. So, herein, pillared graphene materials with a d-spacing of 7.8 and 8.0 Å - obtained with pillars of 1,5-diaminopentane and 1,6-diaminohexane respectively – are tested in various tetraalkylammonium tetrafluoroborate salt solutions in acetonitrile. Impedance analyses were performed under positive and negative polarizations to obtain the distinct anion and cations responses in these materials. RGO, which only displays inter-particle porosity but does not have any inter-layer cross-linked galleries, has been studied as a control material. EIS data have been treated and the evolution of imaginary part of capacitances vs. real impedances have been plotted to investigate the ion transport inside these materials.

3. Results & Discussion

The pillared graphene-based materials studied here were prepared using graphene oxide as a platform for functionalization with alkyl diamines as pillars.[22] The amine groups react with oxygen containing functions such as epoxide and carboxylic acid on GO and bridge GO sheets together (Scheme IV-2).[23] The obtained pillared materials were further reduced using hydrazine to improve their electrical conductivities. [28,29] Depending on the diamine used in the first step, materials were named as 5 RP (1,5-diaminopentane) and 6 RP (1,6-diaminohexane). The detailed protocol about RPs preparation has been published elsewhere and a brief description can be found in materials and methods.[22] The covalent interactions between diamines and graphene layers have also been shown previously using a combination of spectroscopic and electrochemical characterization methods.[22–24] X-ray diffraction (XRD) patterns were obtained (using a Co Kα radiation source of λ=1.79 Å) to readily characterize the impact of cross-linking diamines in RPs (Figure IV-1a). RGO, synthesized as a control, shows a broad peak around 28° corresponding to the graphite-like arrangement (002) with an inter-graphene sheet distance of 3.7 Å. This graphite-like arrangement suggests an efficient reduction of GO leading to a partial restacking of the reduced graphene sheets.[30] The XRD patterns recorded for both RPs display two peaks. The peaks around 25° were again attributed to the partial restacking of graphene stacks upon chemical reduction. The new peaks around 15° in both RPs were ascribed to cross-linking of graphene layers induced by the diamines. 5 RP exhibits a d-spacing of 0.78 nm whereas 6 RP shows 0.80 nm with a larger alkyl chain used.
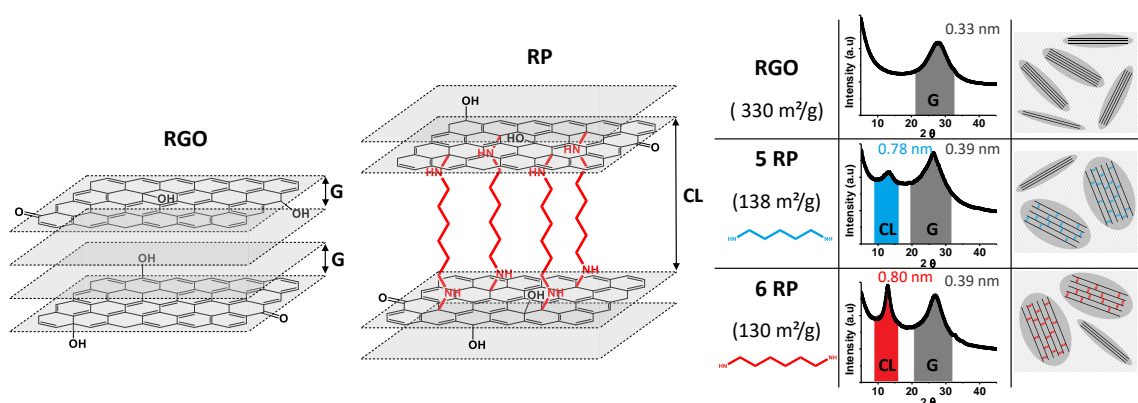
Scheme IV-2 Schematic representation of reduced graphene oxide (RGO) and reduced pillared graphene materials (RPs) showing the specific surface areas and d-spacing values determined from XRD.
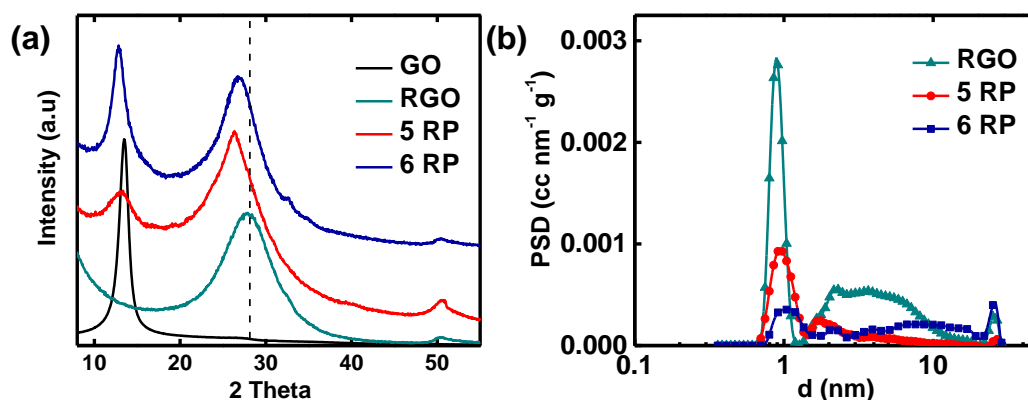
Figure IV-1 (a) X-Ray diffraction patterns of the synthesized materials showing two different regions attributed to graphitic (25-32°) and cross-linked domains (10-15°). (b) Pore size distributions calculated from N_2 sorption isotherms using a 2D non-local density functional theory (NLDFT) treatment and by assuming a graphene-based structural framework for the materials.

The porosity characteristics of the synthesized materials were studied using gas sorption analyses under N_2 (Figure IV-1b). RPs exhibit a SSA of ~ 130 m²/g whereas RGO exhibits more than twice higher (330 m²/g). The pore size distributions (PSDs) of the materials were calculated from the isotherms using 2D non-local density functional theory (2D-NLDFT).[31] RGO possesses a high volume of micropores and a significant contribution of mesopores whereas 5 and 6 RPs show high mesopore content with some micropores (Figure IV-1b). Interestingly, even though the XRD patterns show the existence of the inter-layer galleries in RPs, gas sorption and PSD analyses show no presence of such pores (0.8 nm). This may be due to the inability of N_2 to probe such galleries or due to a partial shrinkage of the pores during sample degassing.[32,33]

The electrochemical responses of RGO and RPs were recorded in various electrolytes with increasing cation size and a constant anion size (Figure IV-2). The unsolvated sizes of the electrolyte ions tested are TEA⁺ – 0.68 nm, TPA⁺ – 0.76 nm, TBA⁺ – 0.82 nm, THA⁺ – 0.95 nm and BF_4^- – 0.48 nm. With TEABF₄ electrolyte, the CVs of RGO and RPs show a rectangular quasi-ideal capacitive behavior (Figure IV-2a). In TPABF₄, with a larger cation (0.76 nm) and the same anion, CVs from RGO and 6 RP remain unchanged while that of 5 RP starts to show decreased currents under negative polarization (Figure IV-2b). Upon further increasing the cation size to TBA⁺ (0.82 nm) and THA⁺ (0.95 nm), both 5 and 6 RPs exhibit a clear reduction in current under negative potentials whereas RGO remains rectangular (Figure IV-2c & Figure IV-3a). Among the two RPs, 5 RP shows greater distortion than 6 RP in both TBABF₄ and THABF₄.

Figure IV-2 Normalized CVs of RGO and RPs obtained at a scan rate of 10 mV/s in the voltage range of -1 V to 1 V vs. Ag in 1 M solutions of (a) TEABF$_4$, (b) TPABF$_4$ and (c) TBABF$_4$ in acetonitrile. Normalization was performed with respective currents observed at open circuit voltages (~ 0.1 V).

When the inter-layer graphene galleries in RPs have a smaller d-spacing than the ion sizes, lower capacitances were recorded, implying that the galleries restrict larger ions (Figure IV-3b). For instance, 5 RP shows a specific capacitance of 130 F/g in TEABF$_4$ but when larger cations were used, a steep decline from 115 F/g (TPABF$_4$) to 42 F/g (THABF$_4$) is noted. Whereas, RGO, which adsorbs ions only at the surface of graphene layers (SSA=330 m²/g), exhibits similar capacitances of ~ 110 F/g in all the electrolytes studied. 5 and 6 RPs have a d-spacing of 0.78 and 0.8 nm respectively and hence are accessible to TEA$^+$ but have limited accessibility for larger cations. The slightly higher capacitances of RPs compared to RGO in TEABF$_4$, despite very low SSAs, again suggest that the inter-layer porous networks are electrochemically accessible but may not be probed by N$_2$. In summary, this electrochemical study revealed ion-sieving based on sizes inside the pillared graphene materials. [22]
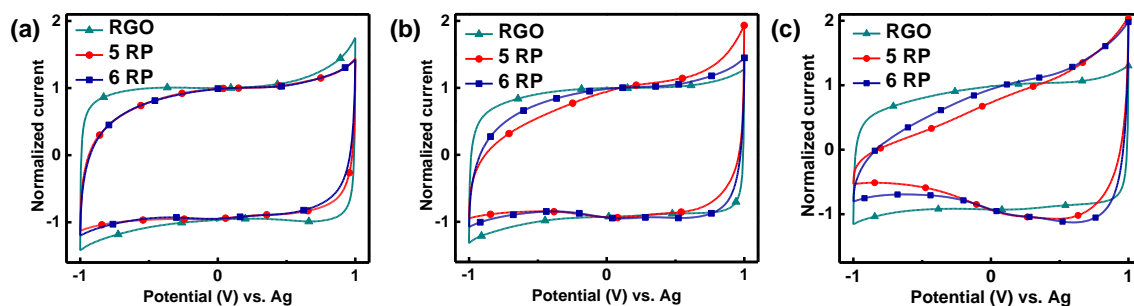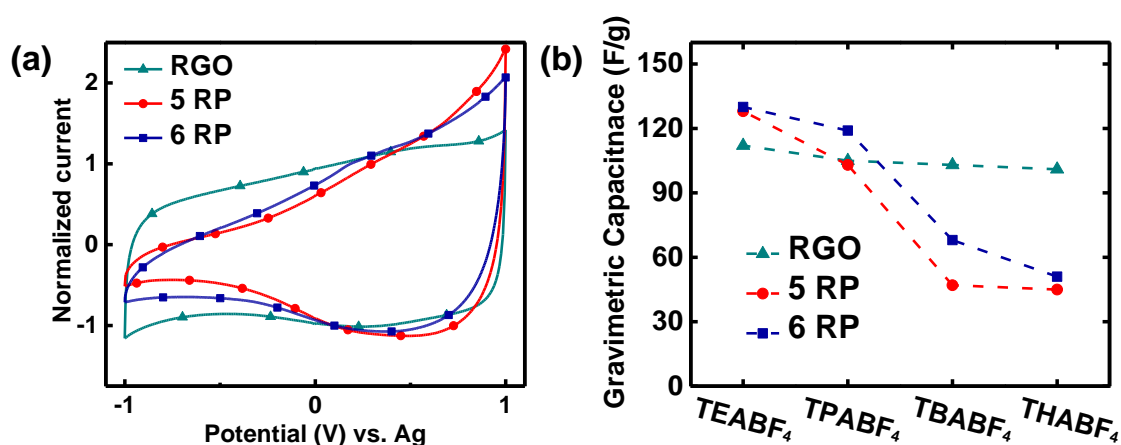

Figure IV-3 (a) Normalized CVs of RGO and RPs obtained at a scan rate of 10 mV/s in the voltage range of -1.0 V to 1.0 V vs. Ag in 1 M solutions of THABF$_4$ in acetonitrile. (b) Specific capacitances calculated for the materials from CVs at 10 mV/s in various electrolytes in the voltage range of -1.0 V to 1.0 V vs. Ag.

To further characterize this ion-sieving and also to gain insights into the ion transport inside the graphene galleries, EIS measurements were performed on RGO and RPs under negative and positive polarizations. The normalized complex plane Nyquist plots are displayed in Figure IV-4. These plots can be divided into three regions.[34–36] At high frequencies, only the electrical conductivity of the electrode (ionic and electronic) can be seen; thus, SC electrodes behave like a resistor (Z''=0). The sharp increase of the imaginary part of the impedance (-Z'') in the low frequency region - where the plot is nearly parallel to the y axis is related to a capacitive behavior. The intermediate 45° region is associated to the ion transport in the porous network of the electrode that corresponds to the electrolyte resistance in the pores.
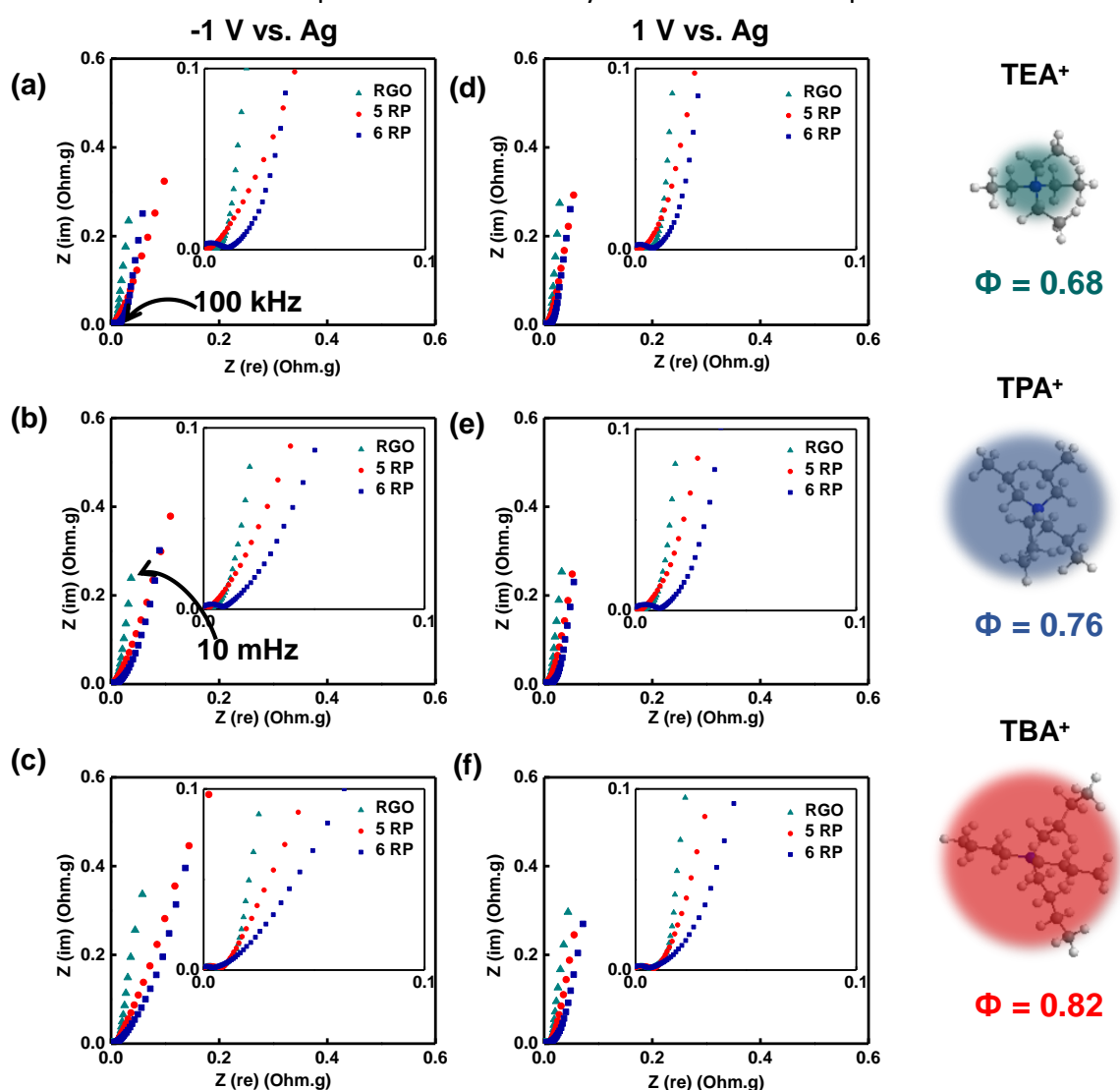
Figure IV-4 Nyquist plots of RGO and RPs in 1 M solutions of (a,d) TEABF$_4$, (b,e) TPABF$_4$ and (c,f) TBABF$_4$ in acetonitrile at -1 V vs. Ag (a,b,c) and 1 V vs. Ag (d,e,f). A zoom of the high and mid-frequency regions is shown in the insets. Unsolvated ion sizes of TEA$^+$, TPA$^+$ and TBA$^+$ are shown on the right.

At -1 V vs. Ag, the electrodes are negatively polarized with respect to open circuit voltages and cations are predominantly adsorbed at the electrode surfaces. [37] The Nyquist plots show clear differences between RGO and RPs in all the electrolytes tested (Figure IV-4a-c). Firstly, in each electrolyte, as compared to RGO, RPs show a larger electrolyte resistance in the porous electrode network that extend into lower frequencies. Due to this resistance, the low frequency capacitive behavior in RPs shifts into higher resistances. Secondly, with increasing cation size, the vertical line indicating capacitance in each RP gradually diverges away from the ideal 90°. The extent of this deviation from the ideal capacitance can be estimated by replacing the capacitance C with a Constant Phase Element (CPE, see Equation IV-1) using α parameter.[38] α values are obtained by measuring the slopes in equation 1 at low frequencies.

$$\log(|z''(w)|) = -\alpha \cdot \log(C\omega) \qquad 0 < \alpha < 1$$

Equation IV-1

A value of 1 for α indicates a fully capacitive behavior of the material. 6 RP shows decline of α values from 0.87 in TEABF$_4$ to 0.77 in TBABF$_4$ while, 5 RP shows low value of ~ 0.80 in all the electrolytes indicating a non-ideal capacitive behavior (Table IV-1). Thus, there is an important influence of the cation size on the frequency responses of RPs under negative polarization.

Material	TEABF$_4$		TPABF$_4$		TBABF$_4$		THABF$_4$	
	+ 1 V	- 1 V	+ 1 V	- 1 V	+ 1 V	- 1 V	+ 1 V	- 1 V
RGO	0.97	0.95	0.95	0.92	0.95	0.93	0.90	0.83
5 RP	0.91	0.80	0.87	0.81	0.88	0.79	0.76	0.80
6 RP	0.93	0.87	0.89	0.81	0.86	0.77	0.79	0.75

Table IV-1 α values were obtained by measuring the slope of $log(|z''(w)|) = -\alpha \cdot log(C\omega)$. To analyze the capacitance behavior of the materials, only low frequency regions (0.1 to 0.01 Hz) of the curve were used to calculate α.

RGO exhibits α values close to 1 from TEABF$_4$ (0.95) to TBABF$_4$ (0.93) electrolytes, evidencing a faster ion transport in the pores. To analyze the capacitance behavior of the materials, only low frequency regions (0.1 to 0.01 Hz) of the curve were used to calculate α.

Ion sorption in RGO occurs in the micro/meso inter-particle pores and thus the TEA^+, TPA^+ and TBA^+ cations access them with relative ease. Therefore, the impedance measurements of RGO show ideal capacitive-like behavior and do not vary a lot in these electrolytes. In RPs, ion sorption occurs significantly in the inter-layer porous network in addition to the inter-particle pores. Access to the inter-layer pores in RPs is regulated by d-spacing/ion size couple. Therefore, the frequency responses of RPs are dependent on their d-spacing and the effective size of the electrolyte ions. 6 RP, with a d-spacing of 0.80 nm, has a performance similar to that of RGO in $TEABF_4$ but extended diffusion regions are seen with larger cations. Impedance data in $THABF_4$ electrolyte further supports the different ion sorption mechanisms for RGO and RPs (Figure IV-5a). In RPs, THA^+ cation (0.95 nm) is larger than the d-spacing values, like with TBA^+, and hence even larger impedances were recorded. Notably, RGO possesses a major contribution from inter-particle pores with a diameter of ~ 0.9 nm and thus only when THA^+ cations are used, a sudden increase in the Warburg region and decrease in α parameter (0.83) are observed (Table IV-1).
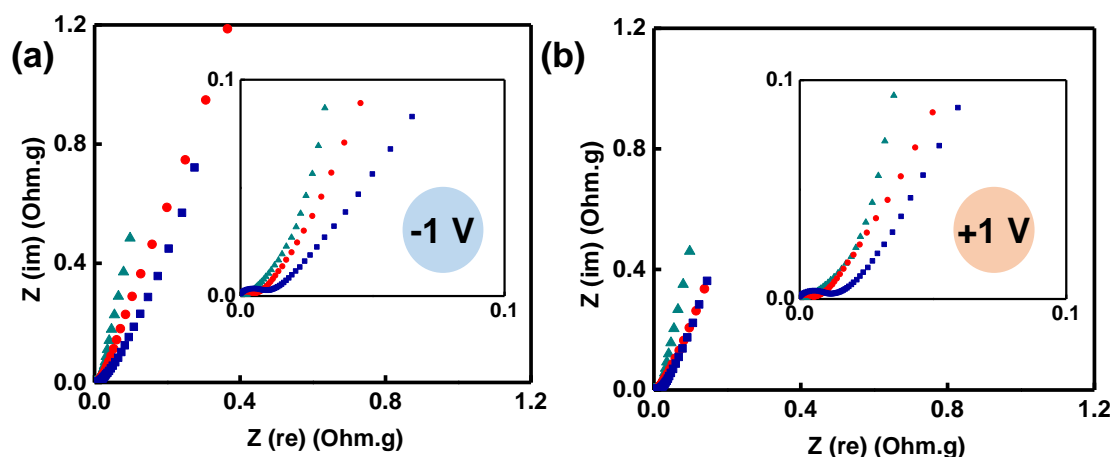
Figure IV-5 Nyquist plots of RGO and RPs in 1 M solution $THABF_4$ in acetonitrile at (a) -1 V (b) 1 V vs. Ag. A zoom of the high frequency regions is shown in insets.

At 1 V vs. Ag, the materials are positively polarized with respect to open circuit voltages and BF_4^- ions are predominantly adsorbed on the electrode surfaces. The Nyquist plots of RGO and RPs show similar shapes among themselves in the three different electrolytes tested (Figure IV-4d-f). The BF_4^- ions are smaller than the gallery pores in RPs and hence display capacitive like behavior similar to RGO. However, the vertical part in the low frequency region slightly shifts away from the ideal behavior from $TEABF_4$ to $TBABF_4$. α values for RGO range from 0.97 to 0.95 whereas RPs range from 0.93 to 0.86 in $TEABF_4$ to $TBABF_4$ (Table IV-1). This interesting shift from ideal behavior despite analyzing the same BF_4^- ions in different electrolytes hints at

a possible role of cations even under positive polarization, such as previously observed [Griffin et al. Nature Materials 2015].[39] In summary, RGO and RPs show similar responses in all electrolytes under positive potentials and an increasing influence of larger cations, in addition to anions, is also noted. This observation was described as an ion exchange mechanism in earlier reports. [39–41] With the largest cation in THABF$_4$, α values of RGO and RPs decrease to 0.90 and ~ 0.76 respectively, indicating a greater cation exchange effect.

The EIS measurements have also allowed determination of the real capacitances (C') according to a complex capacitance model reported by Taberna et al. derived from Cole and Cole.[42–44] C'(w) represents the deliverable capacitance of the cell under DC or low frequency AC conditions. C'(w) is calculated using Equation IV-2, where Z''(w) is the imaginary part of impedance Z and w is the frequency.

$$C'(w) = \frac{-z''(w)}{w|z(w)|^2}$$

Equation IV-2

The evolution of C' with respect to frequency for each sample at +1 V and -1 V vs. Ag was plotted accordingly (Figure IV-6). At higher frequencies, the system acts as a pure resistor and hence capacitance values tend to zero. At lower frequencies, a pure capacitive behavior is observed and typically, a plateau is seen if the maximal C' occurs in the tested frequency range. The intermediate zone gives information about electrolyte access to the electrode
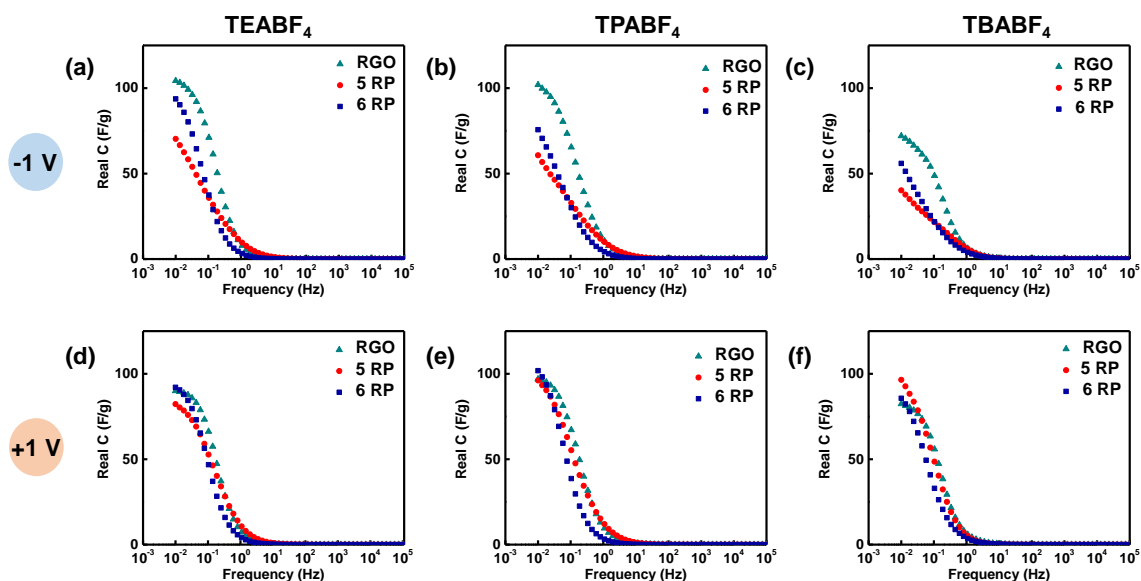

Figure IV-6 Real capacitance vs frequency plots for RGO and RPs in 1 M solutions of (a,d) TEABF$_4$, (b,e) TPABF$_4$ and (c,f) TBABF$_4$ in acetonitrile at (a,b,c) -1 V vs. Ag and (d,e,f) 1 V vs. Ag.

porosity (gallery and inter-particle pores). For example, a porous material with rapid ionic transport displays a steep slope in this intermediate region. [42]

At -1 V vs. Ag, C' vs w plots for RGO approach a maximal C' plateau in TEABF$_4$, TPABF$_4$ and TBABF$_4$ at the lowest frequency tested (10 mHz), revealing a fast transport of electrolytic ions in the electrode material (Figure IV-6a-c). However, in THABF$_4$, RGO displays lower C' values and a non-ideal behavior as the cation size approaches the inter-particle pore sizes in RGO (Figure IV-7a). For 6 RP, C' is closely equivalent to that of RGO in TEABF$_4$ and increasing cation sizes shifts the pure capacitive behavior to lower frequencies. 5 RP, even in TEABF$_4$, does not approach a plateau and the ion transport is gradually limited in other electrolytes. Additionally, with larger cations in RPs, the maximal C' values and the slopes in the intermediate region gradually decrease.
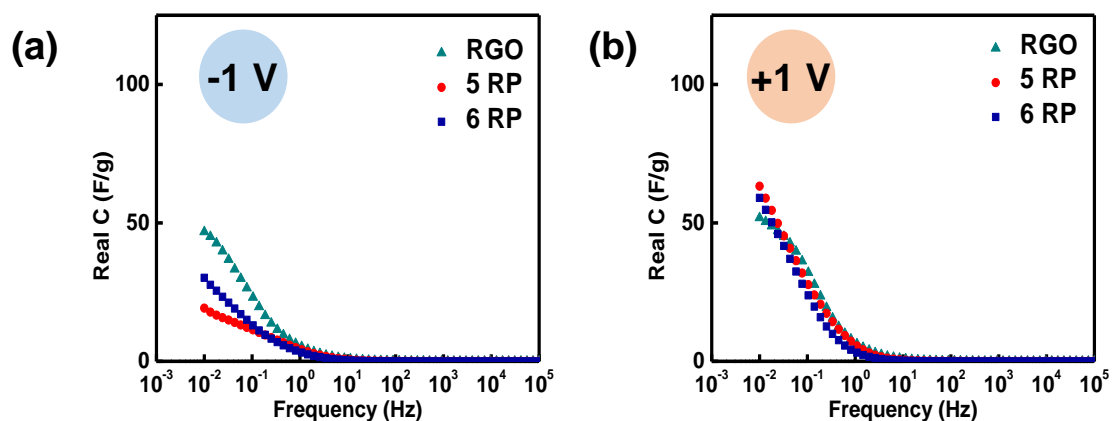
Figure IV-7 C' vs w plots for RGO and RPs in 1 M solution THABF$_4$ in acetonitrile at (a) -1 V and (b) 1 V vs. Ag.

This EIS data under negative polarization really shows a slower ion transport in RPs when larger cations are used. In RPs, steric effects when ion size is in the same range as the inter-layer gallery size lead to limited ion transport and accessibility to adsorption sites. Thus, with a complex dynamic process, RPs do not reach a plateau with full capacitance in this frequency range and confirm resistive behavior. At 1 V vs. Ag, RGO and RPs all show curves with similar maximal C' values and slopes in the intermediary region (Figure IV-6d-f). However, with increasing cation size, it can be noted that the plateaus of C' slightly drift towards lower frequencies. This observation, as noted in the Nyquist plots, could be seen as an influence of cations *via* the existence of an ion exchange mechanism.[39] Results obtained with THABF$_4$ under positive potential show a steep fall of C' values in all the materials, supporting this effect (Figure IV-7b). Moreover, an increase in the alkyl chain length from TEA$^+$ to THA$^+$ ions could

give rise to stronger interactions between graphene sheets and alkyl carbons of the electrolytic ions.

The complex capacitance model also allows the determination of imaginary capacitance (C'') which corresponds to the energy loss arising from irreversible processes at the electrodes.[42] This *C''(w)* parameter was calculated from EIS data using equation 3, where Z'(*w*) is the real part of impedance Z:

$$C''(w) = \frac{-z'(w)}{w|z(w)|^2}$$

Equation IV-3

The imaginary C'' goes through a maximum at a frequency f_0, which defines the transition between purely resistive and capacitive behaviors of a SC. This frequency, known as knee frequency, defines the time constant (τ_0) as minimum time required to extract half of the capacitance from a SC. At -1 V vs Ag. polarization, C'' vs *w* plots for RGO and RPs show dissimilar curves in each electrolyte and are influenced by the ion sizes used (Figure IV-8a-d).

Figure IV-8 C'' vs w plots for RGO and RPs in 1 M solutions of (a) TEABF₄, (b) TPABF₄, (c) TBABF₄ and (d) THABF₄ in acetonitrile at -1 V vs. Ag.

The τ_0 values obtained from these peaks assign better power capability for RGO than RPs (Table IV-2).

Material	TEABF$_4$		TPABF$_4$		TBABF$_4$		THABF$_4$	
	+ 1 V	- 1 V	+ 1 V	- 1 V	+ 1 V	- 1 V	+ 1 V	- 1 V
RGO	6	6	6	6	6	6	7	12
5 RP	7	-	10	-	11	-	-	-
6 RP	10	15	16	25	20	32	41	-

Table IV-2 Time constant (τ0) values (seconds) of RGO and RPs were calculated from the frequencies at which maximum values of C'' occurred.
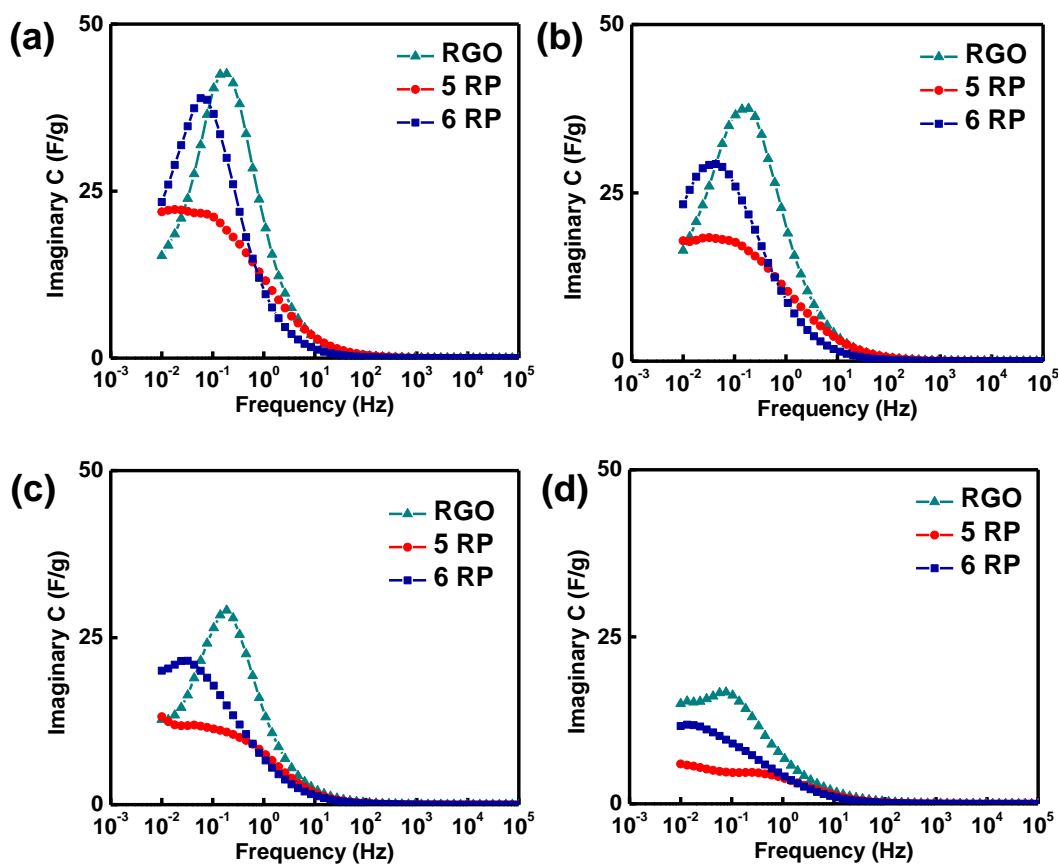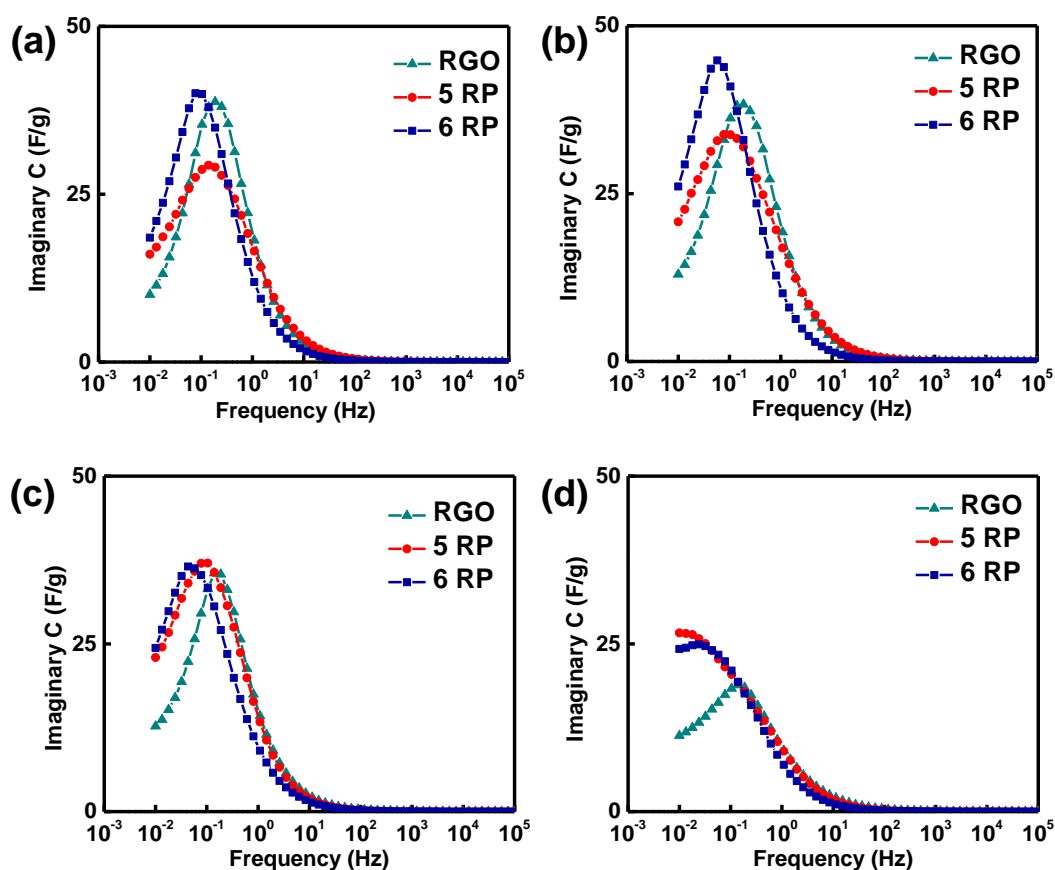

Figure IV-9 C'' vs w plots for RGO and RPs in 1 M solutions of (a) TEABF₄, (b) TPABF₄, (c) TBABF₄ and (d) THABF₄ in acetonitrile at 1 V vs. Ag.

At 1 V vs Ag. polarization, RGO and RPs show identical curves in each electrolyte with clear peaks corresponding to the transition (Figure IV-9a-d). Interestingly, the τ_0 values for 5 RP are

lower than for 6 RP in all the electrolytes tested under positive polarization. For example, τ_0 of 5 and 6 RPs in TBABF$_4$ are 11 and 20 s respectively. This difference between RPs is counter-intuitive as one would expect 6 RP, with a higher d-spacing, to facilitate better transport and lower τ_0 value for BF$_4^-$ anion. As τ_0 values are affected by a combination of ionic, electrical and cell resistances, it seems important to determine the distinct impact of the material properties on ionic resistances.

To do so, herein, we attempted to study C'' with respect to Z'. We believe that such an analysis could enable facile quantitative determination of the ionic resistances (R$_i$) involved in ion transport. Similar to other plots, three different regions could be identified in such a curve (Figure IV-10). At high frequencies the SC performs like a resistor and C'' would be close to zero (Equation IV-3). The mid frequency range is related to the ion transport inside the electrode porous structure hence, a steep increase in C'' would be seen since there is no dielectric loss in an ideal capacitance when $\omega \rightarrow 0$. At low frequencies, an ideal SC would display

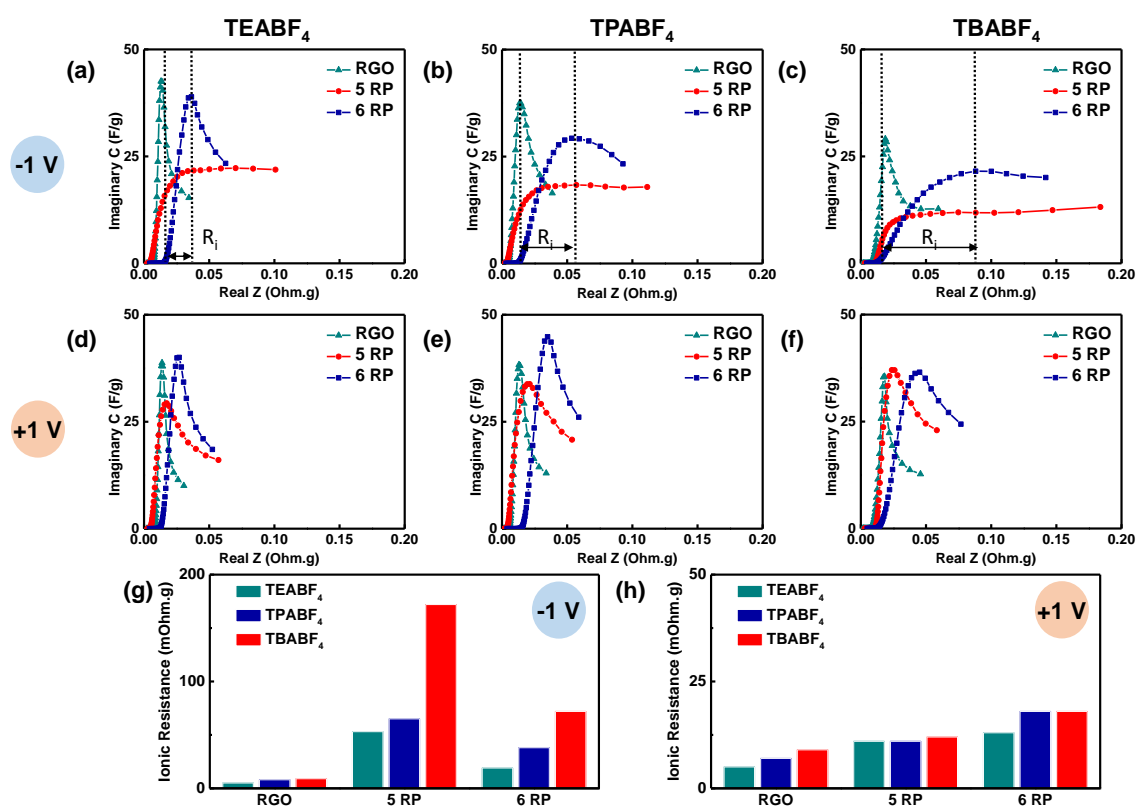*Figure IV-10 Imaginary part of capacitances vs. real impedances for RGO and RPs in 1 M solutions of (a,c) TEABF$_4$, (b,d) TPABF$_4$ and (c,f) TBABF$_4$ in acetonitrile at (a,b,c) 1 V vs. Ag and (d,e,f) -1 V vs. Ag. The arrows in (a), (b) and (c) show increasingly larger ionic resistances (R$_i$) in 6 RP. The obtained R$_i$ values for RGO and RPs at -1 V vs. Ag and 1 V vs. Ag.*

a steep fall in C'' (Equation IV-3). The R_i values were obtained from the real Z values at the start and end of the mid-range frequencies.

The C'' vs Z' plots at -1 V vs Ag show a clear difference between RGO and RPs in TEABF$_4$, TPABF$_4$ and TBABF$_4$ (Figure IV-10a-c). The responses of RGO and RPs under various frequency regions and their evolution in electrolytes could be distinctly identified here compared to Nyquist and Bode plots. RGO displays curves with a clear maxima of C'' occurring at a low resistance and then rapidly decreases along the x-axis. The calculated R_i show close values of around 10 mOhm.g from TEABF$_4$ to TBABF$_4$ (Figure IV-10g). 6RP is closely equivalent to RGO in TEABF$_4$ but, with larger cations, the C'' extends to even higher resistances and eventually shows a continuous plateau with TBABF$_4$. The plateau symbolizes an extended limitation of ion transport inside the porous electrode while the cell not reaching a capacitor-like behavior. This increasingly resistive behavior of 6 RP with larger cations is quantified with rise in R_i values from 20 mOhm.g in TEABF$_4$ to 70 mOhm.g in TBABF$_4$. 5 RP shows continuous plateau with no transition peak even with the smallest cation tested in TEABF$_4$ and already shows a high R_i of 55 mOhm.g. Further increase in cation sizes lead to even higher R_i up to 172 mOhm.g in TBABF$_4$ and much higher values in THABF$_4$ (Figure IV-11). This continuous loss of energy even at the low frequencies led us to examine the leakage currents for all cells. The measured leakage currents show similar values in all cases excluding any faults device fabrication and thus relate the observed plateaus to materials (Table IV-3).

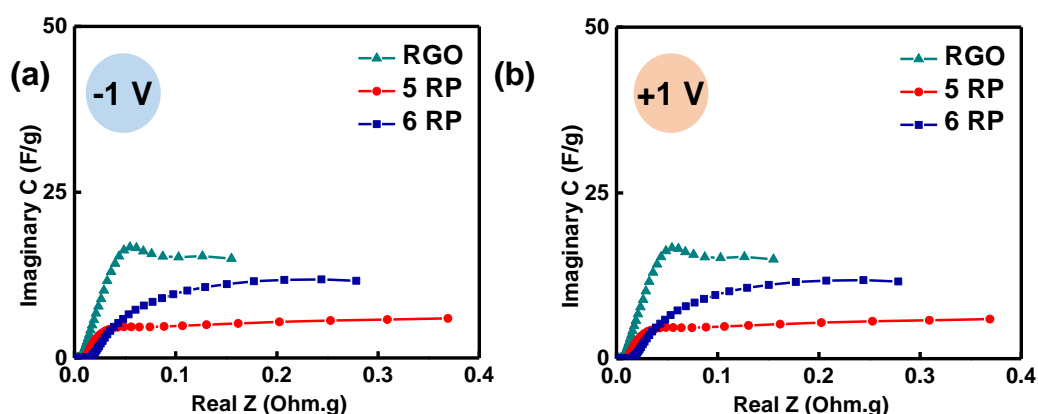*Figure IV-11 C'' vs Z' plots for RGO and RPs in 1 M solution THABF$_4$ in acetonitrile at (a) -1 V and (b) 1 V vs. Ag.*

At 1 V vs. Ag, RGO and RPs show similar curves, however, occurring at different values of real Z (Figure IV-10d-f). The C'' values for RPs occur at greater resistances than RGO indicating greater irreversible energy losses. Among the two RPs, 6 RP has slightly larger ionic resistances

than 5 RP in all the electrolytes (Figure IV-10h). This resistive behavior of 6 RP supports the earlier observed greater τ_0 values than 5 RP. We speculate that the conformation (trans & gauche) of the diamines inside the gallery could be the reason behind this behavior.

Material	TEABF$_4$		TPABF$_4$		TBABF$_4$		THABF$_4$	
	+ 1 V	- 1 V	+ 1 V	- 1 V	+ 1 V	- 1 V	+ 1 V	- 1 V
RGO	15	4	17	4	13	14	11	4
5 RP	4	12	3	12	1	13	1	12
6 RP	3	12	13	3	4	5	23	13

Table IV-3 Leakage currents (µA) for the synthesized cells were obtained by measuring the residual currents after polarizing the fabricated cells at +1 V and -1 V vs. Ag for 1 h.

It has been reported that with increasing alkyl chains lengths in the diamine the ratio of trans-gauche conformations shifts towards higher trans content. [23] Hexanediamine (in 6 RP) may locally occupy higher volume in the gallery than pentanediamine (in 5 RP) and thus have higher ionic resistances. Moreover, the odd and even number of carbons in the diamines used here could also affect the overall polarity and ion sorption in the gallery. The cation sorption at -1 V, masks these fine details among RPs as the steric effects result in large R_i values. As the R_i values at 1 V are smaller, this subtle influence of the alkyl chain conformation on 5 and 6 RPs is seen distinctly.

In short, electrochemical analyses of RGO and RPs through CV and EIS measurements confirm the ion-sieving effect in pillared graphene materials. The access to inter-layer gallery pores in RPs is regulated by the d-spacing/ion size couple. In CVs, RPs show marginally higher specific capacitances than RGO with appropriately smaller ions (TEABF$_4$). With larger ions, access to the galleries is restricted and very low capacitances are recorded. Notably, even in the case of TEABF$_4$, despite their better capacitances, this impedance analysis has confirmed that RPs exhibit sluggish ion transport relative to RGO. This could be due to hindered mobility of the ions in the galleries due to un-adapted porosity or the presence of alkyl diamine pillars. To investigate if the impeded ion transport is due to unsuited porous network, we synthesized and analyzed a pillared graphene hydrogel (GH) that has a 3D percolating network using 1,6-

hexanediamine as the pillar (6 GH) (details in ESI). The 3D percolating network offers multiple ion pathways and is known to show enhanced ion transport characteristics in the hydrogels.[21]
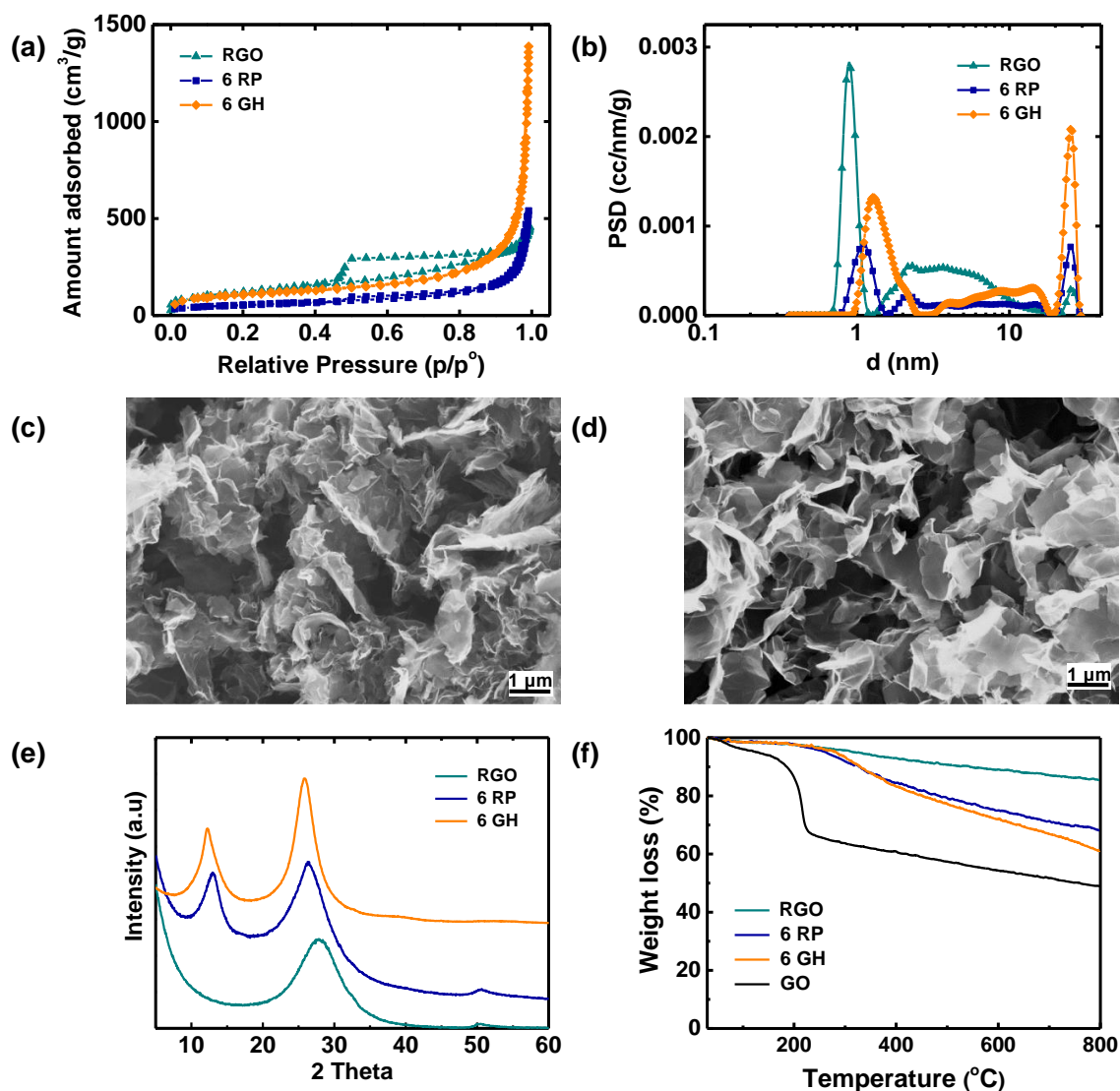
Figure IV-12 (a) Gas sorption isotherms using N_2 and (b) pore size distributions obtained for RGO, 6 RP and 6 GH. Scanning electron microscopy images of (c) 6 RP and (d) 6 GH. (e) X-ray diffraction patterns and (f) thermo-gravimetric curves under N_2 gas for RGO, 6 RP and 6 GH.

The N_2 gas sorption isotherms and corresponding PSDs characterize 6 GH with enhanced micro and mesopores than 6 RP (Figure IV-12a&b). The calculated SSAs indicate increase in the values from 130 m^2/g in 6 RP to 182 m^2/g in 6 GH (Scanning electron microscopic images also reveal more open macro porosity in 6 GH than 6 RP. Additionally, 6 GH shows greater d-spacing of 0.86 nm compared to 0.80 nm of 6 RP probably due to the stronger reaction conditions and diamine consumption during 6 GH synthesis. The TGA profiles of the two materials support this explanation with a greater weight loss due to decomposition of

covalently attached diamines. Electrochemical analysis of 6 GH in 1 M TEABF$_4$, which has sufficiently smaller ions than the d-spacing, shows slightly higher capacitances of 142 F/g than 6 RP (130 F/g) and RGO (117 F/g). This shows that the 3D assembly with improved SSAs, along with the cross-linking at nanoscale, yields enhanced capacitances in these pillared materials. However, the impedance analysis under negative polarizations shows that the ion motion remains very much impeded in 6 GH despite its 3D structure and the larger d spacing (0.86 nm) (Figure IV-13a&b). In fact, the obtained R_i and τ_0 values show greater resistances in 6 GH with higher values of 57 mOhm.g and 23 s compared to 20 mOhm.g and 17 s for 6 RP (Table IV-4).
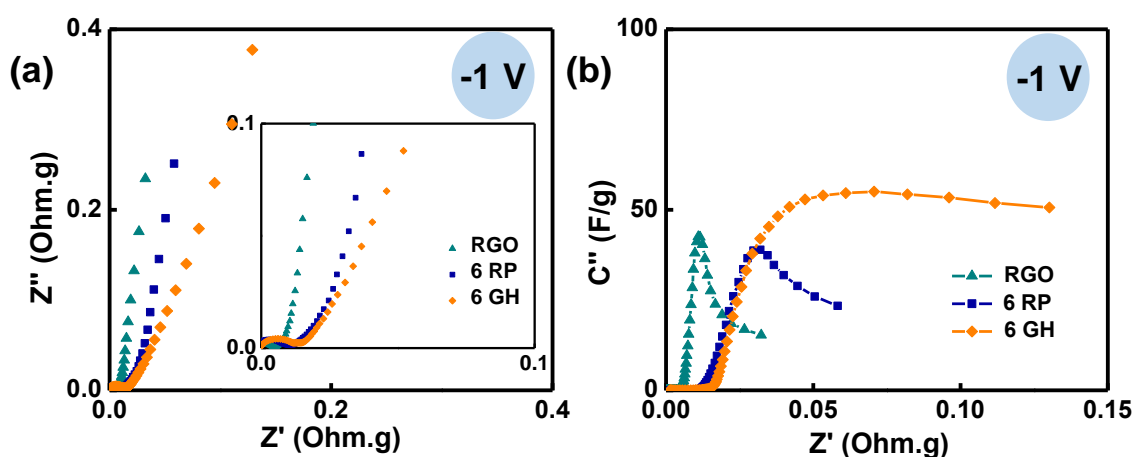
Figure IV-13 (a) Nyquist plots and (b) Imaginary part of capacitances vs. real impedance plots of RGO, 6 RP and 6 GH in 1 M solution of TEABF$_4$ at -1 V vs. Ag. A zoom of the high frequency regions are shown in the inset.

Material	Weight loss (%)	CL d-spacing (nm)	SSA (m^2/g)	Ri mohm.g	τ_0 (s)	Specific Capacitance (F/g)
RGO	15	-	330	6	5	117
6 RP	34	0.80	130	20	17	126
6 GH	39	0.86	182	57	23	142

Table IV-4 Comparison of various parameters between RGO, 6 RP and 6 GH. Ri and τ0 values were obtained under negative polarization of -1 V vs. Ag. in 1 M TEABF$_4$/AN electrolyte. Specific capacitances were calculated from CVs at 20 mV/s in 1 M TEABF$_4$/AN electrolyte in the voltage range of -1 to 1 V vs. Ag.

These observations suggest that the alkyl diamine pillars inside the galleries play an important role in ion transport between the graphene layers. Moreover, the obtained capacitances of both 6 RP and 6 GH are only slightly better than RGO despite ion access to the cross-linked galleries. This is possibly due to excessive filling of the galleries with diamine pillars leading to impeded ion transport to active sites. This understanding of the impact of pillars and the porosity provides new strategies to improve energy and power densities of pillared materials. Decreasing the number of pillars between the graphene layers could be a straightforward strategy for enhanced power and energy values. Integrating additional inter-particle pores could be another strategy for enhancement of energy densities. Collectively, pillared materials with low pillar density and additional inter-particle pores could offer both high energy and power densities.

4. Conclusions

Impedance measurements have been performed to investigate the ion transport dynamics in pillared graphene-based materials. A range of electrolytes with increasing cation sizes and a constant anion size were studied under positive and negative electrode polarizations. Depending on the cation size, Nyquist and Bode plots of RPs exhibited large Warburg like regions and delayed capacitive behaviors whereas RGO responses remained similar. Ionic resistances obtained through C" *vs.* Z' plots enabled a quantitative analysis of these observations and show that the ion transport in RPs is mainly controlled by graphene inter-layer gallery sizes. As RPs sieve ions into the pillared graphene layers, steric effects impede the ion transport when ion size is in the same range as the inter-layer gallery size. RGO adsorbs ions in the inter-particle micro/mesopores and the ion access to the active sites is relatively easier. These results are in accordance with the earlier CV results that have shown that RPs show marginally higher capacitances than RGO but suffer from slow ion transport and exhibit poor power capabilities. This knowledge from cyclic voltammetry and the dynamic ion transport between graphene layers materials gives us perspectives towards enhanced charge storage in graphene materials.

5. Further Conclusions & Perspectives

The electrochemical impedance spectroscopy (EIS) analyses performed in this chapter have supported our earlier observations of ion sieving from cyclic voltammetry (CV) and proposed new ways to improve the performances of pillared graphene materials in SCs. Both 5 and 6 RPs showed high ionic resistances when the ions are larger or of the same sizes of the d-spacing values in the materials. Thus, the findings from the impedance analyses were relatable to the CV experiments.

Even when the smaller TEA$^+$ cation or the anions were studied (under negative and positive polarizations respectively), both the RPs always showed more resistive behavior compared to RGO. The higher ionic resistances of RPs compared to RGO are conceivable as RPs have pillars in the inter-layer galleries that can sterically hinder the ion transport in between graphene layers. In addition, the comparison between 5 and 6 RPs suggests that the presence of bulkier alkyl chains as pillars in 6 RP result in higher ionic resistances among the two RPs.

Furthermore, the comparison of the ionic resistances between 6 RP and 6 GH indirectly highlighted the significant impact of the number of pillars on the overall ion transport. 6 GH, which is synthesized in hydrothermal reaction conditions, has interconnected macro porous network so better ion transport was expected. However, 6 GH displayed higher ionic resistances compared to 6RP which are probably due to the presence of higher amount of diamine pillars in 6 GH compared to 6 RP. The EIS analyses attribute much higher ionic resistances of 60 mOhm.g for 6 GH vs. 20 mOhm.g for 6 RP.

Densely filled galleries　　　　　　　**Sparsely filled galleries**

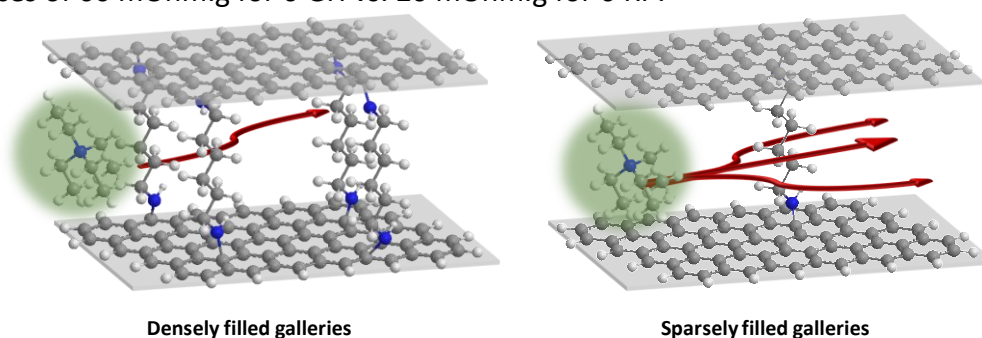*Figure IV-14 Schematic representation of the proposed pillared material with lower number of pillars.*

Overall, it is clear that the pillars in the galleries have a major impact on the ion transport in pillared materials. Hence, we propose to optimize RPs and GHs with a lower number of pillars between the graphene sheets to allow an improved ion transport that could also provide access to the active sites (Figure IV-14).

6. References

1. J. R. Miller and P. Simon, Science, 321, 651 (2008).

2. B. E. Conway, Electrochemical Supercapacitors - Scientific Fundamentals and Technological Applications, Springer International Publishing, NewYork, (1999).

3. P. Simon and Y. Gogotsi, Nat. Mater., 7, 845 (2008).

4. F. Béguin, V. Presser, A. Balducci, and E. Frackowiak, Adv. Mater., 26, 2219 (2014).

5. L. L. Zhang and X. S. Zhao, Chem. Soc. Rev., 38, 2520 (2009).

6. G. Wang, L. Zhang, and J. Zhang, Chem. Soc. Rev., 41, 797 (2012).

7. J. Chmiola et al., Science, 313, 1760 (2006).

8. G. Salitra, A. Soffer, L. Eliad, Y. Cohen, and D. Aurbach, J. Electrochem. Soc., 147, 2486 (2000).

9. C. Largeot et al., J. Am. Chem. Soc., 130, 2730 (2008).

10. E. Raymundo-Piñero, K. Kierzek, J. Machnikowski, and F. Béguin, Carbon, 44, 2498 (2006).

11. M. Salanne et al., Nat. Energy, 1, 16070 (2016).

12. J. Chmiola, C. Largeot, P.-L. Taberna, P. Simon, and Y. Gogotsi, Angew. Chem. Int. Ed., 47, 3392 (2008).

13. C. Pean et al., J. Am. Chem. Soc., 137, 12627 (2015).

14. C. Merlet et al., Nat. Commun., 4, 2701 (2013).

15. R. Raccichini, A. Varzi, S. Passerini, and B. Scrosati, Nat. Mater., 14, 271 (2015).

16. C. Liu, Z. Yu, D. Neff, A. Zhamu, and B. Z. Jang, Nano Lett., 10, 4863 (2010).

17. M. D. Stoller, S. Park, Y. Zhu, J. An, and R. S. Ruoff, Nano Lett., 8, 3498 (2008).

18. Y. Tao et al., Sci. Rep., 3, 2975 (2013).

19. J. Qu et al., J. Phys. Chem. C, 119, 24373 (2015).

20. Y. Xu et al., Nat. Commun., 5, 4554 (2014).

21. C. Li and G. Shi, Adv. Mater., 26, 3992 (2014).

22. H. Banda et al., Chem. Mater., 30, 3040 (2018).

23. M. Herrera-Alonso, A. A. Abdala, M. J. McAllister, I. A. Aksay, and R. K. Prud'homme, Langmuir, 23, 10644 (2007).

24. W.-S. Hung et al., Chem. Mater., 26, 2983 (2014).

25. L. Eliad, G. Salitra, A. Soffer, and D. Aurbach, J. Phys. Chem. B, 105, 6880 (2001).

26. W. S. Hummers and R. E. Offeman, J. Am. Chem. Soc., 80, 1339 (1958).

27. N. Ashok Kumar, S. Gambarelli, F. Duclairoir, G. Bidan, and L. Dubois, J. Mater. Chem. A, 1, 2789 (2013).

28. H. Banda et al., J. Power Sources, 360, 538 (2017).

29. D. Li, M. B. Muller, S. Gilje, R. B. Kaner, and G. G. Wallace, Nat Nano, 3, 101 (2008).

30. I. K. Moon, J. Lee, R. S. Ruoff, and H. Lee, Nat. Commun., 1, 73 (2010).

31. J. Jagiello and J. P. Olivier, Carbon, 55, 70 (2013).

32. G. Srinivas, J. W. Burress, J. Ford, and T. Yildirim, J. Mater. Chem., 21, 11323 (2011).

33. J. W. Burress et al., Angew. Chem. Int. Ed., 49, 8902 (2010).

34. C. Portet, P. L. Taberna, P. Simon, and C. Laberty-Robert, Electrochimica Acta, 49, 905 (2004).

35. R. de Levie, Electrochimica Acta, 8, 751 (1963).

36. R. de Levie, Electrochimica Acta, 9, 1231 (1964).

37. J. Segalini, B. Daffos, P. L. Taberna, Y. Gogotsi, and P. Simon, Electrochimica Acta, 55, 7489 (2010).

38. F. Bardé, P. L. Taberna, J. M. Tarascon, and M. R. Palacín, J. Power Sources, 179, 830 (2008).

39. J. M. Griffin et al., Nat. Mater., 14, 812 (2015).

40. D. Aurbach et al., J. Electrochem. Soc., 155, A745 (2008).

41. R. Lin et al., Electrochimica Acta, 54, 7025 (2009).

42. P. L. Taberna, P. Simon, and J. F. Fauvarque, J. Electrochem. Soc., 150, A292 (2003).

43. K. S. Cole and R. H. Cole, J. Chem. Phys., 9, 341 (1941).

44. B. Abdulhakeem et al., RSC Adv., 4, 39066 (2014).

CHAPTER V

Study of Pillared Graphene Materials with Optimized Pillar Densities for SCs

Chapter V. Study of Pillared Graphene Materials with Optimized Pillar Densities for SCs

1. Objectives & Approach

Learning from the conclusions of the previous two chapters, herein, we aim to study pillared graphene materials (RPs and GHs) that have lower number of pillars (pillar density) between the graphene layers. GHs were synthesized in the previous chapter but were only analyzed for their ion transport behavior. Herein, we study them along with RPs as two materials with a pillared nano structures and different porosities. Overall, the main objective of this chapter is to optimize the proposed pillared graphene materials towards achieving the promised potential of high capacitances through charge storage inside the inter-layer galleries. We speculated that a lower pillar density could allow ion access into the inter-layer galleries and provide additional ion sorption sites. Additionally, low number of pillars could reduce the steric hindrance experienced by ions inside the galleries and thus result in improved ion transport characteristics.

However, decreasing the diamine content in an ad-hoc manner could lead to few undesired consequences including; (i) poor stability of the pillared structures during the electrochemical cycle life and (ii) higher relative content of restacked domains compared to cross-linking domains in the material (leading to loss of active sites). Earlier reports in the literature have suggested a systematic approach of synthesizing the materials with varied amounts of the pillar molecule (equivalents) and analyzing the resulting d-spacing values. Typically, a maximum in d-spacing values is seen with respect to the equivalents of the pillar molecule as most of the highly reactive oxygen functional groups on the GO sheets access a pillar molecule.

As described above, in this final chapter, we wanted to study the impact of the pillar density on the electrochemical performances of the pillared materials and enhance SCs performances through optimization of pillar amount. Thus, we performed syntheses of both the pillared materials (RPs and GHs) using a range of diamine equivalents. Owing to the focused nature of this study, we chose and synthesized all the materials by using one alkyl diamine (1,6-diaminohexane) as the pillar molecule and TEABF$_4$ as the electrolyte. Among the class of materials synthesized, specific materials with similar d-spacing but synthesized with different equivalents were chosen for electrochemical studies. Maintaining similar d-spacing values for

the materials is important for this comparison of pillar density, as two different gallery spacings could lead to different ion transport properties.

Pillared graphene hydrogels were also synthesized using the hydrothermal approach presented in the last chapter. Although a brief comparison of ionic resistances in 6 GHs and 6 RPs was done in the last chapter, a holistic comparative study of overall performances of the optimized materials is presented here. Among the class of materials synthesized, two specific 6 GH and 6 RP materials were chosen with similar d-spacing values but varying bulk porosity for an analysis of their porous characteristics.

Many of the carbon-based materials used for SC applications have low materials densities and thus have low volumetric specific capacitances. Despite the great interest in 6 GHs with its interconnected porosity for SC applications, they have very low densities of < 0.1 g.cm^{-3}, limiting their applications in SCs. Hence, it is important to improve both the gravimetric and volumetric capacitances of the monoliths. Fortunately, as described earlier in the introduction, monoliths and other macroporous structures have large amounts of trapped water and could be densified through capillary compression, i.e. slow evaporation of water. In fact, up on densifying, these 3D materials are expected to have greater materials densities in the range of their 2D counterparts. Thus, we synthesize and analyze the volumetric performances of pillared graphene materials by adapting the simple ambient drying approach from the literature.

The results obtained from this work are written as an article and has been submitted to the journal "*Advanced Energy Materials*".

FD and HB conceptualized the idea and designed the work. HB and SP performed experiments and analysed data. BD and DL performed gas sorption and NMR experiments respectively. PLT, PS, LD, DL and GDP aided with data analysis and discussions. FD and HB complied the work and wrote the manuscript and all authors have discussed the results and contributed to the final manuscript.

Efficient Ion Transport and Storage inside Covalently Pillared Graphene Materials for High Performance Supercapacitors

Harish Banda[†], Sandy Périé[†], Daniel Lee[‖], Barbara Daffos[¶‡], Pierre-Louis Taberna[¶‡], Lionel Dubois[†], Olivier Crosnier[¶§], Patrice Simon[¶‡], Gaël De Paëpe[‖] and Florence Duclairoir[†*]

[†] Univ. Grenoble Alpes, CEA, CNRS, INAC, SyMMES, Grenoble, 38000, France.

[‖] Univ. Grenoble Alpes, CEA, CNRS, INAC, MEM, Grenoble, 38000, France.

[‡] CIRIMAT, Université de Toulouse, CNRS, INPT, UPS, 31062 Toulouse, France.

[§] Institut des matériaux Jean Rouxel (IMN), Université de Nantes, CNRS, Nantes, 44300, France.

[¶] Réseau sur le Stockage Electrochimique de l'Energie (RS2E), FR CNRS, 3459, France.
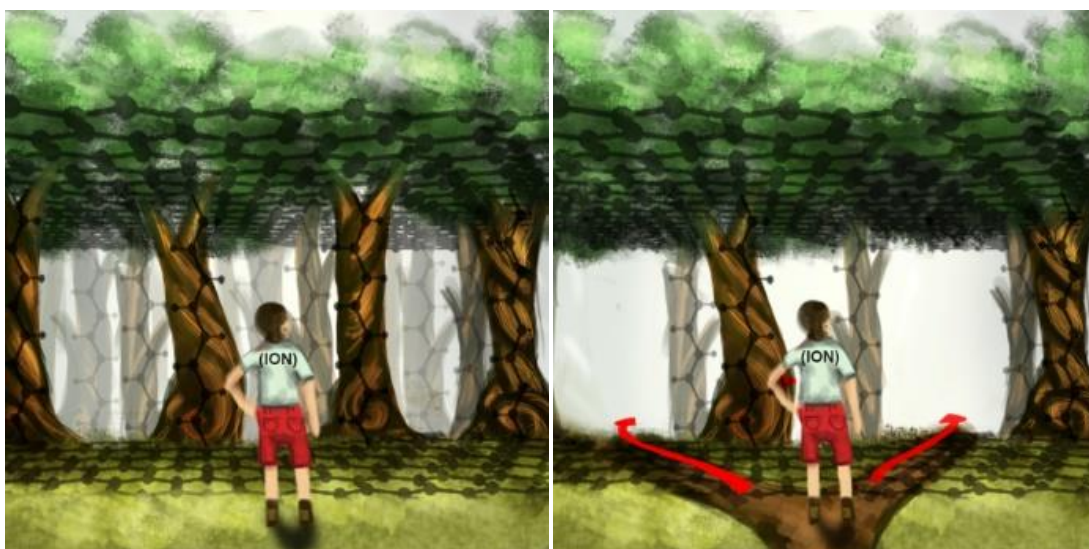
Abstract

Graphene-based materials are extensively studied as promising candidates for high performance supercapacitors (SCs) owing to the high surface area, electrical conductivity and mechanical flexibility of graphene. Reduced graphene oxide (RGO), a close graphene-like material studied for SCs, offers poor specific capacitances (~ 100 F.g⁻¹) as the reduced graphene sheets partially restack through π-π interactions. Herein, we study pillared graphene-based materials to minimize such restacking by forming cross-linked inter-layer

graphene galleries. The pillar molecules, alkyl diamine, were shown to be rigid enough to create cross-linked galleries offering additional ion sorption sites in between graphene layers. [15]N labelled alkyl diamine pillars were used to enable the analysis of the bonding interaction between graphene and the molecules. The related ss-NMR observations allowed, for the first time, to establish the covalent character of this bond. The cyclic voltammetry and electrochemical impedance spectroscopy studies proved that we achieved a simultaneous significant improvement of the specific capacitances (200 $F.g^{-1}$) and power capability through optimization of number of alkyl diamine pillars inside the galleries. Subsequently a simple ambient drying approach was successfully used to densify the synthesized pillared materials and as high volumetric capacitances of 210 $F.cm^{-3}$ were achieved. Overall, this thorough study demonstrates that pillared graphene materials with optimized pillar densities offers a promising route towards realizing the maximum capacitances of graphene-based materials in SCs.

2. Introduction

Electrochemical double-layer capacitors (EDLC), also known as supercapacitors (SCs), are devices that store energy through charge separation from electrolytic ion sorption on charged electrode surfaces.[1] Porous carbons such as activated carbons (ACs) are traditionally used as electrode materials due to their high surface areas and low costs.[2,3] In the last decade, important capacitance contributions from micro pores in carbon materials were discovered in ACs and carbide derived carbons (CDCs).[4–6] Ultra-micro pores (< 1 nm) that were previously thought to be inaccessible for electrolytic ions exhibit significant ion sorption capabilities.[7,8] Extensive studies on materials with tailored pores sizes have revealed that the electrolytic ions partial desolvate and access pores which are otherwise too small to be accessible.[9,10] Further analyses using modelling[11] and *in-situ* techniques[12,13] have shown that the desolvation and confinement of electrolytic ions in such pores restrict charge over-screening and result in efficient charge storage. Researchers have since explored matching pores sizes to electrolytic ions as an efficient strategy for improved energy storage.[14,15] However, difficulties in precisely tuning the pores in traditional carbons along with reliable determination of pore sizes using gas sorption analyses have been the main challenges.[7,8]

In parallel to ACs, various graphene derivatives have been proposed as potential materials for SCs owing to their high electrical conductivities, large surface areas and mechanical flexibilities.[16] Reduced graphene oxide (RGO), readily prepared from graphene oxide (GO), is extensively studied as a model graphene-like material.[17] RGO displays good power capability but suffers from low capacitances as the reduced graphene sheets partially restack through π- π interactions.[18] Various three-dimensional (3D) architectures based on graphene (aerogels, films and fibers) are being evaluated to mitigate such restacking with a focus on tuning the material porosity.[19] Exploring the layered structures of graphene derivatives for ion sorption could be another complementary approach to tuning the material porosity. The graphitic arrangement with 3.3 Å inter-layer separation in restacked graphene derivatives is too small for ion sorption but could be tuned with an intercalant to exhibit an expanded layer structure.[20–23] We speculate that such expanded layered structures could offer additional ion sorption sites through ion desolvation and confinement effects as earlier seen with ultra-micro pores in CDCs.[11]

Recently, we synthesized a class of reduced pillared graphene materials (RPs) with varied inter-layer separation using alkyl diamines as pillars and tested them in SCs.[22] This comprehensive study using ions with various has shown that ions could access the inter-layer graphene galleries as soon as the naked ion sizes are smaller than the gallery height (defined by d-spacing). Although this preliminary study has demonstrated ion-sieving in pillared graphene materials, the observed capacitances remained marginally better than RGO with appropriate electrolytic ions.[22] Further electrochemical impedance analyses have also shown extremely limited ion transport in these galleries. These poor performances probably arise from excessive filling of the galleries with diamine pillars leading to impeded ion transport to active sites.[24,25]

Herein, we report a two-pronged strategy and demonstrate a simultaneous improvement of power and energy densities in pillared materials. Firstly, the number of diamine pillars were systematically lowered for an improved ion transport in the inter-layer galleries of RPs. Secondly, a 3D macro porous graphene hydrogel was synthesized with this low density of pillars and different bulk porosity. Although pillared graphene materials with diamine cross-linkers were proposed a decade ago, the nature of the cross-linking is still being studied.[20,21] Herein, we confirm the covalent attachment between diamines and graphene through solid state nuclear magnetic resonance (ssNMR) studies with ^{15}N labelled diamine. Electrochemical analysis using various electrolytic ions in SCs led to the first observation of ion-sieving[26] in pillared graphene hydrogels. Ion sorption in the inter-layer galleries of the pillared materials with tuned diamine pillar content enabled twice the capacitances (200 F.g^{-1}) compared to RGO (107 F.g^{-1}). Low densities of the gels were overcome by using ambient drying approach and high volumetric capacitance values of 210 F.cm^{-3} were achieved. The definitive evidence of the covalent attachment of diamine and its stability during long electrochemical tests (10000 cycles) brings new perspectives to research on pillared materials for SCs.

3. Material Design & Characterization

GO has been extensively used as an ideal precursor for synthesis of various graphene derivatives owing to its abundant oxygen functional groups.[27] The carboxylic groups at the edges and the epoxy groups distributed on the sheets offer abundant possibilities for functionalization with an organic linker.[28,29] Among others, alkyl diamines are efficient bi-functional groups that could react with these functionalities and cross-link two GO sheets to form pillared graphene materials (Ps).[14,20] We chose 1,6-diaminohexane (6-diamine) as the pillar molecule with a knowledge of the resulting d-spacing (7.8 Å) and the ion sizes of tetraalkylammonium tetrafluoroborate (TAABF$_4$) salts (6.8-9.5 Å for cations and 4.8 Å for anion) from our earlier report.[22] After the initial functionalization of GO with 6-diamine, the resulting 6-Ps were chemically reduced with hydrazine hydrate to give 6-RPs (Scheme V-1a). Diamine functionalized graphene hydrogels (6-GHs) were synthesized in a one-step hydrothermal process by reacting GO with 6-diamine (Scheme V-1b).
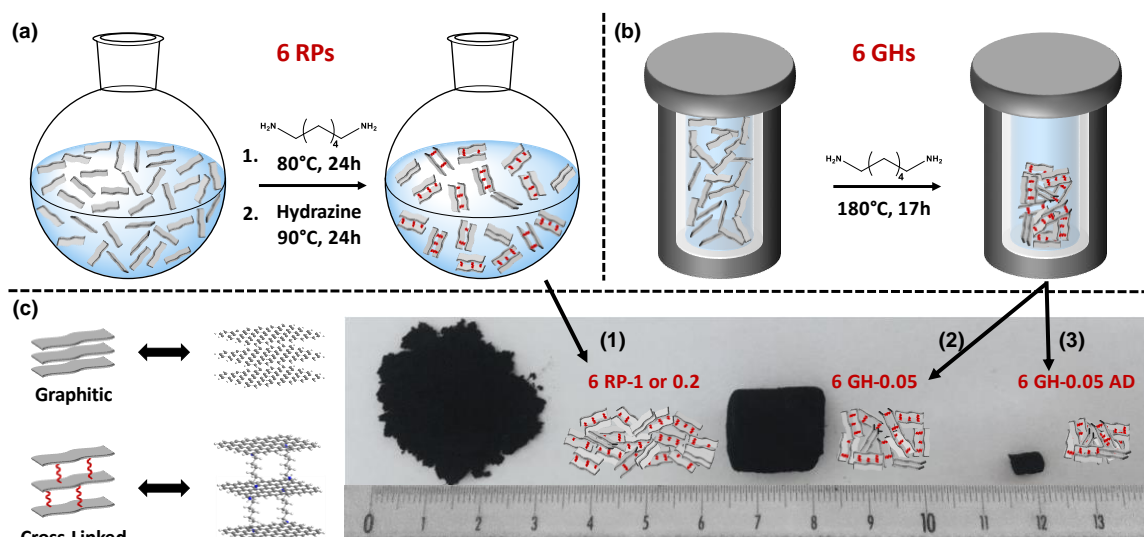
Scheme V-1 Synthesis of reduced pillared graphene materials (RPs) and pillared graphene hydrogels (GHs) using 1,6-diaminohexane. 6-RPs are synthesized in two-step process ; cross-linking and reduction, and (a) dried in vacuum oven at 90°C for 24 h. 6-GHs are synthesized in a one-step process and either (b) freeze-dried or (c) ambient-dried (25°C) for two days. The graphitic and cross-linked domains in each of the materials are represented schematically. The selected materials with chosen equivalents for the electrochemical analyses are presented here in the digital picture with a ruler for scale (cm).

Despite being synthesized in one-step process, the GHs are sufficiently reduced due to the supercritical reaction conditions reached during the hydrothermal process.[30] One equivalent of diamine to GO was chosen as an excess condition where 2 Ns in diamine are available for 1

C in GO (details in materials and methods) and a series of 6-RPs and 6-GHs have been synthesized using X equivalents of diamines with respect to GO and named as 6-RP-X or 6-GH-X. RGO has also been synthesized as a control material by direct reduction of GO with hydrazine hydrate. The synthesized materials were characterized physico-chemically using various spectroscopic techniques and the porosity characteristics were analyzed using scanning electron microscopy (SEM) and gas sorption studies. One-dimensional (1D) and two-dimensional (2D) magic angle spinning (MAS) ssNMR were performed using naturally abundant ^{13}C and ^{15}N-labelled materials.

Pillared graphene materials were proposed in the early 2000s as interesting GO derivatives that could be readily prepared through reaction of the surface epoxy groups with nucleophilic primary amines.[23] Intercalation studies using diamines of various alkyl chain lengths have later allowed to tune the inter-layer spacing of the graphene-based materials.[20] However, the nature of the interaction (i.e. covalent or non-covalent) between alkyl diamines and GO sheets is not clearly understood. Reports in the literature have proposed indirect strategies such as swelling through solvent insertion[21], sequential amine reactions[20] and charge-discharge under polarization to test the robustness of the pillared structures.[22] Although each of the indirect analysis supports the covalent nature of the bond, a direct analysis of the interactions is still lacking. Herein, we perform ^{13}C and ^{15}N ssNMR experiments to directly study the atomic environments of the graphene sheets and the nature of the bond between graphene sheets and the diamine pillars.

^{13}C ssNMR studies were conducted on GO and 6-Ps (0.05, 0.20, 1.00) synthesized with different equivalents of diamines (Figure V-1). These experiments have been restricted to studying 6-Ps rather than 6-RPs as the fully reduced samples display highly conductive behavior, making magic angle sample spinning (MAS) ssNMR studies extremely difficult. Indeed, as 6-P samples are already partially reduced due to mild reducing nature of the alkyl diamine, a large degradation in NMR spectral quality is observed (*vide infra*). The ^{13}C NMR spectrum of the GO starting material shows presence of C=O from carboxylic acids or aldehydes (δ (13C) ~150–200 ppm), aromatic carbons (δ (13C) ~120–140 ppm), C-OH from hydroxyls (δ (13C) ~70 ppm) and C-O-C from epoxides (δ (13C) ~60 ppm) (Figure V-1a).[28,29,31]
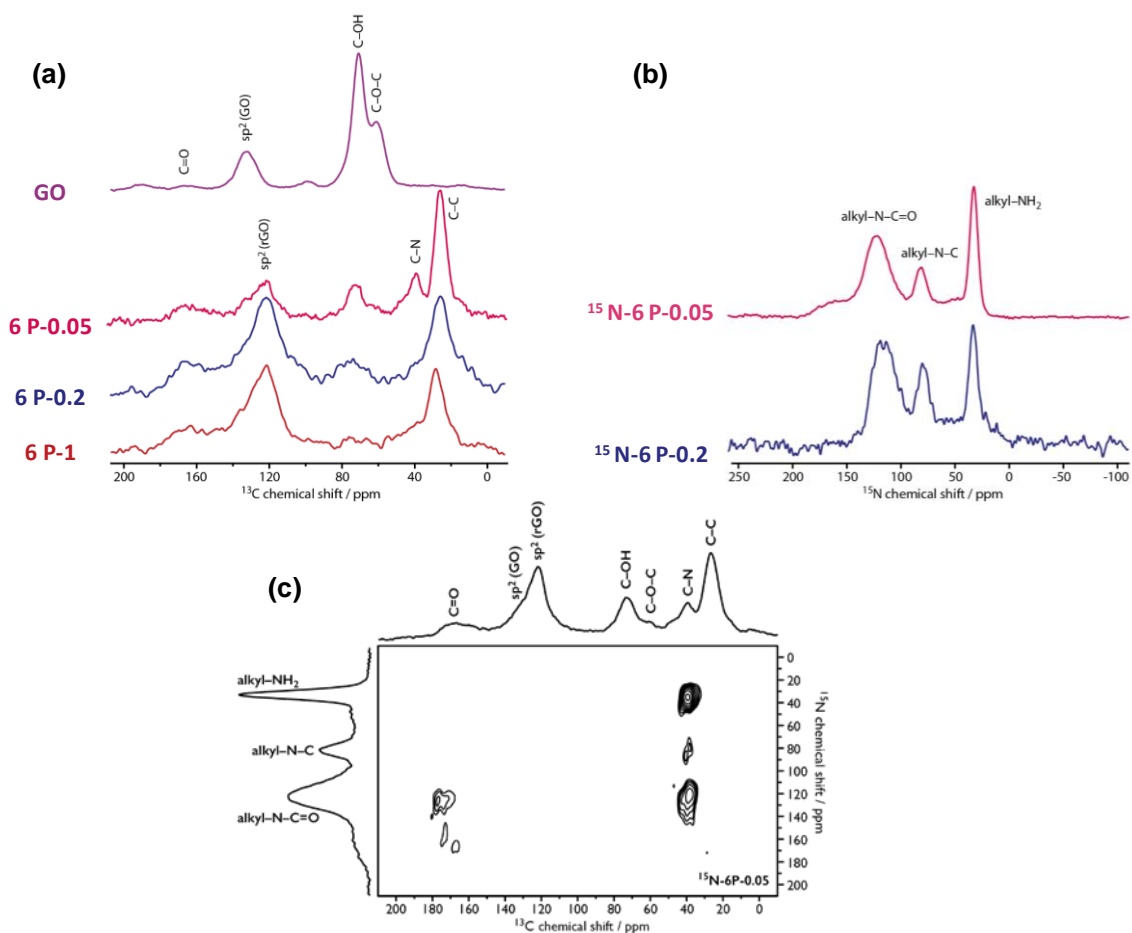
Figure V-1 High resolution 13C ssNMR spectra (natural abundance) were obtained for graphene oxide (GO) and unreduced pillared materials (6-Ps) with varied diamine equivalents. (b) High resolution 15N ssNMR spectra were obtained for the unreduced pillared materials synthesized with different equivalents of ^{15}N labelled 1,6-diaminohexane. (c) 2D ^{13}C/^{15}N chemical-shift correlation ssNMR of 6 P-0.05 synthesized with ^{15}N labelled 1,6-diaminohexane.

After reaction with 1,6-diaminohexane, the ^{13}C spectra of 6-Ps are clearly different to that of GO. New ^{13}C signals (δ (^{13}C) ~10-50 ppm) arising from the alkyl chains of the diamine and reduced GO (δ (^{13}C) ~120 ppm) appear. Carbons in the alkyl chains that are next to the Ns of the diamines are also seen as a different ^{13}C peak (δ (^{13}C) ~40 ppm) in 6-P-0.05. In 6-Ps, the C-O-C epoxides and C-OH hydroxyls signals decrease drastically compared to GO and the C=O moieties signal shift to amide positions (δ (^{13}C) ~150-180 ppm). Even with the low number of diamine equivalents (6-P-0.05 and 6-P-0.2), a large fraction of these functions reacts but the relative amounts of C-OH and C-O-C (δ (^{13}C) ~60-70 ppm) are higher. These observations suggest covalent attachment of the amine groups in pillar molecules with epoxide and carboxylic groups on GO sheets. Still, it is noteworthy here that a simple reduction step and direct adsorption of the pillar molecule may also resemble the above spectral evolution.

The nature of the interaction between the pillar molecules and graphene was further investigated using a ^{15}N-labelled diamine as the pillar. The ^{15}N ssNMR spectra of ^{15}N-6-P-0.05 and ^{15}N-6-P-0.2 display three main peaks (Figure V-1b): (i) δ (^{15}N) ~100-200 ppm, which is assigned to N from amides (formed after reaction of diamine with carboxylic groups on GO sheets), (ii) δ (^{15}N) ~83 ppm, which notably arises from N in α-position relative to aromatic carbon or a C-OH, (iii) δ (^{15}N) ~34 ppm, which is from free amine. The signals at higher nitrogen chemical shifts (δ (^{15}N) >50 ppm) validate that the pillar molecule is covalently grafted, while the peak from free amine reveals that some pillar molecules are either adsorbed on the graphene surface or are mono-grafted. It is possible that the free amine from mono-grafted pillar molecules is able to form hydrogen bonds with functions on the opposite graphene layer, providing additional (non-covalent) interactions. To gain further evidence on the location of the grafted pillar molecules, a through-space (dipolar) 2D [15]N-^{13}C correlation spectrum was recorded on ^{15}N-6-P-0.05. The Transferred Echo Double Resonance (TEDOR) experiment was employed for this purpose, with short mixing time (1.7 ms) so as to detect only directly bonded [15]N-^{13}C pairs. The ^{13}C peak from the C-N carbons (δ (^{13}C) ~40 ppm) correlates with the free amine nitrogen signals ((^{15}N) ~34 ppm), as one would expect for physisorbed or mono-grafted alkyl diamines. Clear correlation peaks can be observed between amide nitrogen (δ (^{15}N) ~110-170 ppm) and amide C=O (δ (^{13}C) ~165-180 ppm) as well as between these same Ns and pillar C-N carbons (δ (^{13}C) ~40 ppm) (Figure V-1c). This proves that the diamines have reacted with the carboxyl functions on GO sheets. Finally, the C-N pillar Cs (δ (^{13}C) ~40 ppm) correlate with the -C-N-C- Ns in α position to aromatics or hydroxyls (δ (^{15}N) ~83 ppm), indicating that the diamine has been grafted to the graphene surface through reactions with epoxides. Overall, these 2D ssNMR experiments on the pillared graphene materials, first on such samples, confirm the covalent grafting of alkyl diamines on graphene.
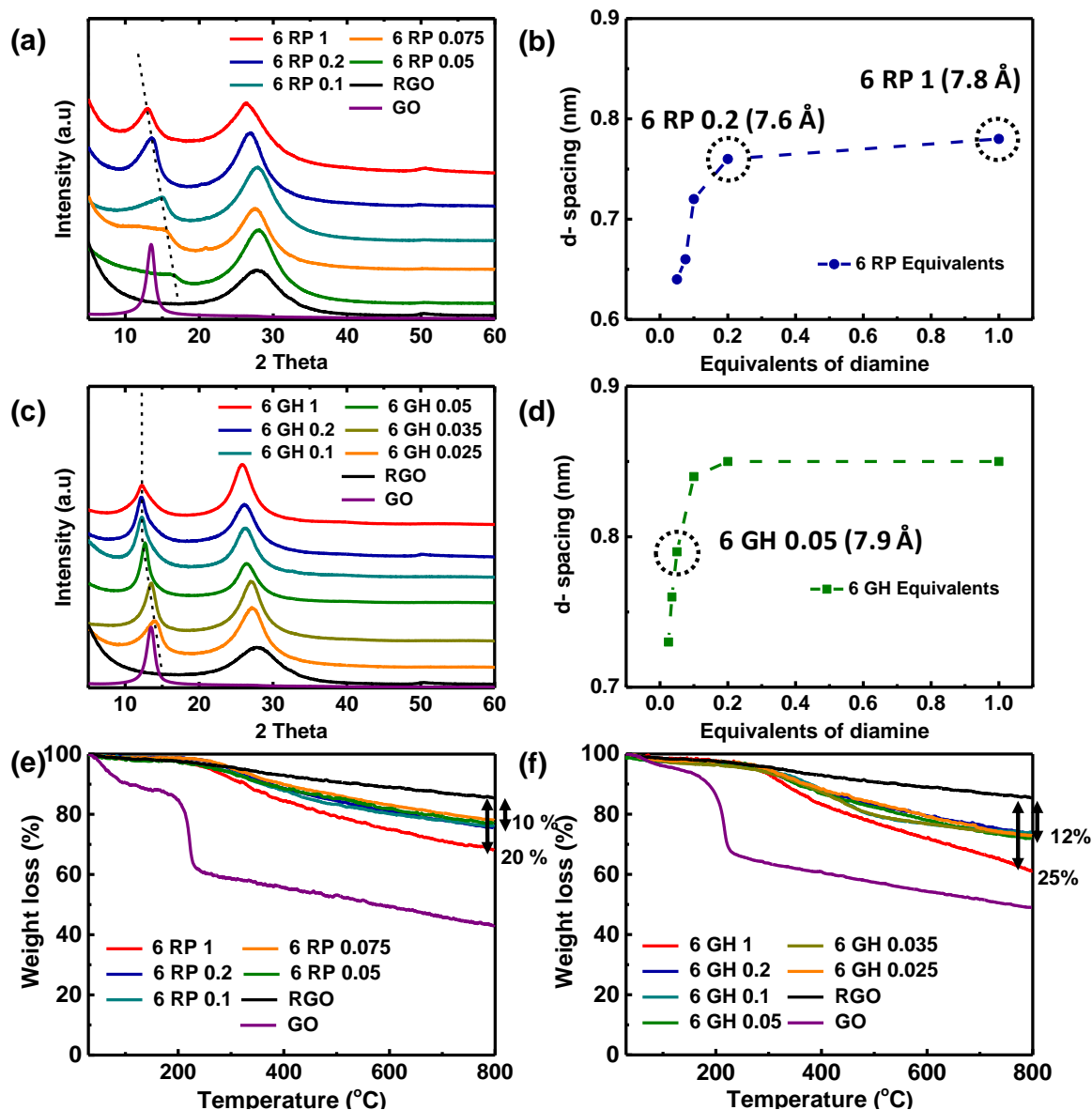
Figure V-2 (a) X-Ray diffraction (XRD) patterns of 6-RPs synthesized with various equivalents and (b) the corresponding d-spacing values of the cross-linked arrangement (CL) (peaks under dotted line). (e) Thermal gravimetric analyses (TGA) of various 6-RPs in the 30-800°C temperature range at 5°C.min⁻¹ ramp rate. (c) XRD patterns, (d) d-spacing values from CL peaks and (f) TGA analyses of 6-GHs synthesized with varied equivalents of diamine. The specific 6-RPs and 6-GH chosen for electrochemical study are highlighted with a dotted circle.

X-ray diffraction (XRD) patterns were obtained to directly analyze the layered structures in the synthesized materials (Figure V-2a&c). Freeze-dried GO shows a sharp peak at a 2θ of 13.5° which relates to a d-spacing of 7.6 Å indicating a high degree of oxidation of the oxidized graphite precursor. Upon direct reduction of GO with hydrazine hydrate, the resulting RGO displays a broad peak at 28° corresponding to a graphite-like pattern (G), suggesting removal of oxygen groups and partial restacking of the reduced graphene sheets.[32] Diamine

functionalization of GO in 6-RPs and 6-GHs shows two distinct diffraction peaks around 25-27° and 11-13°. The peaks at higher angles correspond to G stacking and indicate a reduction degree close to that of RGO. The peaks below 20°, corresponding to diamine intercalation and cross-linking (CL) of graphene sheets, shift with respect to the number of equivalents used.[22] With increasing number of equivalents, the CL peaks of both 6-RPs and 6-GHs systematically shift towards lower angles (higher d-spacing values). The obtained d-spacing values for 6-RP (Figure V-2b) and 6-GH (Figure V-2d) initially increase and then saturate at 0.2 and 1 equivalent for 6-RP and 6-GH respectively. The observed d-spacing values fit well into a chemisorption type model and suggest a grafting of the alkyl diamines on the graphene surfaces instead of a simple physical sorption (Figure V-3).
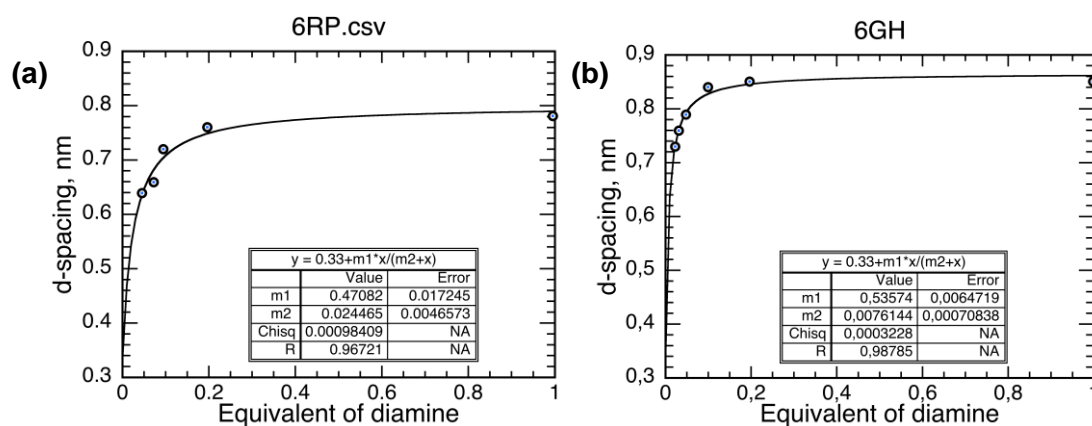
Figure V-3 Variation of d-spacing values with equivalents in (a) 6 RP and (b) 6 GH fit into Langmuir's chemisorption isotherm show good match. Saturation of d-spacing values at higher equivalents suggests grafting instead of physical sorption on the surface.

A closer look at the shape and position of the CL peak reveals important information about evolution of 6-RPs and 6-GH structures with different number of equivalents. 6-RP shows relatively sharper peaks with 1 and 0.2 equivalents whereas increasingly broad and less intense peaks are seen with lower equivalents. On the other hand, whatever the number of equivalent 6-GHs exhibit similar CL peak intensities and width. Nevertheless, in both materials, lower equivalents of diamine lead to lower d-spacing probably due to reduced availability of diamines to react with all epoxides (see discussion on ssNMR). Moreover, 6-RP saturates at a lower d-spacing of ~7.8 Å whereas 6-GH saturates at 8.5 Å. This evolution of shapes and the higher d-spacing values in 6-GH could probably be related to stronger reaction conditions used to prepare GHs compared to RPs. Additional ^{13}C and ^{15}N ssNMR studies were performed on 6-P-0.05 and 6-GH-0.05 to compare the reactivities of epoxides and amine groups under the two

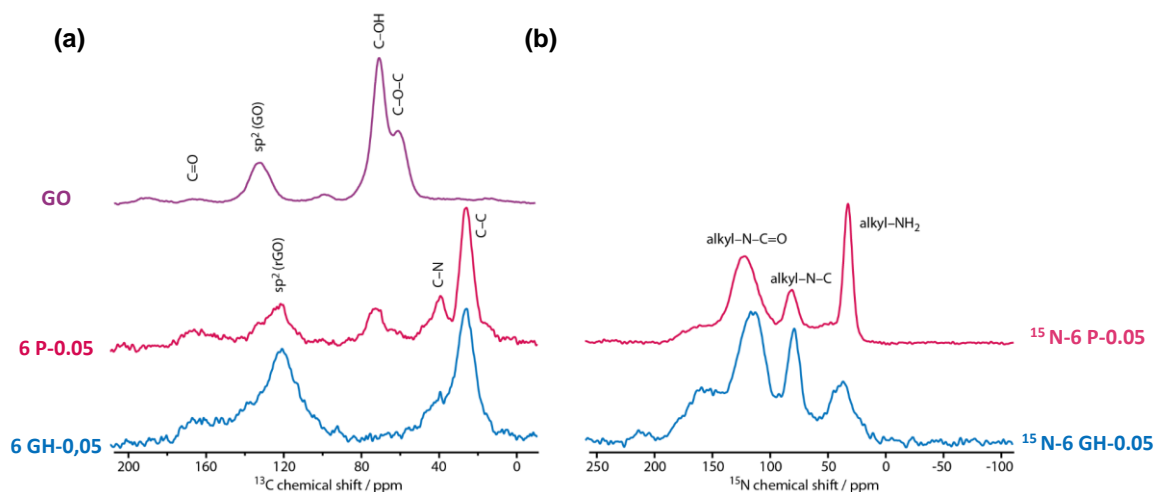*Figure V-4 (a) High resolution 13C ssNMR spectra (natural abundance) were obtained for graphene oxide (GO) and unreduced pillared materials (6Ps) and pillared graphene hydrogel (6GH) with 0.05 equivalents of 1,6-diaminohexane. (b) High resolution 15N ssNMR spectra were obtained for the unreduced pillared materials synthesized with different equivalents of ^{15}N labelled 1,6-hexanediamine.*

different synthesis conditions (Figure V-4). ^{13}C spectra show that 6-GH-0.05 consumes nearly all of the epoxides from the GO precursor whereas 6-P-0.05 still has considerable amounts of unreacted epoxides (Figure V-4a). ^{15}N spectra show an intense peak for free amine (adsorbed/mono grafted amine) in 6-P-0.05 and a relatively weak peak in 6-GH-0.05 (Figure V-4b). The stronger reaction conditions in 6-GHs thus, lead to enhanced cross-linking with diamines and result in higher d-spacing values for same number of equivalents vs. compared to 6-RPs. These reaction conditions enable a diamine anchoring on one GO sheet to find an epoxide group on another GO sheet with relative ease and grow into larger cross-linked particles, also explaining the sharper CL peaks observed for 6-GHs.

The thermal degradation responses of the materials under N_2 are shown in Figure V-2e & f. GO displays two distinct weight loss events corresponding to the first removal of the adsorbed water below 100°C and the decomposition of surface oxygen functional groups around 200°C. A steady drop beyond 200°C is generally attributed to gradual removal of stable functionalities.[33] Upon reduction, RGO only shows a slight weight loss throughout the temperature range suggesting an effective removal of oxygen groups in the synthesis. Both 6-RPs and 6-GHs show a broad weight loss between 300-500°C and a gradual weight loss similar to RGO. This broad weight loss beyond the boiling point of 6-diamine (204°C) is attributed to the removal of non-labile 6-diamine species.[22] Moreover, the absence of loss due to moisture or oxygen functionalities confirms the reduced nature of the functionalized materials.

178

Furthermore, the weight losses between different equivalents of 6-RP or 6-GH show reduced weight losses with lower equivalents, signaling a reduction in diamine grafting densities. Taking RGO as the reference, 6-RP displays weight losses of 20 and 10% with 1 and 0.2 equivalents whereas 6-GH exhibits 25 and 12% (for the same number of equivalents) respectively, corroborating to higher diamine grafting densities as seen in ssNMR (Table V-1).

Material	TGA analyses	XPS - Elemental Composition			XRD analyses		Gas Sorption analyses
	Wt. loss (%)	C %	O %	N %	d (Å) - G	d (Å) – CL	SSA ($m^2.g^{-1}$)
GO	43	74.7	25.3	-	-	7.6	-
RGO	14	91.2	4.5	4.3	3.7	-	330
6 RP 1	34	88.3	5.6	6.3	3.9	7.8	138
6 RP 02	24	87.4	6.3	6.2	3.9	7.6	201
6 GH 005	26	89.3	5.7	5.0	3.9	7.9	206
6 GH 005 AD	27	89.1	5.8	5.1	3.9	7.8	148

Table V-1.Thermal gravimetric weight loss values, elemental composition values from X-ray photoelectron spectroscopy, d-spacing obtained from X-ray diffraction spectra and specific surface area values obtained from N_2 gas sorption analyses for the synthesized materials.

The porosity and morphologies of these chosen materials were observed by N_2 gas sorption and SEM analyses.[34] The tested materials exhibit type II adsorption-desorption isotherms with a hysteresis loop and indicate presence of both micro and mesopores (Figure V-5a).[35] RGO has the highest SSA of 330 $m^2.g^{-1}$, whereas 6-RP-1, 0.2 and 6-GH-0.05 display lower SSA values of 140, 200 and 200 $m^2.g^{-1}$, respectively (Table V-1). Previous reports on pillared materials have suggested that the pillars inside the inter-layer galleries could sterically hinder gas sorption and render the galleries as closed pores.[25] This could be a plausible explanation for the lower SSA values of 6-RPs and 6-GH compared to RGO. Additionally, higher SSA values recorded for 6-RP-0.2 and 6-GH-0.05 (with lower number of equivalents) than for 6-RP-1 also support the explanation that a decreasing number of pillars lead to increased SSAs. The calculated PSDs show major presence of micro pores in RGO and mesopores in 6-RPs and 6-GH-0.05 (Figure V-5b). The expected three-dimensional macro-porous network in 6-GH-0.05 might be too big to be probed through gas sorption analysis. The comparison of SEM images of 6-RP-0.2 (Figure V-6c) and 6-GH-0.05 (Figure V-6d) show this 3D network of large macro-pores arising from the hydrothermal treatment. Hence, we study the electrochemical

performances of 6-RP-1 (high diamine content), 6-RP-0.2 (low diamine content) and 6-GH-0.05 (low diamine content and different macro-porosity) in SCs as materials with different properties.
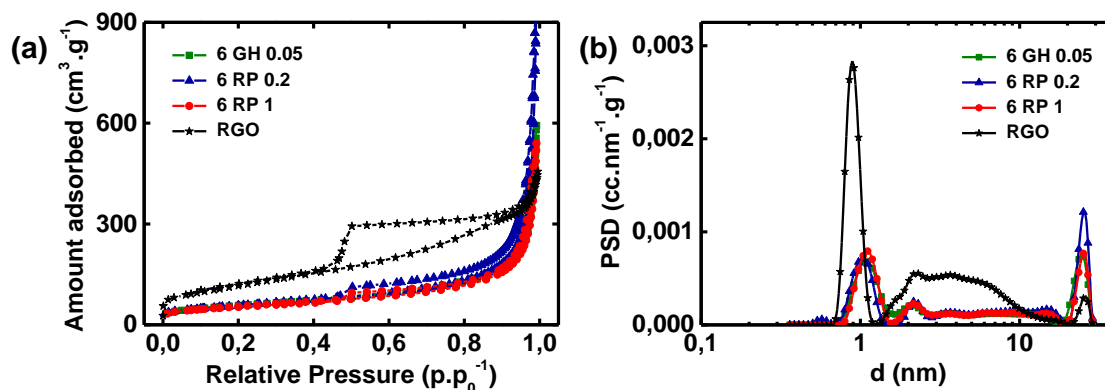
Figure V-5 (a) N_2 sorption isotherms recorded at 77 K and (b) pore size distributions calculated using 2D non-local density functional theory for the synthesized materials.
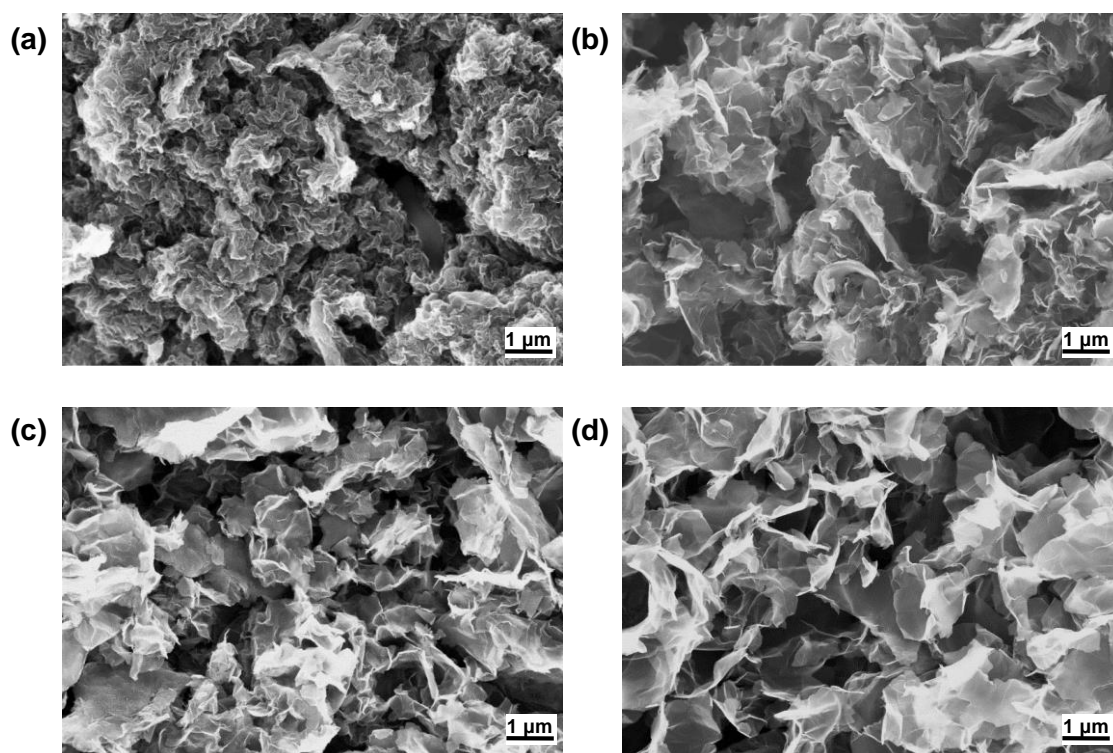
Figure V-6 Scanning electron microscopy images of (a) RGO, (b) 6 RP, (c) 6 RP-0.2 and (d) 6 GH-0.05

In summary, GHs and RPs both are cross-linked with alkyl diamines, are reduced and chemically similar despite synthesis under different reaction conditions. For the current study, we would like to study the impact of the number of diamine pillars in the galleries and the bulk porosities on the overall ion sorption in SCs. Hence, we choose 6-RP 1 as a sample with

high number of diamine pillars in the galleries and 6-RP-0.2 and 6-GH-0.05 as samples with similar d-spacing to 6-RP-1 (~ 7.8 Å) but with a lower diamine filling content (Table V-1). RGO, with no CL galleries, acted as a control sample.

4. Electrochemical Analysis

4.1 Ion-sieving

Cyclic voltammetry (CV) and electrochemical impedance spectroscopy (EIS) studies were performed in SC lab cells to analyze 6-RP-1, 6-RP-0.2, 6-GH-0.05 and RGO. Although the synthesized 6-RP-0.2 and 6-GH-0.05 have similar d-spacing to 6-RP-1 (~ 7.8 Å), the two materials were first analyzed in three electrode-configuration to probe their ion-sieving capabilities. Various 1 M TAABF$_4$ salts in acetonitrile (AN) with increasing cation size and a constant anion size were used as electrolytes; ethyl (TEA$^+$) - 6.8 Å, propyl (TPA$^+$) – 7.6 Å, butyl (TBA$^+$) - 8.2 Å, hexyl (THA$^+$) - 9.5 Å and BF$_4^-$ - 4.8 Å.[36,37] Earlier ion-sieving analyses under positive and negative polarization from open circuit potentials (OCV) of ~ 0.1 V vs. Ag have enabled analyses of anion and cation sorption in SCs.[38] 6-RP-1 displayed rectangular capacitive curves with smaller ions but showed distorted curves and reduced currents under negative polarization when the ion sizes are close or higher to d-spacing (Figure V-7b).
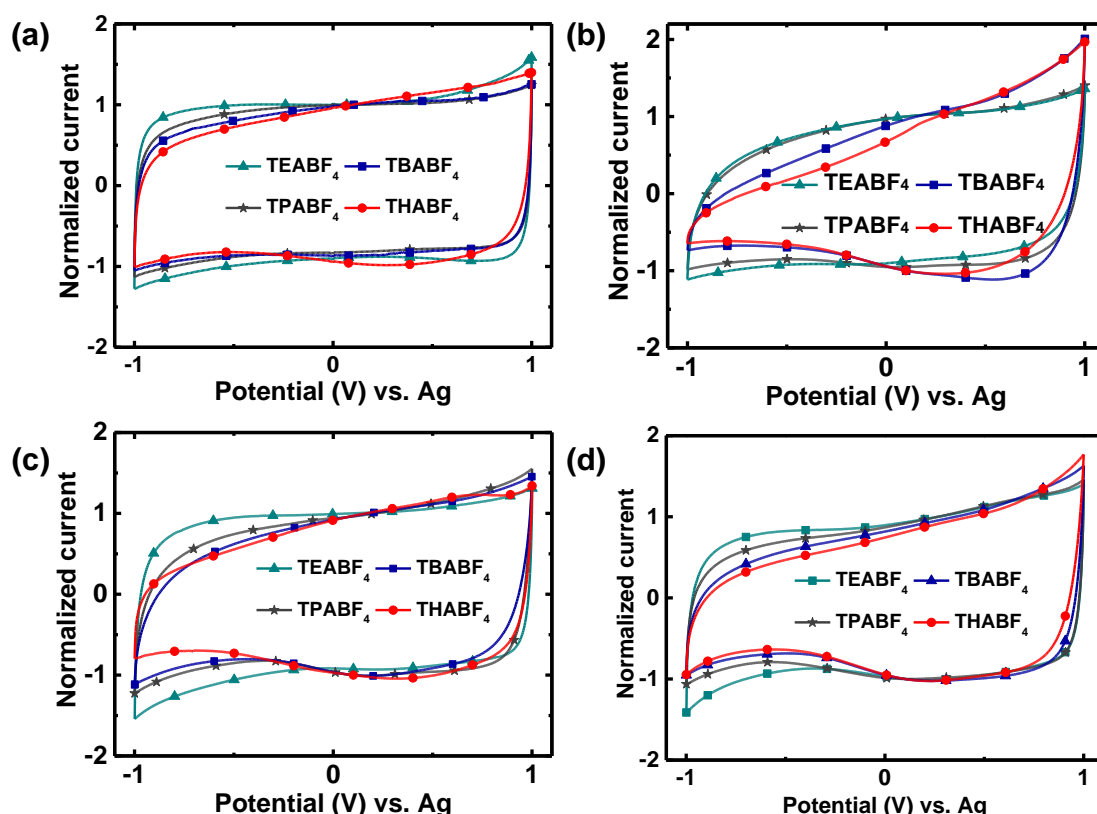

Figure V-7 Normalized three-electrode cyclic voltammograms of (a) RGO, (b) 6 RP, (c) 6 RP-0.2 and (d) 6 GH-0.05 obtained at a scan rate of 0.02 V.s^{-1} in the voltage range of -1 V to 1 V vs. Ag in 1 M solutions of TAABF$_4$ salts in acetonitrile (AN).

Similar tests performed here with 6-RP-0.2 and 6-GH-0.05 show quasi-ideal capacitive behavior under positive polarization where the anion is smaller than the d-spacing in the materials (Figure V-7c&d). Under negative polarization, both materials show gradual reduction in currents as the cation sizes approach d-spacing in the materials. Since 6-RP-0.2 and 6-GH-0.05 both show a lack of ultra-micro inter-particle pores, the observed sieving could be attributed to the inter-layer galleries. Overall, these results affirm ion access to the inter-layer galleries in 6-RP-0.2 and 6-GH-0.05 and could be compared to 6-RP-1 for an analysis of ion transport in the inter-layer galleries.

4.2 Impedance Analyses

The ion transport dynamics in the synthesized materials were studied using EIS measurements. 1 M TEABF$_4$/AN is chosen as an electrolyte with sufficiently small ion sizes that could access the inter-layers galleries of pillared materials. Impedance responses were recorded at 1 V and -1 V vs. Ag to obtain the distinct anion and cation transport characteristics respectively and the normalized complex plane Nyquist plots are displayed in Figure V-8.

These plots can be divided into three regions of high, medium and low frequencies.[39,40] At high frequencies, only the electrical conductivity of the electrode together with bulk electrolyte ionic conductivity can be seen; thus, SC electrodes behave like a resistor (Z"=0). In low frequencies, a sharp increase of the imaginary part of the impedance (-Z") related to capacitive behavior is seen. The intermediate 45° region is associated with the electrolyte resistance arising from ion transport in the porous network of the electrode. At 1 V vs. Ag, the pillared materials and RGO display capacitive-like similar Nyquist curves and indicate comparable anion transport behavior (Figure V-8a). A closer look at the high frequency region (inset) shows slightly larger 45° region for 6-RP-1 compared to others. The slight differences of ion transport could probably be more obvious under -1 V vs. Ag when the larger TEA$^+$ cations are involved. At -1 V vs. Ag, 6-RP-1 exhibits a large 45° region in the medium frequencies compared to others, signaling higher ion transport resistance (Figure V-8c). 6-RP-0.2 and 6-GH-0.05, which possess low number of diamine pillars, show a significantly improved ion transport with smaller 45° region than 6-RP-1. This difference in ion transport highlights the merits of having less pillars. Interestingly, 6-RP-0.2 and 6-GH-0.05 seem to show similar curves despite their differences in material macro-porosity.
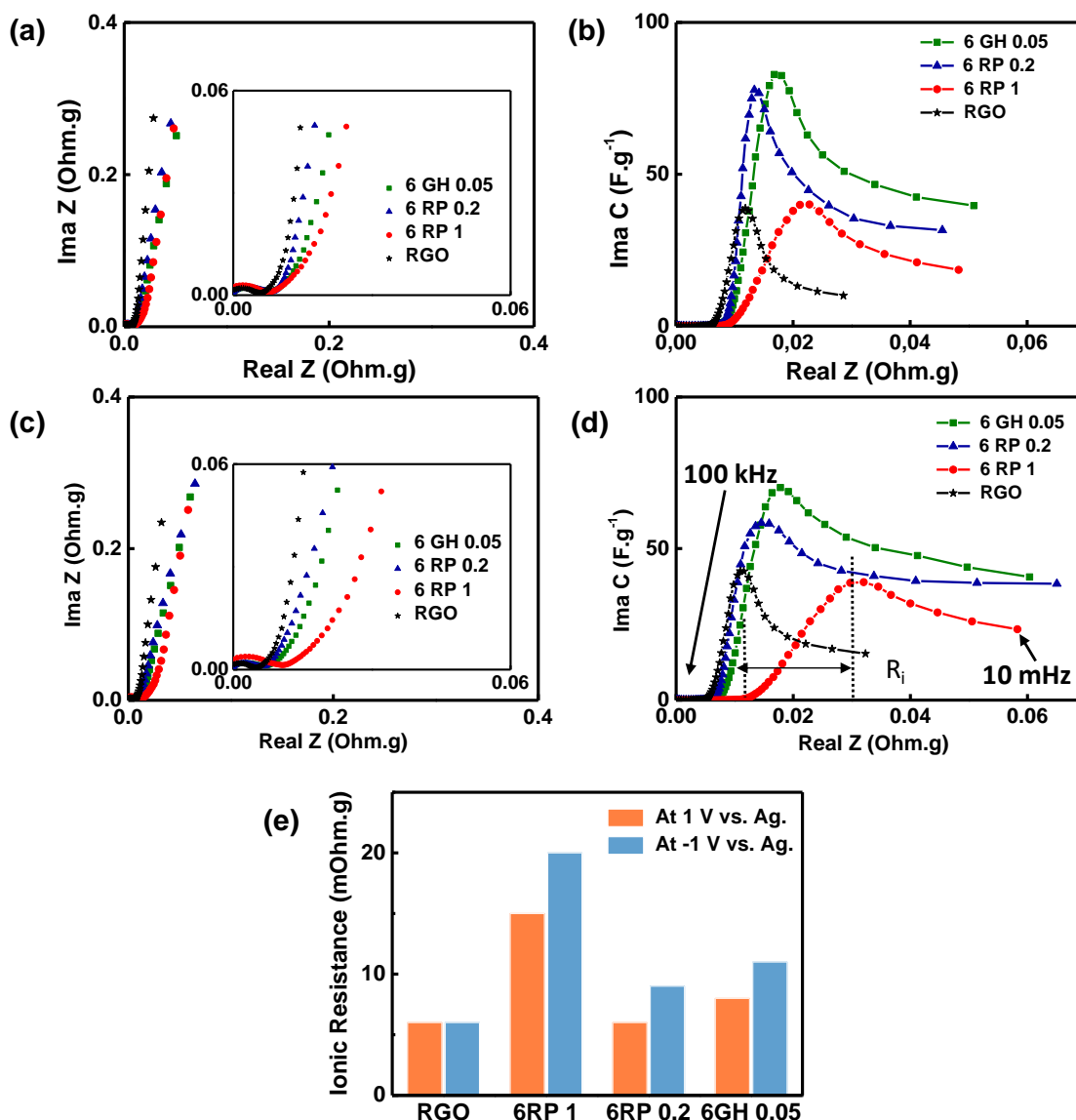
Figure V-8 Electrochemical impedance measurements and CVs were performed on all the synthesized materials in a three-electrode configuration using 1 M TEABF₄/AN as electrolyte. (a) Normalized Nyquist plots obtained at (a) 1 V and (c) -1 vs. Ag. A zoom of the high and mid-frequency regions in Nyquist plots is shown in the insets. Imaginary capacitance vs real impedance plots at (b) 1 V and (d) -1 V vs. Ag. The double-arrow indicates the ionic resistance (R_i) in 6 RP-1. (e) R_i values obtained for the synthesized materials at 1 V and -1 V vs. Ag are shown in a histogram.

The obtained Nyquist plots give an idea about the relative impedances of the materials but are difficult to use to extract information about frequencies. Complex capacitance model reported by Taberna *et al*[41]. derived from Cole and Cole,[42] provides an easier way of studying frequency responses of the materials. The real and imaginary parts of capacitance, defined as C'(w) and C''(w) in Equation V-1 & Equation V-2, represent the available stored energy with respect to frequency and energy losses during the charge storage respectively. Z'(w) and Z''(w) are the real and imaginary parts of impedance Z (w) whereas w is the frequency.

$$C'(w) = \frac{-z''(w)}{w|z(w)|^2}$$

Equation V-1

$$C''(w) = \frac{-z'(w)}{w|z(w)|^2}$$

Equation V-2

As C'' represents the irreversible losses in a SCs, we propose to study C''(w) with respect to Z'(w) (Figure V-8b&d). Such an analysis would relate energy losses to the impedance in various frequency regions and also enable easier determination of the distinct ionic resistances (R_i) in the materials.[22] The C''(w) vs Z'(w) plots at 1 V vs Ag show clear differences between 6-RP-1 and others (Figure V-8b). 6-RP-1 displays a broader curve and occur at high resistances whereas, RGO, 6-RP-0.2 and 6-GH-0.05 exhibit sharper curves and occur at low resistances. With the larger TEA$^+$ cation at -1 V vs. Ag, 6-RP-1 shifts to even higher resistances (Figure V-8d). The R_i values at both the potentials were readily obtained from the C''(w) vs Z'(w) curves and shown in Figure V-8e. R_i values for 6-RP-0.2 and 6-GH-0.05 are close around 6 and 10 mOhm.g under 1 V and -1 V, whereas 6-RP-1 displays higher R_i values of 15 and 20 mOhm.g respectively. These quantified ionic resistances highlight the impact of decreased number of pillars on the ion transport inside the galleries. Additionally, R_i values obtained for the lower number of equivalents (6-RP-0.2 and 6-GH-0.05) are closer to that of RGO that has no cross-linked galleries and highlight the potential in optimizing these pillared materials.

The imaginary C''(w) vs. w curves have a maximum at a frequency f_0 that defines the transition between purely resistive and capacitive behaviors of a SC (Figure V-9a&c). This frequency, known as knee frequency, defines the time constant (τ_0) as minimum time required to extract half of the capacitance from a SC.[41] The τ_0 values of a SC depend on the combination of all the ionic, electrical and cell resistances. 6-RP-0.2 and 6-GH-0.05 exhibits τ_0 values of 5 and 7 s respectively under both polarizations and are close to that of RGO (5 s). 6-RP-1 shows high values of 13 and 17 s under negative and positive polarization respectively (Table V-2). These τ_0 values are highly linked to the improved ion transport dynamics, thanks to a lower the number of pillars in the galleries, and indicate better power capabilities in SCs. The real C'(w) vs. w curves provide an estimation of the available energy stored in the synthesized materials (Figure V-9b&d). The maximal C'(w) values of 6-RP-0.2 and 6-GH-0.05 under both polarizations
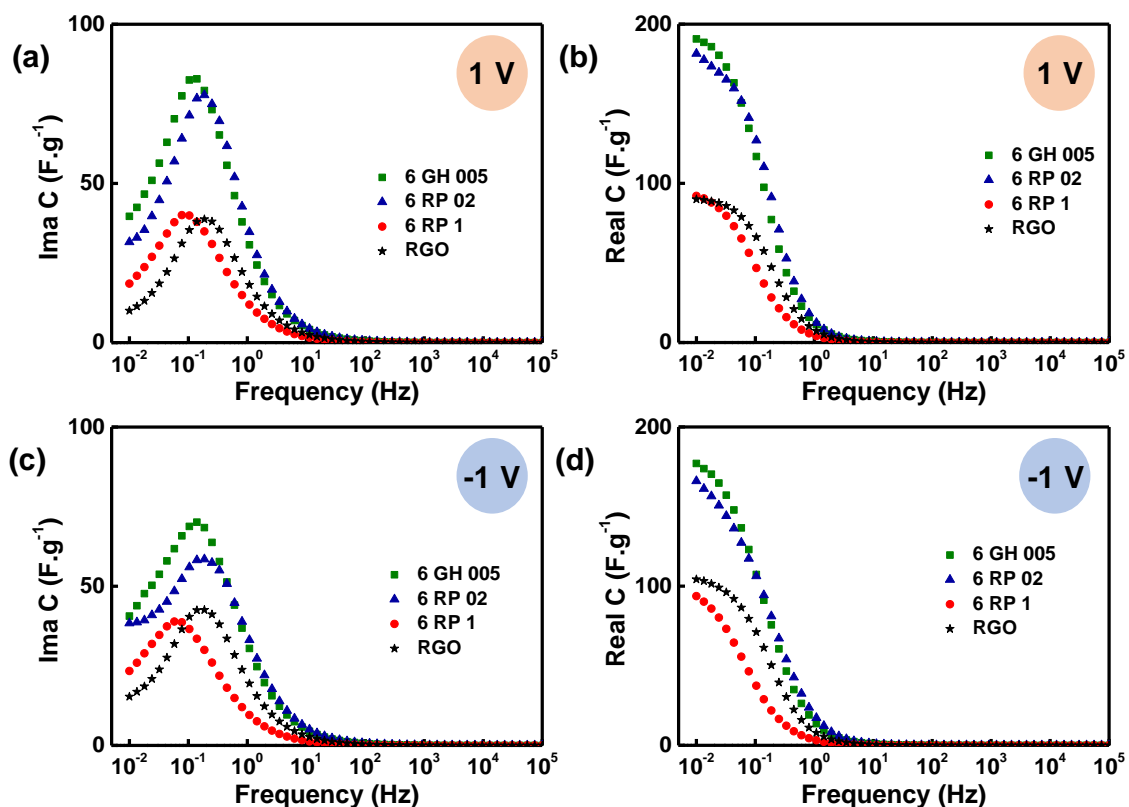
Figure V-9 Imaginary capacitance vs. frequency plots for the synthesized materials in 1 M TEABF$_4$/AN electrolyte at 1 V (a) and -1 V (c) vs. Ag. Real capacitance vs. frequency plots at 1 V (b) and -1 V (d) vs. Ag.

Material	f_0 under +1 V vs. Ag (Hz)	Positive Time Constant (s)	f_0 under -1 V vs. Ag (Hz)	Negative Time Constant (s)
RGO	0.187	5.4	0.187	5.4
6 RP 1	0.078	12.8	0.058	17.3
6 RP 02	0.187	5.4	0.187	5.4
6 GH 005	0.140	7.1	0.140	7.1

Table V-2 The imaginary part of the capacitance goes through a maximum at f$_0$ and is identified from the imaginary capacitance vs frequency plot. Time constant (τ$_0$) values of the synthesized materials were extracted from the f0 values under both positive and negative polarizations vs. Ag.

186

are nearly two times larger than that of 6-RP-1. The low number of pillars probably give access to additional active sites inside the inter-layer galleries that were previously inaccessible and lead to higher capacitances. Additionally, the C'(w) values of 6-RP-0.2 and 6-GH-0.05 are also twice of that for RGO. Since RGO does not have any cross-linked galleries, this difference could be attributed to increased number of adsorption sites inside the cross-linked galleries of 6-RP-0.2 and 6-GH-0.05.

In short, EIS analyses clearly indicate the role of pillars in the ion transport dynamics in the pillared materials. Based on the understanding from the discussion above, a schematic describing the improved ion transport and ion sorption capabilities in the pillared materials with less number of pillars is depicted (Scheme V-2 - right). The τ_0 and R_i values of the optimized 6-RP-0.2 and 6-GH-0.05 account for an improved ion transport compared to 6-RP-1 and are similar to that of RGO. It clearly shows the importance of fine tuning the number of pillars in the material to control efficiently the ion transport and to increase accessibility to adsorption sites. Actually, ion sorption in RGO occurs on the external graphene surfaces whereas pillared materials have additional sorption sites inside the cross-linked galleries (Scheme V-2 - middle & right) (leading to the higher capacitances observed for the latter). Another interesting aspect of ion transport that we expected to study from EIS studies was the role of additional macro-porosity in 6-GH-0.05 compared to 6-RP-0.2. Instead of an improved ion transport that one would expect from the three-dimensional percolating network in 6-GH-0.05, slightly better τ_0 and R_i values were observed for 6-RP-0.2. We believe that the two different synthesis procedures of GHs and RPs may have a role in this. We

External graphene surfaces (RGO)   **Densely filled galleries**   **Sparsely filled galleries**
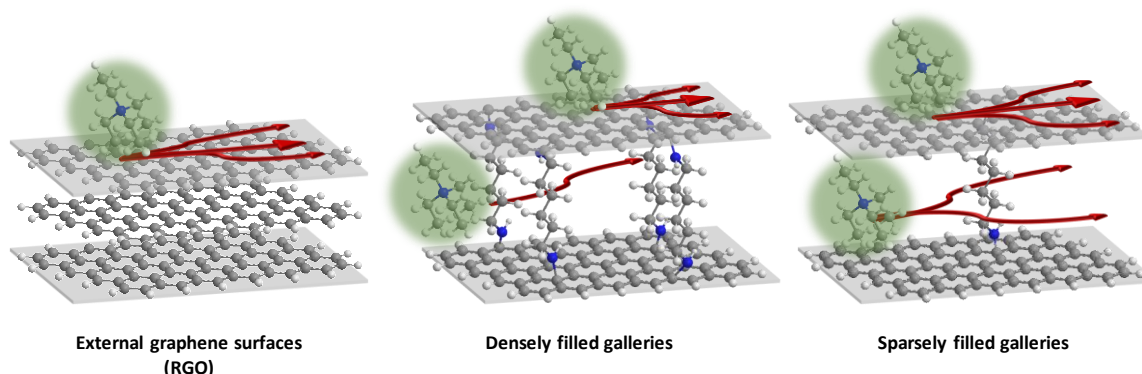
Scheme V-2 Schematic representation of the ion transport in the synthesized materials. Ion sorption in reduced graphene oxide (RGO) occurs on the graphene surfaces in micro/mesopores and the ion transport is relatively easy. In pillared materials, in addition to the external graphene surfaces, ion sorption occurs in the inter-layer galleries. The diamine filling density in the galleries regulates the ion transport in these materials.

speculate that these two synthesis protocols lead to different relative pillar densities and higher electrical conductivities of 6-RP-0.2 than 6-GH-0.05. In fact, earlier discussion on ssNMR and TGA have shown that for a same number of equivalents, 6 GHs have greater cross-linking than 6 RPs. Earlier reports have also shown that a hydrazine hydrate reduced 6 RP has higher electrical conductivity than hydrothermally synthesized 6 GH.

4.3 Power Capability & Volumetric Performances

The enhanced capacitances and ion transport characteristics observed in the EIS section were investigated through a power capability study. Three-electrode CVs were performed in a larger electrochemical window of -1.3 to 1.5 V vs. Ag (a voltage window of 2.8 V) at scan rates of 0.01-1 $V.s^{-1}$ (Figure V-10a&b) in TEABF$_4$/AN. RGO exhibits 145 $F.g^{-1}$ at 0.01 $V.s^{-1}$ and decreases to 50 $F.g^{-1}$ at 1 $V.s^{-1}$ whereas 6-RP-1 exhibits slightly higher values of 170 $F.g^{-1}$ at 0.01 $V.s^{-1}$ and shows a poor power performance with 20 $F.g^{-1}$ at 1 $V.s^{-1}$. The observed values for RGO and 6-RP-1 are slightly higher than those reported in our earlier work for the same materials in a 2 V voltage window. This increase is probably due to electro-wetting of the electrodes in a larger 2.8 V voltage window.[43] Upon reducing the number of pillars, 6-RP-0.2 and 6-GH-0.05 both show much improved capacitances (205 $F.g^{-1}$ and 230 $F.g^{-1}$ at 0.01 $V.s^{-1}$ respectively) and power capabilities (90 $F.g^{-1}$ and 107 $F.g^{-1}$ at 1 $V.s^{-1}$ respectively) compared to 6-RP-1.
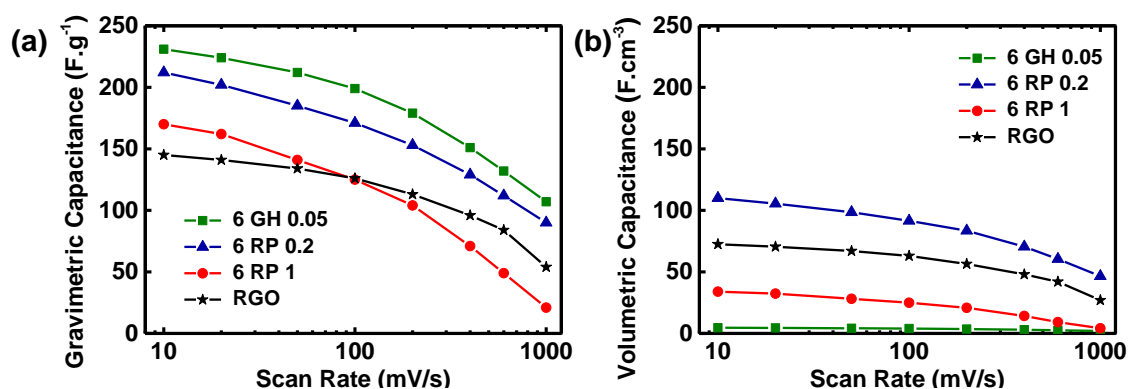
Figure V-10 Gravimetric and (f) volumetric specific capacitances of the synthesized materials obtained from three-electrode CVs performed at 0.001-1 $V.s^{-1}$ scan rates in a larger electrochemical window of -1.3 to 1.5 V vs. Ag.

As discussed before, this increase in capacitance when lowering the pillar number is due to the enhanced access of the active sites inside the inter-layer galleries. Furthermore, low number of pillars also reduce the electrochemically inactive diamine weight and aid the overall

gravimetric capacitances. The enhanced power capabilities are explained by reduced steric hindrance on ion motion by lower number of pillars. A comparison of 6-RP-0.2 and 6-GH-0.05 displays different capacitances with similar power capabilities. While the relative ion transport kinetics have been evoked in the EIS section, the higher capacitance of 6-GH-0.05 compared to that of 6-RP-0.2 could be attributed to higher accessibility brought in by the open 3D percolating network in 6-GH-0.05.

Electrochemical comparison of RGO to the 6-RP-0.2 and 6-GH-0.05 shows the overall merits of synthesizing pillared graphene materials. RGO adsorbs ions on the external graphene surfaces of the graphite-like particles formed by restacking of the recued graphene oxide sheets (Scheme V-2). Pillared materials mitigate this stacking to some extent by forming cross-linked structures and offer great enhancement of the electrochemical active surface area. When the number of pillars is optimized, the enhanced surface area becomes accessible for ion sorption along with a simultaneous improvement of the ion transport inside the inter-layer galleries. Overall, this shows the success of the strategy of designing pillared materials towards realizing the maximum capacitances from graphene-based materials. However, the synthesized pillar materials offer increased gravimetric capacitances than RGO but have very volumetric capacitances owing to their low material densities. RGO, 6-RP-0.2 and 6-GH-0.05 exhibit 70, 110 and 4 $F.cm^{-3}$ with their material densities of 0.5, 0.25 and 0.02 $g.cm^{-3}$ respectively (Figure V-10b).

The 6-GH-0.05 hydrogel gives an opportunity to enhance the material density through a simple ambient drying technique (Scheme V-1). A slow evaporation of the water in the hydrogel is reported to shrink the large macro pores and densify the hydrogel.[44] Hence, we synthesized 6-GH-0.05-AD (ambient-dried) as a high-density counter part of 6-GH-0.05 while increasing the material density from 0.02 to 1.1 $g.cm^{-3}$. The SEM images indicate clear shrinking and densification upon ambient drying (Figure V-11).

Two-electrode symmetrical cells of 6-GH-0.05 and its ambient-dried counterpart 6-GH-0.05 AD were fabricated and studied in a 2.8 V voltage window. The CVs obtained at 0.02 $V.s^{-1}$ in TEABF$_4$/AN show rectangular shaped curves with similar current densities for both 6-GH-0.05 and 6-GH-0.05-AD (Figure V-13a). The gravimetric power capability of the materials from 0.01-1 $V.s^{-1}$ scan rates shows identical profiles for both the materials (Figure V-13b). The close
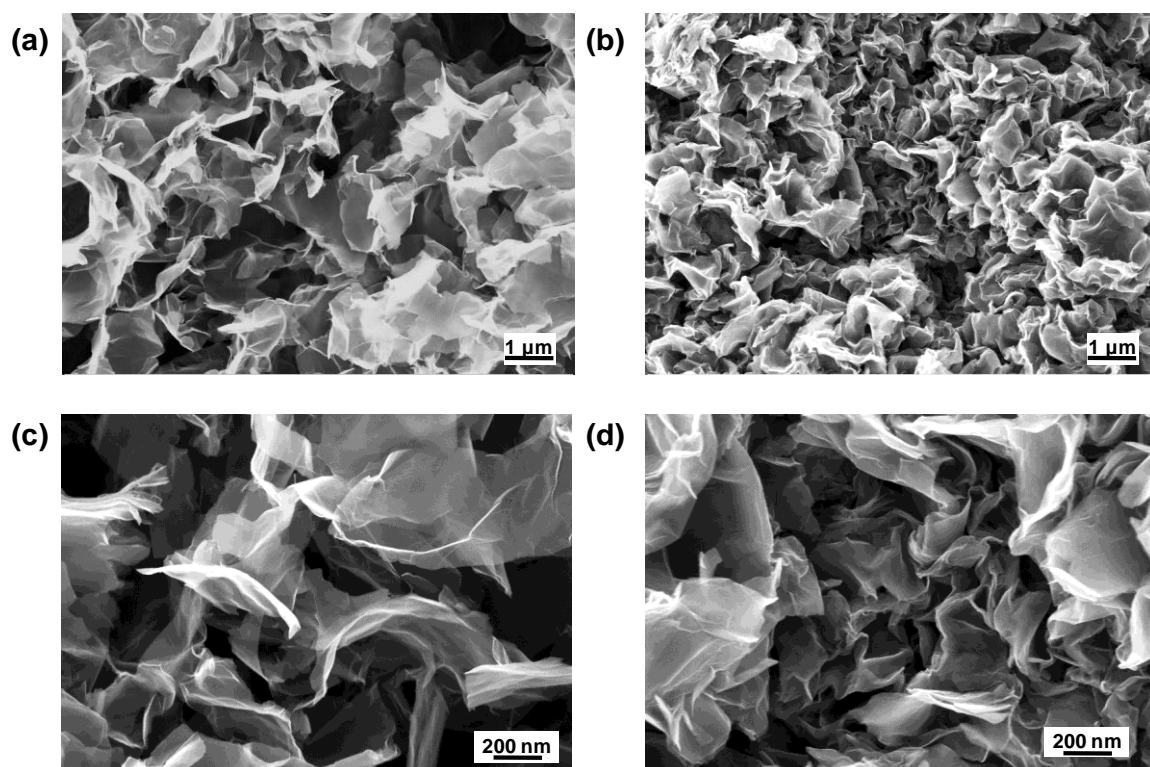
Figure V-11 Scanning electron microscopy images of (a,c) freeze dried 6 GH-0.05 and (c,d) air dried 6 GH-0.05 AD under different magnifications

performances of the freeze-dried and ambient-dried suggest that the shrinking of macro-porous network showed little loss to the overall ion sorption and ion transport. After ambient air drying the volumetric capacitance of 6-GH-0.05-AD has dramatically increased with respect to that of 6 GH-0.05 from 4 to 200 F.cm^{-3}. This value is even four times higher than that of RGO, calculated to be around 50 F.cm^{-3} (Figure V-13c). Cycling of 6-GH-0.05-AD at a high scan rate of 1 V.s^{-1} for 10000 cycles resulted in 93% capacitance retention with nearly 100% columbic efficiency (Figure V-12). The observed volumetric values are among the best performances reported in the literature for carbon based SCs with double-layer charge storage (Table V-3).[45] The single-step synthesis of 6-GH and the subsequent ambient drying process add further merits to the current work compared to other reports. The proposed materials also provide avenues towards even higher performances. Enhancing the relative content of cross-linked particles compared to graphitic-like arrangement or trapping redox molecules in the galleries could be few such strategies.
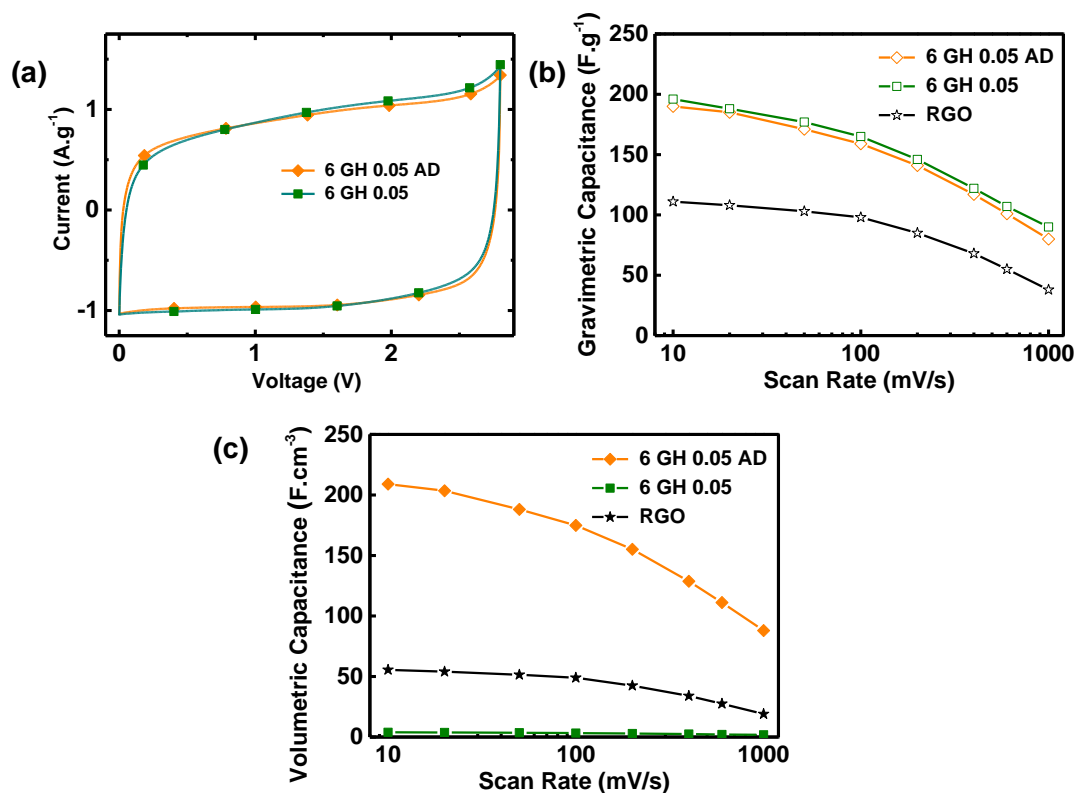
Figure V-13 (a) CVs of freeze-dried 6-GH-0.05 and ambient dried 6-GH-0.05-AD at 0.02 V.s^{-1} scan rate in 1 M TEABF$_4$/AN. (b) Gravimetric and (c) Volumetric specific capacitances of the materials obtained from two-electrode CVs in 1 M TEABF$_4$/AN performed at 0.01-1 V.s^{-1} scan rates.
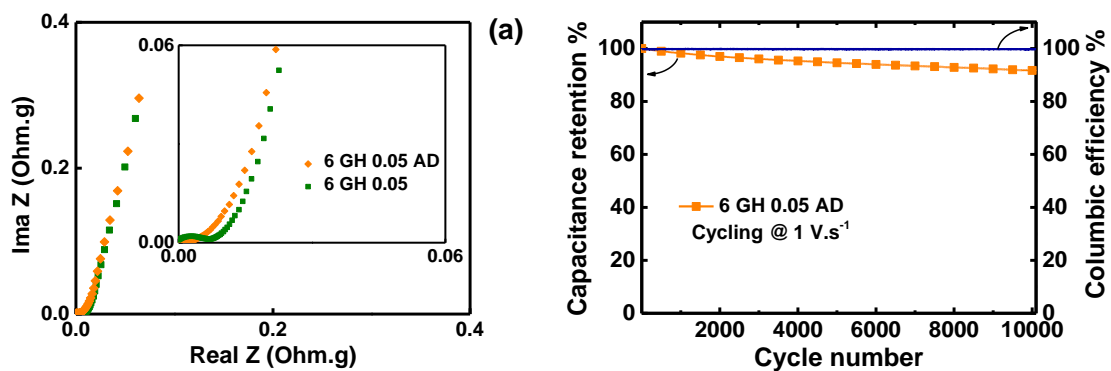
Figure V-12 Cycling 6 GH-0.05 AD at a high rate of 1 V.s^{-1} in 0 - 2.8 V using 1 M TEABF$_4$/AN electrolyte for 10000 cycles resulted in 93% capacitance retention with nearly 100% columbic efficiency.

Material	Electrolyte / Voltage (V)	Scan rate or Current density	Specific Capacitance ($F.g^{-1}$)	Specific Capacitance ($F.cm^{-3}$)	Ref
Activated Carbon	1 M $EMIBF_4$ (3.5 V)	1 $A.g^{-1}$	207	104	[5]
CDC	EMITFSI (3.0 V)	0.3 $A.g^{-1}$	160	85	[6]
MHCN	1 M $EMIBF_4$ (2.5 V)	0.5 $A.g^{-1}$	103	80	[7]
CCNC	1 M $EMIBF_4$ (4.0 V)	1 $A.g^{-1}$	156	206	[8]
EM-CCG	1 M $EMIBF_4$ (3.5 V)	0.1 $A.g^{-1}$	209	261	[9]
Graphene/SWNT film	1 M $EMIBF_4$ (4.0 V)	0.5 $A.g^{-1}$	199	211	[10]
HGF	1 M $EMIBF_4$ (3.5 V)	1 $A.g^{-1}$	298	212	[11]
HPGM	1 M $TEMABF_4$ (2.5 V)	0.1 $A.g^{-1}$	108	171	[12]
Porous carbon	1.5 $TEABF_4$ (2.54 V)	0.002 $V.s^{-1}$	156	145	[13]
Compressed-aMEGO	1 M $EMIMBF_4$ (3.5 V)	0.1 $V.s^{-1}$	147	110	[14]
6 GH 0.05 AD	1 M $TEABF_4$ (2.8 V)	0.01 $V.s^{-1}$	190	210	This work
		0.1 $V.s^{-1}$	159	175	
		1 $V.s^{-1}$	81	90	

Table V-3 Comparison of the tested materials with reports in literature in symmetrical SCs

5. Conclusions

Pillared graphene materials were synthesized from graphene oxide using 1,6-diaminohexane as the pillar molecule to minimize the graphitic restacking in graphene-based materials and achieving higher electrochemical active surface areas. The covalent attachment between diamines and graphene was confirmed through solid-state nuclear magnetic resonance (ssNMR) studies with ^{15}N labelled diamine. Using these materials, we demonstrated a simultaneous improvement in the energy and power performances by following a two-pronged strategy involving low number of diamine pillars and through 3D macro porous hydrogel formation. Upon decreasing this diamine pillars amount the ion transport in the galleries is strongly improved as evidenced by the decrease in time constants from 17 to 5 s (6 RP-1 vs. 6 RP-0.2). When the subsequent 3D gel was obtained from this optimized pillared graphene material, ion sorption in the inter-layer galleries to achieve twice the capacitances (200 F.g^{-1}) compared to RGO (107 F.g^{-1}). High volumetric capacitance values of 210 F.cm^{-3}, nearly four times larger than RGO, were achieved using a simple ambient drying approach and. The definitive covalent attachment of diamine enabled stable electrochemical performances during 10000 cycles. These pillared structures in graphene add new perspectives towards achieving the potentially high capacitances of graphene in SCs.

6. Further Conclusions & Perspectives

Although the previous chapters have given conclusive evidence of ions entering the inter-layer graphene galleries, the obtained specific capacitances were only marginally high. This chapter focused on achieving the promised potential of high specific capacitances from pillared graphene materials through additional ion sorption between the graphene layers.

With the knowledge from previous chapters, we believed that the optimization of the pillar density in the inter-layer galleries could result in simultaneous improvements in ion transport and access to active sites. Thus, through synthesis of a class of materials, we obtained and analyzed materials that have similar d-spacing but have different pillar densities. A clear enhancement in ion transport is noted through determination of time constant and ionic resistance values when pillar density was lowered (6 RP-1 vs. 6 RP-0.2). The specific capacitances and the power capability studies exhibited five times higher gravimetric values for 6 RP-0.2 compared to 6 RP-1 at a high scan rate of 1 V/s. The high capacitances are attributed to enhanced ion sorption in between the graphene layers and the improved power performances could be attributed to the enhanced ion transport characteristics.

A comparison between 6 RP and 6 GH also gave interesting insights about the pillared materials. 6 GH-0.05 showed higher capacitances of 230 F.g^{-1} compared to 205 F.g^{-1} of 6 RP-0.2, probably due to better ion accessibility to the active sites and lower restacking through 3D interconnected network. However, the frequency responses of the two materials assigned slightly higher time constants and ionic resistances to 6 GH-0.05. This finding was surprising as we expected better power capability in the gels facilitated by their 3D structure. Further ssNMR studies have suggested that the stronger reaction conditions of 6 GH-0.05 hydrothermal preparation at 180°C (compared to 6 RP-0.2 preparation at 90°C not under supercritical conditions) may result in greater cross-linking of two sheets in 6 GH instead of a simple mono covalent grafting on one side. Further optimization of 6 GH diamine content may lower the ionic resistances.

Electrical conductivities of 6 RPs and 6 GH were obtained through four-probe measurements to investigate the origin of their differences in power capabilities. 6 RP-1, 6 RP-0.2 and 6 GH-0.05 exhibit 150, 180 and 100 S/m respectively and indicate that the electrical conductivities of the synthesized materials are in the same range. These values, along with the calculated

ionic resistances from the Warburg region in Nyquist plots, provided conclusive evidence that the improvements in power are mainly due to better ion transport in materials achieved with low number of pillars.

A simple ambient drying approach to densify the 6 GH-0.05 gel led to dense packing of the material with the interconnected networks structure. The 6 GH-0.05-AD gel, thus obtained, displayed high volumetric performances that are among the best reported for graphene materials. A direct comparison of RGO, that has no pillared structures, with the best pillared material (6 GH-0.05-AD), has shown the overall merits of the strategy of pillared graphene architectures. Twice the gravimetric capacitances and four times the volumetric capacitances of RGO were observed in 6 GH-0.05-AD.

In addition to the significant higher values seen here, there is still a great scope for improvements of pillared graphene materials. The X-ray diffraction spectra of all the pillared materials studied in this thesis have extensive presence of graphitic domains in addition to the desired cross-linked domains. Further optimization of synthesis strategies towards limiting the direct reduction of GO sheets in pillared materials could offer the maximum capacitances from graphene.

7. References

[1]   B. E. Conway, Electrochemical Supercapacitors - Scientific Fundamentals and Technological Applications, Springer International Publishing, New York, 1999.

[2]   P. Simon, Y. Gogotsi, Nat Mater 2008, 7, 845.

[3]   L. L. Zhang, X. S. Zhao, Chem. Soc. Rev. 2009, 38, 2520.

[4]   J. Chmiola, G. Yushin, Y. Gogotsi, C. Portet, P. Simon, P. L. Taberna, Science 2006, 313, 1760.

[5]   C. Vix-Guterl, E. Frackowiak, K. Jurewicz, M. Friebe, J. Parmentier, F. Béguin, Carbon 2005, 43, 1293.

[6]   E. Raymundo-Piñero, K. Kierzek, J. Machnikowski, F. Béguin, Carbon 2006, 44, 2498.

[7]   M. Salanne, B. Rotenberg, K. Naoi, K. Kaneko, P.-L. Taberna, C. P. Grey, B. Dunn, P. Simon, Nat. Energy 2016, 1, 16070.

[8]   F. Béguin, V. Presser, A. Balducci, E. Frackowiak, Adv. Mater. 2014, 26, 2219.

[9]   J. Chmiola, C. Largeot, P.-L. Taberna, P. Simon, Y. Gogotsi, Angew. Chem. Int. Ed. 2008, 47, 3392.

[10]   C. Largeot, C. Portet, J. Chmiola, P.-L. Taberna, Y. Gogotsi, P. Simon, J. Am. Chem. Soc. 2008, 130, 2730.

[11]   C. Merlet, C. Péan, B. Rotenberg, P. A. Madden, B. Daffos, P.-L. Taberna, P. Simon, M. Salanne, Nat. Commun. 2013, 4, 2701.

[12]   W.-Y. Tsai, P.-L. Taberna, P. Simon, J. Am. Chem. Soc. 2014, 136, 8722.

[13]   J. M. Griffin, A. C. Forse, W.-Y. Tsai, P.-L. Taberna, P. Simon, C. P. Grey, Nat. Mater. 2015, 14, 812.

[14]   K. Lee, Y. Yoon, Y. Cho, S. M. Lee, Y. Shin, H. Lee, H. Lee, ACS Nano 2016, 10, 6799.

[15]   K. Yuan, Y. Xu, J. Uihlein, G. Brunklaus, L. Shi, R. Heiderhoff, M. Que, M. Forster, T. Chassé, T. Pichler, T. Riedl, Y. Chen, U. Scherf, Adv. Mater. n.d., 27, 6714.

[16]   R. Raccichini, A. Varzi, S. Passerini, B. Scrosati, Nat. Mater. 2015, 14, 271.

[17]   I. K. Moon, J. Lee, R. S. Ruoff, H. Lee, Nat. Commun. 2010, 1, 73.

[18]   M. D. Stoller, S. Park, Y. Zhu, J. An, R. S. Ruoff, Nano Lett. 2008, 8, 3498.

[19]   C. Li, G. Shi, Adv. Mater. 2014, 26, 3992.

[20]   M. Herrera-Alonso, A. A. Abdala, M. J. McAllister, I. A. Aksay, R. K. Prud'homme, Langmuir 2007, 23, 10644.

[21]   W.-S. Hung, C.-H. Tsou, M. De Guzman, Q.-F. An, Y.-L. Liu, Y.-M. Zhang, C.-C. Hu, K.-R. Lee, J.-Y. Lai, Chem. Mater. 2014, 26, 2983.

[22]   H. Banda, B. Daffos, S. Périé, Y. Chenavier, L. Dubois, D. Aradilla, S. Pouget, P. Simon, O. Crosnier, P.-L. Taberna, F. Duclairoir, Chem. Mater. 2018, 30, 3040.

[23]   A. B. Bourlinos, D. Gournis, D. Petridis, T. Szabó, A. Szeri, I. Dékány, Langmuir 2003, 19, 6050.

[24]   G. Srinivas, J. W. Burress, J. Ford, T. Yildirim, J. Mater. Chem. 2011, 21, 11323.

[25]   J. W. Burress, S. Gadipelli, J. Ford, J. M. Simmons, W. Zhou, T. Yildirim, Angew. Chem. Int. Ed. 2010, 49, 8902.

[26]   G. Salitra, A. Soffer, L. Eliad, Y. Cohen, D. Aurbach, J. Electrochem. Soc. 2000, 147, 2486.

[27]   W. S. Hummers, R. E. Offeman, J. Am. Chem. Soc. 1958, 80, 1339.

[28]   H. He, T. Riedl, A. Lerf, J. Klinowski, J. Phys. Chem. 1996, 100, 19954.

[29]   W. Cai, R. D. Piner, F. J. Stadermann, S. Park, M. A. Shaibat, Y. Ishii, D. Yang, A. Velamakanni, S. J. An, M. Stoller, J. An, D. Chen, R. S. Ruoff, Science 2008, 321, 1815.

[30]   Y. Xu, K. Sheng, C. Li, G. Shi, ACS Nano 2010, 4, 4324.

[31]   T. Szabó, O. Berkesi, P. Forgó, K. Josepovits, Y. Sanakis, D. Petridis, I. Dékány, Chem. Mater. 2006, 18, 2740.

[32]   H. Banda, D. Aradilla, A. Benayad, Y. Chenavier, B. Daffos, L. Dubois, F. Duclairoir, J. Power Sources 2017, 360, 538.

[33]   S. Stankovich, D. A. Dikin, R. D. Piner, K. A. Kohlhaas, A. Kleinhammes, Y. Jia, Y. Wu, S. T. Nguyen, R. S. Ruoff, Carbon 2007, 45, 1558.

[34]   S. Brunauer, P. H. Emmett, E. Teller, J. Am. Chem. Soc. 1938, 60, 309.

[35]   J. Jagiello, J. P. Olivier, Carbon 2013, 55, 70.

[36]   M. Ue, J. Electrochem. Soc. 1994, 141, 3336.

[37]   R. Mysyk, E. Raymundo-Piñero, J. Pernak, F. Béguin, J. Phys. Chem. C 2009, 113, 13443.

[38]   R. Lin, P. Huang, J. Ségalini, C. Largeot, P. L. Taberna, J. Chmiola, Y. Gogotsi, P. Simon, Electrochimica Acta 2009, 54, 7025.

[39]   C. Portet, P. L. Taberna, P. Simon, C. Laberty-Robert, Electrochimica Acta 2004, 49, 905.

[40]   R. de Levie, Electrochimica Acta 1963, 8, 751.

[41]   P. L. Taberna, P. Simon, J. F. Fauvarque, J. Electrochem. Soc. 2003, 150, A292.

[42]   K. S. Cole, R. H. Cole, J. Chem. Phys. 1941, 9, 341.

[43]   S. Kondrat, P. Wu, R. Qiao, A. A. Kornyshev, Nat. Mater. 2014, 13, 387.

[44]   Y. Tao, X. Xie, W. Lv, D.-M. Tang, D. Kong, Z. Huang, H. Nishihara, T. Ishii, B. Li, D. Golberg, F. Kang, T. Kyotani, Q.-H. Yang, Sci. Rep. 2013, 3, 2975.

[45]   C. Liu, X. Yan, F. Hu, G. Gao, G. Wu, X. Yang, Adv. Mater. 2018, 30, 1705713.

[46]   N. Ashok Kumar, S. Gambarelli, F. Duclairoir, G. Bidan, L. Dubois, J. Mater. Chem. A 2013, 1, 2789.

CHAPTER VI:
General Conclusions
& Perspectives

Chapter VI. General Conclusions & Perspectives

The aim of this thesis work was to develop graphene-based electrode materials with improved energy and power performances in SCs. The main challenge was to minimize the graphitic restacking and the corresponding loss of active surface area that is observed in many graphene-based materials. The primary strategy of the scientific community has been to assemble the graphene sheets into 3D assemblies and limit the continuous 2D stacking of the sheets. The 3D structures had additional benefits of interconnected porous networks that offered better ion and electron transport properties. Despite significant success of this strategy, new strategies were required to realize the theoretical potential of graphene materials for SCs.

1. Pillared Graphene Materials

1.1 Pillared Graphene Materials Limit Graphitic Restacking

In this thesis, we proposed and demonstrated that expanded layered arrangement of graphene (through presence of an intercalant) is a successful strategy to mitigate the graphitic restacking through nanoscale assembly. The proposed expanded layered arrangement needed to allow precise tuning of the inter-layer separation (d-spacing) and be durable for long electrochemical cycling in SCs. Hence, we synthesized pillared graphene materials in which the intercalated molecule cross-links GO sheets through covalent bonds, defining a precise and stable d-spacing. A family of diamines were tested for their ability to act as pillar molecules and interesting insights about covalent cross-linking were obtained. Hydrazine, the shortest diamine molecule tested and a strong reducing agent, exhibited a direct reduction of GO solution resulting in graphitic restacking (G) with no cross-linking (CL). When alkyl diamines with 2, 4, 5, 6 and 8 carbons in the alkyl chains reacted with GO, presence of CL peaks along with G-restacking were seen in XRD spectra for the resulting materials (RPs). Increasing alkyl chain lengths from 2 to 8 carbons led to sharper and more intense CL peaks, suggesting that the longer diamines formed larger CL crystallites.

1.2 Pillared Graphene Hydrogels with 3D structures

In addition to the nanoscale assembly of graphene sheets through pillaring, we aimed to synthesize 3D macroscale assemblies (GHs) of these materials in order to benefit from the

interconnected networks described in the literature. Shorter alkyl diamines of 2 and 4 carbon chain lengths formed monoliths up on direct reaction with aqueous GO solutions. Whereas, the longer diamines, being relatively hydrophobic in nature, required ethanol as a co-solvent to dissolve in the aqueous GO solution and did not form monoliths in the tested conditions. We adapted hydrothermal treatment of GO for monolith formation from the literature and were successful in incorporating alkyl diamines to synthesize pillared graphene hydrogels.

2. Electrochemical Analysis in SCs

Among the materials synthesized, pillared graphene materials obtained using longer alkyl diamines (C = 5, 6 and 8) displayed sharp and intense CL XRD peaks that could be related to specific d-spacing values (0.78 – 0.86 nm). Hence, this group of materials were chosen for a comprehensive ion-sieving study using a family of tetraalkylammonium tetrafluoroborate (TAABF$_4$) salts in acetonitrile as electrolytes. The TAABF$_4$ family offered cation sizes from 0.68 – 0.95 nm and a constant anion size of 0.48 nm.

Electrochemical results from cyclic voltammetry (CV) showed that the inter-layer galleries sieve electrolyte ions based on size constrictions; ions with naked sizes that are smaller than the d-spacing values enter the galleries, whereas the larger ions are restricted. This direct relation between the naked ion sizes and d-spacing values suggested a partial desolvation of the electrolyte ions before entering the galleries. Overall, these results showed the first observations of ion sorption in between graphene layers of a pillared material. However, the obtained specific capacitances of pillared materials were only marginally better that RGO (without pillars), probably due to hindered ion access to the active sites. Further impedance analyses (EIS) have signaled highly resistive ion transport in the pillared materials supporting the above reason.

2.1 Role of Alkyl Diamine Pillars

The results from CV and EIS analyses of the pillared materials suggested that the poor ion transport and accessibility could be due to dense filling of the galleries with pillar molecules. In order to verify the role of diamine pillars and enhance the performances of pillared graphene materials, an optimization study using low amounts of pillars was performed. A clear enhancement in both the specific capacitances and power capabilities was observed when the

pillared materials has low diamine grafting density. Particularly, lowering of pillars from 6 RP-1 to 6 RP-0.2 led to five times increase in capacitances from 20 F/g to 100 F/g at a high scan rate of 1 V/s. Additionally, the frequency responses also reflect the improvement in ion transport with decreased in time constant values from 17 to 5 s in 6 RP-1 and 6 RP-0.2 respectively. Overall, optimized number of pillars allowed greater ion access into the inter-layer galleries and improved the ion transport in pillared graphene materials. The observed capacitances of 6 RP-0.2 (220 F/g) and RGO (140 F/g) quantify the improvements in ion sorption.   The time constant value of 6 RP-0.2 (5 s) is similar to that of RGO (5 s) supports the improved ion transport.

2.2 Role of 3D Macroscale Assemblies

In this thesis work, synthesis of 3D macroscale assemblies of the pillared graphene materials has been a constant theme to achieve enhanced performances through interconnected networks. In the second chapter, a direct comparison between a GH-HD monolith and RGO (2D assembly) was made using an aqueous electrolyte (6 M KOH). The monolith showed higher capacitances and superior power performance of 123 F/g at 100 A/g compared to 17 F/g for RGO. These improvements in the performances through 3D macro-assembly were in line with the reports in literature.

Later in the fourth chapter, working with pillared graphene materials synthesized with 1,6-diaminohexane, we compared the ion transport properties in 6 RP and 6 GH. Despite the presence of the 3D interconnected porous network, 6 GH showed slightly higher time constants of 23 s compared to 17 s of 6 RP (with just the pillared assembly) in 1 M TEABF$_4$/AN. Unlike the case of GH-HD and RGO (above), 6 RP and 6 GH were synthesized under two different synthesis conditions (6 RP was reacted with alkyl diamine at 90°C whereas 6 GH was reacted at 180°C in a sealed autoclave). Hence, the diamine pillar density in 6 GH was higher than in 6 RP and thus explaining the greater time constants values. After lowering the pillar densities, in the fifth chapter, we compared the specific capacitances of the optimized 6 GH to that of 6 RP. 6 GH-0.05 showed higher values of 230 F/g vs compared to 205 F/g for 6 RP-0.2 However, the time constant values of 6 GH-0.05 were again slightly higher compared to 6 RP-0.2 (7s vs 5 s respectively). This could again be due to more diamine cross-linking in 6 GH-0.05 vs 6 RP-0.2 (see Figure V-4).

Overall, the additional 3D macroscale assembly of pillared graphene hydrogels (GHs) provides higher capacitances compared to the nanoscale assembly in RPs. This is made possible through better ion accessibility to the ion sorption sites in the open 3D percolating network of GHs. In terms of ion transport, the stronger reaction conditions of GHs, and the corresponding differences in the number of pillars, has made it difficult to make a fair comparison with RPs. Under the different synthesis conditions, it is difficult to maintain same d-spacing values, pillar densities and electrical conductivities of RPs and GHs and single out their porosity characteristics.

Another interesting aspect was noticed when the ion transport properties of ambient dried 6 GH-0.05-AD hydrogel were studied with respect to its freeze-dried counterpart, 6 GH-0.05. Ambient drying has led to shrinking of the macroscopic pores (~ 1-2 µm to ~ 0.1-0.2 µm) and increased the volumetric capacitances from 4 to 200 F/cm^3. Nevertheless, the SSAs and PSDs from gas sorption, gravimetric capacitances and time constants from electrochemistry remained the same for 6 GH-0.05 and 6 GH-0.05 AD. These results reinforced the current understanding in the literature about the role of various pore sizes: micropores provide ion sorption sites, mesopores offer ion-transport pathways where as small macropores act as electrolyte buffers. Hence, it is preferred to have macropores that are of small size (less than 0.2 µm) in order to achieve high volumetric capacitances and power capabilities.

Broadly, the work done in this thesis gives a new direction to the research on graphene-based materials for SCs. The results obtained on ion sorption in between the graphene layers of the pillared materials were the first of their kind among various carbon-based materials. Building upon the preliminary ion sieving study, great improvements in SC performances were achieved through a simple optimization of the number of pillars. The capacitance values of the optimized materials are among the best values currently reported in the literature for graphene-based materials. In comparison to other double layer charge storage materials such as ACs or CNTs, both the gravimetric and volumetric values are significantly higher (210 F/cm^3 here vs ~ 100 F/cm^3 in the literature (see Chapter I)). Finally, this work offers several perspectives for improvements in SCs and rechargeable batteries based on the pillared architectures of graphene. Some of the perspectives are discussed below.

3. Perspectives

The pillared graphene materials studied in this thesis still show extensive presence of graphitic domains in addition to the desired cross-linked domains. Further optimization of synthesis strategies towards limiting the direct reduction of GO sheets could offer the maximum capacitances of graphene in SCs (Figure VI-1). Few such strategies could be to perform cross-linking reaction at low temperatures or by controlling the pH of the reaction mixture to avoid direct restacking of GO sheets. Recently, holey graphene materials, graphene-based materials that have holes in the graphene sheets, are studied as materials with higher electrochemical active surface areas and ion transport properties (Figure VI-2). Synthesizing pillared architectures using holey graphene sheets would bring the best of the two design strategies.
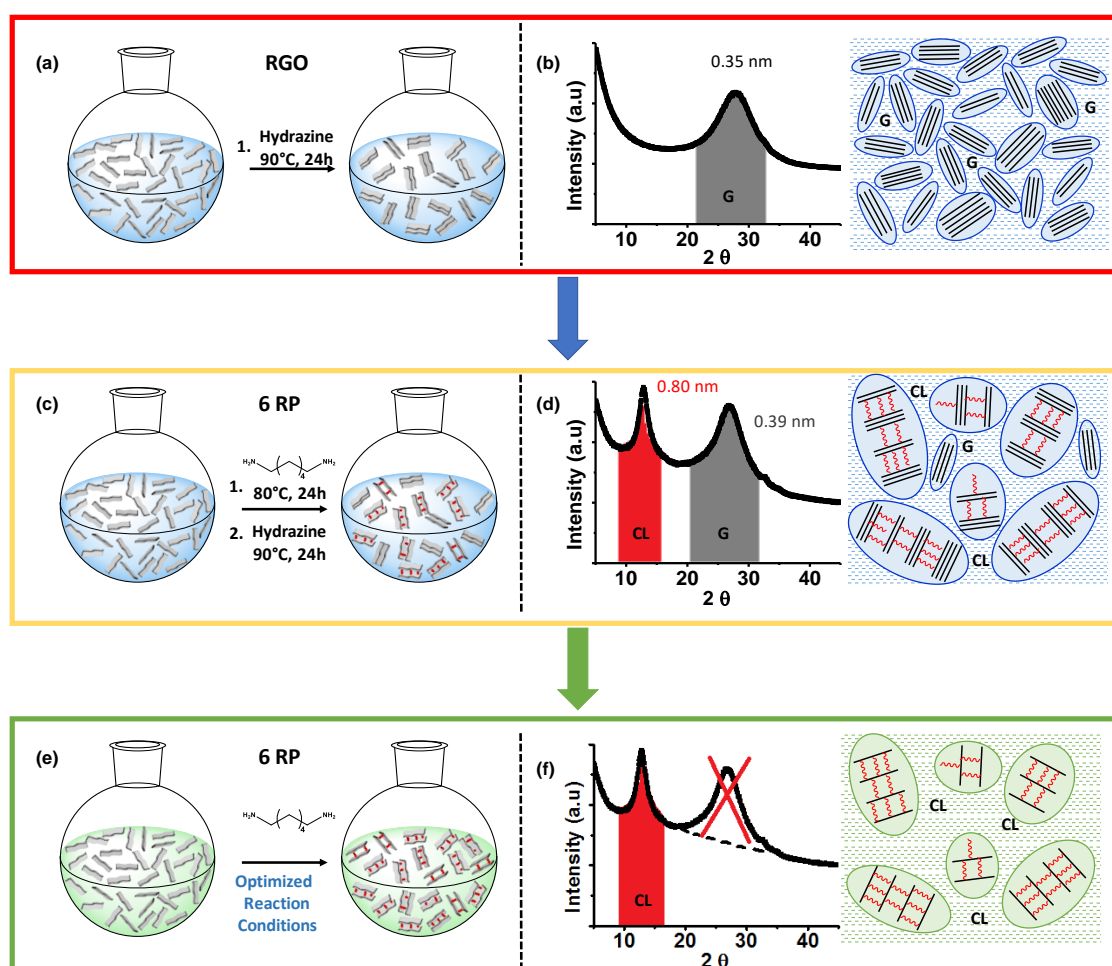

Figure VI-1 (a) Reduced graphene oxide and its (b) X-ray diffraction pattern obtained by direct chemical reduction of GO. A schematic diagram shows the graphitic crystallites in RGO. (c) Reduced pillared graphene materials synthesized and studied in this thesis and their corresponding (d) XRD pattern. The schematic shows presence of both the cross-linked (CL) and graphitic crystallites (G). (e) Proposed future work towards synthesizing pillared graphene materials with minimum presence of graphitic crystallites.
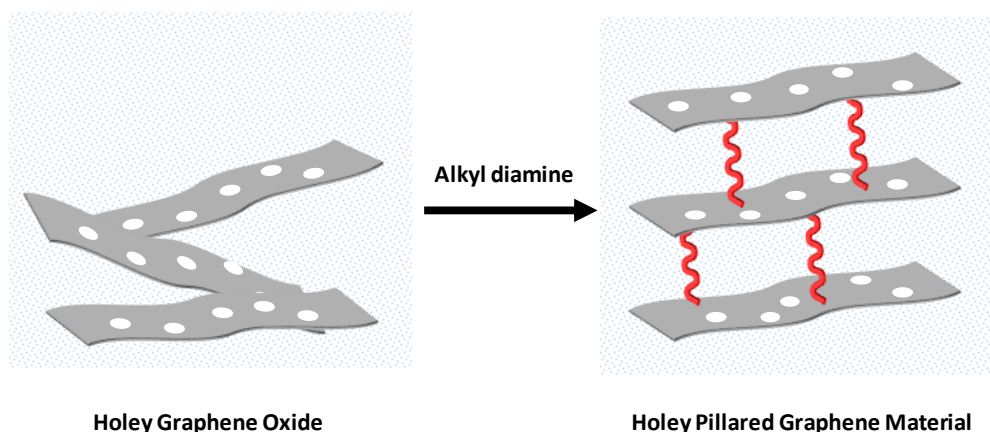
Holey Graphene Oxide　　　　　　　　　　**Holey Pillared Graphene Material**

Figure VI-2 Schematic representation of the holey pillared graphene material

In addition to the double layer charge storage discussed all through this thesis, the pillared graphene architectures could be very good hosts to trap or contain redox active molecules and provide pseudo-capacitive charge storage. The pillared graphene materials could be potential candidates for sodium ion batteries wherein an expanded and durable graphitic structure is of great interest as the natural graphitic spacing of 0.33 nm is smaller for the Na ions.

The pillared graphene materials open up enormous applications in various research fields in addition to electrochemical energy storage (Figure VI-3). Currently, GO is extensively studied for gas storage, water desalination and membrane applications. For example, it has been noted that hydrophobic regions on GO can offer friction less flow for water. However, the main challenge in the above applications has been the swelling of GO membranes upon contact with water. The covalently cross-linked materials proposed here would offer potential solutions. Nevertheless, a pillar in the middle of the channel would impede ion/gas/liquid transport in all the applications. Yet, we are confident that optimization of pillar densities would show bear fruit, just as seen in SCs.
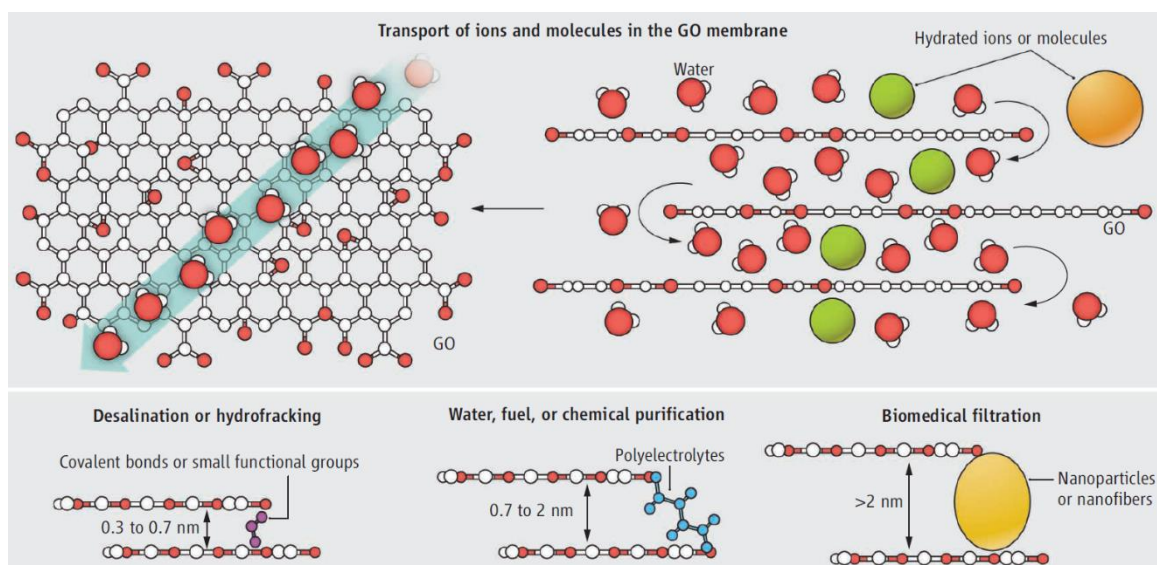
Figure VI-3 Possible applications of GO and its derivatives in various scientific domains. (Reprinted from Science 2014, 343, 740.)

CHAPTER VII:
Materials and Methods

Chapter VII. Materials and Methods

This chapter describes the materials and methods used to obtain, characterize and evaluate the graphene-based materials described in the course of the various chapters of this thesis. Initially, in a first part, the GO precursor, commercial activated carbon (YP-50F), and the electrolyte salts which are used all through the work are described individually. Various physicochemical and electrochemical characterization instruments and the electrochemical sample preparation methodologies are then detailed. Later on, the experimental procedures used for the different materials syntheses and their electrochemical analyses in SC cells are detailed in separate sections corresponding to materials described in each chapter. Graphene oxide was synthesized in bulk quantities from graphite and was used as a precursor for all the synthesis performed in this thesis. A solution of GO in water with a weight concentration of 5 g/L was used in all cases.

1. Common Materials

1.1 Graphene Oxide (GO)

Graphite powder starting material, with a particle size of 2-4 μm was purchased from NanoAmor and all other chemicals used in the synthesis of GO were obtained from Sigma-Aldrich. GO synthesis was performed following a modified-Hummers and Offeman's method.[1,2] Graphite powder (3.1 g) was dispersed in conc. H_2SO_4 (91 mL) under stirring into a 1 L beaker placed in an ice bath. $NaNO_3$ (1.5 g) was then added and the reaction media was stirred vigorously while maintaining the temperature under 2°C. After 2 h, $KMnO_4$ (9 g) was added portion-wise to keep the mixture temperature below 4°C. The reaction media was kept under stirring at such controlled temperature for a further 1 h, before it was let to reach room temperature. Then water (100 mL) was added slowly over a period of 20 minutes maintaining the temperature under 95°C. The beaker was then placed into an oil bath and stirred at 95°C. After 1.5 h, water (300 mL) was added making sure the temperature does not rise above 85°C. Stirring was continued for 1.5 h and then the reaction mixture was let to reach room temperature. H_2O_2 (30 mL) was added and the mixture was stirred for a further 1 h. Finally, water (450 mL) was added and the final reaction media was kept for stirring overnight. The mixture was filtered through a P4 fritted Buchner filter (10-15 μm). The solid graphene oxide

cake was re-dispersed in 600 mL of water, and the dispersion was homogenized under stirring for 1 h and sonication for a further hour. The mixture was then acidified with 100 ml of HCl (35-37%) and left under stirring overnight. The GO dispersion was filtered and centrifuged repeatedly until the supernatant reached a pH 5. Finally, the GO solution was adjusted to a weight concentration of 5 mg/mL by measuring the weight of a lyophilized sample.

1.2 Commercial Activated Carbon

A commercial activated carbon was used as a counter electrode in the three electrode electrochemical cells used for electrochemical characterization of different materials. The carbon (named as YP-50F) was derived from coconut shells and is purchased from Kuraray Chemical Co., Japan. The porosity characteristics of the as received YP-50F carbon were analyzed from Ar sorption isotherm measured at 77 K with Micromeritics ASAP 2020 porosimeter analyzer (Figure VII-1). The pore size distributions (PSD) were calculated from the isotherm by using Quenched Solid Density Functional Theory (QSDFT) assuming a slit pore geometry.
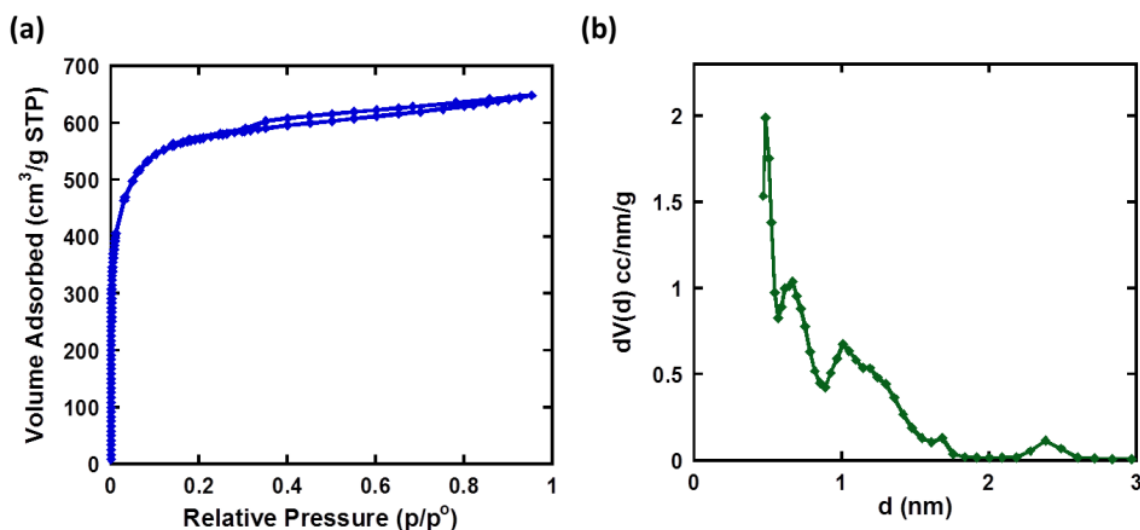

Figure VII-1 Porosity characteristics of the as-received YP-50F carbon obtained from Ar gas sorption experiments. (a) Ar sorption isotherm collected at 77 K and (b) pore size distribution calculated from QSDFT model.

The specific surface area of YP-50F estimated using Brunauer-Emmett-Teller (BET) method was found to be 1732 m^2/g. The PSD calculated from the isotherm assigns an average pore size of 0.9 nm, and a total pore volume of 0.75 cm^3/g. The suppliers assign particle sizes in the range of 5-20 μm and average moisture content around 3% by weight.

1.3 Electrolytes

Aqueous and organic electrolytes were used for the electrochemical analyses of the materials in two and three-electrode SC configurations. In the second chapter, graphene hydrogels self-assembled from aqueous GO solutions were characterized in SCs using an aqueous electrolyte (6 M KOH). In the third, fourth and fifth chapters, pillared graphene materials were analyzed using a family of tetraalkylammonium tetrafluoroborate ($TAABF_4$) salts dissolved in anhydrous acetonitrile as electrolytes. All the salts and acetonitrile were purchased as electrochemical grade products from Sigma Aldrich and were used without any chemical purification processes. The salts and electrolytes are stored and handled in a glove box (< 0.1 ppm H_2O and O_2). Various alkyl chain lengths of ethyl (TEA^+), propyl (TPA^+), butyl (TBA^+) and hexyl (THA^+) offered varied cation sizes from 0.68 - 0.95 nm. The un-solvated ion sizes and the limiting oxidation and reduction potentials of the salts are given in Table VII-1.[3]
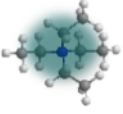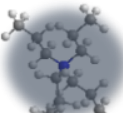
Electrolyte	Cation Size (nm)	Anion Size (nm)	E_{Red} (V vs. SCE)	E_{Ox} (V vs. SCE)
$TEABF_4$	0.68	0.48	-3.00	3.65
$TPABF_4$	0.76	0.48	-3.05	3.65
$TBABF_4$	0.82	0.48	-3.05	3.65
$THABF_4$	0.95	0.48	-3.10	3.65
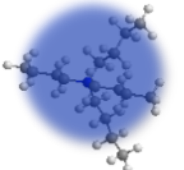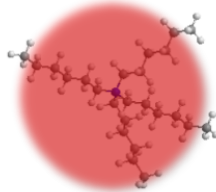
Table VII-1 Un-solvated ion sizes and the limiting reduction and oxidation potentials of the electrolyte ions.

2. Instrumentation Details

2.1 Characterization Techniques

Various instruments used for physicochemical characterization of the materials are detailed below with the corresponding sample preparation procedures. The data from various techniques were exported as text and were later plotted in graphing software Origin 8.1.

The changes in the chemical bonding were analyzed by Fourier transformed infrared spectroscopy (FT-IR, Thermofischer ES 50) in the frequency range of 4000–400 cm^{-1}. The sample of interest was mixed with dry KBr powder and pressed into pellets in a hydraulic press at a pressure of 10 MPa. The pellet was placed on the mount and the sample chamber in the spectrometer was flushed with nitrogen gas for 10 minutes before a spectrum was acquired. The base lines in the acquired spectra were corrected with OMNIC Spectra software.

The thermogravimetric analysis (TGA) of all samples were performed with Setaram TGA 92 at a heating ramp rate of 5°C/min from 30 to 800°C under nitrogen atmosphere. A Pt crucible was used as the sample holder. The Pt holder was maintained at 30°C for 30 minutes before start of the acquisition on each sample.

Lyophilization of the synthesized gels was performed using a Freeze Dryer. Wet samples were first frozen at 77 K using liquid nitrogen and were then subjected to sublimation for 48 h by using a freeze dyer.

The crystallographic structures of the materials were determined by a wide-angle X-ray diffraction (XRD) system on a Panalytical X'pert PRO X-ray diffractometer using a Co Kα radiation source (λ=1.79 Å). The diffraction data were acquired from the 2θ angles of 5° to 65° in all the cases. The d-spacing values were obtained using X'pert High Score Plus software. Monoliths and pieces of gels were analyzed by directly placing on the sample holder (disoriented Si plate) whereas powder samples were pressed as pellets at a pressure of 5 MPa. A control spectrum was obtained on a pressed monolith to evaluate the effect of the pressing. No peaks were found to be suppressed or given any obvious preferential arrangement were observed at these pressures. Nevertheless, intensities of the peaks were found to be mildly higher after pressing.

X-ray photoelectron spectroscopy (XPS) analyses were performed using a PHI Versa Probe II spectrometer with a monochromatized Al Kα X-ray source (1486.6 eV) focalized to a spot of 100 μm and with an electron take-off angle of θ = 45°. Survey spectra of the photo-emitted electrons were recorded with a pass energy of 117 eV and the high-resolution spectra with a pass energy of 23.5 eV. Spectra were calibrated with respect to sp^2 C1s signal at 284.3 eV. The deconvolution of C 1s and N 1s core-level spectra was performed by fitting the individual components using Casa XPS software. Spectra were fitted into Gaussian-Lorentzian (30:70) shaped curves with full width at half maximum values kept under 1.5 in all cases. Samples were pressed on a conducting copper tape stuck on to a sample holder with a diameter of 16/25 mm.

Porosity characteristics were calculated from nitrogen sorption isotherms measured at 77 K with Micromeritics ASAP 3020 porosimeter. Prior to the analysis samples were subjected to a degazing process at 100°C for 24h. The specific surface area was estimated by using Brunauer–Emmett–Teller (BET) method. The pore volumes and the pore size distributions (PSD) were calculated from adsorption isotherms by using quenched solid density functional theory (QSDFT) method assuming a slit pore geometry. Later on, SSAs and PSDs were also calculated by assuming a graphene-based structural framework and using a 2D non-local density functional theory (NLDFT) treatment of the fluid density in the pores which are considered as energetically heterogeneous.[5]

The morphology of the materials was characterized using a Zeiss Ultra 55 electron microscope at an accelerating voltage of 5 kV. Samples were pressed onto conducting copper tapes and were then transferred onto stubs. Imaging was performed by maintaining working distances of 5-6 mm from the high-tension gun. Images were obtained at varied magnifications from 2000 x to 130000 x using an Inlens detector.

Electrical conductivity measurements performed using a Lucas Signatone QuadPro Resistivity System. Samples were prepared as thin films of ~ 100 μm by pressing under 10 T of pressure.

Solid-state nuclear magnetic resonance (ssNMR) spectroscopy was performed using a Bruker AVIII 400 MHz spectrometer equipped with 4 mm ambient-temperature and 3.2 mm low-temperature magic angle sample spinning (MAS) probes. {^{1}H-}^{13}C and {^{1}H-}^{15}N cross-polarization (CP) MAS experiments were recorded using 100 kHz nutation for ^{1}H π/2 pulses

and SPINAL-64 heteronuclear decoupling, a ramped (50-100%) power to match a Hartmann-Hahn CP condition when using 50 kHz for ^{13}C or ^{15}N nutation during 2 ms CP spin-locking and using a spin-echo of two rotor periods total duration (50 kHz for ^{13}C or ^{15}N π -pulses) before free-induction decay (FID) acquisition. A minimum of 8192 and 4096 transients were recorded for the {^{1}H-}^{13}C and {^{1}H-}^{15}N CPMAS experiments, respectively, using a recycle delay of 0.5 s between transients and 250 Hz exponential apodization before Fourier transformation of the FID. The 2D z-filtered TEDOR ^{15}N–^{13}C dipolar correlation spectrum was recorded with a starting {^{1}H-}^{13}C CP step of 2 ms, 1.3 ms total TEDOR mixing (to ensure correlation peaks are only from bonded ^{15}N–^{13}C pairs), 6400 transients for each of 16 complexes (States-TPPI) t_1 increments of 123.35 μs, using a recycle delay of 0.5 s between transients and 250 Hz exponential apodization in both dimensions before double Fourier transform.

2.2 Electrochemical Techniques

A multichannel VMP3 potentiostat with EC-Lab software (Biologic) was used for all electrochemical measurements. The fabricated cells were tested using cyclic voltammetry (CVs), galvanostatic charge-discharge (CDs) and electrochemical impedance spectroscopy (EIS) techniques. CVs were performed in a range of scan rates from 10 mV/s to 1 V/s. CD curves were obtained using current densities in the range from 0.5 to 100 A/g. EIS measurements were studied with a sinusoidal voltage amplitude of 5mV within a frequency range spanning from 100 kHz to 10 mHz. The fundamental about these techniques are described in annex I. Cells were fabricated in three and two-electrode configurations for fundamental and device performances study respectively. In the case of two-electrode configuration, a symmetrical SC was fabricated by using two electrodes of same weight prepared from the same materials. In case of a three-electrode configuration, a Ag wire served as reference electrode and an electrode of YP-50F porous carbon served as counter electrode. The mass of counter electrode were always at least 10 times higher than that of the working electrode. Specific details about the device configurations, components, electrolytes and the electrochemical test conditions are given in the next sections in the respective chapters.

3. Experimental Details from Chapter II

In this chapter, graphene hydrogels were prepared from GO solutions using hydrazine hydrate, 1,2-diaminoethane and 1,4-diaminobutane as gel formation agents. All the reagents were purchased from Sigma Aldrich and used as such. The gels thus formed are named as GH-HD, GH-ED and GH-DB. Initially, an optimization of the concentrations of GO and the diamine was performed by studying the gel formation process of GH-HD. Later, the optimized conditions of GO concentration and diamine equivalents were later used to synthesize GH-ED and GH-DB. Reduced graphene oxide (RGO), was also synthesized as a control material using hydrazine hydrate as the reducing agent. GO was synthesized following the protocol described in section 1.1.1 and was as the precursor for all the syntheses. Varied concentrations of GO were obtained by diluting or concentrating the 5 mg/mL precursor solution.

3.1 Synthesis of Graphene Hydrogels (GHs)

An earlier report in the literature describing the effort to synthesize GH with 1.5 mg/mL GO and 41 mmol/L of hydrazine hydrate was unsuccessful.[4] Hence, we chose to perform a series of control experiments to identify if a monolith could be assembled for specific values of GO concentration and diamine equivalents. A specific amount of diamine, ensuring excess of N atoms in the reaction mixture, was first calculated. For one mole of GO, one molar equivalent of diamine, providing two molar equivalents of N atoms, was assumed to be a sufficiently excess condition (considering no stirring during reaction). Firstly, formula weight of the synthesized GO was calculated from the elemental composition obtained by XPS. The elemental percentages of 72.5 and 27.5 for C and O in the synthesized GO assign its formula weight as 13.1 g. One mg of GO thus corresponds to 0.076 mmol of GO. Hence, we decided to attempt synthesizing hydrazine assisted gel using 3.7 μL of hydrazine monohydrate (corresponding to 0.076 mmol of pure hydrazine) for 1 mg of GO.

Later, a range of GO concentrations (0.5, 1, 2, 3, 4 and 5 mg/mL) were chosen to test the feasibility of gel formation. In a typical reaction procedure, 15 ml of GO solution (with a certain concentration) was mixed with 3.7 μL of hydrazine monohydrate per 1 mg of GO in a sealed vial. The mixture was sonicated for 10 minutes to ensure homogenized solution. Later, the sealed vial was heated in an oil bath at 80°C for 24 h under no stirring condition. After cooling

the vials to room temperature gel formation was visually analyzed by transferring the contents into petri dishes (Figure VII-2). No gel formation was observed with low GO concentrations of 0.5, 1 and 2 mg/mL. In the case of 3 and 4 mg/mL GO concentrations, lumps of fragile gels were observed. A rigid gel could be obtained with 5 mg/mL GO concentration and is shown here after washing with plenty of water (250 mL) and transferred into the petri dish. Hence, 5 mg/mL GO concentration and one equivalent diamine condition successfully demonstrates gel formation.
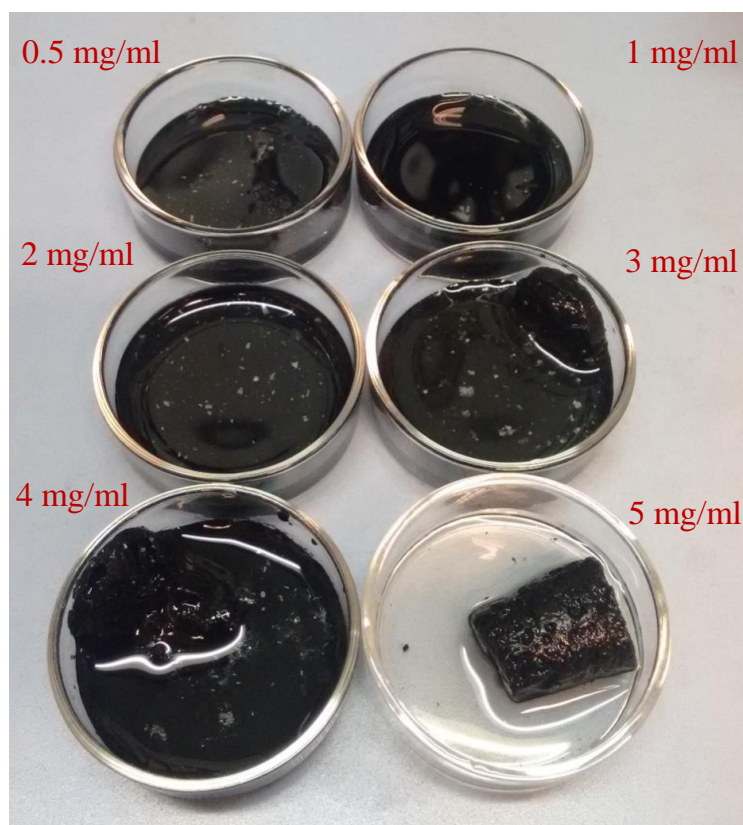

Figure VII-2 Digital photograph showing the end products of gel formation reaction with different concentration of GO. 5 mg/mL GO concentration results in a rigid gel that could be washed and transferred into petri dish as a monolith.

Further, we studied the influence of equivalents of hydrazine with a constant GO concentration of 5 mg/mL. Apart from the one equivalent of hydrazine studied above, 0.2, 0.5 and 2 equivalents were also tested under similar reaction conditions (Figure VII-3). The gel pieces formed were transferred into petri dishes for visual analysis. At low equivalents of 0.2 and 0.5 small and fragile lumps of gel could be seen whereas 1 and 2 equivalents form stable gels. Four probe measurements of 1 and 2 equivalents gels showed close electrical conductivity values of 1141 and 1180 S/m. Hence, 1 equivalent diamine and 5 mg/mL GO concentration were chosen for further analysis with other diamines.

GH-HD, GH-ED and GH-DB were obtained by reaction of hydrazine monohydrate (0.28 mL), 1,2-diaminoethane (0.38 mL) and 1,4-diaminobutane (0.5 g) respectively with 15 mL of 5 mg/mL GO. The synthesized gels were washed with copious amounts of water through a P4 filtration funnel. Material characterization was performed on freeze dried gels and electrochemical testing was done on cut pieces of these gels.
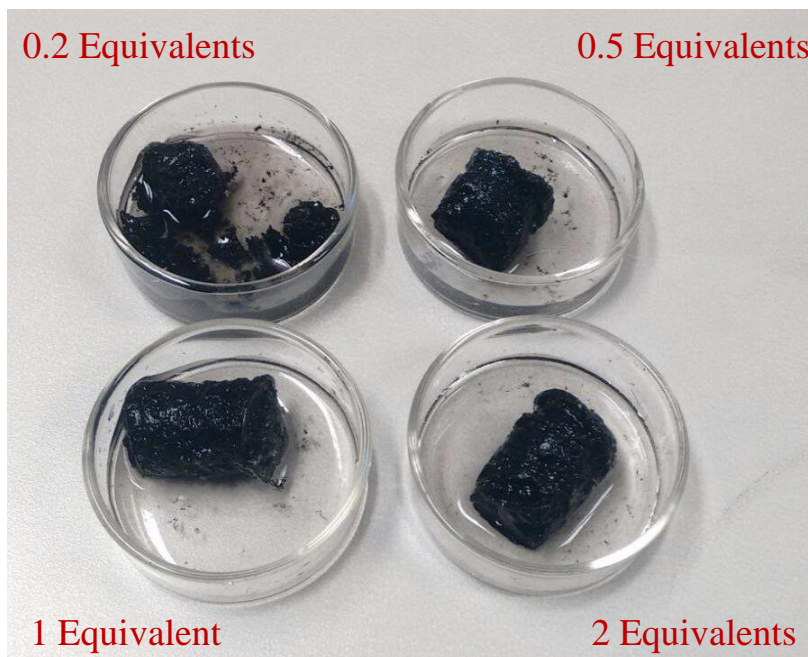

Figure VII-3 Digital photograph showing the end products of gel formation reaction with different equivalents of hydrazine. 1 and 2 equivalents form stable gels whereas 0.2 and 0.5 equivalents form fragile pieces of gels.

3.2 Synthesis of Reduced Graphene Oxide (RGO)

RGO was prepared through chemical reduction of GO to critically understand the implications of porous structure in supercapacitor performances. RGO was synthesized by reacting hydrazine hydrate with GO solution under the same reaction conditions that are used for GH-HD, except for an additional stirring. The synthesized product was washed with copious amounts of water through a P4 filtration funnel. The end product was dried under vacuum at 65°C overnight.

3.3 Methylene Blue Adsorption

The specific surface area of the gels was measured using the methylene blue (MB) adsorption method. This is a common analytical technique to determine the surface area of graphitic materials in wet form. UV-vis spectra recorded at a wavelength of 655 nm are used to draw a

calibration line. MB is known to physically adsorb onto graphene; hence the surface area was calculated by adding a known mass of gel (~2 mg) into a standard concentration of methylene blue (75 ml of $5*10^{-5}$ M) in deionized water. The methylene blue and gel mixture were continuously stirred for 36 h to enable maximum MB adsorption. The mixture was then allowed to settle and further centrifuged to remove any graphene derived suspended material. The remaining unadsorbed methylene blue concentration was determined by analyzing the supernatant. Knowing the initial and unabsorbed concentrations, the adsorbed MB concentration can be deduced. Considering that 1 mg of MB represents 2.54 m^2, the solvated surface area is then extrapolated.

3.4 Electrochemical measurements

The as prepared cylindrical GHs were cut into several slices of GH (~ 1 mm thickness) (Figure VII-5). In order to find out the exact mass, a calibration of the dried mass to wet mass of the slices was established by freeze drying some of the cut pieces. Two slices of wet gels with same mass were chosen and pressed onto nickel foams under 10 MPa pressure. A piece of filter paper (Whatman filter paper) was used as a separator between the electrodes. Electrodes and filter paper, soaked overnight in 6 M KOH electrolyte, were assembled as a layered structure into a home-made Swagelok-type two electrode cell configuration with Ni foam as current collector (Figure VII-4). Similarly, three electrode measurements were performed in 6 M KOH using a home-made three electrode experimental set-up with Pt wire as counter and saturated calomel electrode as reference.

The performance of SCs were evaluated using cyclic voltammetry (CV), galvanostatic charge-discharge (GCD) cycles and electrochemical impedance spectroscopy (EIS). CV and charge-discharge measurements in two electrode set-ups were performed between 0 to 1 V with scan rates from 10 to 1000 mV/s and 0.5 to 100 A/g respectively. CVs were obtained at 10 and 100 mV/s in a three-electrode configuration in the voltage range of -0.9 to 0.1 V. Graphene hydrogels were used as working electrodes, platinum foil as counter electrode and calomel as reference electrode. The gravimetric capacitances (C_{wt}) of GHs derived from galvanostatic discharge curves were calculated by using the equation $C_{wt} = 2I/(m(\Delta V/\Delta t))$, where I is the constant discharge current, m is the mass of one electrode and ΔV and Δt represent voltage change (excluding V_{drop}) on discharge and time for full discharge respectively. The

corresponding volumetric capacitances (C_{vol}) were calculated as follows: $C_{vol} = C_{wt} \times \rho$, where ρ is the packing density of GH. The gravimetric energy and power densities were calculated as $E_{wt} = C_{wt}V^2/8$ and $P = E_{wt}/\Delta t$. Packing densities were obtained by calculating the mass of the dried gel with a precision of 0.01 mg and by measuring the dimensions using scanning electron microscopy.
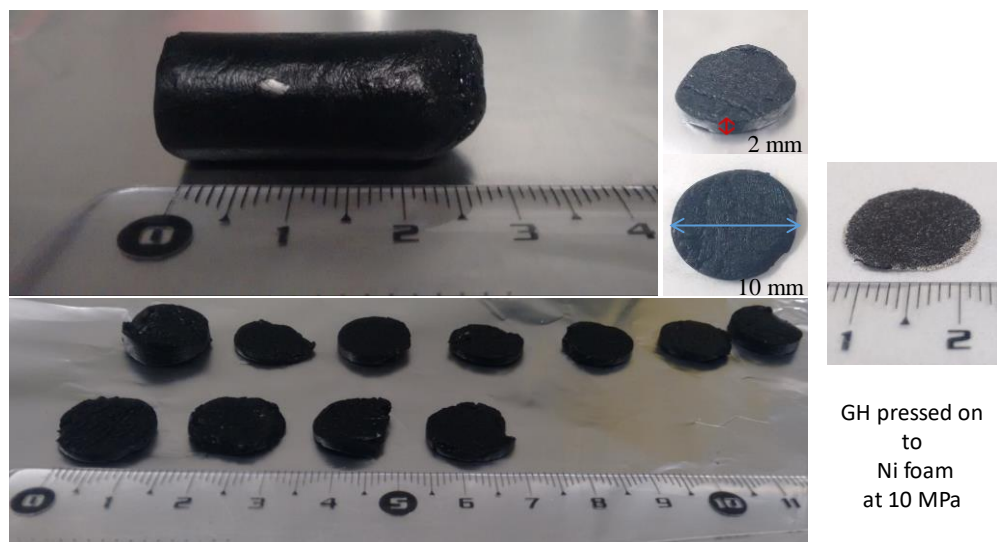

2 mm

10 mm

GH pressed on
to
Ni foam
at 10 MPa

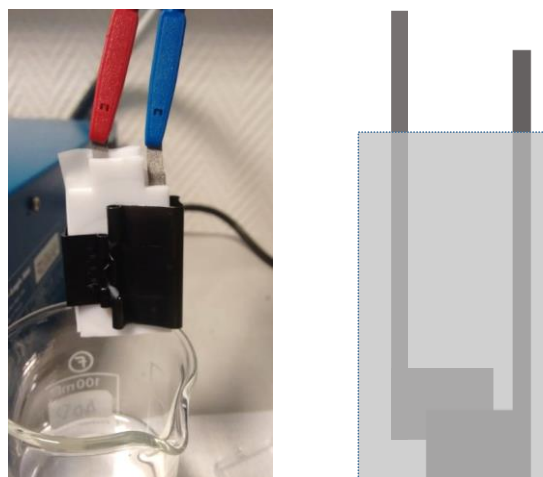*Figure VII-5 Digital pictures of the typical electrode fabrication procedure from the gels.*

Figure VII-4 The home-made set-up used for electrochemical tests in a two-electrode configuration. Electrode slices are pressed on to the rectangular part of the L shaped Ni foam pieces.

4. Experimental Details from Chapter III

In this chapter, pillared graphene materials were prepared from GO solutions using 1,5-diaminopentane, 1,6-diaminohexane and 1,8-diaminooctane as cross-linking agents. A two-step process of diamine cross-linking and chemical reduction process were done (Scheme VII-1). All the reagents were purchased from Sigma Aldrich and used as such.

4.1 Synthesis of Reduced Pillared Graphene Materials (RPs)

At first, 150 mL of 5 mg/mL GO solution and 57 mmol of each alkyl diamine dissolved in 150 ethanol were mixed and sonicated for 10 minutes. The chosen alkyl diamine equivalents are the same as those used in the previous chapter. The mixtures were heated at 80°C in a round bottom flask fitted with a condenser for 24 h under continuous stirring. The reaction mixtures were then filtered and cleaned with excess of water and ethanol and dried overnight under a vacuum at 100°C. The obtained pillared materials (Ps) were further reduced by treating with excess of hydrazine hydrate. Approximately 50 ml of hydrazine monohydrate was mixed with 150 mg of dried 5 P/ 6 P / 8 P in a round bottom flask and heated at 90°C under reflux for 24 h using continuous stirring. The reaction mixtures were later cooled, filtered through P3 filter and washed with copious amounts of ethanol, water and ethanol sequentially. The obtained product was then dried in the vacuum oven at 100°C overnight. The obtained materials were labelled as respective RPs (5 RP, 6 RP and 8 RP). As a control to the RPs, RGO was also synthesized by treating GO with hydrazine hydrate. For reliable comparisons, the above two-step protocol was followed for RGO as well.
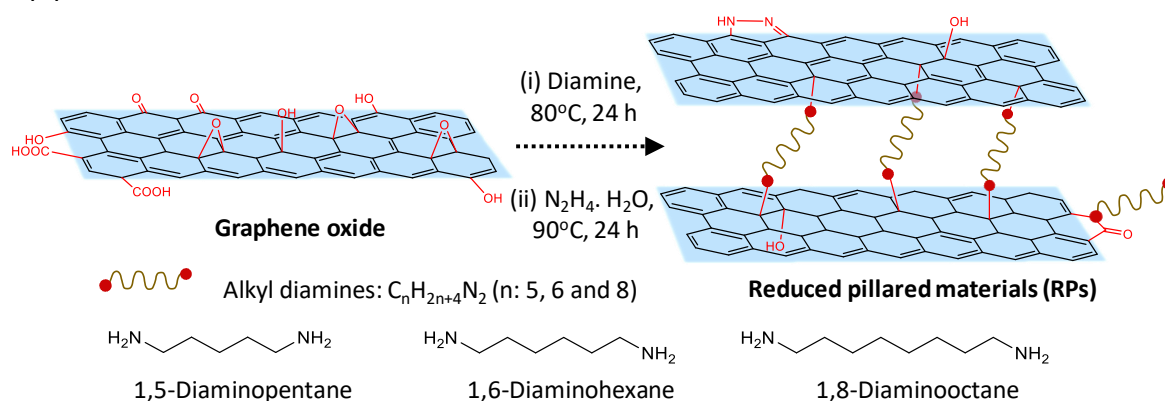
Scheme VII-1 Schematic representation for the synthesis of RPs. For simplicity, the materials are depicted with single graphene sheets.

223

4.2 Electrochemical Analysis

The synthesized materials were tested in a three-electrode supercapacitor configuration with porous carbon (YP-50F) as counter, silver wire as reference electrodes and a 25 μm thick cellulose sheet as a separator. Large porous carbon electrodes with excess weight (> 10 x) were used to counter the charges and ensure distinct responses from the working electrodes. A custom-built Swagelok® type cell (Figure VII-6) was used and the assembly was done in a glove box (< 0.1 ppm of H_2O and O_2). The working electrodes were fabricated as a slurry by mixing active materials, polyvinylidene fluoride (PVDF) and acetylene black carbon in a ratio of 80:10:10 using N-methyl-2-pyrrolidone and are coated onto 0.5 cm^2 stainless steel disks. The as prepared electrodes were dried at 65°C in air for 3 h prior to drying under vacuum at 120°C overnight. The dried electrodes were noted to weigh 1-1.5 mg resulting in loading densities of 2-3 mg/cm^2. 1 M tetralkylammonium tetrafluoroborate (TAABF$_4$) salt solutions in anhydrous acetonitrile with varying cations; ethyl (TEABF$_4$), propyl (TPABF$_4$), butyl (TBABF$_4$) and hexyl (THABF$_4$), are used as electrolytes. The performances of SC were evaluated using cyclic voltammetry (CV) at various scan rates (10, 20 and 50 mV/s). CV measurements were performed between - 1 to 1 V vs. Ag. at a scan rate of 20 mV/s. The gravimetric capacitances (C) were derived from CV curves using the equation C = (∫ I(v).dv) /(m(dv/dt).V), where ∫ I(v).dv
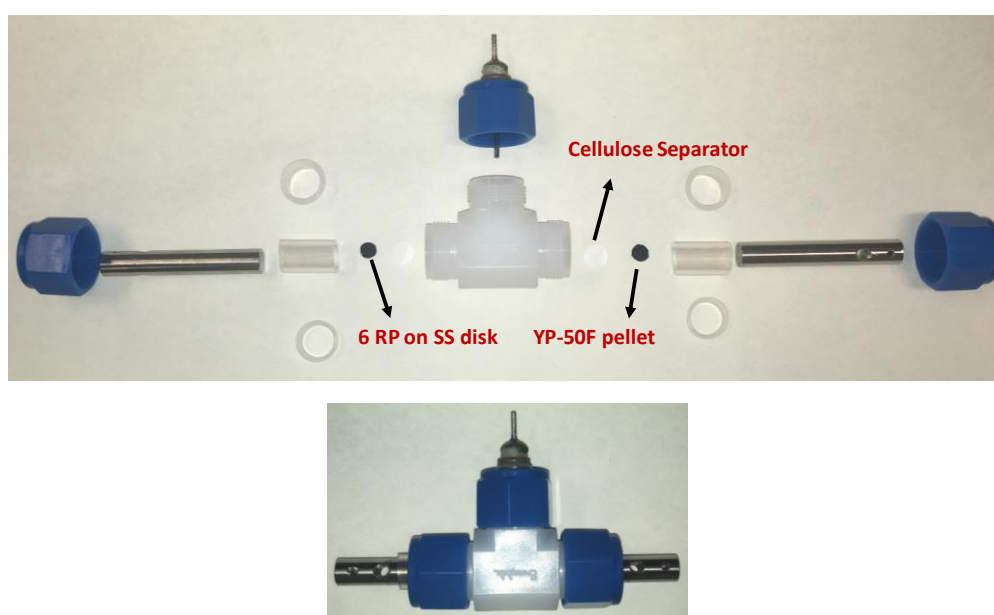

Figure VII-6 Custom-built Swagelok® cells were used to perform the electrochemical measurements. Top picture shows the individual components of the cell with a 6 RP coated SS-electrode, a cellulose separator, YP-50F counter electrode and a Ag wire as reference electrode. The bottom picture shows the fabricated cell.

is the total area under the curve in the potential window, dv/dt is the scan rate, m is the mass of the active material in the working electrode and V is the total potential window.

5. Experimental Details from Chapter IV

In this chapter, reduced pillared graphene materials (RPs) synthesized with 1,5 diaminopentane and 1,6-diaminohexane (details in previous section) were studied using EIS analyses. Additionally, pillared graphene hydrogels (GHs) were also synthesized in a one-step process with 1,6-diaminohexane as the pillar molecule (6 GH) (Scheme VII-2).

5.1 Synthesis of Pillared Graphene Hydrogel (6 GH)

15 ml of GO (5 mg/mL) and 1.21 g of diamine were mixed and sonicated for 10 min and then reacted in a sealed 23 ml Teflon vessel at 180°C for 17 h in an autoclave. The number of equivalents of alkyl diamine with respect to GO is the same as in the previous chapters. The resulting hydrogel was cleaned with excess amount of ethanol and water sequentially and freeze-dried using liquid N_2 to obtain 6 GH aerogels.
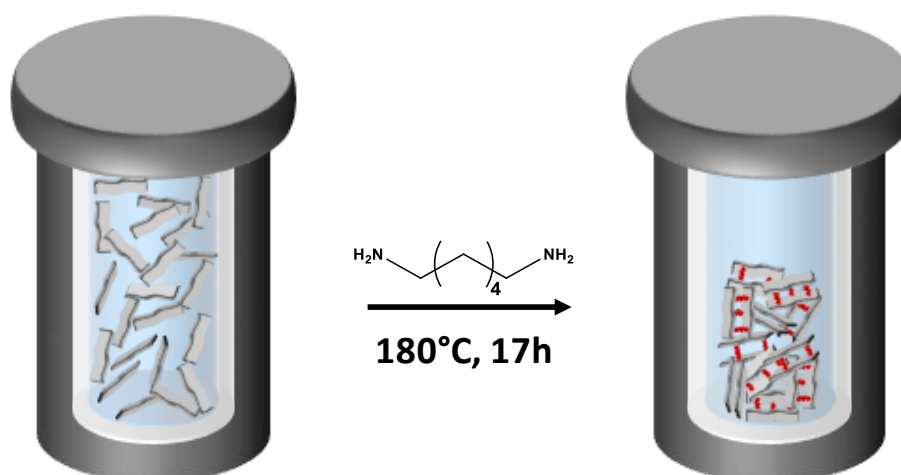
Scheme VII-2 Schematic representation of the synthesis of pillared graphene hydrogel in an autoclave.

5.2 Electrochemical Analysis

The synthesized RPs and GHs were studied in a three-electrode Swagelok® type electrochemical device as described in the last section (Figure VII-6). The components are assembled in a glove box (< 0.1 ppm of H_2O and O_2). 1M tetralkylammonium tetrafluoroborate (TAABF$_4$) salt solutions in anhydrous acetonitrile with varying cations; ethyl (TEABF$_4$), propyl (TPABF$_4$), butyl (TBABF$_4$) and hexyl (THABF$_4$), are used as electrolytes. The working electrodes were fabricated as a slurry by mixing active materials, polyvinylidene fluoride (PVDF) and acetylene black carbon in a ratio of 80:10:10 using N-methyl-2-pyrrolidone and are coated onto 0.5 cm^2 stainless steel disks. The as prepared electrodes were dried at 65°C in air for 3 h

prior to drying under vacuum at 120°C overnight. The dried electrodes were noted to weigh 1 - 1.5 mg resulting in loading densities of 2-3 mg/cm^2. Prior to EIS measurements, the cells were cycled at 50 mV/s scan rates in CVs until the electrolyte wets the whole porous material volume and the electrochemical signature reached gets a steady state – the area under the curve stabilizes (~100 cycles). For EIS measurements, cells were held at +1 V or -1 V vs. Ag in this three-electrode configuration until the current is almost null and then the frequency responses were measured. Obtained impedance values were normalized with electrode thicknesses and geometrical surface areas for plotting.

6. Experimental Details from Chapter V

In this chapter, 6 RPs and 6 GHs were synthesized with varied amounts of 1,6-hexanediamine equivalents. The synthesized materials were studied in two and three-electrode configurations using Swagelok® type cells described above (Figure VII-6).

6.1 Reduced Pillared Graphene Materials with Varied Equivalents

An aqueous solution of well-dispersed 5 mg/mL GO was prepared and used as a precursor for all syntheses. 6 RPs were synthesized in a two-step process of cross-linking with 1,6-diaminohexane and further chemical reduction with hydrazine hydrate. One equivalent of diamine to GO was used as a sufficiently excess condition providing two molar equivalents of N for 1 C in GO. The formula weight of the synthesized GO was calculated as 13.01 g from the elemental composition obtained by X-ray Photoelectron Spectroscopy (XPS). Each synthesis was performed with 75 ml of GO (28 mmol) with 1, 0.2, 0.1, 0.075 and 0.05 equivalents of diamine using 3.27, 0.651, 0.325, 0.243 and 0.162 g of 1,6-diaminohexane respectively. 75 ml of GO and diamine dissolved in 75 ml of ethanol were sonicated for 10 minutes and then heated under reflux at 80°C for 24 h in a round bottom flask while being continuously stirred. The reaction mixtures were later cooled, filtered through P4 filter and washed with copious amounts of ethanol, water and ethanol sequentially. The obtained product was then dried in the vacuum oven at 100°C overnight. The obtained pillared materials were further reduced by treating with excess of hydrazine hydrate at 90 °C under reflux for 24 h while being continuously stirred. The obtained reduced pillared materials were cleaned with an excess of water, dried under a vacuum at 100 °C, and labelled as the respective 6RPs.

6.2 Pillared Graphene Hydrogels with Varied Equivalents

An aqueous solution of well-dispersed 5 mg/mL GO was prepared and used as a precursor for all syntheses. 6 GHs were synthesized in a one-step hydrothermal process using 1,6-diaminohexane as cross-linking agent. Each synthesis was performed with 15 ml of GO (5.6 mmol) with 1, 0.2, 0.1, 0.05, 0.035 and 0.025 equivalents of diamine using 1.21, 0.242, 0.121, 0.060, 0.042 and 0.016 g of 1,6-diaminohexane respectively. 15 ml of GO and the required amount of diamine were sonicated for 10 min and then reacted in a sealed 23 ml Teflon vessel at 180°C for 17 h in an auto-clave. The resulting hydrogel was cleaned with excess amount of

ethanol and water sequentially and freeze-dried using liquid N_2 to obtain 6 GH aerogels. Ambient dried gels were obtained by drying the hydrogels at room temperature for 2 days and the remaining moisture was removed by heating in vacuum at 80°C overnight.

6.3 Electrochemical Analysis

For the ion sieving study, 1 M tetralkylammonium tetrafluoroborate (TAABF$_4$) salt solutions in anhydrous acetonitrile with varying cations; ethyl (TEABF$_4$), propyl (TPABF$_4$), butyl (TBABF$_4$) and hexyl (THABF$_4$), are used as electrolytes. The working electrodes were fabricated as a slurry by mixing active materials, polyvinylidene fluoride (PVDF) and acetylene black carbon in a ratio of 80:10:10 using N-methyl-2-pyrrolidone and are coated onto 0.5 cm^2 stainless steel disks. The as prepared electrodes were dried at 65°C in air for 3 h prior to drying under vacuum at 120°C overnight. The dried electrodes were noted to weigh 1 - 1.5 mg resulting in loading densities of 2-3 mg/cm^2. The components are assembled in a glove box (< 0.1 ppm of H_2O and O_2). CVs were obtained at 20 mV/s, as a sufficiently low scan rate, for the ion sieving study. Later on, TEABF$_4$ was chosen as an electrolyte with sufficiently small ions to enter the galleries of 6 RPs and 6 GHs. CVs were performed in -1.3 to 1.5 V vs. Ag potential window at various scan rates ranging from 10 to 1000 mV/s to obtain the power capabilities of the synthesized materials. The gravimetric capacitances (C) were derived from CV curves using the equation C = ($\int$ I(v).dv) /(m(dv/dt).V). $\int$ I(v).dv is the total area under the curve in the potential window, dv/dt is the scan rate, m is the mass of the active material in the working electrode and V is the total potential window. EIS analyses were performed at -1 and 1 V vs. Ag in a three-electrode configuration. Two-electrode CVs were performed using equal weights of active materials in both the electrodes and tested in a 0-2.8 V voltage range at 10-1000 mV/s scan rates.

7. References

(1)   Hummers, W. S.; Offeman, R. E. Preparation of Graphitic Oxide. J. Am. Chem. Soc. 1958, 80 (6), 1339–1339.

(2)   Ashok Kumar, N.; Gambarelli, S.; Duclairoir, F.; Bidan, G.; Dubois, L. Synthesis of High Quality Reduced Graphene Oxide Nanosheets Free of Paramagnetic Metallic Impurities. J. Mater. Chem. A 2013, 1 (8), 2789–2794.

(3)   Wang, G.; Zhang, L.; Zhang, J. A Review of Electrode Materials for Electrochemical Supercapacitors. Chem. Soc. Rev. 2012, 41 (2), 797–828.

(4)   Chen, W.; Yan, L. In Situ Self-Assembly of Mild Chemical Reduction Graphene for Three-Dimensional Architectures. Nanoscale 2011, 3 (8), 3132–3137.

(5)   Jagiello, J.; Olivier, J. P. 2D-NLDFT Adsorption Models for Carbon Slit-Shaped Pores with Surface Energetical Heterogeneity and Geometrical Corrugation. Carbon 2013, 55, 70–80.

Annex

Annex: Electrochemical Characterization of SCs

Electrochemical analyses of the synthesized materials were performed using two or three-electrode cell configurations. In a three-electrode cell configuration, the material of interest is used as working electrode and its current/potential/frequency response is obtained with respect to reference electrode. A porous carbon with nearly 10 times the weight of the working electrode and that has sufficient charge storage capability is chosen as the counter electrode. In a two-electrode cell configuration, symmetric SCs were studied using the material of interest as both the working and counter electrode. Additionally, the counter is used as the reference electrode.

Different electrochemical techniques used in this thesis work to analyze the materials are described in this section. The three main techniques, used in this thesis are cyclic voltammetry, chronopotentiometry (generally called as charge-discharge cycling) and electrochemical impedance spectroscopy. The information that can be extracted from these techniques concerning the materials and their responses in an electrochemical cell are also discussed.

Cyclic Voltammetry

Cyclic voltammetry (CV) is the most widely used technique to acquire quantitative information about electrochemical reactions. CV provides information on redox processes, heterogeneous electron transfer processes and faradaic adsorption processes. The CV technique involve scanning the potential of the working electrode with respect to the reference electrode using a triangular potential waveform with respect to time. Essentially, the working electrode is cycled between two pre-selected potential values with a chosen sweep rate (potential change per second). During the potential sweep, ions in the electrolytes gradually adsorb on the electrodes that are oppositely polarized. The resulting current from the electrochemical processes is recorded in relation to the applied potential. The current response thus plotted with respect to the applied potential is called as a cyclic voltammogram. This technique provides useful information such as the stable electrochemical window of the electrolyte, specific capacitance of the electrode and cyclability of the active materials or devices.

Different equivalent circuit models of EDLCs and the corresponding CV profiles are shown in (Figure-1). An ideal double layer capacitor (Figure1-a) exhibits perfect rectangular CV profile, however, in reality, more complex CV are observed. Two simplified examples are shown in Figure-1b&c. A non-ideal CV could involve charge transfer across the electrode surface (represented in faradaic or leakage resistance, R_F, in parallel with the double layer capacitance), giving a sloping CV curve (Figure-1b). The slope of the CV ($\Delta I/\Delta E$) corresponds to the reciprocal of faradaic resistance ($1/R_F$). Another general non-ideal case arises from the resistances corresponding to bulk electrolyte (low ionic conductivity) and contact between the
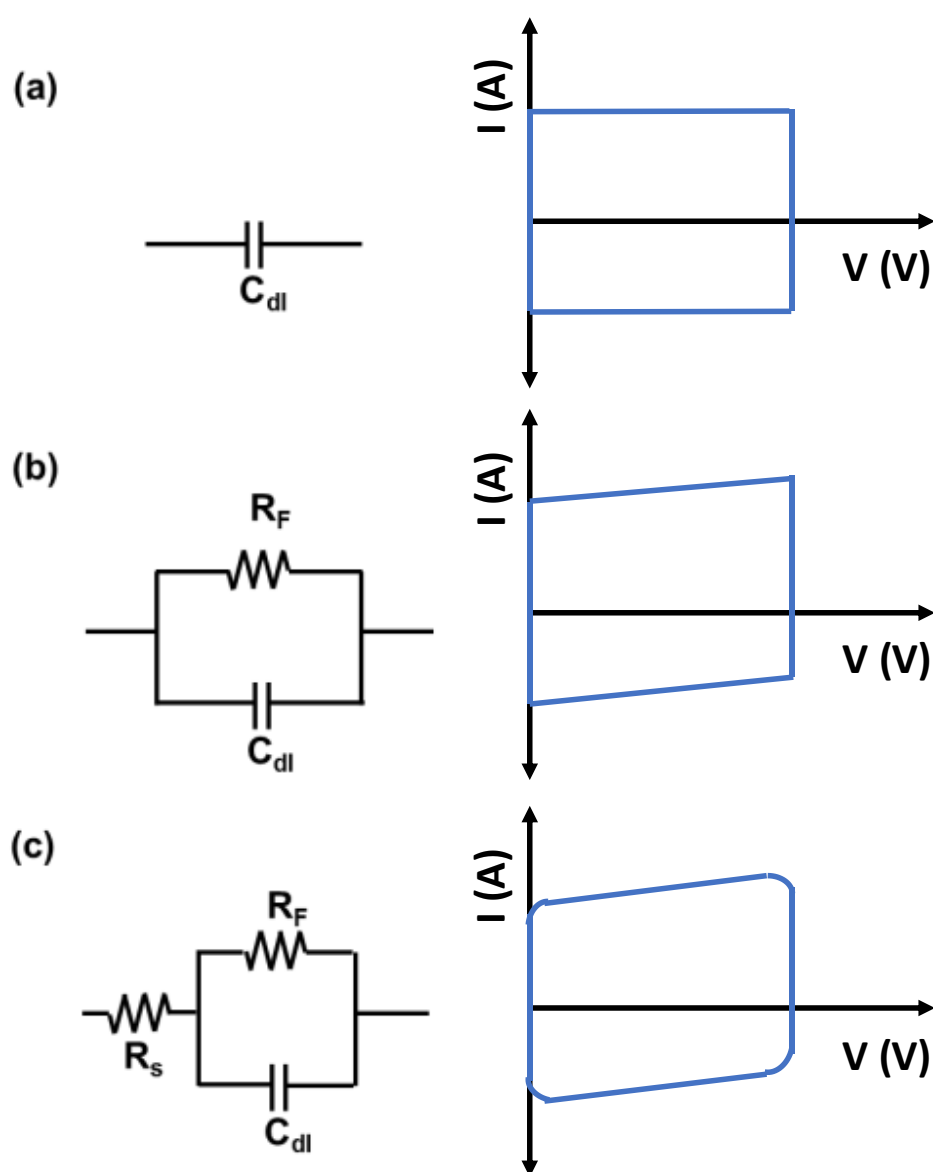

Figure-1 Equivalent circuit models and corresponding cyclic voltammograms of (a) ideal double layer capacitor, (b) capacitor in parallel with leakage resistance and (c) simplified supercapacitors model taking leaking resistance and equivalent series resistance into account.

current collector and the electrode material. These resistances result in deviations in the CV curves at the corners of the plots (Equation-1c).

Capacitances of the electrode can be calculated from the cyclic voltammogram by Equation 1. C is the electrode capacitance in Farads per gram (F/g) in a three-electrode cell, I is the

$$C = \frac{I}{\left(\dfrac{dV}{dt}\right).m}$$

Equation 1

recorded current in Amperes (A), dV/dt is the scan rate used (V/s) and m is the mass of the electrode material. For two-electrode symmetrical cells, since the measured capacitance corresponds to the whole cell, the value must be multiplied by 2 to obtain the single electrode capacitances and average mass of both the electrodes is used as m.

Chronopotentiometry

The electrochemical behavior of a material can also be studied through a constant current technique. Typically, positive and negative currents are used to charge and discharge the electrodes and the corresponding changes in potential are observed with respect to time. During the charge and discharge processes, electrolytic ions adsorb and desorb respectively on the oppositely polarized electrodes. Several cycles of the charge-discharge processes are performed to analyze the cycle life of the SC performances. This technique resembles the charging and discharging processes that the energy storage devices undergo in practical applications. Figure-2a&b show the applied currents and the resulting potential waveform in an ideal EDLC SCs. However, the cell resistances arising from various components (electrolyte, material and contacts) can result in an ohmic drop at the start of each charge and discharge cycle (Figure-2c). Large drop due to such resistances mean irreversible losses through energy dissipation, which are crucial when large currents are used. Capacitances of the materials tested could be obtained from using the slope of the potential vs time curve (Equation 1).
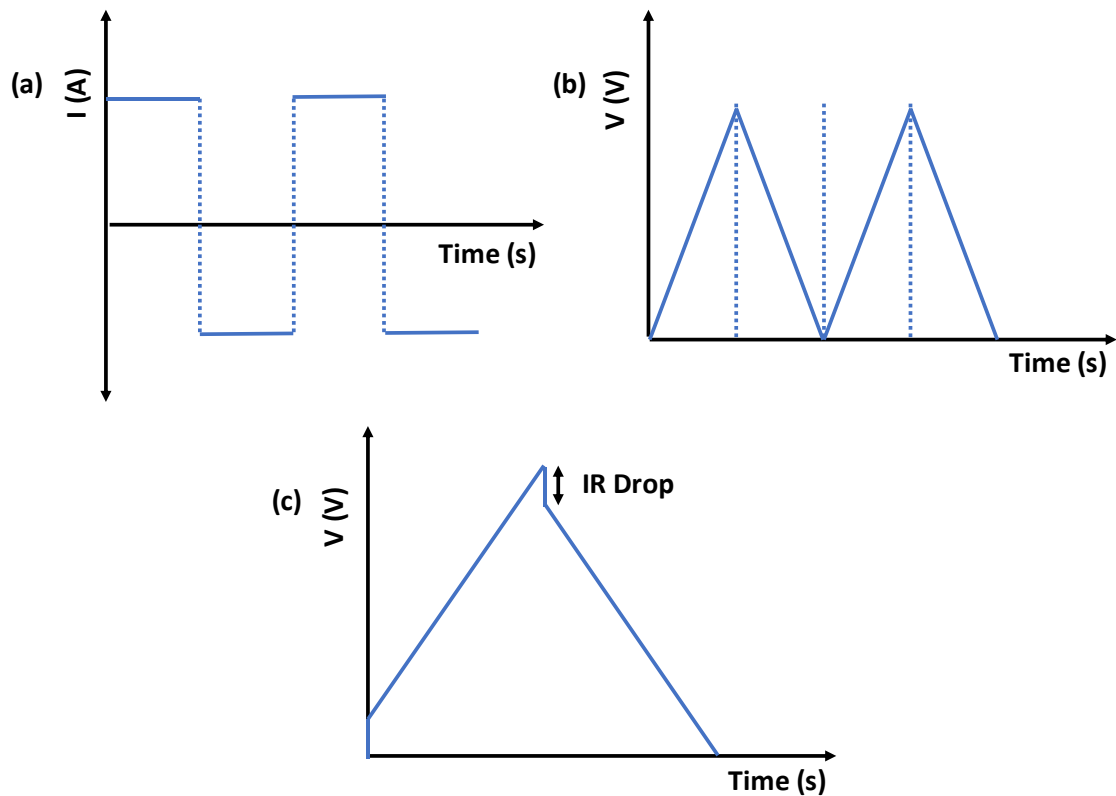
Figure-2 (a) The current profile in a typical chronopotentiometry technique and (b) the corresponding voltage profile in an ideal EDLC SC. (c) In real SCs, a drop in the potential arising from the ohmic drop is seen in the profile.

Electrochemical Impedance Spectroscopy (EIS)

Electrochemical Impedance Spectroscopy (EIS) is an important method for characterizing SCs. By investigating the alternating current (ac) response generated by an alternating voltage (av) addressed to the electrode over a range of frequencies, EIS allows the capacitance of the electrode or cell to be determined as a function of frequency. Moreover, each physical/chemical phenomenon in the electrochemical process has its unique relaxation time and can be described with corresponding equivalent circuit. By sweeping over a wide range of frequency, each physical/chemical process in the system could be separated, and the equivalent circuit of the electrochemical system could be modelled, thus, the equivalent series resistance (ESR) of a SC could be evaluated. The ESR is an important parameter for SC device design as the power performances of the SCs is often limited by this internal cell resistance.

EIS is performed by applying a low-amplitude sinusoidal wave of alternating voltage (~ 5 mV) with a range of frequencies from few mHz to hundreds of KHz. The applied alternating voltage is expressed in (Equation 2) where V_0 is the amplitude (maximum) of the voltage signal in Volt, ω is the angular frequency in radian per second, related to the frequency by the $\omega = 2\pi f$.

$$V(\omega) = V_0 \sin(\omega t)$$

Equation-2

The alternating current (in Amperes) in response to the applied alternating voltage is measured and expressed as a sinusoidal function with a peak value of I_0 (Equation-3).

$$I(\omega) = I_0 \sin(\omega t + \Phi)$$

Equation-3

Applying Euler's formula; $e^{jx} = \cos x + j \sin x$, Equation-2 can be presented in a complex notion as Equation-4.

$$V(\omega) = V_0 \exp(j\omega t)$$

Equation-4

$$I(\omega) = I_0 \exp(j(\omega t + \Phi))$$

Equation-5

The impedance is defined as the ratio between complex and current complex in Equation-6.

$$Z(\omega) = \frac{V_0}{I_0} \exp(-j\Phi)$$

Equation-6

The complex impedance Z can also be represented as Equation-7 and the modulus defined as Equation-8 where Z' and Z'' are the real and imaginary parts of the complex impedance respectively.

$$Z(\omega) = |Z| \exp(-j\Phi) = Z' + jZ''$$

Equation-7

$$|Z(\omega)| = \frac{V_0}{I_0} = \sqrt{(Z'^2 + Z''^2)}$$

Equation-8

The impedance of the three commonly used ideal electrical elements; capacitors (Z_C), Ohmic resistors (Z_R) and inductors (Z_L), described by Equation-9, Equation-10 and Equation-11 respectively. C, R and L are capacitor, resistance and inductance respectively.

$$Z_c = \frac{1}{j\omega C}$$

Equation-9

$$Z_R = R$$

Equation-10

$$Z_L = j\omega L$$

Equation-11

Nyquist plot is commonly used for EIS studies with real and imaginary components of impedance on X and Y axes respectively. Figure-3 shows such plots for two simple equivalent circuits mentioned in Figure-1 The equivalent model shown in is still too simplified and a common Nyquist plot obtained for a EDLC SC is displayed in Figure-4. Some key characteristics of this plot could be seen clearly; (i) at high frequencies, the SC behave like pure resistance. The point where the curve intercepts the x-axis corresponds to the series resistance of the cell. (ii) A semi-circle loop can be observed at high frequencies (Zone I). This loop originates from the current collector − carbon electrode interface and can be removed by proper elaboration of the current collector. (iii) A line with a slope of 45º in the mid-range is related to the electrolyte penetration inside the porous electrode (Zone II). The time required for the ions to adsorb in the inner pore surfaces is longer than for the accessible outer pores. This non-uniform charging rate on the available electrode surface is revealed on the impedance as a characteristic curve with the 45º slope. (iV) At low frequency, the impedance tends toward a pure capacitive behavior hence a vertical line is observed (Zone III). The ESR of the SC ($\Omega.m^2$) can be obtained by Equation-12, where R_s is the impedance that intercepts the X-axis in Ω, and A is the surface area of the electrode in m^2.
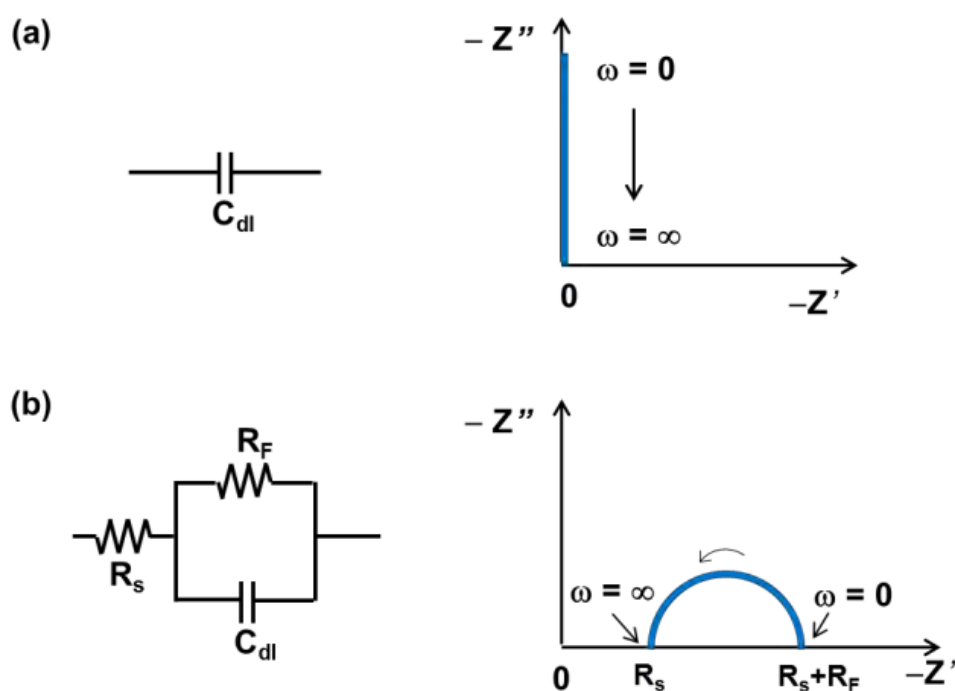
$$ESR = R_S.A$$

Equation -12

Figure-3 Equivalent circuit and its corresponding Nyquist plots of (a) an ideal double-layer capacitor (C_{dl}) and (b) a more complex model, which considers the leakage resistance (R_F) and the equivalent series resistance (R_s).
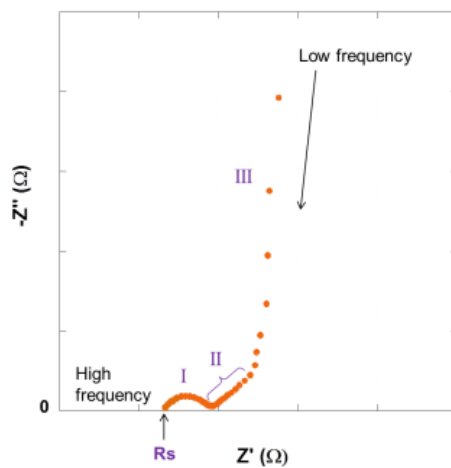

Figure-4 Typical Nyquist plot of a EDLC SC with three different responses in low, mid and high frequency ranges.

240

Résumé:

Ce travail de thèse décrit le développement de matériaux dérivés d'oxyde de graphène testés pour le stockage électrochimique de l'énergie. Les propriétés particulières de ce matériau, telles que sa grande surface développée et sa conductivité élevée, font du graphène un matériau d'intérêt pour des applications dans des systèmes de type supercondensateur. L'impact de la macroporosité des dérivés de graphène est un point clé adressé dans de nombreuses études décrivant notamment les effets de la structuration 3D du graphène. Néanmoins, malgré la morphologie en feuillets du graphène peu d'études sont menées sur l'impact de sa potentielle structuration lamellaire.

Dans ces travaux de thèse, une famille de dérivés de graphène pontés présentant des distances inter-feuillets de graphène (d) variées a été étudiée de façon à établir et de comprendre le lien entre les valeurs de capacité obtenues et cet espacement d. Des diamino alcanes de longueurs de chaines alkyles différentes ont été utilisés comme agent pontant et ont permis d'obtenir l'assemblage de feuillets de graphène présentant des distances inter-feuillet d désirées pour l'étude électrochimique (7-12 Å). Des études ss-NMR ont permis de mettre en évidence le caractère covalent de l'interaction entre les molécules pontantes et le graphène. Pour réaliser les mesures électrochimiques sur ces matériaux, la famille des tetrafluoroborate de tetraalkyl ammonium dans l'acétonitrile a été utilisée comme electrolyte. L'intérêt de cette famille est que la taille du cation peut être modulées (6.8 Å pour tetraethyl à 9.5 Å pour tetrahexyl), alors que la taille de l'anion reste constante. Une étude électrochimique complète a été menée pour différents couples de matériaux avec un espacement inter-feuillet d donné et de cation électrolytique ayant un diamètre donné. Les résultats obtenus ont révélé que les ions de taille inférieure à la distance d peuvent s'insérer au sein des galeries formées par les feuillets de graphène pontés, alors que les ions de dimensions supérieures voient l'accès à cette porosité fortement restreint voir bloqué. Les différences d'accès à ces sites d'adsorption en fonction du couple d/taille du cation est clairement illustrée par les valeurs de capacité obtenues (pour une graphène ponté avec des chaines alkyles comptant 6C: 130 F/g TEA et 50 F/g pour THA). Compte-tenu du fait que la taille des ions solvatés est toujours supérieure à d, cette corrélation directe entre d et taille du cation suggère que les ions accèdent aux galeries après avoir partiellement perdu leur

sphère de solvatation. Des mesures d'électrochimie d'impédance ont confirmé ces résultats d'électrochimie et ont mis en évidence que le transport des ions au sein des galeries était limité, notamment par la présence des molécules pontantes. Ainsi, une optimisation de la densité de greffage et de la porosité à l'extérieur des galeries a été effectuée conduisant à l'obtention de matériaux permettant d'atteindre des capacités volumiques (210 F/cm^3) parmi les meilleures rapportées dans la littérature et présentant des densités de puissance (90 F/cm^3 at 1 V/s) importantes.

Mots clés: Supercondensateur, adsorption d'ions, dérivés de graphene, fonctionnalisation

Abstract:

This PhD thesis focuses on developing graphene-based materials for electrochemical energy storage. Graphene-based materials have been extensively studied for applications in supercapacitors due to their favorable material characteristics. However, much of this interest is focused on the bulk porosity of graphene derivatives with a surprisingly little attention given to their unique layered structures. In this thesis, the role and capacitance contributions of the inter-layer galleries were investigated in a model class of pillared graphene materials with varying inter-layer separation (d-spacing). Alkyl diamines with varying chain lengths were used to obtain cross-linked graphene layers with desired d-spacing (7-12 Å). A family of tetraalkylammonium tetrafluoroborate (TAABF4) electrolytes with varying cation (6.8 for tetraethyl to 9.5 Å for tetrahexyl) and constant anion (4.8 Å) sizes were used to investigate these materials properties. A comprehensive study with different d-spacing values and ion sizes has revealed that the ions with smaller naked sizes than the d-spacing access the inter-layer galleries whereas the larger ions are restricted. This direct correlation between naked ion size and the gallery spacing suggests partial desolvation of the electrolyte ions during adsorption. Electrochemical impedance analyses have supported these findings and have also indicated extremely impeded ion transport in the galleries. Finally, through optimization of diamine pillar density and porosity of the pillared materials, high volumetric capacitances (210 F/cm^3) in graphene materials with excellent power density (90 F/cm^3 at 1 V/s) were achieved. The robustness of the pillars has been confirmed indirectly by electrochemical cycling and X-ray diffraction investigation and directly through ss-NMR studies that provided evidence of the covalent link between the organic molecules and graphene.

Keywords: Supercapacitors, ion sorption, pillared graphene materials